KU LEUVEN

UNIVERSITAT DE BARCELONA

ARENBERG DOCTORAL SCHOOL
Faculty of Science

PARADISE: a model for energetic particle transport in the solar wind

Nicolas Wijsen

Dissertation presented in partial fulfilment of the requirements for the degree of Doctor of Science (PhD): Mathematics (KU Leuven) and the degree of Doctor of Physics (Universitat de Barcelona)

Supervisors:
Prof. Dr. S. Poedts
Dr. À. Aran

April 2020

PARADISE: a model for energetic particle transport in the solar wind

Nicolas WIJSEN

Examination committee:
Prof. Dr. M. Zambon, chair
Prof. Dr. S. Poedts, supervisor
Dr. À. Aran, supervisor
Prof. Dr. R. Keppens
Prof. Dr. R. Vainio
(University of Turku)
Prof. Dr. B. Sanahuja
(University of Barcelona)
Dr. J. Pomoell
(University of Helsinki)

Dissertation presented in partial fulfilment of the requirements for the degree of Doctor of Science (PhD): Mathematics by the KU Leuven and the degree of Doctor by the Universitat de Barcelona in the doctoral programme in Physics.

April 2020

© 2020 KU Leuven – Faculty of Science
Uitgegeven in eigen beheer, Nicolas Wijsen, Celestijnenlaan 200B , B-3001 Leuven (Belgium)

Alle rechten voorbehouden. Niets uit deze uitgave mag worden vermenigvuldigd en/of openbaar gemaakt worden door middel van druk, fotokopie, microfilm, elektronisch of op welke andere wijze ook zonder voorafgaande schriftelijke toestemming van de uitgever.

All rights reserved. No part of the publication may be reproduced in any form by print, photoprint, microfilm, electronic or any other means without written permission from the publisher.

Preface

At the time of writing this preface, exactly five years have passed since I was a first-year master student, trying to choose a thesis subject out of a list of numerous interesting astrophysical topics. Little did I know that the choice I would make on that day would determine my career for the following five years, and maybe even for many years still to come. Eventually, I stumbled upon a topic proposed by Prof. Stefaan Poedts, which was situated in the domain of solar and space weather physics. Upon meeting with Stefaan, his enthusiasm and long-term vision quickly convinced me to delve into those fields of research, first as a master student and later as a PhD student. Five years have passed, and with the extra information I have required during those years, I would still advice my past me to make the same decision as I did back then. This is because the past few years have been filled with memorable experiences, and there are many people I would like to thank for that.

First of all, I wish to express my sincere appreciation to my supervisor Stefaan, for his enthusiasm, impressive knowledge, and for always being available to provide me with excellent advice. His confidence in my research work inspired me to continue improving and developing my skills as a researcher. By involving me into larger international projects, he continuously fuelled my motivation to succeed in this endeavour. Moreover, I would like to thank Stefaan for giving me the opportunity to obtain a double Phd at the KU Leuven and the University of Barcelona.

An equal amount of gratitude goes to Dr. Àngels Aran, my supervisor at the University of Barcelona. I am very grateful for her excellent guidance and the constant support, which have been essential in the completion of this thesis. Our long afternoon discussions on solar energetic particles were very fruitful and educative to me. The same can be said about our discussions on the complex political situation concerning Catalonia, whilst taking a tallat-break. I also which to thank Àngels for all the assistance that she provided to get the administration for this double PhD in order.

I would like to express my gratitude to Dr. Jens Pomoell, who has been very helpful by providing me advice and critical feedback throughout this project. It was his suggestion

to look into stochastic differential equations, which eventually formed the backbone of the work presented in this thesis.

I would like to thank Prof. Marco Zambon, the chair of my examination committee, for taking care of the organization of the defence during the Coronavirus pandemic. Many thanks to Prof. Rony Keppens, Prof. Blai Sanahuja, and Prof. Rami Vainio, for their willingness to read and review my dissertation, and for their insightful comments that were very useful to me for improving the quality of this thesis. In particular, I would like to acknowledge Prof. Rami Vainio for his help in interpreting the physics behind the simulation results presented in Chapter 8 of this manuscript.

My sincere thanks also go to Prof. Dr. Du Toit Strauss, for the interesting discussions, for giving me the opportunity to complete a research stay in South Africa, and for introducing me to the his excellent research team. In particular, I would like to thank Jabus van den Berg for the helpful discussions on the derivation of the focused transport equation.

It is a pleasure to thank all my wonderful colleagues of the CmPA and the ICCUB, who made going to work an enjoyable experience on a daily basis. Many thanks also to my friends Matthias and Daan, for teaching me to ski again; a most welcome distraction during this work. Likewise, I am very grateful to the members of the Chill Zone, Brecht, Hendrik-Jan, Cedric, Iris, Elien, Ben, Wim, Julie, Pieter, Lore, Dani, and the newest acquisition, Eleanor, for the exquisite reunions and the memorable holiday trips. Furthermore, I wish to thank Toni, Gerard, Marc, David, Dani, Noelia, and Inma, for making my stay in Barcelona very enjoyable. I would also like to express my deepest gratitude to Clara, Chiara, and Claudia, for always supporting me. Finally, a sincere 'thank you' to my old friends, Mathieu and Ilias, for all the memorable nights out in Aalst, a tradition that we should never stop doing.

Bij deze wil ik ook heel graag mijn geweldige Bomma bedanken voor "het logeerbed staat altijd klaar", iets waar ik de afgelopen 3 jaar veelvuldig gebruik van heb gemaakt. De geweldige gastvrijheid, zelfs wanneer een paar weken logeren uiteindelijk een paar maanden werd, zal ik nooit vergeten. Wetende dat ik bij mijn terugkomst uit Barcelona altijd een gezellige plaats in Leuven had om te verblijven heeft mij enorm veel stress bespaard, en heeft zondermeer bijgedragen tot de goede afloop van deze dissertatie. Bedaank!

I would also like to express my gratitude for having two such amazing big brothers, and, last but not least, words cannot express how grateful I am for having such wonderful parents that have always given me their unconditional support and endless encouragements. Thank you for always listening to me, for providing me with great advice whenever I stumble upon a problem, and for all the days that I spent at home in Welle, without having to worry about anything. Thank you for being there.

Abstract

Our modern society is becoming increasingly dependent on the constant stream of information sent out by satellites orbiting Earth. However, highly energetic rays traversing the near-Earth space environment pose a constant threat to the electronics on board these satellites. In addition, humankind renewed interest in manned missions to the Moon and Mars requires the protection of the spacecraft crew members against the high radiation doses that they will encounter during their interplanetary voyage. A profound understanding of the ever changing radiation conditions in our solar system is thus crucial, in order to efficiently protect our space-based assets and to succeed in our future ventures in space.

A major part of the high intensity radiation in interplanetary space has a solar origin, and consists of electrons, protons, and heavier ions that have undergone significant acceleration during solar eruptive events such as flares and coronal mass ejections (CMEs). These particles are referred to as solar energetic particles (SEPs), and are typically much more energetic than solar wind particles. The solar wind is a continuous stream of charged particles originating from the Sun and filling up the entire heliosphere. This highly conductive plasma drags the magnetic field of the Sun out into space, hence inducing an interplanetary magnetic field (IMF). This IMF can be very complex, since the solar wind is a highly turbulent flow which in addition contains large scale structures such as CMEs and corotating interaction regions (CIRs), which are regions of compressed plasma that are formed when a fast solar wind stream overtakes a preceding slow solar wind.

Since SEPs are electrically charged particles, they are subject to the Lorentz force arising from the IMF, which makes the particles gyrate along the magnetic field lines. The turbulent fluctuations present in the IMF can act as scattering centres, altering the energetic particles' speed and propagation direction. In addition, turbulence can transport particles across the average background magnetic field in a diffusive manner, which is commonly referred to as cross-field diffusion. Guiding centre (GC) drifts due to electric and varying magnetic fields may also transport particles across the IMF lines. These particle drifts can be very strong near shock waves, which are typically found in

front of CMEs and at the trailing edges of CIRs. Shock waves are believed to be an important source of energetic particles, through mechanisms like first order Fermi and shock-drift acceleration.

The transport and acceleration of energetic particles can be described by the focused transport equation (FTE). This equation can be derived from the Vlasov equation, under the assumptions that the particle distribution is gyrotropic, and that energetic particles travel in a collisionless manner through a turbulent background plasma. The effects of the turbulence are modelled through a set of different diffusion processes in phase space. Moreover, as illustrated in Chapter 2, the effect of the GC drifts can be included in the FTE if an appropriate transformation is made to GC coordinates, which in addition leads to a pitch-angle dependent cross-field diffusion process.

In this thesis, we develop a numerical model that calculates energetic particle intensities in the inner heliosphere by solving the FTE under realistic solar wind conditions. This model is called PARADISE, an acronym for *Particle Radiation Asset Directed at Interplanetary Space Exploration*. As detailed in Chapter 3, PARADISE solves the FTE by integrating a set of Itô stochastic differential equations forward in time, while assuming a solar wind configuration obtained from a magnetohydrodynamic (MHD) model. The time-dependent MHD module of the *EUropean Heliospheric FORecasting Asset* (EUHFORIA) is used to calculate the different solar wind configurations considered in this work.

In Chapters 4, 5, and 6, the transport of SEPs in a solar wind containing a CIR is investigated in detail. It is illustrated how a CIR can alter SEP distributions by acting as an efficient magnetic mirror and by re-accelerating particles in its associated compression and shock waves. Moreover, it is shown that the intricate magnetic topology near and within the CIR can strongly affect the efficiency of cross-field diffusion in spreading particles through interplanetary space.

In Chapter 7, the effects of the magnetic field curvature and gradient drifts on the decay phase of SEP events are studied. It is illustrated that even for low energy protons (< 36 MeV), drifts can potentially inhibit the phenomenon known as the SEP flood, unless they are mitigated through e.g., a sufficiently strong cross-field diffusion process. It is also shown that particle drift effects become increasingly important in non-nominal solar wind conditions, such as near a CIR.

In Chapter 8, the transport and acceleration of 100 keV protons in a solar wind containing a CME are modelled. This is done by using the cone CME model of EUHFORIA. The chapter illustrates the current capabilities of PARADISE to model the evolution of energetic particle distributions in a dynamic solar wind containing a large-scale transient structure.

In Chapter 9, the main results of this thesis are summarized and some possible follow-up studies are discussed.

Beknopte samenvatting

Onze hoogtechnologische maatschappij wordt steeds afhankelijker van de constante informatiestroom die verzonden wordt via satellieten. Hoogenergetische kosmische straling vormt echter een constante bedreiging voor de elektronica aan boord van deze satellieten. Bovendien is er in recente jaren een hernieuwde interesse ontstaan voor bemande ruimtevaartmissies naar de maan en naar Mars. De bemanningsleden van deze missies zullen tijdens hun reis blootgesteld worden aan deze levensbedreigende straling. Om onze satellieten, ruimtesondes en astronauten te beschermen is het dus van cruciaal belang dat we een diepgaande kennis verwerven van de immer veranderende stralingscondities in ons zonnestelsel.

Een groot deel van de kosmische straling in de interplanetaire ruimte is afkomstig van de zon en bestaat voornamelijk uit hoog energetische elektronen, protonen en zwaardere ionen. Deze deeltjes hebben een significante versnelling ondergaan tijdens zonne-uitbarstingen, zoals coronale massa ejecties (CMEs) of zonnevlammen, en worden in de Engelstalige wetenschappelijke literatuur aangeduid met de term SEP (*solar energetic particle*). De energie van een dergelijke SEP ligt typisch ver boven die van een deeltje afkomstig uit de zonnewind. De zonnewind bestaat uit een continue stroom van laag energetische geladen deeltjes die de zon verlaat en vervolgens de interplanetaire ruimte van ons zonnestelsel opvult. Vermits de zonnewind een plasma en dus een heel efficiënte geleider is, sleept hij als het ware het magnetische veld van de zon met zich mee doorheen de ruimte. Bijgevolg is ons zonnestelsel ingebed in een interplanetair magnetisch veld (IMF). Dit IMF kan zeer complex zijn, vermits de zonnewind een turbulent medium is dat bovendien grootschalige structuren kan bevatten zoals CMEs en coroterende interactie regio's (CIRs). Deze CIRs zijn regio's van samengedrukt plasma die ontstaan wanneer een snelle stroom in de zonnewind een voorafgaande langzamere stroom inhaalt en bijgevolg samendrukt.

Door de lage dichtheid van de zonnewind bewegen SEPs zich voort door de ruimte nagenoeg zonder te botsen met andere deeltjes. Vermits SEPs evenwel een elektrische lading hebben, zijn ze onderworpen aan de Lorentzkracht afkomstig van het IMF. Bijgevolg zullen de deeltjes voornamelijk in een spiraalvormige beweging langsheen

de magnetische veldlijnen voortbewegen. De turbulente fluctuaties van het IMF kunnen echter fungeren als verstrooiingscentra, waardoor de snelheid en de bewegingsrichting van energetische deeltjes continu worden gewijzigd. Bovendien kan turbulentie ervoor zorgen dat de deeltjes op een diffusieve manier de magnetische veldlijnen loodrecht doorkruisen, een fenomeen dat cross-field diffusie wordt genoemd. Ook de zogenaamde guiding centre (GC) drifts, veroorzaakt door bijvoorbeeld een elektrisch of een variërend magnetisch veld, zullen ervoor zorgen dat deeltjes loodrecht op de IMF lijnen voortbewegen. Deze GC drifts kunnen zeer sterk zijn in de buurt van schokgolven, welke bijvoorbeeld ontstaan aan de grenzen van CIRs of aan de voorkant van CMEs die zich door de zonnewind voortbewegen. Schokgolven worden beschouwd als een belangrijke bron van hoogenergetische deeltjes, via mechanismes zoals de eerste orde Fermi versnelling.

Het transport en de versnelling van energetische deeltjes kunnen worden beschreven door de zogenaamde focused transport equation (FTE). Deze vergelijking kan worden afgeleid uit de Vlasov vergelijking, onder de aanname dat de deeltjesverdeling gyrotroop is en dat hoogenergetische deeltjes zich op een botsingsvrije manier door de zonnewind voortbewegen. In de FTE wordt het effect van de turbulentie beschreven door middel van verschillende diffusieprocessen in de faseruimte. Bovendien illustreren we in hoofdstuk 2 dat het effect van de GC drifts kan worden beschreven door een algemenere versie van de FTE, middels een gepaste transformatie naar de bijhorende GC coördinaten. Deze transformatie leidt daarenboven op een natuurlijke wijze tot de inclusie van een cross-field diffusieproces in de FTE.

In deze thesis ontwikkelen we een numeriek model dat de intensiteit van de energetische deeltjes in de ruimte berekent door de FTE op te lossen onder de aanname van een realistische zonnewind. Dit model wordt PARADISE genoemd, acroniem voor *Particle Radiation Asset Directed at Interplanetary Space Exploration*. Zoals beschreven in hoofdstuk 3 wordt dit numerieke model bekomen door een systeem van Itô stochastische differentiaalvergelijkingen voorwaarts in tijd te integreren, uitgaande van een zonnewindconfiguratie verkregen uit een magnetohydrodynamisch (MHD) model. In deze thesis wordt de tijdsafhankelijke MHD module van de *EUropean Heliospheric FORecasting Asset* (EUHFORIA) gebruikt om verschillende zonnewindconfiguraties te genereren.

In de hoofdstukken 4, 5 en 6 wordt het transport van SEPs onderzocht in een zonnewind die een CIR bevat. Er wordt geïllustreerd dat een CIR de SEPs kan beïnvloeden door als een efficiënte magnetische spiegel te fungeren en door deeltjes in de schokgolven aan de grenzen van de CIR verder te versnellen. Er wordt ook aangetoond dat de efficiëntie van een cross-field diffusieproces sterk kan worden beïnvloed door de complexe magnetische topologie nabij de CIR.

In hoofdstuk 7 wordt het effect van de GC-drifts op energetische protonen bestudeerd. We illustreren dat deze drifts een significante invloed kunnen hebben op het transport

van protonen, zelfs indien deze een relatief lage energie hebben (< 36 MeV). Een proces zoals cross-field diffusie kan de invloed van drifts echter significant verzwakken. We tonen ook aan dat het effect van GC drifts veel groter wordt nabij een CIR.

In hoofdstuk 8 worden het transport en de versnelling van 100 keV-protonen gemodelleerd in een zonnewind die een CME bevat. Dit wordt gedaan door gebruik te maken van het ijshoorn (cone) CME model van EUHFORIA. Dat hoofdstuk illustreert dat PARADISE in staat is om de evolutie van energetische deeltjes te beschrijven in een dynamische zonnewind.

In hoofdstuk 9 worden de belangrijkste resultaten van dit proefschrift samengevat en enkele mogelijke opvolgstudies worden besproken.

Resum

La societat moderna cada dia és més dependent del flux continu d'informació que ens envien els satèl·lits que orbiten la Terra. Tanmateix, la radiació de partícules extremadament energètiques que creuen l'entorn espacial proper a la Terra (el "veïnat espacial" terraqui) representen un perill constant per l'electrònica embarcada en satèl·lits. A més a més, el renovat interès de la humanitat per enviar missions tripulades a la Lluna i a Mart demana definir i dissenyar acuradament la protecció dels astronautes enfront d'aquesta radiació corpuscular, ja que les dosis que poden rebre els astronautes durant llur viatge interplanetari poden ser molt altes. Per a poder protegir de forma eficient naus, instruments i tripulacions, i assegurar així l'èxit de missions en l'espai interplanetari, és imprescindible entendre en profunditat les condicions físiques, sempre canviants, de la radiació de partícules en l'heliosfera.

Gran part de la intensitat de radiació corpuscular mesurada a l'espai interplanetari és d'origen solar. Aquesta radiació està formada per electrons, protons i altres ions més pesants que han estat significativament accelerats durant esdeveniments solars eruptius, bàsicament fulguracions i ejeccions de coronals de massa (CMEs). Aquestes partícules accelerades s'anomenen partícules energètiques solars (SEPs, el seu acrònim en anglès). Les SEPs tenen una energia molt més alta que l'energia típica de les partícules que conformen el vent solar. El vent solar és un flux continu de partícules ionitzades que s'origina al Sol, a la corona solar, i que omple tota l'heliosfera. Aquest plasma d'alta conductivitat arrossega el camp magnètic del Sol, donant lloc al camp magnètic interplanetari (IMF, en anglès). Aquest camp magnètic té una estructura espacial molt complexa i variable en el temps perquè el vent solar és un flux de plasma altament turbulent que, a més a més, conté grans estructures interplanetàries també molt variables, com les esmentades CMEs o les regions interactives corrotacionals (CIRs). Les CIRs són regions de plasma comprimit que és formen quan un doll de vent solar ràpid que es propaga per l'espai encalça una regió de vent solar lent que la precedeix.

Com que les SEPs són partícules amb càrrega elèctrica estan subjectes a la força de Lorentz deguda al IMF i per tant, giren a mida que es propaguem al llarg de les línies

de camp del camp magnètic interplanetari. Per altra banda, les fluctuacions turbulentes presents en el IMF actuen com centres de dispersió, alterant la velocitat i la direcció de propagació d'aquestes partıcules energètiques. A més a més, la turbulència pot transportar les SEP a través del camp magnètic mitjà. Aquesta difusió transversal de les SEPs es coneix com difusió perpendicular o a través del camp. Degut a la variabilitat espacial i temporal dels camps elèctrics i magnètics que les SEPs troben en llur propagació, el centre guia (GC) de cadascuna pateix una deriva que també dóna lloc a un transport de partícules transversal a les línies del IMF. Aquestes velocitats de deriva poden ser molt grans a prop de les ones de xoc que es propaguen en el si del vent solar, típicament davant de CMEs i a les vores (davantera i posterior) que defineixen les CIRs. Els xocs interplanetaris són llocs importants d'acceleració de partícules, bàsicament, per processos com el mecanisme d'acceleració de Fermi de primer ordre o acceleració de deriva en el camp elèctric, al front del xoc.

El transport i l'acceleració de partícules energètiques molt habitualment es descriu mitjançnt l'equació de transport focalitzat (FTE). La FTE es deriva de l'equació de transport de Vlasov, tot suposant que la distribució de partícules és girotròpica, que no es produeixen interaccions entre elles en el decurs llur viatge (és 'acolisional') en el si d'un plasma turbulent. Al capítol segon es descriu com els efectes de la turbulència magnètica sobre les SEPs poden ser modelitzats, tot emprant un conjunt de diferents processos de difusió a l'espai de fases. A més, tal i com es es descriu en aquest capítol, l'efecte de la deriva del GC es pot incloure dins la FTE, tot fent una transformació apropiada que permeti expressar aquests processos en el sistema de coordenades del GC. Aquesta transformació també permet expressar el procés de difusió transversal al camp magnètic, en funció de l'angle entre la velocitat de la partícula i la direcció del camp mitjà.

En aquesta tesi, desenvolupem un model numèric que calcula la intensitat de les partícules energètiques a l'heliosfera interior (< 1 AU), tot resolent la FTE en condicions realistes pel vent solar. Aquest model s'anomena PARADISE, acrònim anglès de "Particle Radiation Asset Directed at Interplanetary Space Exploration". PARADISE resol la FTE integrant un conjunt d'equacions diferencials estocàstiques d'Itô, endavant en el temps. Per al plasma de fons s'assumeix una configuració de vent solar determinada obtinguda d'un model magnetohidrodinàmic (MHD) tri-dimensional per a aquest plasma. Aquestes configuracions pel vent solar es calculen amb el mòdul temps-dependent MHD del codi EUFHORIA (European Heliospheric Forecasting Asset).

En els capítols 4, 5 i 6, s'investiga en detall el transport de les SEPs en l'escenari d'un vent solar que conté una CIR. S'hi il·lustra com una CIR pot alterar la distribucions de la població de SEPs en actuar com un mirall magnètic eficient i com pot re-accelerar partìcules a la regió de compressió i a les ones de xoc (anterior i posterior) associades. També es mostra l'eficiència de la difusió perpendicular al IMF mitjà com a diseminadora de partícules per l'espai interplanetari, queda fortament afectada per la

topologia complexa del camp magnètic a prop i dins de la CIR.

En el capítol 7 s'estudia els efectes de la deriva de la curvatura i gradient del camp magnètic en la fase de decreixement dels perfils d'intensitat dels esdeveniments de SEPs (que es troba freqüentment a la regió posterior a l'ona de xoc). Es demostra que fins i tot per a protons de baixa energia, els efectes de deriva poden inhibir el fenomen conegut com a "SEP-inundació" ('SEP-flood'), però que aquest efecte poc quedar emmascarat, per exemple, per un procés prou eficient de difusió tranversal al IMF. També es demostra que els efectes de deriva de la partícula poden esdevenir molt importants en condicions de vent solar no-estàndard, per exemple, a prop d'una CIR.

En el capítol 8, es modela el transport i l'acceleració de protons de 100 keV, en un escenari interplanetari de vent solar nominal, que conté una CME. La modelització de la CME s'aconsegueix tot fent servir el model de con per CMEs, existent a EUHFORIA. En aquest capítol s'il·lustren les capacitats actuals de PARADISE per modelitzar l'evolució de distribucions de partícules energètiques dins d'un vent solar dinàmic que conté un estructura transitòria de grans dimensions.

En el capítol 9 es presenten resumits els resultats més importants d'aquesta tesi, i es discuteixen diverses línies de recerca per desenvolupar en el futur, a partir dels resultats obtinguts en aquest treball de tesi.

List of Abbreviations

1D One-Dimensional.

2D Two-Dimensional.

3D Three-Dimensional.

5D Five-Dimensional.

ACR Anomalous Cosmic Ray.

AGN Active Galactic Nucleus.

AU Astronomical Unit.

AWSoM Alfvén-Wave-turbulence based Solar atmosphere Model.

BATS-R-US Block Adaptive-Tree Solar-wind Roe-type Upwind Scheme.

BGK Bhatnagar–Gross–Krook.

CIR Corotating Interaction Region.

CM Central Meridian.

CME Coronal Mass Ejection.

cobpoint Connecting with the Observer point.

CORHEL Corona-Heliosphere.

CR Cosmic Ray.

CS Current Sheet.

DSA Diffusive Shock Acceleration.

EM Euler-Maruyama.

ENLGC Extended Non-Linear Guiding Centre theory.

EPREM Energetic Particle Radiation Environment Module.

ESA European Space Agency.

ESP Energetic Storm Particle.

EUHFORIA EUropean Heliospheric FORecasting Information Asset.

FD Finite Difference.

FLAMPA Field Line Advection Model for Particle Acceleration.

FLRW Field Line Random Walk.

FTE Focused Transport Equation.

GC Guiding Centre.

GNSS Global Navigation Satellite System.

IMF Interplanetary Magnetic Field.

IMP Interplanetary Monitoring Platform.

IP Interplanetary.

ISEE-3 International Sun-Earth Explorer-3.

KBE Kolmogorov Backward Equation.

KFE Kolmogorov Forward Equation, also known as the Fokker–Planck equation.

M-FLAMPA Multiple Field Line Advection Model for Particle Acceleration.

MAS Magnetohydrodynamic Algorithm outside a Sphere.

MC Monte Carlo.

MHD Magnetohydrodynamics.

MPI Message Passing Interface.

NASA National Aeronautics and Space Administration.

NLGC Non-Linear Guiding Centre theory.

ODE Ordinary Differential Equation.

PAD Pitch-Angle Distribution.

PARADISE PArticle Radiation Asset Directed at Interplanetary Space Exploration.

PDE Partial Differential Equation.

PSP Parker Solar Probe.

QLT Quasi-Linear Theory.

SAS Small Angle Scattering.

SDE Stochastic Differential Equation.

SEP Solar Energetic Particle.

SEPMOD Solar Energetic Particle Model.

SI Stream Interface.

SIR Stream Interaction Region.

SN Super Nova.

SNR Super Nova Remnant.

SOHO Solar and Heliospheric Observatory.

SolO Solar Orbiter.

STAT Solar Particle Event Threat Assessment.

STEREO A Solar Terrestrial Relations Observatory Ahead.

TGK Taylor–Green–Kubo.

UNLT Unified Non-Linear Transport theory.

YSO Young Stellar Object.

Contents

Abstract iii

Beknopte samenvatting v

Resum ix

List of Abbreviations xv

Contents xvii

1 Introduction 1

1.1 Space weather 1

1.2 The solar wind 3

1.3 Energetic particles in the solar system 5

1.3.1 Solar origin 5

1.3.2 Interplanetary origin 7

1.3.3 Extrasolar origin 9

1.4 Energetic particle transport in the heliosphere 10

1.4.1 The effect of the large-scale solar wind structure 11

1.4.2 The effect of the small-scale solar wind structure 11

1.5 Modelling energetic particle transport 13

1.5.1 The focused transport equation . . . 13
1.5.2 When the test particle approach fails . . . 18
1.6 Existing global 3D MHD-SEP models . . . 19
1.7 Motivation and outline of this work . . . 21

2 The focused transport equation 23

2.1 Introduction . . . 24
2.2 A transport equation for test particles propagating in a relativisic colisionless plasma . . . 25
2.2.1 Terminology and transformations . . . 25
2.2.2 The Vlasov equation in mixed phase space coordinates . . . 27
2.2.3 The connection coefficients in mixed coordinates . . . 30
2.2.4 The transport equation to first order in U/c . . . 30
2.3 Guiding centre coordinates and the differential intensity . . . 34
2.4 Particle motion in a turbulent plasma . . . 35
2.5 A gyrotropic distribution function . . . 41
2.6 Turbulence . . . 43
2.6.1 The wave approach . . . 44
2.6.2 The statistical approach . . . 44
2.6.3 The slab/2D composite turbulence model . . . 47
2.6.4 The wave spectrum . . . 48
2.7 Quasi-linear theory . . . 49
2.7.1 Pitch-angle diffusion . . . 51
2.7.2 Cross-field diffusion: field line random walk . . . 54
2.8 Non-linear cross-field diffusion theories . . . 56
2.8.1 Non-linear guiding centre theory . . . 57
2.8.2 Pitch-angle dependent cross-field diffusion . . . 59
2.9 Phenomenological approaches to cross-field diffusion . . . 61

2.10 Momentum and mixed diffusion coefficients 62
2.11 Summary and discussion 62

3 PARADISE 67

3.1 Introduction 67
3.2 Itô stochastic differential equations 68
3.2.1 Itô calculus 68
3.2.2 Numerical integration of SDEs 70
3.2.3 The FTE as a set of forward or backward SDEs 72
3.2.4 Pseudo-particles 74
3.2.5 Injecting the pseudo-particles 75
3.2.6 Sampling the differential intensity $\mathcal{J}$ 77
3.3 The PARADISE model 78
3.3.1 The SDEs in spherical coordinates 78
3.3.2 Cross-field diffusion 80
3.3.3 The time step 81
3.3.4 Injecting the pseudo-particles 82
3.3.5 Boundary conditions 82
3.3.6 Sampling the pseudo-particles 83
3.3.7 The background plasma 84
3.3.8 The diffusion coefficients 85

4 Modelling the transport of SEPs in a CIR 91

4.1 Introduction 92
4.2 Particle transport model 93
4.3 SEP propagation in uniform wind conditions 95
4.4 SEP propagation in mixed solar wind conditions 100
4.4.1 A corotating interaction region 100

4.4.2 SEP transport in the heliosphere . . . 104
4.4.3 Particle acceleration . . . 107
4.4.4 Proton fluxes measured by virtual observers . . . 110
4.5 Summary and conclusions . . . 117

5 The interplanetary spread of SEPs near a CIR 121
5.1 Introduction . . . 122
5.2 Simulation set-up . . . 123
5.3 Results . . . 125
5.3.1 Particle intensities along a magnetic field line . . . 125
5.3.2 Longitudinal intensity profiles . . . 130
5.3.3 Radial evolution of the longitudinal width . . . 135
5.3.4 Latitudinal variation of particle intensity . . . 138
5.4 Summary . . . 139

6 Spreading protons in the heliosphere: a note on cross-field diffusion effects 141
6.1 Introduction . . . 142
6.2 Simulation of SEP transport within a CIR . . . 143
6.3 The spread of SEPs in the solar equatorial plane . . . 145
6.4 The effect of cross-field diffusion on shock accelerated particle populations . . . 149
6.5 Summary and discussion . . . 152

7 The effect of drifts on the decay phase of SEP events 157
7.1 Introduction . . . 158
7.2 Modelling SEP transport . . . 160
7.3 Results . . . 162
7.3.1 Observers along IMF lines . . . 162

7.3.2 Observers at different latitudes . . . 167
7.3.3 The intensity decay rates . . . 170
7.3.4 Peak-intensity energy spectra . . . 170
7.3.5 Energy spectra of fluence . . . 173
7.3.6 The effect of cross-field diffusion . . . 174
7.3.7 A magnetic bottle . . . 176
7.4 Summary and discussion . . . 179

8 A gradual SEP event **183**
8.1 Introduction . . . 184
8.2 Modelling set-up . . . 187
8.2.1 A CME in a uniform solar wind . . . 187
8.2.2 100 keV proton injection . . . 189
8.3 Results . . . 192
8.3.1 Case 1 ($\lambda_\parallel = \lambda_\parallel^s = 0.1$ AU) . . . 192
8.3.2 Case 2 ($\lambda_\parallel^s = 0.01$ AU) and Case 3 ($\lambda_\parallel^s = 0.001$ AU) . . . 196
8.3.3 Case 4 . . . 200
8.4 Summary and discussion . . . 202

9 Conclusion **205**
9.1 Summary . . . 205
9.2 Outlook . . . 208

A Gyro-averaging the particle's transport equation **211**

B The Guiding Centre Drifts **217**

C Stochastic Differential Equations **221**

Bibliography **225**

Curriculum Vitae **241**

Chapter 1

Introduction

"The dinosaurs became extinct because they didn't have a space programme."
– Larry Niven

1.1 Space weather

Contrary to popular belief, interplanetary space is not a perfect vacuum. Instead, it is home to numerous particle populations originating from both inside and outside our solar system. In the near-Earth space environment, these particles include electrons, protons, and various different ions as well as some neutral atoms. Despite the fact that the density of these particle populations is extremely low, even compared to the ultra-high vacuum regimes attained in laboratories, they are responsible for many different phenomena observed at Earth. These phenomena range from processes like the beautiful aurora Borealis and Australis observed near Earth's polar regions, to processes that pose a serious and constant threat to our high-tech society. The latter became clear from space missions launched in the twentieth century, which illustrated that the heliosphere is a very dynamic and active environment, with the main culprit being our own star, the Sun.

The most abundant particle population in interplanetary space is the solar wind, which consists of charged particles streaming away from the Sun at a continuous rate, filling the entire heliosphere. Besides the solar wind outflow, the Sun also loses particles through violent solar eruptions called coronal mass ejections (CMEs), which arise from

magnetic instabilities in the solar atmosphere. When a CME is ejected in the direction of Earth, it can cause a geomagnetic storm upon impacting our planet. During these storms, the intrinsic magnetic field of the CME interacts with Earth's magnetosphere, which can result in large-scale magnetic fluctuations that generate electric currents in conductors at ground level; a consequence of Faraday's law. These ground-induced currents can cause corrosion in steel pipelines and can in extreme cases even damage the transformers of our power grids, leading to electrical black-outs (Hapgood, 2011; Schrijver et al., 2014; Schrijver et al., 2015). Moreover, while propagating through the corona and interplanetary space, CMEs drive shock waves that can act as powerful accelerators of charged particles. Some of the resulting high-energy particles, known as solar energetic particles (SEPs), can penetrate the magnetosphere of Earth and damage the electronics on board satellites. This can for example lead to the disruption of our Global Navigation Satellite System (GNSS), on which a vast and growing range of economic activities depend. Some of the potentially devastating effects of SEPs on our modern society are described by Schrijver et al. (2015) as:

> Impacts are seen throughout the multitude of industry sectors that use satellite-based navigation systems, including on the aviation industry as it seeks to exploit GNSS as a way to optimize aircraft routing and hence airspace capacity; on the development of self-driving cars that rely on GNSS; on the accuracy of maritime drilling operations; on the timing systems that synchronize power and cellphone networks in some countries, and on the finance industry as it moves to microsecond-resolution time stamping of financial transactions.

In addition, SEPs can pose a life-threatening hazard to astronauts, by causing tissue damage and increasing the risk of cancer among other effects (see e.g., Chancellor et al., 2014). Furthermore, SEPs associated with CMEs are just one of the many different energetic particle populations that are encountered in the heliosphere. For example, galactic and extragalactic cosmic rays (CRs) are charged particles that originate from outside our solar system, and can have energies that are even much higher than SEPs.

The ever-changing conditions in the heliosphere are referred to as the space weather of our solar system. Due to the potentially destructive effects of space weather storms, it is desirable to have a well-working and accurate space weather forecast, since much of the damage can be reduced or even avoided if precautionary measures can be taken. Such space weather forecasts will also be essential for the success of the tentative plans of humankind to send astronauts back to the Moon and eventually even to Mars or beyond. However, developing reliable space weather forecasts has proven to be a formidable task due to two main reasons. First, space weather is the result of a vast number of different physical processes occurring over a wide range of different length, time, and energy scales. Developing a physics-based space weather forecast requires a profound understanding of the complex dynamics occurring at

the Sun, in the interplanetary medium, and in Earth's magnetosphere and ionosphere. These vastly different environments are coupled to each other in a non-trivial manner through, for example, gravity, electromagnetic fields, shock waves, and electric currents. Second, only a handful of real-time measurements of the Sun and the space weather conditions at different locations in the heliosphere are available. This is because in-situ observations require the development, launch, and maintenance of expensive spacecraft, which have in addition only a limited lifespan. As a consequence, the reliability of the existing forecasting tools remains poor, and our space-based assets remain thus largely unprotected against the occasionally harsh space weather conditions. Moreover, even with better observations at hand, a more complete understanding of the various space weather phenomena is imperative to advance the current state of the predictive capabilities of our forecasting tools.

In this thesis, we focus on the physics behind the transport of energetic particles in the solar system. In particular, we study to what extent non-nominal solar wind conditions and the associated interplanetary magnetic field (IMF) influence the properties of energetic particle events in the inner heliosphere. This chapter starts by giving an overview of the different charged particle populations that are found in the heliosphere, including the solar wind (Section 1.2) and the different high-energy particle populations of both solar and extrasolar origin (Section 1.3). In Section 1.4, we summarize the typical transport conditions that energetic particles encounter while propagating through a turbulent solar wind, and in Section 1.5 we explain how this can be modelled. In Section 1.6, an overview of existing three-dimensional (3D) SEP modelling tools is provided. The chapter is concluded in Section 1.7, by providing the motivation and outline of this thesis.

1.2 The solar wind

Every second, the solar wind carries away from the Sun approximately a billion kilograms of charged particles, mostly electrons, protons and alpha particles, but also trace amounts of heavier ions (Geiss et al., 1995). This plasma expands from the Corona into interplanetary space, filling a region called the heliosphere. The low density of the solar wind makes collisions between the particles very unlikely, and as a result it is not well described by a Maxwell–Boltzmann thermal equilibrium state. Instead, the solar wind velocity distribution consists of a thermal core and a halo suprathermal population, which can more accurately be described by a kappa-distribution (see Pierrard & Lazar, 2010, and references therein). The solar wind electron distribution has also a strahl component, which consists of supra-thermal electrons focused along the interplanetary magnetic field (e.g., Pilipp et al., 1987; Anderson et al., 2012).

The solar wind comes in two different flavours, namely the fast solar wind which has a typical speed around 750 km/s, and the slow solar wind which has a typical speed around 350 km/s. Both solar wind components are accelerated away from the Sun and become quickly supersonic, meaning that their bulk speed is above the magnetosonic speed (Parker, 1958). The fast solar wind is relatively steady and consists of plasma escaping from the Sun along the open magnetic field lines that characterise coronal holes (Feldman et al., 1976; Gosling, 1996). In contrast, the slow solar wind is much more variable and appears to emerge from the streamer belt, although its precise origin is not well understood yet (see Cranmer et al., 2017, and references therein). Due to the high conductivity of the solar wind plasma, the IMF can be assumed to be frozen into the plasma. As a result, for a solar wind that flows radially away from the rotating Sun, the IMF lines will have the shape of an Archimedean spiral. In the context of the solar wind, the latter is often referred to as a Parker spiral, named after Eugene Parker who derived the first model for a supersonic solar wind (Parker, 1958). The IMF is indeed observed to have a spiral structure when averaging over long enough time periods. However, in practice the solar wind is a highly turbulent flow, which can in addition contain large-scale transient structures like CMEs.

The solar wind is often described by using a fluid approach, that is, by using the equations of magnetohydrodynamics (MHD). These equations do often a fairly good job in describing the large-scale behaviour of a plasma, since they are all exact conservation laws, except for the closure equation (e.g., Goedbloed et al., 2019). Only when kinetic processes occurring on sufficiently small length scales affect the large-scale structure of the plasma, the standard MHD approach breaks down. This happens for example for cross-scale phenomena like collisionless shock waves and turbulence. However, this does not imply that MHD cannot be used to model a plasma configuration containing a shock wave. Instead, it means that the standard MHD equations cannot be used to model the finite thickness of the shock structure, as this is determined by microphysics that is not included in the MHD equations. As a result, a shock wave will appear as a sharp discontinuity in an ideal-MHD solution. Similarly, turbulence is a process that covers an entire range of length scales. Although standard MHD can capture the low-frequency turbulent structures in a plasma, it cannot capture the entire kinetic and magnetic energy cascade from the largest length scales to the very small length scales, where the turbulent fluctuations are eventually dissipated. The latter can for example happen through a wave-particle interaction mechanism, in which the turbulent fluctuation have cascaded to small enough scales for e.g., cyclotron or Landau wave-damping to occur, hence heating the plasma. Alternatively or additionally, magnetic reconnection and current sheets can help dissipating the turbulence (see Goldstein et al., 2015). The detailed physics behind these processes will however not be captured by the standard MHD equations, as they again involve microphysics.

The MHD equations can be used to describe large-scale structures in the solar wind, such as corotating interaction regions (CIRs; Smith & Wolfe, 1976). These are regions

of compressed solar wind plasma that form when a stream of slow solar wind is followed by a stream of fast solar wind. In that case, the fast wind overtakes the slow wind and a compression region forms between the two plasma populations. The trailing edges of this compression region can steepen into shock waves, which typically happens several astronomical units (AUs) away from the Sun, although it is not uncommon to observe such shock waves already near the orbit of Earth (Richardson, 2018). A CIR is thus bounded by a forward shock accelerating the slow solar wind and a reverse shock decelerating the fast solar wind (e.g., Pizzo, 1991). In the solar wind reference frame, the forward shock propagates radially outward whereas the reverse shock propagates radially inward, hence their naming. However, in a heliocentric reference frame, both the reverse and forward shock waves travel radially outward. In the centre of the CIR, a tangential discontinuity called the stream interface (SI) is found, and it marks the location where the shocked slow and fast solar wind plasma populations meet (e.g., Burlaga, 1974; Gosling et al., 1978; Crooker et al., 1999). Moreover, if the solar wind source conditions do not change, a CIR can last for several weeks up to months[1] (Tsurutani et al., 1982).

1.3 Energetic particles in the solar system

When referring to energetic particles residing in the heliosphere, one typically means charged particles that have energies "substantially" higher than the average energy of the ambient solar wind plasma. This definition can be ambiguous since the solar wind itself contains a supra-thermal tail. The distinction between energetic and solar wind particles becomes clearer when instead referring to the source or the acceleration mechanisms of the particles. It turns out that the various particle populations in the heliosphere are created under very different circumstances and have therefore different compositions, ionization states, and cover a different energy range. Figure 1.1 gives a diagram of a typical energy spectrum of oxygen nuclei observed in the near-Earth space environment. Indicated on the figure are the contributions of the different particle populations and their corresponding energy range. In the following, we give a brief description of these various energetic particle populations.

1.3.1 Solar origin

As the name suggests, SEPs are associated with solar eruptive phenomena like CMEs and flares. The energy spectrum of SEPs covers a range from a few tens of keV

[1] CIRs that last for less than one solar rotation are often referred to as *stream interaction regions* (SIRs)(e.g., Jian et al., 2006).

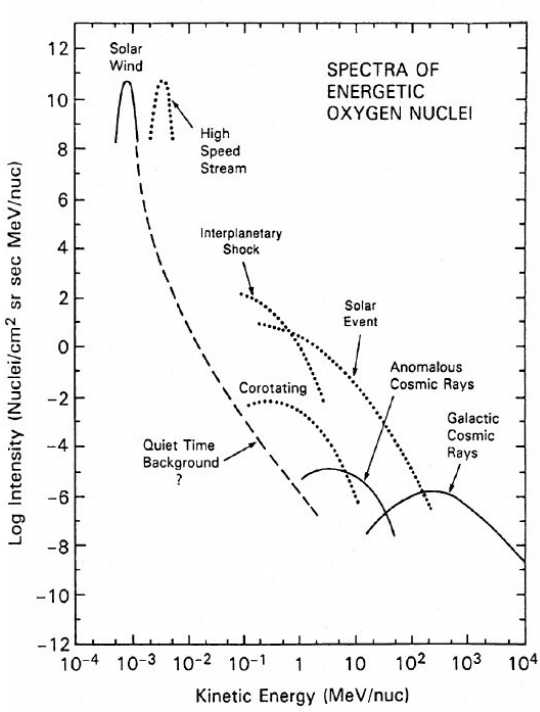

Figure 1.1: Representation of the different components of the energy spectrum of oxygen nuclei observed near Earth. The different particle populations mentioned in the figure are discussed in the text. Adapted from Stone et al. (1990).

to several hundreds of MeV, and in some extreme events even up to a few GeV (Meyer et al., 1956). SEP events are often classified into two different groups, named impulsive and gradual events (see Reames, 1999, and references therein). In the original picture, impulsive events are associated with particle acceleration processes occurring at the parent-sites of solar flares. Possible acceleration mechanisms include resonant wave-particle interactions (Temerin & Roth, 1992; Roth & Temerin, 1997) and Fermi acceleration occurring in collapsing magnetic islands associated with magnetic reconnection processes (e.g., Drake et al., 2009, 2013). Gradual SEP events are associated with shock waves driven by CMEs, in which particles are believed to accelerate through diffusive shock acceleration (DSA; Axford et al., 1977; Krymsky, 1977; Bell, 1978; Blandford & Ostriker, 1978). However, not every CME has an associated SEP event, which can for example be due to the shock geometry, the amount of turbulence, or the lack of a seed population that is energetic enough to

return upstream of the shock wave, which is necessary to commence the DSA process[2]. Possible sources of such suprathermal seed populations include, among others, previous CMEs, solar flares, and small-scale solar activity (Verkhoglyadova et al., 2015).

Gradual and impulsive SEP events accelerate particles at distinct locations and potentially through different mechanisms. As a result, the typical duration, element abundances, and ionization states of both types of SEP events are different (Reames, 1999). Impulsive events typically only last for a couple of hours, whereas gradual events can last for several days. The long duration of gradual events is a consequence of continuous particle acceleration occurring at the CME driven shock wave while it propagates through the solar corona and the interplanetary medium. Associated with gradual events are energetic storm particles (ESP), which is a term used to denote the energetic particle intensity enhancements measured when a CME driven shock passes a spacecraft. ESPs are the result of continuous DSA and the trapping of particles near the shock wave due to increased levels of turbulence.

It should be noted that many SEP events show characteristics of both impulsive and gradual events, which is to be expected since CMEs and flares often happen in conjunction. In that case, particles accelerated at the parent-site of flares can also be accelerated further if they cross the shock wave driven by a CME (Reames, 2013, 2017; Desai & Giacalone, 2016).

1.3.2 Interplanetary origin

Corotating interaction regions

When a CIR passes a spacecraft, energetic particles with energies ranging from a few keV up to several MeV are occasionally measured (Barnes & Simpson, 1976; Marshall & Stone, 1978; Decker et al., 1981). Originally, these particles were believed to be mainly accelerated through DSA at the reverse and forward shocks bounding the CIR (e.g., Fisk & Lee, 1980). However, as pointed out by Giacalone et al. (2002), particle acceleration is also possible in compression regions, as long as there are sufficient turbulent fluctuations embedded in the converging plasma flows that scatter the particles. This explains the finding of Desai et al. (1998), who used Ulysses observations to illustrate that many CIRs show signatures of energetic particles, even if these CIRs are not bounded by shock waves. In addition to shock and compressional acceleration, it has been suggested that second-order Fermi acceleration (Fermi, 1949) induced by the increased levels of turbulence inside the CIR may play a role in the acceleration of low energy (< 100 keV) particles (see Richardson, 2004, and references therein).

[2]This is commonly referred to as the "injection problem" of DSA (e.g., Jokipii, 1987).

To allow efficient particle acceleration to MeV energies, the compression waves bounding the CIR need to steepen sufficiently, which often only happens at distances past the orbit of Earth. As a result, the most energetic particles associated with a CIR are typically observed near Earth when they stream in the sunward direction (Marshall & Stone, 1978). Moreover, the seed population of particles that undergo acceleration in the CIR are believed to originate from the suprathermal tail of the solar wind (Chotoo et al., 2000; Mason et al., 2012). However, not all CIRs show accelerated particle enhancements, and it remains a largely unanswered question why this is the case (see e.g., Richardson, 2018, for a discussion).

Jovian electrons

An important source of energetic electrons in the heliosphere is the Jovian magnetosphere. This was unambiguously illustrated by Teegarden et al. (1974), using the data obtained from the Pioneer 10 spacecraft while it was approaching Jupiter. Jovian electrons are observed at Earth during quiet solar times, with a periodicity of approximately 13 months (McDonald et al., 1972). This is because Jupiter completes an orbit around the Sun in 11.86 years, such that the Earth's synodic period with respect to Jupiter is 13 months.

The energy of Jovian electrons is typically beneath 50 MeV, which is low compared to CR electrons (see Section 1.3.3). The exact acceleration and release mechanism of Jovian electrons is still under debate. Originally, the electrons were believed to be accelerated through a betatron and Fermi process, while diffusing radially through the Jovian magnetosphere (de Pater & Goertz, 1990). However, the observations of the Galileo and Cassini spacecraft have indicated that wave-particle interactions may play a prominent role in the acceleration of the Jovian electrons (Bolton et al., 2002; Horne et al., 2008).

Once accelerated, the electrons can leak from the Jovian magnetosphere into interplanetary space, possibly through some particle transport process across the magnetic field (Krupp et al., 2002). When studying energetic electron densities in the large-scale heliosphere, the Jovian magnetosphere can be well approximated by a continuously emitting point source (Pyle & Simpson, 1977). This source can be assumed to be time-independent, such that the variability associated with observed Jovian electron events is mostly attributed to particle transport effects in the solar wind (Chenette et al., 1977). As a result, Jovian electrons can be very useful to study energetic particle transport processes like e.g., cross-field diffusion in the heliosphere.

1.3.3 Extrasolar origin

Galactic and extragalactic cosmic rays

Galactic and extragalactic cosmic rays are high-energy particles originating from outside the solar system. They cover an energy range from a few MeV up to 10^{21} eV. One of the most energetic CR ever detected is the so-called *Oh-My-God particle*, which had an energy of $(3.2 \pm 0.9) \times 10^{20}$ eV (Bird et al., 1995). The Oh-My-God particle belongs to the class of ultra-high-energy CRs, which have energies above $\sim 10^{18}$ eV and are believed to originate from outside the Milky Way galaxy (Pierre Auger Collaboration et al., 2017). Several acceleration mechanisms for these ultra-high-energy CRs have been proposed, including DSA in galactic jets and centrifugal acceleration inside the magnetospheres of pulsars or active galactic nuclei (AGN) (see e.g., Honda & Honda, 2004; Mahajan et al., 2013; Osmanov et al., 2014).

The CRs below $\sim 10^{15}$ eV are believed to originate from super nova remnants (SNRs) inside our Milky Way galaxy, as was first suggested by Baade & Zwicky (1934). That some CRs indeed originate from SNRs has been confirmed, for example, by detecting the gamma rays associated with the decay of neutral pions which are produced when CRs interact with interstellar material (Ackermann et al., 2013). At $\sim 5 \times 10^{15}$ eV, the composition of CRs becomes more dominated by heavy particles, and a steepening appears in the CR energy spectrum. This transition is referred to as the *knee* of the spectrum (Blasi, 2013). A plausible acceleration mechanism of galactic CRs in SNRs is through DSA (Krymsky, 1977; Blandford & Ostriker, 1978; Bell, 1978), although it has not yet been shown unambiguously that DSA is efficient enough to accelerate particles up to the knee of the energy spectrum (e.g., Blasi, 2013, and references therein).

The CR energy spectrum observed in the near-Earth space environment shows a sudden drop around ~1 GeV, as is also illustrated in Fig. 1.1. This is a consequence of the solar wind and its embedded magnetic field, which prevents these CRs of lower energy to easily propagate into the inner heliosphere. This effect is known as CR modulation, and its effectiveness strongly depends on the solar cycle through the variations of the IMF strength and polarity (see e.g., Potgieter, 2013, for a review).

Anomalous cosmic rays

As indicated in Fig. 1.1, anomalous cosmic rays (ACRs) have an energy range between ~10 MeV to ~100 MeV, and are produced as follows. Due to the relative motion between the local interstellar medium and the solar system, neutral interstellar matter can flow freely into the heliosphere. These neutral particles will eventually ionize, either through photo-ionization or through charge-exchange with solar wind particles (Fisk et al., 1974). The formed ions are now suddenly subject to the Lorentz force

induced by the IMF, and are as a result convected with the solar wind. For this reason, these particles are commonly known as *pickup ions*. Upon reaching the outer edge of the heliosphere, the pickup ions encounter the heliospheric termination shock. At this shock, they can be energised through DSA, after which they are called ACRs (Pesses et al., 1981). A consequence of the interstellar origin of ACRs is that they consist mostly of protons, helium, nitrogen, oxygen, and, neon, with relative abundances different from, for example, SEPs (Klecker et al., 1995). This, together with the fact that they are often only singly charged, explains why they were termed "anomalous".

It should be pointed out that DSA predicts an energy spectrum that follows a power-law with an exponential rollover at high energies (e.g., Drury & Voelk, 1981). However, upon crossing the termination shock, the Voyager 1 and 2 spacecraft did not observe such an energy spectrum (Stone et al., 2005, 2008). Only when the spacecraft were well inside the heliosheath, the energy spectrum evolved into the expected DSA upstream spectrum. Numerous different explanations have been proposed to explain these observations, including a blunt shock shape, a dynamic shock, CR mitigation of the shock wave, acceleration processes through magnetic reconnection, and diffusive compression in the heliosheath (see Giacalone et al., 2012, for a review).

1.4 Energetic particle transport in the heliosphere

The number density of the solar wind and the energetic particles is sufficiently low that a close interaction between two charged particles is unlikely, that is, the interplanetary plasma is nearly collisionless. However, the collective electromagnetic field of the plasma will influence the motion of individual particles. In the inner heliosphere, the solar wind is by far the densest particle population, and is therefore the main contributor to the global interplanetary electromagnetic field. In contrast, the number density of the high-energy particles is often sufficiently low, such that its influence on the interplanetary electromagnetic field can be neglected. When this assumption holds, it is reasonable to treat the energetic particles as test particles, which assumes that they do not interact between themselves, and that they also have zero influence on the state of the solar wind plasma. The test particles are therefore only subject to the Lorentz force arising from the electromagnetic field embedded in the ambient solar wind. As explained in Section 1.2, the solar wind contains both large-scale structures and small-scale turbulent fluctuations, which can both have a strong influence on the transport of energetic particles. This will be discussed in more detail in the remainder of this section.

1.4.1 The effect of the large-scale solar wind structure

In an ideal solar wind that is free of any turbulence and waves, the energetic particles would gyrate around the IMF lines while conserving their first adiabatic invariant (Goedbloed et al., 2019). When travelling in the anti-sunward direction in the expanding solar wind, the conservation of the first adiabatic invariant causes a particle's velocity vector to get focused along the magnetic field direction (e.g., Roelof, 1969). In contrast, when energetic particles travel sunwards, they can eventually get mirrored, that is, reverse their propagation direction, due to the converging magnetic field topology towards the Sun. Moreover, the centre of the particle's gyration, the guiding centre (GC), can drift across the magnetic field due to, for example, electric fields or a non-uniform IMF (e.g., Dalla et al., 2013).

Large-scale structures such as CIRs and CMEs will also affect the transport of energetic particles significantly, since they strongly perturb the topology of the IMF. This can lead to the formation of regions of enhanced particle focussing or mirroring, and also the strength of the GC drifts will be affected (e.g., Wijsen et al., 2020). Moreover, as already touched upon in the previous sections, the shock and compression waves associated with CMEs and CIRs can accelerate particles. In contrast, in the expanding solar wind, particles will lose energy due to particle drifts along the motional electric field (le Roux et al., 2007; Dalla et al., 2015) and through the interactions with diverging scattering centres. This latter process is termed adiabatic deceleration (e.g., Parker, 1965; Webb & Gleeson, 1979; Ruffolo, 1995).

1.4.2 The effect of the small-scale solar wind structure

The solar wind is a highly turbulent medium (Bruno & Carbone, 2005), which complicates the motion of the energetic particles through phase-space considerably. A charged particle can for example resonate with a circularly polarised wave whose angular frequency is a harmonic multiple of the particle's cyclotron frequency, and whose electric field rotates in the same direction as the gyromotion of the particle (Tsurutani & Lakhina, 1997). In a turbulent plasma, there is a whole spectrum of waves present, such that resonant interactions between waves and particles are a common occurrence. Such resonant wave-particle interactions can alter the particle's energy and its propagation direction, i.e., scatter the particle. In a reference frame co-moving with the wave, the energy of the particles is conserved, and only the propagation direction of the particle is altered (Tsurutani & Lakhina, 1997). However, in the rest frame of the plasma this is not the case and there will be a net energy transfer between the waves and the particles, which depends on the relative speed between both entities.

A significant component of the solar wind's magnetic turbulence is purely two-dimensional (2D), as it consists of transverse[3] fluctuations that also have their wave vectors perpendicular to the mean background (e.g., Matthaeus et al., 1990; Bieber et al., 1994). The effect of such pure 2D turbulence on the magnetic field topology can be understood intuitively by imagining a group of IMF lines which perform a random walk independently of the neighbouring field lines. Whereas the group of field-lines might originally have constituted one regular magnetic flux-tube, the random walks will quickly braid the field lines together in a chaotic-like fashion. In addition, pure 2D turbulence can also give rise to magnetic "islands" around O-points of the associated magnetic potential function (e.g., Ruffolo & Matthaeus, 2013; Chuychai et al., 2007).

Pure 2D turbulence is different from Alfvénic slab turbulence, which consists of transverse fluctuations with wave vectors that are aligned to the background magnetic field. In such a configuration, a group of neighbouring field lines will all perform the same random walk, such that the integrity of the flux-tube constituted by these field-lines is conserved. The difference between pure 2D and slab turbulence was nicely illustrated in the simulations performed by Matthaeus et al. (1995). Moreover, Bieber et al. (1996) illustrated that the solar wind turbulence can often be well-described by a composite slab/2D turbulence model, where 85% of its energy is contained in the 2D component and 15% is contained in the slab component.

For energetic particles, the transverse complexity of the solar wind turbulence implies that they can propagate transverse to the average background magnetic field. Both theoretical and modelling efforts have indicated that in a plasma with a significant 2D turbulent component, an energetic particle population will often spread diffusively across the mean background magnetic field (see Shalchi, 2009, for a review). This process is in general non-linear, and is thus not described properly by quasi-linear theory (QLT; Jokipii, 1966) which is similar to a first-order perturbation approach. As a result, several different non-linear cross-field diffusion theories with different assumptions have been developed and an overview is given in Shalchi (2009).

It remains an unresolved question how efficient cross-field diffusion is in the solar wind. Multipoint observations have illustrated that the spatial width of SEP distributions can be highly variable, with some events being observed simultaneously by spacecraft that are widely separated (e.g., Dresing et al., 2012; Lario et al., 2013; Dresing et al., 2014). There have even been observations of circumsolar SEP events (Gómez-Herrero et al., 2015). This might indicate that cross-field diffusion can occasionally be very efficient. However, there exist many alternative mechanisms that could spread energetic particles over an extended region in the heliosphere, including an extended particle source region like a CME driven shock wave, multiple near-simultaneous widely separated solar eruptive events (Schrijver et al., 2013), or a complex coronal magnetic field topology (e.g., Klassen et al., 2018) among others. Moreover, some SEP events show sudden

[3] With respect to the mean background magnetic field.

short-lasting dropouts in their intensities (Mazur et al., 2000), which is also hard to reconcile with a very efficient cross-field process (Wang et al., 2014; Strauss et al., 2017).

1.5 Modelling energetic particle transport

1.5.1 The focused transport equation

An equation that is often used to describe the evolution of the SEP distribution function in the solar corona or in interplanetary space is the *focused transport equation* (FTE; Roelof, 1969; Skilling, 1971; Webb, 1985; Ruffolo, 1995; Isenberg, 1997; le Roux & Webb, 2009). The FTE can be derived from the Vlasov equation by assuming that the distribution function is gyrotropic and that the energetic particles travel as test particles through a prescribed background solar wind. For a non-relativistic background plasma like the solar wind, this equation can be written as (see Chapter 2)

$$\begin{aligned}
&\frac{\partial f}{\partial t} + (\mathbf{V}_{\rm sw} + v\mu\mathbf{b} + \mathbf{V}_d)\cdot\nabla f \\
&+ \frac{1-\mu^2}{2}\left[v\nabla\cdot\mathbf{b} + \mu\nabla\cdot\mathbf{V}_{\rm sw} - 3\mu\mathbf{bb}:\nabla\mathbf{V}_{\rm sw} - \frac{2}{v}\mathbf{b}\cdot\frac{d\mathbf{V}_{\rm sw}}{dt}\right]\frac{\partial f}{\partial\mu} \\
&+ \left[\frac{1-3\mu^2}{2}(\mathbf{bb}:\nabla\mathbf{V}_{\rm sw}) - \frac{1-\mu^2}{2}\nabla\cdot\mathbf{V}_{\rm sw} - \frac{\mu}{v}\mathbf{b}\cdot\frac{d\mathbf{V}_{\rm sw}}{dt}\right]p\frac{\partial f}{\partial p} \\
&= \frac{1}{p^2}\frac{\partial}{\partial\zeta^i}\left(p^2 D_{\zeta_i\zeta_j}\frac{\partial f}{\partial\zeta^j}\right),
\end{aligned} \tag{1.1}$$

where $f(\mathbf{x}, p, \mu, t)$ is the gyro-averaged phase-space distribution of the energetic particles, and $\mathbf{x}$ denotes the guiding centre coordinate measured in an inertial frame. In contrast, the cosine of the pitch angle μ, the momentum magnitude p are expressed in a frame co-moving with the solar wind. The particle speed v is defined as $v = p/(\gamma m)$, with γ the Lorentz factor associated with v and m the rest mass of a particle. Moreover, $\mathbf{V}_{\rm sw}$ is the background plasma velocity, $\mathbf{b}$ is the unit vector in the direction of the mean magnetic field, $\mathbf{V}_d$ are the GC drifts with respect to the mean magnetic field, and $D_{\zeta_i\zeta_j}$ are the diffusion processes describing the effect of the turbulence, with $\boldsymbol{\zeta} = (\mathbf{x}, p, \mu)$. In the last term of (1.1), the Einstein summation convention was used. The momentum coordinates are expressed in the co-moving plasma frame, since it is assumed that the turbulent fluctuations are (on average) frozen into the solar wind flow. The particle scattering processes will thus isotropize the distribution function in the plasma frame and not in the inertial frame.

The diffusion coefficients can either be estimated from observations or derived from quasi-linear or non-linear particle transport theories (e.g., Shalchi, 2009). For the average background solar wind configuration, either an analytical model like the Parker spiral can be used, or an MHD model can be used in which case the solar wind can contain e.g., shear flows, accelerated flows, rarefaction regions, compression regions, and shock waves. As explained in Section 1.4.1, these structures will all affect the energetic particle distribution function in a non-trivial manner. The FTE contains the necessary physics to describe the effects of such intricate solar wind conditions, as long as the test particle assumption is fulfilled.

Solving the FTE can be challenging, as it is a time-dependent five-dimensional (5D) partial differential equation (PDE), containing both advective and diffusive terms. There exist two classes of computational algorithms that are often employed to solve the FTE, i.e., finite difference (FD) methods and Monte Carlo (MC) methods. The optimal method depends strongly on the details of the specific application, as is explained in more detail in the following two sections.

Finite difference methods

The high dimensionality of the FTE and the fact that it has both the properties of parabolic and hyperbolic PDEs makes solving the FTE by means of FD methods a non-trivial matter. However, in a nominal solar wind with weak GC drifts and limited amounts of pure 2D turbulence, particles will stream mainly along the background IMF. In other words, the perpendicular transport of particles across magnetic field lines is negligible compared to the parallel transport along the average magnetic field, such that the spatial dimensions perpendicular to the IMF can be neglected. Hence, the FTE only needs to be solved along an IMF line, which reduces the spatial dimensions of the equation from three to one. Alternatively, one can also lower the dimensionality of the FTE by ignoring the momentum changes of the energetic particles. This can to a certain extent be reasonable for near-relativistic electrons propagating in a Parker solar wind configuration (e.g., Strauss & Fichtner, 2015).

By lowering the number of dimensions, the FTE is more easily solved using a FD approach by applying, for example, an additive operator-splitting technique. The hyperbolic part of the FTE can be written in conservative form and solved by means of a finite volume method like an upwind scheme with an appropriate flux limiter. The parabolic part of the FTE can be solved using e.g., an explicit time-forward central difference scheme[4]. Such an approach is for example used by the model introduced in Strauss & Fichtner (2015), which solves the FTE in a Parker solar wind by disregarding

[4]The explicit time-forward central difference scheme is only first order in the time step Δt but so is the additive operator splitting technique. Hence, utilising a higher order scheme for the parabolic part of the FTE is only sensible if also a higher order scheme for the splitting operator is utilised.

any momentum changes but retaining two spatial dimensions. Other models that utilise FD methods to solve the FTE along a single field line in a Parker solar wind, including momentum changes, are presented in e.g., Ruffolo (1995), Lario (1997).

When using these FD models, one has to be aware of the possible presence of numerical artefacts in the obtained solutions. For example, numerical diffusion can lead to non-zero particle intensities before the actual physical onset of the SEP event, which can also produce spurious oscillations in the anisotropies. These numerical artefacts can, to some extent, be mitigated by introducing a small non-zero background intensity in the computational domain (see e.g., Heita, 2019).

Solving the FTE along a magnetic field line is straightforward in a Parker solar wind, since the solar wind velocity is assumed to be purely radial and constant, and the IMF is therefore an Archimedean spiral which can be described analytically. However, the large-scale structure of the solar wind is often not well described by such a Parker configuration, in which case MHD models can be used to obtain a more realistic solar wind description. Solving the FTE along a single magnetic field line requires then keeping track of the IMF line while the MHD solar wind evolves. In an ideal MHD configuration, the magnetic field is frozen into the plasma, such that utilising a Lagrangian mesh of nodes constitutes a natural way of tracing individual IMF lines along which the FTE can be solved (see e.g., Sokolov et al., 2004; Schwadron et al., 2010).

An advantage of a Lagrangian grid is that the nodes will pile-up near compression and shock waves, as these structures are characterised by converging plasma flows. This leads thus automatically to a high resolution near these plasma structures, which is typically desired as compression and shock waves are regions where particle acceleration occurs. However, a pile-up of grid nodes can also be disadvantageous, since a small spacing between nodes requires a small time step for stability reasons, and it is in addition superfluous to have a node spacing that is significantly smaller than the resolution of the MHD simulation (see Linker et al., 2019, for a discussion). Rarefaction regions will automatically have a low density of Lagrangian nodes, such that it might be necessary to increase the amounts of nodes in these regions to obtain an acceptable resolution.

Since spacecraft are normally not corotating with the Sun, multiple IMF lines will sweep over the spacecraft during an SEP event. Hence, to compare observations with the output of the model, it is necessary to trace multiple field lines and to solve the FTE along each one of them. Furthermore, magnetic reconnection processes pose another challenge for solving the FTE along single magnetic field lines in an MHD solar wind. In principle, magnetic reconnection is not possible in an ideal MHD setting, but in practice it can occur due to numerical diffusivity that is unavoidably present in standard grid-based numerical MHD simulations.

In a non-nominal solar wind, cross-field transport due to GC drifts might no longer be negligible. For example, substantial magnetic field enhancements found near shock waves can produce strong magnetic field gradient drifts, as will be discussed in detail in Chapter 7. CMEs and CIRs are often also characterised by increased amounts of turbulence, such that efficient cross-field diffusion might occur. It is possible to extend the Lagrangian method discussed above to solve the fully 5D FTE, as is for example done in the Energetic Particle Radiation Environment Module (EPREM; Schwadron et al., 2010). In EPREM, the FTE is solved along multiple magnetic field lines simultaneously, and when updating the spatial part of the FTE on a certain node, the nearest nodes residing on other field lines need to be identified such that a FD scheme can be applied in all three spatial dimensions. Such a method strongly increases the complexity of the model, and it can be difficult to achieve an acceptable spatial resolution across the magnetic field without having to trace many field lines and hence spend a lot of computational effort. In addition, the perpendicular diffusion coefficient might be highly variable in the inner heliosphere, which can occasionally lead to the requirement of very small time steps to ensure the stability of the numerical scheme. This issue can be resolved by using an implicit scheme to handle the cross-field diffusion, as is discussed by Lampa (2011).

In conclusion, FD methods can be very useful when the parallel propagation of the particles dominates, such that the FTE only needs to be solved along single magnetic field lines. In this case, the FD methods are very computationally efficient, and likely outperform any other method to solve the FTE. Since the onset time and the attained peak intensity of an SEP event are typically due to particles propagating along IMF lines, FD methods can be of great use in SEP forecasting applications. However, the use of FD methods becomes more intricate in solar wind configurations containing shock waves, magnetic reconnection processes, and if the particle transport across the magnetic field becomes important. In such settings, the stochastic methods presented in the next section can offer a flexible and straightforward alternative approach to solve the FTE.

Monte Carlo methods

Monte Carlo or stochastic methods solve the FTE by using that the FTE can be formulated as a Kolmogorov forward or backward equation (KFE or KBE). Itô calculus can then be applied to formulate a set of stochastic differential equations (SDEs) that is equivalent to the FTE (e.g., Zhang, 1999; Qin et al., 2005; Dröge et al., 2010). The solutions of these SDEs describe the trajectories through phase space of so-called *pseudo-particles*, which can under certain conditions be regarded as the trajectories of phase-space density elements (Strauss & Effenberger, 2017). To some extent, SDEs resemble first order ordinary differential equations, yet with the important difference that they contain an additional stochastic term. A consequence of this stochastic term

is that a different trajectory through phase-space is obtained each time that the SDEs are integrated. However, it turns out that the energetic particle distribution function can be obtained by sampling these stochastic trajectories (Gardiner, 2004). A solution to the FTE is therefore obtained by integrating the equivalent set of SDEs for many pseudo-particles, such that good statistics are obtained for the sampled distribution function.

The test particle assumption of the FTE translates into pseudo-particles that likewise do not interact with each other nor do they influence the background plasma, such that the SDE method constitutes an embarrassingly parallel problem which can thus easily be implemented on a supercomputer. Moreover, it is straightforward to solve the fully 5D form of the FTE, as the pseudo-particles are not bound to any computational grid and stochastic integration schemes like the Euler-Maruyama (EM) method are unconditionally stable if the diffusion coefficients appearing in the FTE are sufficiently regular functions (Kloeden & Platen, 1992). We will elaborate much more on this matter in Chapter 3, where we introduce our own model that uses a stochastic approach to solve the FTE.

The stochastic methods can be further subdivided into two different classes: the time forward and the time backward SDEs. As the name suggests, the time forward integration approach traces pseudo-particles forward in time, after they have been injected from a certain source region described by the initial or boundary conditions of the system. The time forward approach resembles thus the actual physical situation in which energetic particles propagate through space. However, this analogy has its limits since pseudo-particles differ from real particles, as explained in more detail in Section 3.2.4 or in Strauss & Effenberger (2017) and Kopp et al. (2012). By sampling the pseudo-particles, the time evolution of the energetic particle intensity can be obtained in a computational domain covering a large spatial, pitch-angle, and energy range. This makes the forward integration method a viable and flexible tool to study the different transport and acceleration mechanisms affecting energetic particles in different regions of space. The main drawback of the forward integration method is that many pseudo-particles need to be injected in order to get sufficiently high statistics everywhere in the computational domain.

For SEP forecasting applications, one is typically only interested in the energetic particle intensities at the location of certain spacecraft and Earth. In that case, the forward integration method wastes a lot of computational effort by calculating the particle intensities at locations in space that are of no interest. For such applications, the backward integration method provides a better approach, as it integrates pseudo-particles backward in time starting from a prescribed time and point in phase-space. The pseudo-particles are traced backwards in time until they either hit a boundary of the computational domain or some time integration limit is reached. When that happens, the particle receives a statistical weight which is derived from the boundary condition in the former case and from the initial condition in the latter case (e.g., Strauss &

Effenberger, 2017).

A drawback of the backward method is that pseudo-particles only contribute to the statistics if they reach a boundary of the computational domain which has a non-zero boundary condition or if they end up in a region with a non-zero initial condition. For SEP applications, the source region is often located close to the Sun, where the IMF lines are strongly diverging. This causes many pseudo-particles to be mirrored before reaching the source located near the Sun, such that only very few pseudo-particles eventually contribute to the statistics. In other words, a lot of computational effort is wasted into pseudo-particles that are focused towards the outer heliosphere where no SEP source is located. This issue can be remedied to some extent by introducing an artificial convective term into the FTE, which forces pseudo-particles towards the source region. The obtained distribution function is then not equal to the energetic particle distribution function, but the latter can be derived from the former, a method known as *importance sampling*. An example of importance sampling in the context of SEPs is given by Qin et al. (2005) and Zhang et al. (2009), who use an artificial convection term in pitch-angle space which counteracts the magnetic mirroring effect that sunward travelling pseudo-particles experience in the inner heliosphere.

In conclusion, MC methods are an interesting approach to solve the FTE due to their stability and their straightforward parallel implementation. The downside is that it can be very computationally demanding to obtain reasonable statistics for the sampled distribution. The forward integration method is in particular useful when studying the evolution of the particle distribution function in extended spatial domains and over large energy ranges. The backward method is useful when the particle intensity needs only to be determined at fixed points in phase space, which is typically the case for space weather forecast applications and when comparing data obtained from spacecraft. Moreover, MC methods can propagate pseudo-particles through a solar wind generated by an MHD model, by interpolating the plasma variables to the position of the pseudo-particle. The time forward method can propagate pseudo-particles in parallel with the MHD simulation, something which is not possible with the time backward method.

1.5.2 When the test particle approach fails

When deriving the FTE from the Vlasov equation, it is assumed that the particles behave as test particles and have thus no influence on the mean background plasma, nor on the turbulence. This assumption is however not always justifiable, especially near shock waves where a considerable amount of particles can efficiently gain energy through DSA. When streaming away from the shock wave, these suprathermal particles can excite Alfvén waves which can in turn resonate with other energetic particles, hence further facilitating the DSA mechanism (e.g., Bell, 1978; Lee, 1983; Vainio, 2003). In other words, near shock waves the energetic particles and the turbulence

are coupled to each other, such that a test particle approach is no longer applicable. However, under the assumption that energetic particles only influence the turbulent state of the background plasma and not its average large scale structure, one can still use a standard MHD model for the background plasma. The FTE can also still be used, but the diffusion coefficients appearing in the FTE will now indirectly depend on the energetic particle distribution function itself. This is because the diffusion coefficients describe the effect of turbulence on the energetic particles, and near shock waves the energetic particles modify the turbulence and in turn thus the diffusion coefficients. Models that take into account the non-linear coupling between the energetic particles and Alfvénic turbulence were presented in, for example, Ng & Reames (1994); Vainio & Laitinen (2007, 2008); Ng & Reames (2008); Afanasiev & Vainio (2013); Afanasiev et al. (2015).

In some cases, it is possible that energetic particles not only modify the small-scale turbulence, but also the large scale structure of the background plasma. Near collisionless shock waves, it can happen that the pressure exerted by the energetic particles is comparable or even larger than the magnetic and thermal pressure of the thermal plasma. This has been observed during the passage of some CMEs, when high SEP intensities are observed (Russell et al., 2013; Lario et al., 2015a,b). Similarly, observations of the Voyager spacecraft have indicated that suprathermal pickup ions might modify the structure of the heliospheric termination shock (e.g., Florinski et al., 2009), and CRs are likewise believed to mediate the shock waves of SNRs (e.g., Blandford, 1980; Malkov & Drury, 2001; Blasi, 2004). In these cases, a shock precursor develops, a region upstream of the shock where the pressure exerted by the energetic particles decelerates the thermal plasma flow (Drury & Voelk, 1981; Axford et al., 1982; Webb, 1983). The effect of the energetic particles on the large scale structure of the thermal plasma can thus not be ignored, such that the standard MHD equations are no longer a valid description of the background plasma. A possible way to obtain a more accurate description of the thermal background plasma, is by including terms describing the pressure, energy density, and energy flux of the energetic particle population into the MHD equations (e.g., Webb, 1983). The MHD equations and the FTE need then to be solved together like a two-fluid system. Such an approach can be regarded as a “hydrodynamic" description of the energetic particle population, since they are treated as a gas and their direct contribution to the electromagnetic field is neglected (see Zank, 2014, and references therein).

1.6 Existing global 3D MHD-SEP models

To fully comprehend the observed complexity of space weather events, increasingly sophisticated models for the coronal plasma, the solar wind, and SEPs have been developed over the recent years. However, only few attempts have been made to couple

these different models into one global model that can represent the evolution of both the low and high-energy particles in the inner heliosphere.

As explained in Section 1.5, one approach to achieve this is by solving the FTE on a Lagrangian grid along single magnetic field lines, obtained from a time-dependent 3D MHD model. Such an approach was taken by Kóta et al. (2005), who used the MHD model named BATS-R-US (Block Adaptive-Tree Solar-wind Roe-type Upwind Scheme; Powell et al., 1999). Sokolov et al. (2004) presented a similar model named the Field Line Advection Model for Particle Acceleration (FLAMPA), which also uses the MHD model BATS-R-US. However, FLAMPA solves the Parker equation (Parker, 1965) instead of the FTE, which is only valid under strong scattering conditions when the particles' pitch-angle distribution is isotropic. Recently, Borovikov et al. (2018) have presented the Multiple-FLAMPA (M-FLAMPA) model, which solves the Parker equation along multiple magnetic field lines derived from coronal and solar wind plasma configurations obtained from the model AWSoM (Alfvén-Wave-turbulence based Solar atmosphere Model; van der Holst et al., 2014).

The EPREM model presented in Schwadron et al. (2010) also uses a Lagrangian grid to solve the FTE along single magnetic field lines. In addition, EPREM includes a perpendicular transport process by tracing multiple field lines simultaneously and solving for cross-field diffusion and particle drifts using a separate pitch-angle averaged convection-diffusion equation (Schwadron et al., 2010). Kozarev et al. (2010) and Schwadron et al. (2015) have used EPREM together with the MHD models of CORHEL (Corona-Heliosphere Riley et al., 2012), that is, the inner heliospheric model Enlil (Odstrcil, 2003; Odstrcil et al., 2004) and the model MAS (Magnetohydrodynamic Algorithm outside a Sphere) which was developed by Predictive Science[5]. Recently, an improved version of EPREM has been combined with CORHEL to form the model STAT (Solar Particle Event Threat Assessment; Linker et al., 2019).

Luhmann et al. (2010) have developed SEPMOD (Solar Energetic Particle Model), which calculates the particle intensities during a gradual SEP event. This is done by tracing the magnetic field lines that connect an observer to the CME shock front, in a solar wind generated by the MHD model Enlil. In contrast to the previously discussed models, SEPMOD assumes scatter-free transport, such that the first adiabatic invariant of the particles is exactly conserved. The particle acceleration at the shock front is treated as a black-box, by injecting the energetic particles according to a semi-empirical function that depends on the properties of the modelled CME shock (see also Lario et al., 1998; Aran, 2007; Rodríguez-Gasén et al., 2011; Pomoell et al., 2015). The approach of SEPMOD is especially interesting for SEP forecasting tools, where efficiency is of great importance. In addition, the particle parallel mean free path in the heliosphere is poorly constrained and can vary strongly across different SEP events, especially in complex solar wind conditions. Consequently, solving the complete FTE

[5] www.predsci.com

with a certain prescribed mean free path is not guaranteed to provide a significantly more accurate SEP forecast than a scatter-free particle model.

1.7 Motivation and outline of this work

In Section 1.1 it was explained that energetic particles can have strongly adverse effects on the space-based infrastructure of our society and on humankind's future plans to establish manned outposts on the Moon or Mars. Therefore, it is of primordial importance to have a good understanding of the acceleration and transport processes of the high-energy particles in our solar system. Despite intensive research performed over the past decades, various questions concerning these energetic particle populations in the heliosphere remain unanswered. This is partly due to the limited number of spacecraft available in the heliosphere that can measure these particles. In this regard, a big game-changer for the study of SEPs, and for solar and space physics in general, is Parker Solar Probe (PSP; Fox et al., 2016), a spacecraft that was launched by the National Aeronautics and Space Administration (NASA) in August 2018 and which will approach the Sun eventually within 9.86 solar radii. In addition, the Solar Orbiter spacecraft (SolO; Müller et al., 2013, 2020), developed by the European Space Agency (ESA), was launched successfully from Cape Canaveral in Florida on the ninth of February 2020. This spacecraft will come as close as 60 solar radii to the Sun and its trajectory will be inclined by ~25° with respect to the ecliptic plane (~33° by the end of the extended mission phase), providing for the first time a view of the polar regions of the Sun. By combining the data received from PSP, SolO, and spacecraft orbiting at 1 AU like e.g., the Solar and Heliospheric Observatory (SOHO; Domingo et al., 1995) and the Solar Terrestrial Relations Observatory A (STEREO A; Kaiser et al., 2008), we will have high-quality SEP observations from at least four different vantage points in our solar system. This will allow us to study, for example, the effect of the solar wind on the spreading of SEPs in the inner heliosphere.

To interpret the data received from these various spacecraft, it is necessary to develop fully 3D and time-dependent solar wind and energetic particle models. Only when the observations correspond to what our mathematics-based models predict, we can claim to fully understand the physics of the transport and acceleration mechanisms of energetic particles in the heliosphere. Such a correspondence between observations and theory is however far ahead of us, yet understanding the discrepancies between both helps us to improve our models and gain insight in the complex mechanisms that affect energetic particles in space. These advances are aided by the increasing availability and capabilities of supercomputers, which allow us to solve more easily the complex systems of mathematical equations that describe the state of particle populations in space.

In this thesis, we develop a numerical model that calculates energetic particle intensities in the inner heliosphere by solving the FTE under realistic solar wind conditions. This model is called PARADISE, an acronym for *PArticle Radiation Asset Directed at Interplanetary Space Exploration*. PARADISE solves the FTE in a stochastic manner, by propagating pseudo-particles in a solar wind that is obtained from the *EUropean Heliospheric FORecasting Information Asset* (EUHFORIA; Pomoell & Poedts, 2018), which is a data-driven 3D time-dependent MHD model. Multiple quasi-linear and non-linear particle diffusion theories are implemented in PARADISE, to model the effect of the turbulent fluctuations of the background plasma on the energetic particle transport. By using PARADISE, this work aims at improving our understanding of the influence of the solar wind on energetic particle transport.

The outline of this thesis is the following. In Chapter 2, a derivation of the FTE equation is provided, starting from the Vlasov equation and the continuity equation of phase space. The presented derivation is valid under the approximation of special relativity, that is, a Minkowski spacetime is assumed. Moreover, an overview is given of different turbulence models and we discuss various energetic particle diffusion theories that are based on these turbulence models. In Chapter 3, the relevant notions of SDEs and Itô calculus are introduced, and the numerical details of the PARADISE model are provided. In Chapters 4, 5 and, 6, PARADISE is used to model the transport of SEPs in a solar wind containing a CIR. This solar wind is generated by the EUHFORIA model and contains multiple non-nominal structures, such as forward and reverse shock waves, a stream interface, and a rarefaction region. We find that all these plasma structure affect the particle transport in a significant manner. Chapter 7 discusses the effects of the particles' GC drifts in the heliosphere, and how the effects of these drifts are affected in non-nominal solar wind conditions. In Chapter 8, PARADISE is utilised to model the acceleration and transport of 100 keV protons in a solar wind containing a CME. Finally, in Chapter 9 the main results of this work are summarized and some future prospects are provided.

Chapter 2

The focused transport equation

"The path to paradise begins in hell."
– Dante Alighieri (The Divine Comedy)

Abstract. In this chapter, we present a derivation of the FTE, starting from the Vlasov equation and assuming a flat spacetime. The connection coefficients for a reference frame co-moving with a general background plasma are derived, and the definition of a mixed phase space distribution in a relativistic setting is discussed. Furthermore, it is illustrated how a transformation to GC coordinates introduces the GC drifts into the spatial part of the FTE, which is retained after gyro-averaging the equation. It is shown that this GC drift term can give rise to a pitch-angle dependent cross-field diffusion process in a turbulent plasma, and under the assumptions of QLT the field line random walk limit is recovered. Furthermore, we review how the pitch-angle diffusion coefficient is derived under the assumptions of QLT, and we briefly discuss some of the known shortcomings of QLT. Finally, an overview of existing phenomenological and non-linear cross-field diffusion theories is provided.

2.1 Introduction

The acceleration and transport of energetic particle populations in astrophysical plasmas can be described by means of their time-dependent phase space distribution function. In such a statistical approach, information on the individual energetic particles is lost, but the relevant physical information on the energetic particle population as a whole is retained. This is often the only viable approach, since many astrophysical plasmas are highly turbulent flows such that the phase space trajectories of individual energetic particles propagating through these plasmas are affected in a stochastic manner.

In this chapter, we derive the FTE, which was introduced in Section 1.5. This equation describes the evolution of a gyrotropic energetic particle population in a turbulent background plasma (e.g., Roelof, 1969). The FTE is derived by rewriting the Vlasov equation in terms of mixed phase space coordinates, meaning that the spatial coordinate is expressed in an inertial frame whereas the momentum coordinate is expressed in a frame co-moving with the background plasma. This transformation is performed for the ease of handling the scattering of particles on turbulent fluctuations, which are assumed to be advecting with the plasma. Under the assumption of a gyrotropic distribution function, the transport equation is averaged over the gyrophase giving the FTE. Over the years, the FTE has been presented by several authors under different assumptions and approximations, often however without detailing its derivation. Typical assumptions include:

1. Assuming a background Parker solar wind configuration (e.g., Ruffolo, 1995).
2. Assuming a uniform background magnetic field. (e.g., Kirk et al., 1988; Schlickeiser, 2002)
3. Omitting a transformation to the GC coordinates before gyro-averaging the equation, hereby losing information on the particle GC drifts. (Skilling, 1971; Webb, 1985; Ruffolo, 1995; Isenberg, 1997; Zank, 2014).
4. Neglecting any relativistic effects by considering Galilean coordinate transformations (e.g., Isenberg, 1997; Zhang, 2006; le Roux & Webb, 2009)

The derivation of the FTE presented in this chapter does not make any of the above assumptions, and all the calculations that are needed to obtain the equation are detailed, without omitting any steps (some of the lengthy algebra is provided in the appendix). Specifically, we follow the approach of Kirk et al. (1988) to take into account relativisic effects, and we transform to GC coordinates following Chapter 12 of Schlickeiser (2002). Contrary to Kirk et al. (1988) and Schlickeiser (2002), we do not make any assumption regarding the average background IMF, and we derive thus the connection coefficients for a reference frame co-moving with a general plasma (Section 2.2.3).

In Section 2.2.2, special attention is paid to the definition of the mixed phase space distribution function, since using two different reference frames introduces two different time coordinates in a relativistic setting. Furthermore, important in our version of the FTE is that it contains all the GC drifts in the spatial part of the FTE. It is illustrated in Sections 2.3 and 2.4 that these drift terms arise from a transformation to the GC coordinates, which needs to be performed before gyro-averaging the transport equation (Section 2.5).

After introducing the necessary terminology on turbulence (Section 2.6), we review how turbulent fluctuations affect the particle distribution under the assumptions of QLT (Section 2.7). Moreover, we show how the use of GC coordinates introduces a pitch-angle dependent spatial diffusion process in the FTE, which under the assumptions of QLT corresponds to the field line random walk (FLRW) derived by Jokipii (1966) in a different manner. In Section 2.8, an overview is provided of some non-linear cross-field diffusion theories that were developed to address the shortcomings of QLT. Section 2.9 reviews some phenomenological approaches to cross-field diffusion, and Section 2.10 briefly discusses diffusion processes in the momentum coordinate. We conclude the chapter in Section 2.11 with a summary and a discussion.

2.2 A transport equation for test particles propagating in a relativisic colisionless plasma

In this section, a transport equation is derived that describes the evolution of the six-dimensional phase space distribution function of energetic charged particles. The energetic particles are assumed to be test particles, propagating through a collisionless, turbulent, and possibly relativistic background plasma. It is hereby assumed that the turbulent fluctuations are convected with the bulk plasma flow, and hence it is convenient to transform the momentum phase space coordinate to the reference frame co-moving with the plasma. Furthermore, a flat spacetime is assumed such that any effect of gravity on the energetic particles is neglected. Before presenting the derivation, we shortly introduce the necessary terminology and relativistic transformations.

2.2.1 Terminology and transformations

We start by summarizing some concepts of special relativity and explain the notation that will be used in the remainder of the chapter. A four-vector is denoted as $w^\alpha = (w^0, w^a)$, where the standard convention is used that Latin indices take values for spatial components and Greek indices take values for space and time components. The spatial part of the four vector will often also be denoted in bold face, i.e., $\mathbf{w} = w^a$.

Two important four-vectors are time-space $x^\alpha = (ct, x^a)$ and four-momentum $p^\alpha = (E/c, p^a) = \gamma m(c, v^a)$, where c is the speed of light, m is the rest mass of the particle, $\gamma = (1 - v^2/c^2)^{-1/2}$ is the Lorentz factor associated with the speed of the particle, and E denotes the energy of the particle. Moreover, we have that

$$p^\alpha = m\frac{dx^\alpha}{d\tau}, \tag{2.1}$$

where τ denotes the proper time of the particle.

The calculations presented below make use of both an inertial frame and the (non-inertial) plasma frame, which moves with a velocity $\mathbf{U} = (U_x, U_y, U_z)$ with respect to the inertial frame. The Lorentz transformation matrix associated with a boost of speed U in the direction defined by the unit vector $\mathbf{u} = \mathbf{U}/U = (u_x, u_y, u_z)$ is given by

$$\Lambda^\nu{}_\mu = \begin{pmatrix} \Gamma & -U_x\Gamma/c & -U_y\Gamma/c & -U_z\Gamma/c \\ -U_x\Gamma/c & 1+(\Gamma-1)u_x^2 & (\Gamma-1)u_xu_y & (\Gamma-1)u_xu_z \\ -U_y\Gamma/c & (\Gamma-1)u_xu_y & 1+(\Gamma-1)u_y^2 & (\Gamma-1)u_yu_z \\ -U_z\Gamma/c & (\Gamma-1)u_xu_z & (\Gamma-1)u_yu_z & 1+(\Gamma-1)u_z^2 \end{pmatrix}, \tag{2.2}$$

with $\Gamma = (1-U^2/c^2)^{-1/2}$ the Lorentz factor associated with the transformation. The time-space and momentum four-vectors are both contravariant vectors, hence transforming as

$$\tilde{x}^\nu = \Lambda^\nu{}_\mu x^\mu, \qquad \tilde{p}^\nu = \Lambda^\nu{}_\mu p^\mu.$$

The four-gradient

$$\frac{\partial}{\partial x^\alpha} = \left(\frac{\partial}{\partial x^0}, \frac{\partial}{\partial x^1}, \frac{\partial}{\partial x^2}, \frac{\partial}{\partial x^3}\right)$$

is a covariant vector and transforms thus as

$$\frac{\partial}{\partial \tilde{x}^\nu} = \tilde{\Lambda}^\mu{}_\nu \frac{\partial}{\partial x^\mu}, \tag{2.3}$$

where $\tilde{\Lambda} := \Lambda^{-1}$. The following notation will be used for the mixed electromagnetic field tensor:

$$F^\mu{}_\nu = \begin{pmatrix} 0 & E_x/c & E_y/c & E_z/c \\ E_x/c & 0 & B_z & -B_y \\ E_y/c & -B_z & 0 & B_x \\ E_z/c & B_y & -B_x & 0 \end{pmatrix}, \tag{2.4}$$

where E_i and B_i are the electric and magnetic fields, respectively.

Finally, because the plasma frame is a non-inertial frame, we need to introduce the connection coefficients $\Gamma^\alpha_{\mu\nu}$, which can be defined as (e.g., Misner et al., 2017)

$$\frac{\partial e_\alpha}{\partial x^\beta} = \Gamma^\gamma_{\alpha\beta} e_\gamma, \tag{2.5}$$

where e_α are the basis vectors of a reference frame. Useful is the following transformation law for connection coefficients (e.g., Riffert, 1986)

$$\tilde{\Gamma}^{\kappa}_{\alpha\beta} = \Lambda^{\kappa}{}_{\tau}\tilde{\Lambda}^{\mu}{}_{\beta}\left(\tilde{\Lambda}^{\nu}{}_{\alpha}\Gamma^{\tau}_{\nu\mu} + \frac{\partial\tilde{\Lambda}^{\tau}{}_{\alpha}}{\partial x^{\mu}}\right) = \Lambda^{\kappa}{}_{\tau}\tilde{\Lambda}^{\mu}{}_{\beta}\frac{\partial\tilde{\Lambda}^{\tau}{}_{\alpha}}{\partial x^{\mu}}, \tag{2.6}$$

where $\tilde{\Gamma}^{\kappa}_{\alpha\beta}$ denotes the connection coefficient of the plasma frame. Remark that the last equality of this transformation law is only valid when the observer's frame is a Cartesian[1] inertial frame. Other useful identities are (Misner et al., 2017)

$$\Gamma^{0}_{0\alpha} = 0, \qquad \Gamma^{i}_{j\alpha} = -\Gamma^{j}_{i\alpha}, \qquad \Gamma^{i}_{0\alpha} = \Gamma^{0}_{i\alpha}. \tag{2.7}$$

From the second identity it follows that

$$\Gamma^{i}_{i\alpha} = -\Gamma^{i}_{i\alpha} = 0. \tag{2.8}$$

2.2.2 The Vlasov equation in mixed phase space coordinates

To derive the FTE, we start by formulating the Vlasov equation in the inertial frame, that is,

$$\frac{dx^{\alpha}}{d\tau}\frac{\partial f}{\partial x^{\alpha}} + \frac{dp^{a}}{d\tau}\frac{\partial f}{\partial p^{a}} = 0. \tag{2.9}$$

The equation of motion of a particle subjected to the electromagnetic Lorentz force is

$$\frac{dp^{a}}{d\tau} = \frac{q}{m}F^{a}{}_{\alpha}p^{\alpha} - \frac{1}{m}\Gamma^{a}_{\alpha\beta}p^{\alpha}p^{\beta}, \tag{2.10}$$

with q the electric charge of the particle. If there are no electromagnetic fields, this equation reduces to the geodesic equation. In an inertial Cartesian reference frame, the term containing the connection coefficients becomes zero. In contrast, for the non-inertial plasma frame, this term can be regarded as the fictitious forces acting on the particle.

By substituting Eqs. (2.1) and (2.10) into the Vlasov equation, and multiplying by the rest mass, the following equation is obtained

$$p^{\alpha}\frac{\partial f}{\partial x^{\alpha}} + qF^{a}{}_{\alpha}p^{\alpha}\frac{\partial f}{\partial p^{a}} - \Gamma^{a}_{\alpha\beta}p^{\alpha}p^{\beta}\frac{\partial f}{\partial p^{a}} = 0. \tag{2.11}$$

As explained in the introduction, we will work in mixed coordinates. This means that the position vector needs to be expressed in the inertial observer's frame, while the

[1] If one would use e.g., spherical coordinates, the connection coefficients are not zero in the inertial frame.

momentum needs to be expressed in a frame co-moving with the local plasma velocity. In these mixed coordinates, the Vlasov equation becomes (Riffert, 1986; Kirk et al., 1988)

$$\tilde{p}^\beta \tilde{\Lambda}^\alpha{}_\beta \frac{\partial f}{\partial x^\alpha} + q\tilde{F}^a{}_\alpha \tilde{p}^\alpha \frac{\partial f}{\partial \tilde{p}^a} - \tilde{\Gamma}^a_{\alpha\beta}\tilde{p}^\alpha \tilde{p}^\beta \frac{\partial f}{\partial \tilde{p}^a} = 0, \tag{2.12}$$

where the components measured in the plasma frame are denoted with a tilde symbol. To obtain the first term of Eq. (2.12) we used transformation (2.3).

Remark that although Eq. (2.12) is written in mixed coordinates, the distribution function f in this equation is not expressed in mixed coordinates. More precisely, in the first term of Eq. (2.12) f is the distribution function in the reference frame (x^α, p^α), while in the last two terms f is the distribution function in the reference frame $(\tilde{x}^\alpha, \tilde{p}^\alpha)$, i.e.,

$$\tilde{p}^\beta \tilde{\Lambda}^\alpha{}_\beta \frac{\partial f}{\partial x^\alpha} = \tilde{p}^\beta \tilde{\Lambda}^\alpha{}_\beta \frac{\partial}{\partial x^\alpha} f(x^\alpha, p^a),$$

and

$$\left(q\tilde{F}^a{}_\alpha \tilde{p}^\alpha \frac{\partial}{\partial \tilde{p}^a} - \Gamma^a_{\alpha\beta}\tilde{p}^\alpha \tilde{p}^\beta \frac{\partial}{\partial \tilde{p}^a}\right) f = \left(q\tilde{F}^a{}_\alpha \tilde{p}^\alpha \frac{\partial}{\partial \tilde{p}^a} - \Gamma^a_{\alpha\beta}\tilde{p}^\alpha \tilde{p}^\beta \frac{\partial}{\partial \tilde{p}^a}\right) f(\tilde{x}^\alpha, \tilde{p}^a).$$

This is indeed possible since the distribution function is invariant, i.e.,

$$f(x^\alpha, p^a) = f(\tilde{x}^\alpha, \tilde{p}^a), \tag{2.13}$$

which is a non-trivial result in a relativistic setting (e.g., Debbasch et al., 2001). For example, since $d\mathbf{x}d\mathbf{p}$ is not a Lorentz invariant, we have in general that

$$f(\mathbf{x}, \mathbf{p}, t)d\mathbf{x}d\mathbf{p} \neq f(\tilde{\mathbf{x}}, \tilde{\mathbf{p}}, \tilde{t})d\tilde{\mathbf{x}}d\tilde{\mathbf{p}}, \tag{2.14}$$

when the distribution function f is defined as

$$dN = f(\mathbf{x}, \mathbf{p}, t)d\mathbf{x}d\mathbf{p}.$$

In the latter expression, dN denotes the number of particles in the infinitesimal volume $d\mathbf{x}d\mathbf{p}$, belonging to a hypersurface t = constant in spacetime. The left-hand side of Eq. (2.14) represents thus the number of particles counted at a *fixed point in time* t, whereas the right-hand side is the number of particles counted at a *fixed point in time* t', such that equating both sides is not meaningful due to the relativity of time (that is, a constant time in one reference frame will not be constant in an other frame). For a thorough discussion on this subject we refer to Debbasch et al. (2001).

A mixed phase space distribution can be defined as

$$dN = \mathcal{F}(\mathbf{x}, \tilde{\mathbf{p}}, t)d\mathbf{x}d\tilde{\mathbf{p}},$$

where dN is the number of particles in the infinitesimal volume $d\mathbf{x}d\tilde{\mathbf{p}}$ at a fixed time t. The particles are thus always counted at a point in time that is fixed in the inertial

reference frame. The relation between the distribution function f and the mixed distribution function $\mathcal{F}$ is then

$$\mathcal{F}(\mathbf{x}, \tilde{\mathbf{p}}, t) = J_\psi f\left(\psi(\mathbf{x}, \tilde{\mathbf{p}}), t\right),$$

where J_ψ is the Jacobian of the coordinate transformation

$$\psi : \mathbb{R}^6 \to \mathbb{R}^6 : (\mathbf{x}, \tilde{\mathbf{p}}) \mapsto (\mathbf{x}, \mathbf{p}) = \left(\mathbf{x}, \tilde{\mathbf{p}} + \tilde{\gamma} m \mathbf{U}\left[\frac{\tilde{\boldsymbol{v}} \cdot \mathbf{U}}{U^2}(\Gamma - 1) + \Gamma\right]\right). \tag{2.15}$$

By noting that

$$\frac{\partial x^i}{\partial \tilde{p}^j} = 0, \qquad \frac{\partial x^i}{\partial x^j} = \delta_{ij}, \tag{2.16}$$

the Jacobian of transformation (2.15) can be simplified to

$$J_\psi = \left|\frac{\partial(\mathbf{x}, \mathbf{p})}{\partial(\mathbf{x}, \tilde{\mathbf{p}})}\right| = \det\left(\frac{\partial p^i}{\partial \tilde{p}^j}\right) \tag{2.17}$$

Since[2] $d(\tilde{\gamma} m)/d\tilde{p}^i = \tilde{p}^i / \tilde{\gamma} m c^2$, we obtain that

$$\frac{\partial p^i}{\partial \tilde{p}^j} = \delta_{ij} + U^i \frac{\tilde{p}^j}{\tilde{\gamma} m c^2}\Gamma + \frac{U^i U^j}{U^2}(\Gamma - 1), \tag{2.18}$$

such that a straightforward calculation leads to

$$J_\psi = \Gamma\left(1 + \frac{\mathbf{U} \cdot \tilde{\boldsymbol{v}}}{c^2}\right). \tag{2.19}$$

The mixed phase space distribution function $\mathcal{F}$ relates thus to the distribution function f as (see also Webb & Gleeson, 1979)

$$\mathcal{F}(\mathbf{x}, \tilde{\mathbf{p}}, t) = \Gamma\left(1 + \mathbf{U} \cdot \tilde{\boldsymbol{v}}/c^2\right) f(\psi(\mathbf{x}, \tilde{\mathbf{p}}), t). \tag{2.20}$$

Finally, defining

$$\mathscr{F}(\mathbf{x}, \tilde{\mathbf{p}}, t) \coloneqq \frac{\mathcal{F}(\mathbf{x}, \tilde{\mathbf{p}}, t)}{\Gamma\left(1 + \mathbf{U} \cdot \tilde{\boldsymbol{v}}/c^2\right)}, \tag{2.21}$$

allows to write down the relativistic Vlasov equation in mixed coordinates as:

$$\tilde{p}^\beta \tilde{\Lambda}^\alpha{}_\beta \frac{\partial \mathscr{F}}{\partial x^\alpha} + q \tilde{F}^a{}_\alpha \tilde{p}^\alpha \frac{\partial \mathscr{F}}{\partial \tilde{p}^a} - \tilde{\Gamma}^a_{\alpha\beta} \tilde{p}^\alpha \tilde{p}^\beta \frac{\partial \mathscr{F}}{\partial \tilde{p}^a} = 0. \tag{2.22}$$

It is worth stressing that $\mathcal{F}$ is the distribution function in mixed phase space, and not $\mathscr{F}$. Only in the limit of a non-relativistic background plasma for which $U/c \to 0$, we have $\mathscr{F} = \mathcal{F} = f$.

[2] From $\gamma = \left(1 - \frac{p^2}{(\gamma m)^2 c^2}\right)^{-1/2}$, it follows that $\gamma = \left(1 + \frac{p^2}{m^2 c^2}\right)^{1/2}$, such that $\frac{d(\gamma m)}{dp^i} = \frac{p^i}{\gamma m c^2} = \frac{p^i}{E}$.

2.2.3 The connection coefficients in mixed coordinates

By utilising the Lorentz transformation (2.2), one obtains after a straightforward calculation that

$$\tilde{p}^{\beta}\tilde{\Lambda}^{\alpha}{}_{\beta}\frac{\partial \mathscr{F}}{\partial x^{\alpha}} = m\tilde{\gamma}\Gamma\left(1+\frac{\mathbf{U}\cdot\tilde{\boldsymbol{v}}}{c^2}\right)\frac{\partial \mathscr{F}}{\partial t} + m\tilde{\gamma}\left\{\tilde{\boldsymbol{v}}+\Gamma\mathbf{U}+[(\Gamma-1)\mathbf{u}\cdot\tilde{\boldsymbol{v}}]\,\mathbf{u}\right\}\cdot\nabla\mathscr{F}, \quad (2.23)$$

where $\tilde{\gamma} = (1-\tilde{v}^2/c^2)^{-1/2}$ and $\mathbf{u} = \mathbf{U}/U$. Moreover, by using Eq. (2.7), the following expressions for the connection coefficients are obtained:

$$\tilde{\Gamma}^{i}_{00} = \frac{\Gamma^2}{c^2}\left[\frac{dU^i}{dt} + (\Gamma-1)\frac{U^i}{U}\frac{dU}{dt}\right] \quad (2.24)$$

$$\tilde{\Gamma}^{i}_{j0} = \frac{\Gamma(\Gamma-1)}{cU^2}\left(U^j\frac{dU^i}{dt} - U^i\frac{dU^j}{dt}\right) \quad (2.25)$$

$$\begin{aligned}\tilde{\Gamma}^{i}_{0j} =& \frac{\Gamma}{c}\left[\frac{\Gamma U^j}{c}\left(\frac{\partial U^i}{\partial x^0} + (\Gamma-1)\frac{U^i}{U}\frac{\partial U}{\partial x^0}\right) + \frac{\partial U^i}{\partial x^j}\right.\\ &\left. + \frac{(\Gamma-1)}{U}\left(\frac{U^jU^k}{U}\frac{\partial U^i}{\partial x^k} + U^i\frac{\partial U}{\partial x^j} + (\Gamma-1)\frac{U^iU^jU^l}{U^2}\frac{\partial U}{\partial x^l}\right)\right]\\ =& \frac{\Gamma+1}{c}\left[\frac{\Gamma U^j}{c}\frac{\partial}{\partial x^0} + \frac{\partial}{\partial x^j} + (\Gamma-1)\frac{U^jU^k}{U^2}\frac{\partial}{\partial x^k}\right]\left(\frac{\Gamma U^i}{\Gamma+1}\right)\end{aligned} \quad (2.26)$$

$$\begin{aligned}\tilde{\Gamma}^{i}_{jk} =& \frac{\Gamma(\Gamma-1)U^k}{cU^2}\left(U^j\frac{\partial U^i}{\partial x^0} - U^i\frac{\partial U^j}{\partial x^0}\right) + \frac{(\Gamma-1)^2U^kU^l}{U^4}\left(U^j\frac{\partial U^i}{\partial x^l} - U^i\frac{\partial U^j}{\partial x^l}\right)\\ &+ \frac{(\Gamma-1)}{U^2}\left(U^j\frac{\partial U^i}{\partial x^k} - U^i\frac{\partial U^j}{\partial x^k}\right),\end{aligned} \quad (2.27)$$

where we have introduced the convective derivative

$$\frac{d}{dt} = \frac{\partial}{\partial t} + U^i\frac{\partial}{\partial x^i}. \quad (2.28)$$

The remaining connection coefficients follow from identities (2.7) and (2.8).

2.2.4 The transport equation to first order in U/c

In many astrophysical plasmas it is reasonable to neglect the terms in the transport equation which are of second or higher order in U/c. This is for example a good approximation for jets around young stellar objects (YSO), for which $U/c \sim 3\times10^{-4}$

(e.g., Woitas et al., 2002), and for many SNe and SNRs. For core-collapse SNe and Type Ia SNe, stellar ejecta is accelerated to speeds of order $\sim 5 \times 10^3$ km/s (i.e., $U/c \sim 1.7 \times 10^{-2}$) and $\sim 10^3$ km/s (i.e., $U/c \sim 3 \times 10^{-2}$), respectively (e.g., Alsabti & Murdin, 2017, and references therein). Neglecting terms of order $O(U^2/c^2)$ is also a good approximation for any plasma residing in the solar system. For example, in the slow solar wind we have $U/c \sim 10^{-3}$, whereas for a very fast CME we have $U/c \sim 10^{-2}$. In fact, for heliospheric plasmas it is even a good approximation to also neglect the $O(U/c)$ terms, but for the sake of generality we retain terms to first order in U/c in the calculations presented below.

It is worth stressing that by neglecting the $O(U/c)$ or $O(U^2/c^2)$ terms in the transport equation, no assumptions are being made regarding the speed of the energetic particles. Instead, only the speed of the background plasma is limited, and hence the obtained equations are still valid for particles travelling at relativistic speeds.

It holds to first order in U/c that $\Gamma \approx 1$, such that Eq. (2.23) and the connection coefficients (2.24) – (2.27) simplify to

$$\tilde{p}^\beta \tilde{\Lambda}^\alpha_\beta \frac{\partial \mathscr{F}}{\partial x^\alpha} \approx \tilde{\gamma} m \left(1 + \frac{\mathbf{U} \cdot \tilde{\boldsymbol{v}}}{c^2}\right) \frac{\partial \mathscr{F}}{\partial t} + \tilde{\gamma} m \left(\tilde{\boldsymbol{v}} + \mathbf{U}\right) \cdot \nabla \mathscr{F}, \tag{2.29}$$

$$\tilde{\Gamma}^i_{j0} p^0 p^j \approx 0, \tag{2.30}$$

$$\tilde{\Gamma}^i_{0j} p^0 p^j \approx (\tilde{\gamma} m)^2 \tilde{v}^j \frac{\partial U^i}{\partial x^j}, \tag{2.31}$$

$$\tilde{\Gamma}^i_{jk} p^j p^k \approx 0, \tag{2.32}$$

$$\tilde{\Gamma}^i_{00} p^0 p^0 \approx (\tilde{\gamma} m)^2 \frac{dU^i}{dt}. \tag{2.33}$$

Hence, the following transport equation is obtained:

$$\begin{aligned} &\tilde{\gamma} m \left(1 + \frac{\mathbf{U} \cdot \tilde{\boldsymbol{v}}}{c^2}\right) \frac{\partial \mathscr{F}}{\partial t} + \tilde{\gamma} m \left(\tilde{\boldsymbol{v}} + \mathbf{U}\right) \cdot \frac{\partial \mathscr{F}}{\partial \mathbf{x}} + q \tilde{F}^a{}_\alpha \tilde{p}^\alpha \frac{\partial \mathscr{F}}{\partial \tilde{p}^a} \\ &- (\tilde{\gamma} m)^2 \left\{ \frac{\partial \mathbf{U}}{\partial t} + \left[\left(\tilde{\boldsymbol{v}} + \mathbf{U}\right) \cdot \nabla\right] \mathbf{U} \right\} \cdot \frac{\partial \mathscr{F}}{\partial \tilde{\mathbf{p}}} = 0. \end{aligned} \tag{2.34}$$

Substituting the electromagnetic field tensor into this equation and dividing[3] by the rest mass m gives

$$\begin{aligned}&\tilde{\gamma}\left(1+\frac{\mathbf{U}\cdot\tilde{\boldsymbol{v}}}{c^2}\right)\frac{\partial\mathscr{F}}{\partial t}+\gamma\left(\tilde{\boldsymbol{v}}+\mathbf{U}\right)\cdot\frac{\partial\mathscr{F}}{\partial\mathbf{x}}\\&+\tilde{\gamma}\left\{\frac{q}{m}\left(\tilde{\mathbf{E}}+\tilde{\boldsymbol{v}}\times\tilde{\mathbf{B}}\right)-m\tilde{\gamma}\left(\frac{\partial\mathbf{U}}{\partial t}+\left[\left(\tilde{\boldsymbol{v}}+\mathbf{U}\right)\cdot\nabla\right]\mathbf{U}\right)\right\}\cdot\frac{\partial\mathscr{F}}{\partial\tilde{\mathbf{p}}}\\&=0.\end{aligned}\tag{2.35}$$

The electromagnetic fields of the inertial and plasma frames can be related through:

$$\begin{aligned}\tilde{\mathbf{E}}&=\Gamma\left(\mathbf{E}+\mathbf{U}\times\mathbf{B}\right)+\left(1-\Gamma\right)\frac{\mathbf{E}\cdot\mathbf{U}}{c^2}\mathbf{U}\approx\mathbf{E}+\mathbf{U}\times\mathbf{B}\\\tilde{\mathbf{B}}&=\Gamma\left(\mathbf{B}-\frac{1}{c^2}\mathbf{U}\times\mathbf{E}\right)+\left(1-\Gamma\right)\frac{\mathbf{B}\cdot\mathbf{U}}{v^2}\mathbf{U}\approx\mathbf{B}-\frac{1}{c^2}\mathbf{U}\times\mathbf{E},\end{aligned}\tag{2.36}$$

where the last equalities hold to first order in U/c. For an ideal plasma, the electric field vanishes in the rest frame of the plasma, i.e., $\tilde{\mathbf{E}}=0$, and we obtain to first order in U/c that

$$\tilde{\mathbf{B}}=\mathbf{B}+\frac{1}{c^2}\mathbf{U}\times\left(\mathbf{U}\times\mathbf{B}\right)\approx\mathbf{B}.\tag{2.37}$$

Substituting this result into Eq. (2.35) gives then

$$\begin{aligned}&\tilde{\gamma}\left(1+\frac{\mathbf{U}\cdot\tilde{\boldsymbol{v}}}{c^2}\right)\frac{\partial\mathscr{F}}{\partial t}+\tilde{\gamma}\left(\tilde{\boldsymbol{v}}+\mathbf{U}\right)\cdot\frac{\partial\mathscr{F}}{\partial\mathbf{x}}\\&+\tilde{\gamma}\left\{q\tilde{\boldsymbol{v}}\times\mathbf{B}-m\tilde{\gamma}\left(\frac{\partial\mathbf{U}}{\partial t}+\left[\left(\tilde{\boldsymbol{v}}+\mathbf{U}\right)\cdot\nabla\right]\mathbf{U}\right)\right\}\cdot\frac{\partial\mathscr{F}}{\partial\tilde{\mathbf{p}}}=0,\end{aligned}\tag{2.38}$$

which was previously presented by e.g., Skilling (1971). The last term in Eq. (2.38) illustrates how the particle momentum in the plasma frame is changed due to the magnetic Lorenz force and a fictitious force[4].

Equation. (2.38) was derived from the Vlasov equation, and can thus be considered as the Vlasov equation in mixed coordinates. For referential convenience we reformulate Eq. (2.38) as

$$\frac{dx^\alpha}{d\tau}\frac{\partial\mathscr{F}}{\partial x^\alpha}+\frac{d\tilde{p}^a}{d\tau}\frac{\partial\mathscr{F}}{\partial\tilde{p}^a}=0,\tag{2.39}$$

[3]This division is necessary, since we started our derivation from Eq. (2.11), which is the Vlasov equation multiplied by m.

[4]This "fictitious" force term contains in fact the momentum changes due to the GC drifts along the motional electric field (e.g., le Roux et al., 2007)]

with

$$\frac{dx^0}{d\tau} = c\frac{dt}{d\tau} = c\tilde{\gamma}\left(1 + \frac{\mathbf{U}\cdot\tilde{\boldsymbol{v}}}{c^2}\right), \tag{2.40}$$

$$\frac{d\mathbf{x}}{d\tau} = \tilde{\gamma}\left(\tilde{\boldsymbol{v}} + \mathbf{U}\right), \tag{2.41}$$

$$\frac{d\tilde{\mathbf{p}}}{d\tau} = q\tilde{\gamma}\tilde{\boldsymbol{v}}\times\mathbf{B} - m\tilde{\gamma}^2\left(\frac{\partial\mathbf{U}}{\partial t} + \left[\left(\tilde{\boldsymbol{v}} + \mathbf{U}\right)\cdot\nabla\right]\mathbf{U}\right). \tag{2.42}$$

The proper time can be eliminated from these equations by dividing Eq. (2.39) by $dt/d\tau$ and by applying the chain rule, which gives

$$\frac{\partial\mathscr{F}}{\partial t} + \frac{dx^a}{dt}\frac{\partial\mathscr{F}}{\partial x^a} + \frac{d\tilde{p}^a}{dt}\frac{\partial\mathscr{F}}{\partial\tilde{p}^a} = 0, \tag{2.43}$$

with

$$\frac{d\mathbf{x}}{dt} = \left(1 - \frac{\mathbf{U}\cdot\tilde{\boldsymbol{v}}}{c^2}\right)\tilde{\boldsymbol{v}} + \mathbf{U}, \tag{2.44}$$

$$\frac{d\tilde{\mathbf{p}}}{dt} = \left(1 - \frac{\mathbf{U}\cdot\boldsymbol{v}}{c^2}\right)q\tilde{\boldsymbol{v}}\times\mathbf{B} - \tilde{\gamma}m\left(\frac{\partial\mathbf{U}}{\partial t} + \left[\left(\tilde{\boldsymbol{v}} + \mathbf{U}\right)\cdot\nabla\right]\mathbf{U}\right), \tag{2.45}$$

where these last two equations hold to first order in U/c. Finally, we can also formulate the continuity equation in mixed phase space, i.e.,

$$\frac{\partial\mathcal{F}}{\partial t} + \frac{\partial}{\partial x^a}\left(\frac{dx^a}{dt}\mathcal{F}\right) + \frac{\partial}{\partial\tilde{p}^a}\left(\frac{d\tilde{p}^a}{dt}\mathcal{F}\right) = 0. \tag{2.46}$$

This continuity equation can also be derived from Eq. (2.43) by using Eq. (2.21) and[5]

$$\frac{\partial}{\partial t}\left(\frac{\gamma}{\tilde{\gamma}}\right) + \frac{\partial}{\partial x^a}\left(\frac{\gamma}{\tilde{\gamma}}\frac{dx^a}{dt}\right) + \frac{\partial}{\partial\tilde{p}^a}\left(\frac{\gamma}{\tilde{\gamma}}\frac{d\tilde{p}^a}{dt}\right) = 0, \tag{2.47}$$

where the factor $\gamma/\tilde{\gamma} = \left(1 + \mathbf{U}\cdot\tilde{\boldsymbol{v}}/c^2\right)$ follows from Eq. (2.40).

[5] To prove this formula, note that to first order in U/c

$$\frac{\partial}{\partial t}\left(\frac{\gamma}{\tilde{\gamma}}\right) = \frac{\tilde{\boldsymbol{v}}}{c^2}\cdot\frac{\partial\mathbf{U}}{\partial t}, \quad \frac{\partial}{\partial x^a}\left(\frac{\gamma}{\tilde{\gamma}}\frac{dx^a}{dt}\right) = \nabla\cdot\mathbf{U}, \quad \frac{\partial}{\partial\tilde{p}^a}\left(\frac{\gamma}{\tilde{\gamma}}\frac{d\tilde{p}^a}{dt}\right) = -\nabla\cdot\mathbf{U} - \frac{\tilde{\boldsymbol{v}}}{c^2}\cdot\frac{\partial\mathbf{U}}{\partial t},$$

where the last equation can be derived by using the result of footnote 2.

2.3 Guiding centre coordinates and the differential intensity

In order to include the particle GC drift terms explicitly in the transport equation, we perform a transformation to the GC coordinates, which are defined as

$$\mathbf{X} = (X, Y, Z) = \mathbf{x} - \mathbf{r}_L = \mathbf{x} + \frac{\tilde{\mathbf{p}} \times \mathbf{B}}{qB^2}. \tag{2.48}$$

In this expression, $\mathbf{r}_L$ denotes the instantaneous Larmor radius at location $\mathbf{x}$, which means that the magnetic field vector appearing in Eq. (2.48) is equal to $\mathbf{B}(\mathbf{x})$ and not to $\mathbf{B}_g = \mathbf{B}(\mathbf{X})$[6]. In addition, we express the momentum vector in spherical coordinates, i.e., $(p, \mu = \cos(\theta), \phi)$, where the polar axis is aligned with the magnetic field measured at the GC location. The coordinate p denotes thus the magnitude of the momentum vector, ϕ the gyrophase, and $\mu = \mathbf{b}_g \cdot \mathbf{p}/p = \cos(\theta)$, where $\mathbf{b}_g = \mathbf{B}_g/B_g$ and θ is called the pitch-angle. Note that the momentum coordinate is still expressed in a frame co-moving with the plasma (at the GC location), and we have omitted the tilde symbol from the coordinates (p, μ, ϕ) for notational convenience.

In summary, the following transformation is thus considered:

$$(x, y, z, \tilde{p}_x, \tilde{p}_y, \tilde{p}_z) \mapsto (X, Y, Z, p, \mu, \phi). \tag{2.49}$$

In order for the spatial part of this transformation (i.e., the $\mathbf{x} \mapsto \mathbf{X}$) to be well-defined, it is necessary to require that the magnetic field varies on a characteristic length scale, L, that is significantly larger than the Larmor radius[7] (see also Appendix B). In that case, one can show that the Jacobian of the transformation $\mathbf{x} \mapsto \mathbf{X}$ equals approximately unity[8].

[6] I would like to thank J.P. van den Berg for pointing this out to me.

[7] One can see why this is necessary by considering for example the following magnetic field

$$\mathbf{B}(\mathbf{x}) = \begin{cases} \frac{p_0}{q} \frac{1}{r_0 - x} \mathbf{e}_z, & x < r_0/2 \\ 2B_0 \mathbf{e}_z & x \geq r_0/2, \end{cases}$$

with $r_0 := p_0/(qB_0)$. The variables p_0 and B_0 denote a reference momentum and a magnetic field magnitude, respectively. For $x < r_0/2$ it holds thus that $dB/dx = B(x)/\hat{r}(x)$, with $\hat{r}(x) := p_0/(qB)$. Moreover, the GC transformation gives that $X(x) = x + \frac{p_y}{p_0}(r_0 - x)$ for $x < r_0/2$. Hence, all particles with $p_y = p_0$ and $x < r_0/2$ will have $X = r_0$, independent of their x coordinate. Clearly, transformation (2.49) is in this case thus not a bijective map. This can also be seen by calculating the Jacobian J of the transformation $\mathbf{x} \mapsto \mathbf{X}$ (footnote 8), which equals in this case $J = 1 - p_y/p_0$, and is thus not invertible on the phase space hypersurface $p_y = p_0$.

[8] It is actually easier to calculate the Jacobian of the inverse transformation $\mathbf{x} \mapsto \mathbf{X}$, which equals

$$J = 1 - \frac{\tilde{\mathbf{p}}}{q} \cdot \nabla \times \left(\frac{\mathbf{b}_g}{B_g} \right) + O(\delta^2) = 1 + O(\delta), \tag{2.50}$$

with $\delta = r_L/L$. For notational simplicity, we will not make any distinction between the distribution functions of $\mathbf{x}$ or $\mathbf{X}$. However, it should be kept in mind that the distribution function of the stochastic vector $(\mathbf{X}, \tilde{\mathbf{p}})$ equals $J^{-1}(\mathbf{X})\mathcal{F}(t, \mathbf{x}(\mathbf{X}, \tilde{\mathbf{p}}), \tilde{\mathbf{p}})$.

In Section 2.5, the FTE will be derived by assuming a particle distribution that is independent of the gyrophase ϕ and by subsequently averaging the transport equation over this angle. However, before performing the latter averaging procedure, it is necessary to transform to GC coordinates if one wants to include the effects of the GC drifts in the spatial term of the FTE. As discussed in Appendix A, the appearance of these drift terms in the FTE results from the definition of the gyro-averaging operator, which differs depending on whether the distribution function is expressed in the regular coordinates $\mathbf{x}$ or in the GC coordinates $\mathbf{X}$. In addition (Section 2.7.2), the transformation to GC coordinates leads to a cross-field diffusion process in the FTE, which is otherwise lost.

The particle transport equation (2.39) can be written as

$$\frac{dt}{d\tau}\frac{\partial \mathscr{F}}{\partial t} + \frac{dX^a}{dt}\frac{\partial \mathscr{F}}{\partial X^a} + \frac{dp^a}{d\tau}\frac{\partial \mathscr{F}}{\partial p^a} = 0, \tag{2.51}$$

with $p^a = (p, \mu, \phi)$. Expressions for $dX^a/d\tau$ and $dp^a/d\tau$ will be derived in the next section. Likewise, the continuity equation (2.46) can be written as

$$\frac{1}{p^2}\frac{\partial}{\partial t}\left(p^2\mathcal{F}\right) + \frac{1}{p^2}\frac{\partial}{\partial x^a}\left(\frac{dX^a}{dt}p^2\mathcal{F}\right) + \frac{1}{p^2}\frac{\partial}{\partial p^a}\left(\frac{dp^a}{dt}p^2\mathcal{F}\right) = 0, \tag{2.52}$$

where p^2 is the Jacobian of the transformation

$$(p, \mu, \phi) \mapsto \left(p\sqrt{1-\mu^2}\cos(\phi), p\sqrt{1-\mu^2}\sin(\phi), p\mu\right).$$

We conclude this section by introducing the differential intensity $\mathcal{J}$, which can be defined as

$$\mathcal{J}(\mathbf{X}, \mathbf{p}, t) := p^2\mathcal{F}(\mathbf{X}, \mathbf{p}, t). \tag{2.53}$$

Since $\mathcal{F}$ is the particle distribution function in mixed phase space, the differential intensity satisfies

$$dN = \mathcal{J}d\mathbf{X}dpd\mu d\phi,$$

where dN counts the number of guiding centres residing in the infinitesimal $d\mathbf{X}dpd\mu d\phi$. Equation (2.52) becomes thus

$$\frac{\partial \mathcal{J}}{\partial t} + \frac{\partial}{\partial x^a}\left(\frac{dX^a}{dt}\mathcal{J}\right) + \frac{\partial}{\partial p^a}\left(\frac{dp^a}{dt}\mathcal{J}\right) = 0. \tag{2.54}$$

2.4 Particle motion in a turbulent plasma

Since space plasmas like the solar wind are often turbulent, we will decompose the velocity and electromagnetic fields as the superposition of an average and a fluctuating

part, that is,

$$\begin{aligned}\mathbf{U} &= \mathbf{U}_0 + \delta\mathbf{U},\\ \mathbf{B} &= \mathbf{B}_0 + \delta\mathbf{B},\\ \mathbf{E} &= \delta\mathbf{E},\end{aligned} \tag{2.55}$$

with

$$\langle\delta\mathbf{U}\rangle = \langle\delta\mathbf{B}\rangle = \langle\delta\mathbf{E}\rangle = 0. \tag{2.56}$$

Here, $\langle\cdot\rangle$ denotes an ensemble average, which will be precisely defined in Section 2.6. We note that $\mathbf{E}_0 = 0$, since it is assumed that there are no mean electrostatic fields possible due to charge separation in the rest frame of the plasma. The latter frame is here defined as the reference frame moving with the average plasma velocity vector $\mathbf{U}_0$ at the GC location, and not with the instantaneous or total velocity vector $\mathbf{U}_0 + \delta\mathbf{U}$. This implies that we have to add a "$+q\gamma\delta\mathbf{E}$" term on the right-hand side of Eq. (2.42), since we previously dropped the electric field term out of this equation assuming that we were in the frame moving with total plasma velocity[9]. Moreover, in the following the GC coordinate $\mathbf{X}$ is defined with respect to the average background magnetic field, i.e., the magnetic field appearing in Eq. (2.48) is taken equal to $\mathbf{B}_0$.

In the remainder of this section, expression for the proper time derivatives of the phase space variables $(\mathbf{X}, p, \mu, \phi)$ are computed. Similar derivations can be found in (Zhang, 2006), for the non-relativistic case where $U/c \to 0$ and $\gamma \to 1$. Furthermore, for notational convenience, we will drop the subscript "0" from the ensemble average field variables in the following.

By using Eqs. (2.41), (2.42), and (2.48), the velocity of the GC is obtained as follows:

$$\begin{aligned}\frac{d\mathbf{X}}{d\tau} =& \frac{d\mathbf{x}}{d\tau} + \frac{\mathbf{p}}{q}\times\frac{d}{d\tau}\left(\frac{\mathbf{B}}{B^2}\right) + \frac{1}{qB^2}\frac{d\mathbf{p}}{d\tau}\times\mathbf{B}\\ =& \gamma\boldsymbol{v} + \gamma\mathbf{U}_g + \frac{\mathbf{p}}{q}\times\frac{d}{d\tau}\left(\frac{\mathbf{B}}{B^2}\right) + \frac{\gamma}{B^2}(\boldsymbol{v}\times\mathbf{B})\times\mathbf{B}\\ &- \frac{m\gamma^2}{qB^2}\left(\frac{\partial\mathbf{U}_g}{\partial t} + \left[(\boldsymbol{v}+\mathbf{U}_g)\cdot\nabla\right]\mathbf{U}_g\right)\times\mathbf{B}\\ &+ \gamma q\frac{\delta\mathbf{E}\times\mathbf{B}}{B^2} + \frac{\gamma}{B^2}(\boldsymbol{v}\times\delta\mathbf{B})\times\mathbf{B},\end{aligned} \tag{2.57}$$

[9] In fact, since we work in a reference frame co-moving with the plasma at the GC location, it holds that $\mathbf{E}_0(\mathbf{X}) = 0$, but not necessarily that $\mathbf{E}_0(\mathbf{x}) = 0$. Hence, we should in principle also add a "$+q\gamma\mathbf{E}_0(\mathbf{x})$" term to the right-hand side of Eq. (2.42). However, it holds that $\mathbf{E}_0(\mathbf{x}) = 0$ to second order in r_L/L (Appendix B), and we will therefore neglect this term.

where we have also omitted the tilde symbol from $\mathbf{p}$ and from the Lorentz factor[10] γ. Moreover, since the GC coordinate $\mathbf{X}$ is defined with respect to the average background magnetic field $\mathbf{B}$ instead of the total magnetic field $\mathbf{B} + \delta\mathbf{B}$, the fluctuating electromagnetic field terms in Eq. (2.57) arise solely from $d\mathbf{p}/dt$.

By denoting $\mathbf{b} = \mathbf{B}/B$ and using the vector triple product identity[11], Eq. (2.57) can be further simplified as

$$\begin{aligned}\frac{d\mathbf{X}}{d\tau} =& \gamma(\boldsymbol{v}\cdot\mathbf{b})\mathbf{b} + \gamma\mathbf{U}_g + \frac{\mathbf{p}}{q}\times\frac{d}{d\tau}\left(\frac{\mathbf{B}}{B^2}\right)\\ &- \frac{m\gamma^2}{qB^2}\left(\frac{\partial\mathbf{U}_g}{\partial t} + \left[(\boldsymbol{v}+\mathbf{U}_g)\cdot\nabla\right]\mathbf{U}_g\right)\times\mathbf{B}\\ &+ \gamma q\frac{\delta\mathbf{E}\times\mathbf{B}}{B^2} + \frac{\gamma}{B^2}(\boldsymbol{v}\times\delta\mathbf{B})\times\mathbf{B}.\end{aligned} \tag{2.58}$$

Equation (2.40) can now be used to write the proper time derivative $d/d\tau$ in terms of the time derivative d/dt, i.e.,

$$\frac{d}{d\tau} = \frac{dt}{d\tau}\frac{d}{dt} = \gamma\left(1+\frac{\mathbf{U}_g\cdot\boldsymbol{v}}{c^2}\right)\frac{d}{dt} = \gamma\left(1+\frac{\mathbf{U}_g\cdot\boldsymbol{v}}{c^2}\right)\left(\frac{\partial}{\partial t}+\boldsymbol{v}'\cdot\nabla\right), \tag{2.59}$$

where $\boldsymbol{v}'$ denotes the particle velocity in the inertial frame[12]. By writing $\boldsymbol{v}'$ in terms of $\boldsymbol{v}$ we find[13]

$$\frac{d}{d\tau} = \gamma\left(1+\frac{\mathbf{U}_g\cdot\boldsymbol{v}}{c^2}\right)\frac{\partial}{\partial t} + \gamma\left(\boldsymbol{v}+\mathbf{U}_g\right)\cdot\nabla, \tag{2.62}$$

Replacing the proper time derivative in Eq. (2.58) by (2.62) gives then

$$\frac{d\mathbf{X}}{d\tau} = \frac{d\mathbf{X}_0}{d\tau} + \frac{d\mathbf{X}_\delta}{d\tau}, \tag{2.63}$$

[10] It is however important to keep in mind that we cannot replace $\gamma d\tau$ by dt, since t is the time measured in the inertial frame and γ is now the Lorentz factor of the particle speed in the plasma frame.

[11] $(\boldsymbol{v}\times\mathbf{B})\times\mathbf{B} = (\mathbf{B}\cdot\boldsymbol{v})\mathbf{B} - B^2\boldsymbol{v}$

[12] There is a slight inconsistency in notation here, since we previously denoted the velocity in the inertial field simply as $\boldsymbol{v}$, i.e., without the prime. However, since we omitted the tilde symbol from the co-moving frame coordinates, we add a prime here to make the distinction between both frames clear.

[13] The velocity transforms under a Lorentz transformation as:

$$\Gamma\left(1+\frac{\mathbf{U}_g\cdot\boldsymbol{v}}{c^2}\right)\boldsymbol{v}' = \boldsymbol{v} + \mathbf{U}_g\left(\frac{\boldsymbol{v}\cdot\mathbf{U}_g}{U_g^2}(\Gamma-1)+\Gamma\right), \tag{2.60}$$

which becomes to first order in U/c,

$$\left(1+\frac{\mathbf{U}_g\cdot\boldsymbol{v}}{c^2}\right)\boldsymbol{v}' = \boldsymbol{v} + \mathbf{U}_g, \tag{2.61}$$

where

$$\frac{d\mathbf{X}_0}{d\tau} := \gamma\Big[(\boldsymbol{v}\cdot\mathbf{b})\mathbf{b} + \mathbf{U}_g + \mathbf{V}_d\Big], \tag{2.64}$$

$$\frac{d\mathbf{X}_\delta}{d\tau} := \gamma\left[(\boldsymbol{v}\cdot\mathbf{b})\frac{\delta\mathbf{B}}{B} - \left(\mathbf{b}\cdot\frac{\delta\mathbf{B}}{B}\right)\boldsymbol{v} + q\frac{\delta\mathbf{E}\times\mathbf{B}}{B^2}\right], \tag{2.65}$$

and

$$\begin{aligned}\mathbf{V_d} = \frac{\mathbf{p}}{q}\times\left[\left(1+\frac{\mathbf{U}_g\cdot\boldsymbol{v}}{c^2}\right)\frac{\partial}{\partial t}\left(\frac{\mathbf{B}}{B^2}\right) + \left(\boldsymbol{v}+\mathbf{U}_g\right)\cdot\nabla\left(\frac{\mathbf{B}}{B^2}\right)\right] \\ -\frac{\gamma m}{qB}\left(\frac{\partial\mathbf{U}_g}{\partial t} + \Big[(\boldsymbol{v}+\mathbf{U}_g)\cdot\nabla\Big]\mathbf{U}_g\right)\times\mathbf{b}.\end{aligned} \tag{2.66}$$

This last equation corresponds to the GC drifts with respect to the average background magnetic field, and is discussed in more detail in Section 2.5 and Appendix B. It is worth noting that the electric field drift is included in the first two terms of Eq. (2.64) (and not in $\mathbf{V}_d$), yet it does not appear explicitly due to the usage of mixed coordinates[14].

Equation (2.65) describes the GC motion due to turbulent fluctuations. As shown in Section 2.7.2, this term can give rise to a spatial diffusion process perpendicular to the background magnetic field. Moreover, we remark that the first term of Eq. (2.64) together with the first term of Eq. (2.65) describe how particles stream along the perturbed magnetic field lines. The second term of Eq. (2.65) become zero under the assumption of incompressible magnetic turbulence ($\mathbf{B}\cdot\delta\mathbf{B} = 0$). Finally, it is worth pointing out that the magnetic field appearing in Eqs. (2.64) – (2.66) is the average background field defined at the particle's location $\mathbf{x}$, and not at the corresponding GC location $\mathbf{X}$.

Upon denoting the unit vector in the direction of the momentum vector as $\mathbf{e}_p = \mathbf{p}/p$, the following expression for the proper time derivative of the momentum magnitude is found

$$\begin{aligned}\frac{dp}{d\tau} &= \mathbf{e}_p\cdot\frac{d\mathbf{p}}{d\tau} \\ &= -\gamma^2 m\mathbf{e}_p\cdot\left(\frac{\partial\mathbf{U}_g}{\partial t} + \Big[(\boldsymbol{v}+\mathbf{U}_g)\cdot\nabla\Big]\mathbf{U}_g\right) + q\gamma\mathbf{e}_p\cdot\delta\mathbf{E} \\ &= \frac{dp_0}{d\tau} + \frac{dp_\delta}{d\tau},\end{aligned} \tag{2.67}$$

[14] To illustrate this, we note that the electric field drift in the inertial frame equals

$$\mathbf{V}_E = \frac{\mathbf{E}\times\mathbf{B}}{B^2} = \frac{-(\mathbf{U}\times\mathbf{B})\times\mathbf{B}}{B^2} = \mathbf{U} - (\mathbf{U}\cdot\mathbf{b})\mathbf{b} \equiv \mathbf{U}_\perp.$$

Hence, Eq. (2.64) can be reformulated as $(\boldsymbol{v}\cdot\mathbf{b})\,\mathbf{b} + \mathbf{U} + \mathbf{V}_d = \boldsymbol{v}_\parallel + \mathbf{U}_\parallel + \mathbf{V}_E + \mathbf{V}_d$.

where Eq. (2.42) is used to obtain the second equality and

$$\frac{dp_0}{d\tau} := -\gamma^2 m \mathbf{e}_p \cdot \left(\frac{\partial \mathbf{U}_g}{\partial t} + \Big[(\boldsymbol{v} + \mathbf{U}_g) \cdot \nabla \Big] \mathbf{U}_g \right) \tag{2.68}$$

$$\frac{dp_\delta}{d\tau} := q\gamma \mathbf{e}_p \cdot \delta\mathbf{E}. \tag{2.69}$$

These equations illustrate that the magnitude of the momentum, as measured in the plasma rest frame, only changes either due to inertial forces or a turbulent electric field. It can be shown that the inertial force term incorporates the GC drifts along the motional magnetic field (e.g., le Roux et al., 2007).

For the proper time derivative of the pitch-angle cosine we find

$$\begin{aligned} \frac{d\mu}{d\tau} &= \frac{d}{d\tau} \left(\frac{\mathbf{p} \cdot \mathbf{B}_g}{p B_g} \right) \\ &= \mathbf{e}_p \cdot \frac{d\mathbf{b}_g}{d\tau} - \frac{\mu}{p} \frac{dp}{d\tau} + \frac{1}{p} \mathbf{b}_g \cdot \frac{d\mathbf{p}}{d\tau}. \end{aligned}$$

Upon using Eqs. (2.42) and (2.67), this becomes

$$\begin{aligned} \frac{d\mu}{d\tau} = \mathbf{e}_p \cdot \frac{d\mathbf{b}_g}{d\tau} - \frac{\gamma}{v} \Big(\mathbf{b}_g - \mu \mathbf{e}_p \Big) \cdot \left(\frac{\partial \mathbf{U}_g}{\partial t} + \Big[(\boldsymbol{v} + \mathbf{U}_g) \cdot \nabla \Big] \mathbf{U}_g \right) \\ + \frac{q\gamma}{p} \Big(\mathbf{b}_g - \mu \mathbf{e}_p \Big) \cdot \delta\mathbf{E} + \frac{q\gamma v}{p} \Big(\mathbf{b}_g \times \mathbf{e}_p \Big) \cdot \delta\mathbf{B}_g. \end{aligned} \tag{2.70}$$

Replacing the proper time derivative by (2.62) gives then

$$\frac{d\mu}{d\tau} = \frac{d\mu_0}{d\tau} + \frac{d\mu_\delta}{d\tau}, \tag{2.71}$$

where

$$\begin{aligned} \frac{d\mu_0}{d\tau} :=& \gamma \left(1 + \frac{\mathbf{U}_g \cdot \boldsymbol{v}}{c^2} \right) \mathbf{e}_p \cdot \frac{\partial \mathbf{b}_g}{\partial t} + \mathbf{e}_p \cdot \Big[\gamma \Big(\boldsymbol{v} + \mathbf{U}_g \Big) \cdot \nabla \mathbf{b}_g \Big] \\ & - \frac{\gamma}{v} \Big(\mathbf{b}_g - \mu \mathbf{e}_p \Big) \cdot \left(\frac{\partial \mathbf{U}_g}{\partial t} + \Big[(\boldsymbol{v} + \mathbf{U}_g) \cdot \nabla \Big] \mathbf{U}_g \right), \end{aligned} \tag{2.72}$$

$$\frac{d\mu_\delta}{d\tau} := \frac{q\gamma}{p} \Big(\mathbf{b}_g - \mu \mathbf{e}_p \Big) \cdot \delta\mathbf{E} + \frac{q\gamma v}{p} \Big(\mathbf{b}_g \times \mathbf{e}_p \Big) \cdot \delta\mathbf{B}_g. \tag{2.73}$$

In the next section, we will assume a particle distribution that is gyrotropic, i.e., independent of the gyrophase ϕ. However, for completeness we also illustrate how the

proper time derivative of the gyro-angle, i.e., $d\phi/d\tau$, can be derived. To do so, we first express $\mathbf{p}$ in a Cartesian frame $\{\mathbf{e}_x, \mathbf{e}_y, \mathbf{b}_g\}$ as

$$\mathbf{p} = \mu \mathbf{b}_g + p\sqrt{1-\mu^2}\left(\cos\phi \mathbf{e}_x + \sin\phi \mathbf{e}_y\right), \tag{2.74}$$

and we define the unit vector $\mathbf{e}_L$ as

$$\mathbf{e}_L = \frac{\mathbf{b}_g \times \mathbf{p}}{p\sqrt{1-\mu^2}} = -\sin\phi \mathbf{e}_x + \cos\phi \mathbf{e}_y. \tag{2.75}$$

By taking the dot product of $\mathbf{e}_L$ with the proper time derivative of Eq. (2.74), one obtains after some algebra that[15]

$$\frac{d\phi}{d\tau} = \frac{1}{p\sqrt{1-\mu^2}}\mathbf{e}_L \cdot \frac{d\mathbf{p}}{d\tau} - \frac{\mu}{\sqrt{1-\mu^2}}\mathbf{e}_L \cdot \frac{d\mathbf{b}_g}{d\tau} + \mathbf{e}_x \cdot \frac{d\mathbf{e}_y}{d\tau}. \tag{2.76}$$

Substituting (2.42) in this expression gives then after some calculations

$$\frac{d\phi}{d\tau} = \frac{d\phi_0}{d\tau} + \frac{d\phi_\delta}{d\tau}, \tag{2.77}$$

with

$$\begin{aligned}\frac{d\phi_0}{d\tau} :=& -\gamma\Omega + \mathbf{e}_x \cdot \frac{d\mathbf{e}_y}{d\tau} - \frac{\gamma}{v\sqrt{1-\mu^2}}\left(\frac{\partial \mathbf{U}_g}{\partial t} + \left[(\boldsymbol{v}+\mathbf{U}_g)\cdot\nabla\right]\mathbf{U}_g\right)\cdot\mathbf{e}_L \\ &- \frac{\mu\gamma}{\sqrt{1-\mu^2}}\left[\left(1+\frac{\mathbf{U}_g\cdot\boldsymbol{v}}{c^2}\right)\frac{\partial \mathbf{b}_g}{\partial t} + \left(\boldsymbol{v}+\mathbf{U}_g\right)\cdot\nabla\mathbf{b}_g\right]\cdot\mathbf{e}_L,\end{aligned} \tag{2.78}$$

$$\frac{d\phi_\delta}{d\tau} := \frac{q\gamma}{p\sqrt{1-\mu^2}}\mathbf{e}_L\cdot\delta\mathbf{E} + \frac{q\gamma}{m\sqrt{1-\mu^2}}\left(\mathbf{e}_L\times\mathbf{e}_p\right)\cdot\delta\mathbf{B}, \tag{2.79}$$

where $\Omega = qB_g/\gamma m$ is the gyrofrequency. The term $\mathbf{e}_x \cdot d\mathbf{e}_y/d\tau$ arises because the definition of the gyrophase depends on the utilised reference triad (Littlejohn, 1988). Finally, substituting Eqs. (2.63), (2.67), (2.71), and (2.77) into Eq. (2.51) gives the following transport equation

$$\begin{aligned}&\frac{dt}{d\tau}\frac{\partial \mathscr{F}}{\partial t} + \left(\frac{d\mathbf{X}_0}{d\tau} + \frac{d\mathbf{X}_\delta}{d\tau}\right)\cdot\frac{\partial \mathscr{F}}{\partial \mathbf{X}} + \left(\frac{dp_0}{d\tau} + \frac{dp_\delta}{d\tau}\right)\frac{\partial \mathscr{F}}{\partial p} \\ &\quad + \left(\frac{d\mu_0}{d\tau} + \frac{d\mu_\delta}{d\tau}\right)\frac{\partial \mathscr{F}}{\partial \mu} + \left(\frac{d\phi_0}{d\tau} + \frac{d\phi_\delta}{d\tau}\right)\frac{\partial \mathscr{F}}{\partial \phi} = 0.\end{aligned} \tag{2.80}$$

[15] To obtain this result, one should use the identities $\mathbf{e}_x \cdot d\mathbf{e}_x/d\tau = \mathbf{e}_y \cdot d\mathbf{e}_y/d\tau = 0$, and $\mathbf{e}_x \cdot d\mathbf{e}_y/d\tau = -\mathbf{e}_y \cdot d\mathbf{e}_x/d\tau$, which follow from the properties of perpendicular unit vectors.

2.5 A gyrotropic distribution function

The transport equation (2.80) can be simplified by assuming that the particle distribution is independent of the gyrophase ϕ. This is for example a valid assumption when the gyroperiod Ω^{-1} and the Larmor radius r_L are both much smaller than any other time and length-scale in the system. A gyrotropic distribution function implies that $\partial\mathscr{F}/\partial\phi = 0$, such that the following transport equation is obtained after substituting Eqs. (2.40), (2.64), (2.68) and (2.72) into Eq. (2.80)

$$\begin{aligned}
&\gamma\left(1+\frac{\mathbf{U}_g\cdot\boldsymbol{v}}{c^2}\right)\frac{\partial\mathscr{F}}{\partial t}+\gamma\left[(\boldsymbol{v}\cdot\mathbf{b})\mathbf{b}+\mathbf{U}_g+\mathbf{V}_d\right]\cdot\frac{\partial\mathscr{F}}{\partial\mathbf{X}}\\
&+\gamma\left\{\left(1+\frac{\mathbf{U}_g\cdot\boldsymbol{v}}{c^2}\right)\mathbf{e}_p\cdot\frac{\partial\mathbf{b}_g}{\partial t}+\mathbf{e}_p\cdot\left[(\mathbf{U}_g+\boldsymbol{v})\cdot\nabla\mathbf{b}_g\right]\right.\\
&\left.-\frac{1}{v}\left(\mathbf{b}_g-\mu\mathbf{e}_p\right)\cdot\left[\frac{\partial\mathbf{U}_g}{\partial t}+(\mathbf{U}_g+\boldsymbol{v})\cdot\nabla\mathbf{U}_g\right]\right\}\frac{\partial\mathscr{F}}{\partial\mu}\\
&-\gamma^2 m\left(\mathbf{e}_p\cdot\frac{d\mathbf{U}_g}{dt}\right)\frac{\partial\mathscr{F}}{\partial p}\\
&=\left(\frac{\delta\mathscr{F}}{\delta t}\right)_{\text{turb}}.
\end{aligned}\tag{2.81}$$

The term on the right-hand side of this equation contains all the perturbative terms, and it will be shown in Section 2.7 that this term transforms into a set of phase space diffusion processes under the assumptions of QLT.

By averaging Eq. (2.81) over the gyrophase and dividing by $dt/d\tau$ (see Appendices A and B for details), we obtain the FTE in the form of a Vlasov equation,

$$\frac{\partial\mathscr{F}}{\partial t}+\frac{d\mathbf{X}}{dt}\cdot\nabla\mathscr{F}+\frac{d\mu}{dt}\frac{\partial\mathscr{F}}{\partial\mu}+\frac{dp}{dt}\frac{\partial\mathscr{F}}{\partial\mu}=\left(\frac{\delta\mathscr{F}}{\delta t}\right)_{\text{turb}},\tag{2.82}$$

or in a conservative form (see Eq. (2.54)),

$$\frac{\partial\mathcal{J}}{\partial t}+\nabla\cdot\left(\frac{d\mathbf{X}}{dt}\mathcal{J}\right)+\frac{\partial}{\partial\mu}\left(\frac{d\mu}{dt}\mathcal{J}\right)+\frac{\partial}{\partial p}\left(\frac{dp}{dt}\mathcal{J}\right)=\left(\frac{\delta\mathcal{J}}{\delta t}\right)_{\text{turb}},\tag{2.83}$$

with,

$$\frac{d\mathbf{X}}{dt} = \mathbf{U}_g + \left(1 - \frac{\mu v \mathbf{U}_g \cdot \mathbf{b}_g}{c^2}\right)\left(\mu v \mathbf{b}_g + \mathbf{V}_{gd}\right), \tag{2.84}$$

$$\frac{d\mu}{dt} = \frac{1-\mu^2}{2}\left[\frac{v\mathbf{U}_g}{c^2}\cdot\frac{\partial \mathbf{b}_g}{\partial t} + v\left(1 - \frac{\mu v \mathbf{U}_g \cdot \mathbf{b}_g}{c^2}\right)\nabla\cdot\mathbf{b}_g + \mu\nabla\cdot\mathbf{U}_g \right.$$
$$\left. -3\mu\mathbf{b}_g\mathbf{b}_g : \nabla\mathbf{U}_g - \frac{2}{v}\mathbf{b}_g\cdot\frac{d\mathbf{U}_g}{dt}\right], \tag{2.85}$$

$$\frac{dp}{dt} = \left(\frac{1-3\mu^2}{2}\mathbf{b}_g\mathbf{b}_g : \nabla\mathbf{U}_g - \frac{1-\mu^2}{2}\nabla\cdot\mathbf{U}_g - \frac{\mu}{v}\mathbf{b}_g\cdot\frac{d\mathbf{U}_g}{dt}\right)p. \tag{2.86}$$

In Eq. (2.84), the GC drift $\mathbf{V}_{gd}$ is given by (Appendix B)

$$\mathbf{V}_{gd} := \frac{\mu p}{qB_g}\left(\mathbf{b}_g \times \frac{d\mathbf{b}_g}{dt}\right)$$
$$+ \frac{vp}{c^2 qB_g}\left[\frac{1-\mu^2}{2B_g}\frac{\partial B_g}{\partial t}\left(\mathbf{b}_g\times\mathbf{U}_g\right) + \mu^2\left(\mathbf{U}_g\times\frac{\partial\mathbf{b}_g}{\partial t}\right)_\perp\right]$$
$$+ \frac{vp}{qB_g}\left[\frac{1-\mu^2}{2B_g}\mathbf{b}_g\times\nabla B_g + \mu^2(\nabla\times\mathbf{b}_g)_\perp\right]$$
$$+ \mathbf{b}_g\times\frac{\gamma m}{qB_g}\left[\frac{d\mathbf{U}_g}{dt} + \mu v\left(\mathbf{b}_g\cdot\nabla\right)\mathbf{U}_g\right], \tag{2.87}$$

where the subscripts $\perp$ and $\|$ are with respect to the magnetic field vector at the GC location (see Eqs. B.10 – B.13 for the precise definition). The first and the second term on the right-hand side of this equation are the GC drifts due to time varying magnetic fields. The third term contains the drifts due to the magnetic field gradient and curvature. The last term of Eq. (2.87) contains the polarization drift, which arises from a varying electrical field[16]. This term is also called the inertia drift, because of its proportionality to the mass of the particles.

By considering the limit $U/c \to 0$ in Eqs. (2.82) – (2.86), we find the following "non-relativistic" forms of the FTE,

$$\frac{\partial f}{\partial t} + \frac{d\mathbf{X}}{dt}\cdot\nabla f + \frac{d\mu}{dt}\frac{\partial f}{\partial\mu} + \frac{dp}{dt}\frac{\partial f}{\partial\mu} = \left(\frac{\delta f}{\delta t}\right)_{\text{turb}}, \tag{2.88}$$

[16] Although the electrical field is zero in the solar wind frame, it is not zero in the inertial frame. As a consequence, the polarization drift appears in the solar wind frame as the result of a force proportional to $d\mathbf{U}/dt$.

or

$$\frac{\partial j}{\partial t} + \nabla \cdot \left(\frac{d\mathbf{X}}{dt} j\right) + \frac{\partial}{\partial \mu}\left(\frac{d\mu}{dt} j\right) + \frac{\partial}{\partial p}\left(\frac{dp}{dt} j\right) = \left(\frac{\delta j}{\delta t}\right)_{\text{turb}}, \tag{2.89}$$

with,

$$\frac{d\mathbf{X}}{dt} = \mathbf{U}_g + \mu v \mathbf{b}_g + \mathbf{V}_{gd}, \tag{2.90}$$

$$\frac{d\mu}{dt} = \frac{1-\mu^2}{2}\left(v\nabla \cdot \mathbf{b}_g + \mu \nabla \cdot \mathbf{U} - 3\mu \mathbf{b}_g \mathbf{b}_g : \nabla \mathbf{U} - \frac{2}{v}\mathbf{b}_g \cdot \frac{d\mathbf{U}_g}{dt}\right), \tag{2.91}$$

$$\frac{dp}{dt} = \left(\frac{1-3\mu^2}{2}\mathbf{b}_g \mathbf{b}_g : \nabla \mathbf{U}_g - \frac{1-\mu^2}{2}\nabla \cdot \mathbf{U}_g - \frac{\mu}{v}\mathbf{b}_g \cdot \frac{d\mathbf{U}_g}{dt}\right) p, \tag{2.92}$$

where $j := p^2 f$, and we used that $\mathscr{F} = f$ and $\mathcal{J} = j$ when $U/c \to 0$.

Comparing Eqs. (2.88) – (2.92) with Eqs. (2.82) – (2.86) illustrates that all extra terms in the former equation scale as vU/c^2. In the solar wind, these terms will be negligible compared to the other terms in the FTE, even for fully relativistic particles for which $v \sim c$. This is because U/c is of the order of 10^{-3} in regular solar wind conditions and 10^{-2} near fast CMEs. In fact, calling Eqs. (2.88) – (2.92) "non-relativistic" is confusing, since the "non-relativistic" terminology refers here only to the state of the background plasma and not to the energetic particles. This can be understood by realizing that Eqs. (2.88) – (2.92) are derived from Eqs. (2.82) – (2.86) in the limit $U/c \to 0$, while no assumptions are made regarding the particles' speed. However, we stress that for modelling relativistic particles, it is important to use the momentum as the phase space coordinate and the velocity of the particles should be determined by taking their Lorentz factor into account, that is, through $\mathbf{p} = \gamma m \boldsymbol{v}$. In conclusion, Eqs. (2.88) – (2.92) describes the transport of relativistic particles propagating in non-relativistic plasma flows, as long as the distribution function is expressed in terms of the momentum coordinates and the particle Lorentz factor γ is taken into account when calculating the particle speed or energy.

In the remainder of this chapter, the subscript "g" will be dropped from the background plasma variables for notational convenience. Since we have expressed all the plasma variables appearing in the FTE at the GC position, there is no confusion possible.

2.6 Turbulence

The remainder of this chapter provides a review on how the turbulence term $(\delta\mathscr{F}/\delta t)_{\text{turb}}$ in Eq. (2.83) can be calculated. To do so, it will be necessary to assume a certain model for the interplanetary turbulence. Developing realistic models for turbulence in

space plasmas has proven to be a complicated matter and is still an ongoing topic of research. Turbulence in a collisionless plasma can be described following two different approaches: a statistical turbulence viewpoint and a wave viewpoint. Both descriptions have their merit and are briefly introduced below.

2.6.1 The wave approach

In the wave viewpoint, turbulence is regarded as the superposition of various types of plasma-waves, where the waves have different frequencies, phases and amplitudes. Depending on the type of wave, a different dispersion relation governs the corresponding wave frequency. Since it is well known that waves and particles can exchange momentum through wave-particle interactions (e.g., Tsurutani & Lakhina, 1997), the wave viewpoint of turbulence provides an intuitive and physical explanation of how turbulence modifies particle distributions in space. Moreover, the wave viewpoint is especially important when studying the acceleration of particles at quasi-parallel shock waves. At such shock waves, energetic protons can be an important source of plasma turbulence by generating Alfvén waves through the streaming instability (e.g., Bell, 1978; Vainio, 2003). These waves will then act as scattering centres for other protons, hence facilitating multiple particle shock-crossings and therefore the acceleration of these particles. This process is typically referred to as first-order Fermi acceleration, and is considered as one of the main acceleration mechanisms of both SEPs and CRs (Axford et al., 1977; Krymsky, 1977; Bell, 1978; Blandford & Ostriker, 1978).

2.6.2 The statistical approach

The statistical turbulence approach derives from hydrodynamic turbulence studies and starts from the premises that when a plasma is turbulent, it is impossible to detail the exact behaviour of the velocity field and magnetic field. The latter holds because any small perturbation in the initial or boundary conditions of the system can grow rapidly in a finite amount of time. In mathematical terminology, this means that turbulence corresponds to an ill-posed problem (Hadamard, 1902). In practice, initial and boundary conditions are always only known with finite accuracy, which implies that the exact plasma state at later times becomes unpredictable. Hence, given a certain set of initial and boundary conditions only differing from each other within a finite degree of accuracy (introduced e.g., by instrumentation limitations), the resulting set of plasma states derived from these conditions will, after a finite time, begin to diverge completely from one another. Since all these solutions can be considered as equally valid realizations of the turbulent flow, it is natural to proceed with a statistical approach.

In the statistical turbulence approach, it is common to split the variables as the sum of the average background field and a fluctuating component, commonly referred to as the Reynolds decomposition. For the magnetic field this becomes

$$\mathbf{B}(\mathbf{r}, t) = \mathbf{B}_0(\mathbf{r}, t) + \delta\mathbf{B}(\mathbf{r}, t), \tag{2.93}$$

with

$$\langle \delta\mathbf{B} \rangle = 0. \tag{2.94}$$

The operator $\langle \cdot \rangle$ denotes an ensemble average, which is an average over all the possible realizations of a turbulent flow. This ensemble average is not necessarily equivalent to a space or time average. Instead, the time average is only equivalent to the ensemble average under the ergodicity hypothesis, which is satisfied when turbulence is stationary in time (Batchelor, 1953). Stationarity means that the turbulence probability distribution and its moments are only a function of time differences, and not of individual points in time. For example, the two-point two-time correlation tensor, which is defined for the magnetic field as,

$$R_{ij}(t_1, \mathbf{r_1}, t_2, \mathbf{r_2}) = \left\langle \delta B_i(t_1, \mathbf{r}_1) \delta B_j(t_2, \mathbf{r}_2,) \right\rangle, \tag{2.95}$$

is for a stationary process equal to

$$R_{ij}(t_1, \mathbf{r_1}, t_2, \mathbf{r_2}) = R_{ij}(0, \mathbf{r}_1, \Delta t, \mathbf{r}_2) \tag{2.96}$$

where $\Delta t = t_2 - t_1$. Similar to stationarity, a turbulence is homogeneous in space if the ensemble average becomes equivalent to a spatial average. Homogeneity means that the turbulence probability distribution is invariant to translations along a line in space. Hence the statistical moments like the two-point two time-correlation tensor depend only on the distance Δr between the two points.

Using a dataset spanning two years of in-situ observations, Matthaeus & Goldstein (1982) illustrated that the solar wind magnetic field turbulence approximately satisfies ergodicity, when organized non-statistical phenomena driven by the solar rotation and solar eruptions are neglected in the data. Upon application of the Taylor hypothesis (Taylor, 1938), Matthaeus & Goldstein (1982) also concluded that the solar wind magnetic turbulence is approximately homogeneous. This spatial homogeneity is only locally valid, since it is broken by the presence of large-scale coherent magnetic structures. Moreover, these results were obtained using datasets from the International Sun-Earth Explorer-3 (ISEE-3) and the Interplanetary Monitoring Platform (IMP) spacecraft, which were located at 1 AU, and from the Voyager 1 spacecraft when it was near 5 and 10 AU.

Since turbulence is a phenomenon that covers many length-scales, it is often convenient to use the formalism of Fourier transforms. For example, the Fourier transform of the magnetic field fluctuations is

$$\delta B_i(\mathbf{r}, t) = \int \delta B_i(\mathbf{k}, t) e^{i\mathbf{k}\cdot\mathbf{r}} d^3k, \tag{2.97}$$

and the Fourier transform of the two-point two-time correlation tensor in homogeneous stationary turbulence is[17]

$$\delta R_{ij}(\mathbf{r},t) = \int P_{ij}(\mathbf{k},t) e^{i\mathbf{k}\cdot\mathbf{r}} d^3k, \tag{2.98}$$

where

$$P_{ij}(\mathbf{k},t) = \left\langle \delta B_i(\mathbf{k},t) \delta B_j^*(\mathbf{k},0) \right\rangle \tag{2.99}$$

is called the spectral correlation tensor and the superscript $*$ denotes the complex conjugate.

For simplicity, it is useful to assume that all the components of the spectral tensor have the same temporal dependence which can be separated from the spatial dependence. In that case, the spectral tensor becomes (e.g., Bieber et al., 1994)

$$P_{ij}(\mathbf{k},t) = P_{ij}(\mathbf{k})\Gamma(\mathbf{k},t), \tag{2.100}$$

with $\Gamma(\mathbf{k},0) = 1$. In this formula, the quantity $P_{ij}(\mathbf{k})$ is called the magnetostatic correlation tensor and $\Gamma(\mathbf{k},t)$ the dynamical correlation function.

It can be shown that for turbulence which is axisymmetric around the background magnetic field, $P_{ij}(\mathbf{k})$ assumes the following general form (Chandrasekhar, 1950; Matthaeus & Smith, 1981):

$$P_{ij}(\mathbf{k}) = A(k_\perp, k_\parallel)\left(\delta_{ij} - \frac{k_i k_j}{k^2} + i\sigma(k_\perp, k_\parallel)\epsilon_{ijk}\frac{k_k}{k}\right), \tag{2.101}$$

where the subscripts $\perp$ and $\parallel$ refer to the perpendicular and parallel directions with respect to the background magnetic field, δ_{ij} is Kronecker's delta and ϵ_{ijk} is the Levi-Civita symbol. Moreover, $A(k_\perp, k_\parallel)$ is a real valued function describing the turbulence geometry and the wave spectrum, and $\sigma(k_\perp, k_\parallel)$ is the normalized magnetic helicity[18], which has values between -1 and $+1$ (e.g., Howes & Quataert, 2010).

[17] For homogeneous stationary turbulence, the two-point two-time correlation tensor is a function of $\Delta r = r_2 - r_1$ and $\Delta t = t_2 - t_1$ and, hence, without loss of generality, we can choose $r_1 = 0$ and $t_1 = 0$ and omit the subscripts from r_2 and t_2. In addition, to obtain Eq. (2.98), it is used that for homogeneous turbulence $\left\langle \delta B_i(\mathbf{k}_1,t_1)\delta B_j^*(\mathbf{k}_2,t_2)\right\rangle = P_{ij}(\mathbf{k}_1,t_1,t_2)\delta(\mathbf{k}_1 - \mathbf{k}_2)$.

[18] Equation (2.101) can also be formulated as (Matthaeus & Smith, 1981)

$$P_{ij}(\mathbf{k}) = \left(\delta_{ij} + \frac{k_i k_j}{k^2}\right)\mu_0 E_m(k_\parallel, k_\perp) + \frac{i}{2}\epsilon_{ijk}k_k H_m(k_\parallel, k_\perp),$$

where μ_0 is the permittivity of free space, $E_m(\mathbf{k}) := \left\langle |\delta\mathbf{B}(\mathbf{k})|^2 \right\rangle / 2\mu_0$, and $H_m(\mathbf{k}) := \langle \delta\mathbf{A}(\mathbf{k}) \cdot \delta\mathbf{B}^*(\mathbf{k})\rangle$. In the latter expression, $\mathbf{A}(\mathbf{k})$ denotes the Fourier transform of the vector potential of the magnetic field that satisfies the Coulomb gauge . We find thus that $\sigma = kH_m/(2\mu_0 E_m)$.

2.6.3 The slab/2D composite turbulence model

For many applications concerning energetic particle transport in the heliosphere, the helicity term in Eq. (2.101) is assumed to be zero for simplicity (see however Strauss & le Roux, 2019, for a discussion on the effects of a non-vanishing σ). Under the additional assumption of incompressible magnetic turbulence, i.e., $\delta\mathbf{B} \cdot \mathbf{B}_0 = 0$, Eq. (2.101) simplifies to

$$P_{ij}(\mathbf{k}) = \begin{cases} A(k_\perp, k_\parallel)\left(\delta_{ij} - \frac{k_i k_j}{k^2}\right), & \text{if } i, j \in \{x, y\} \\ 0, & \text{otherwise.} \end{cases} \tag{2.102}$$

This 2D turbulence model can further be decomposed into a slab component and a pure 2D component, that is,

$$P_{ij}^{\text{comp}}(\mathbf{k}) = P_{ij}^{\text{2D}}(\mathbf{k}) + P_{ij}^{\text{slab}}(\mathbf{k}), \tag{2.103}$$

which is referred to as the slab/2D composite or two-component turbulence model (e.g., Matthaeus et al., 1990). In a coordinate system with the z-axis aligned with the mean magnetic field, slab turbulence depends only on the z-coordinate, i.e., $\delta\mathbf{B}^{\text{slab}}(\mathbf{r}) = \delta\mathbf{B}^{\text{slab}}(z)$, whereas the pure 2D turbulence depends on the coordinates perpendicular to the mean magnetic field, i.e., $\delta\mathbf{B}^{\text{2D}}(\mathbf{r}) = \delta\mathbf{B}^{\text{2D}}(x, y)$. In terms of the Fourier transforms, slab turbulence only depends on wave numbers that are parallel to the mean magnetic field, i.e., $\mathbf{k} \parallel \mathbf{B}_0$, whereas pure[19] 2D turbulence only depends on wave numbers that are perpendicular to the mean magnetic field, i.e., $\mathbf{k} \perp \mathbf{B}_0$. We can thus write

$$A^{\text{slab}}(k_\perp, k_\parallel) = g^{\text{slab}}(k_\parallel)\frac{\delta(k_\perp)}{k_\perp} \tag{2.104}$$

and

$$A^{\text{2D}}(k_\perp, k_\parallel) = g^{\text{2D}}(k_\perp)\frac{\delta(k_\parallel)}{k_\perp}, \tag{2.105}$$

where the division through $k_\perp$ simply follows from the definition of the Dirac Delta function in cylindrical coordinates. The functions $g^{\text{slab}}(k_\parallel)$ and $g^{\text{2D}}(k_\perp)$ describe the wave spectrum of the turbulent fluctuations and are discussed below. The decomposition (2.102) is mathematically justified since slab and 2D turbulence are uncorrelated for axisymmetric turbulence with zero helicity, i.e., $\left\langle \delta\mathbf{B}^{\text{2D}} \delta\mathbf{B}^{\text{slab}} \right\rangle = 0$.

The slab/2D composite model is often assumed to be a good representation of the solar wind turbulence (Matthaeus et al., 1990; Bieber et al., 1994). Moreover, using Helios magnetometer data, Bieber et al. (1996) obtained that the solar wind turbulence is dominated by the pure 2D component, which typically contains ~85 % of the turbulence energy, whereas the slab component only accounts for ~15% of the total energy budget.

[19] The term “pure" refers thus to the fact that both $\delta\mathbf{B}$ and $\mathbf{k}$ are perpendicular to $\mathbf{B}_0$.

2.6.4 The wave spectrum

Turbulence typically consists of a macro-structure and a micro-structure, which are dynamically decoupled by an inertial range (e.g., Batchelor, 1953). The macro-structure of a plasma is described by the energy range of the wave spectrum, and it corresponds thus to the turbulent fluctuations with the largest length scales and the lowest frequencies. In interplanetary space, these large-scale fluctuations can result from the variable properties of the solar wind source regions, which may produce instabilities due to the presence of e.g., shear flows and density or magnetic inhomogeneities. The part of the wave spectrum describing the micro-structure is called the dissipation range, as it corresponds to the scales in which the turbulence loses energy through e.g., wave damping. The energy and dissipation ranges are separated by the inertial range, in which energy is transferred from the macro-structure to the micro-structure of the plasma. This transfer of energy is typically referred to as the energy cascade. The bend-over scale $\ell_{\mathrm{slab/2D}}$ is the length scale at which the energy range evolves into the inertial range. Similarly, there exists a dissipation wave number $k_{\mathrm{slab/2D}}$ at which the inertial range evolves into the dissipation range.

It was Kolmogorov (1941) who first reasoned that the inertial range is independent of both the macro- and micro-scales. This allowed him to use a straightforward dimensional analysis to derive that the wave spectrum should decrease according to $k^{-5/3}$ in the inertial range. Numerous hydrodynamic experiments have indeed confirmed the existence of an inertial range with a $k^{-5/3}$ wave spectrum. Important to note is that Kolmogorov performed his dimensional analysis for a non-magnetised fluid. However, the $k^{-5/3}$ is often measured in the inertial range of solar wind turbulence as well (see Goldstein et al., 1995, and references therein), and is therefore also regularly used in applications concerning energetic particle transport.

The energy range of the solar wind turbulence spectrum is less well understood, but it is typically assumed to scale as $\sim k^{-1}$ or flatter (e.g., Hedgecock, 1975; Bieber et al., 1993; Bruno et al., 2009). At the largest length scales, the energy range of pure 2D turbulence may even scale as a positive power law, to ensure a finite energy content (Matthaeus et al., 2007). In the dissipation range, the solar wind wave spectra follows a power-law with an average spectral index of -3 (e.g., Markovskii et al., 2006). However, the variability of the obtained spectral indexes is large, with the measured values typically ranging between -1 and -4 (Smith et al., 2006; Bruno et al., 2014).

Analytical forms of the slab and 2D wave-number spectra that are often used in applications concerning energetic particle transport are (Shalchi & Weinhorst, 2009)

$$g(k_{\parallel}) = \frac{D(s, q_{\mathrm{slab}})}{2\pi} \delta B^2_{\mathrm{slab}} \ell_{\mathrm{slab}} \frac{(k_{\parallel}\ell_{\mathrm{slab}})^{q_{\mathrm{slab}}}}{\left[1 + (k_{\parallel}\ell_{\mathrm{slab}})^2\right]^{(q_{\mathrm{slab}}+s)/2}}, \tag{2.106}$$

and

$$g(k_\perp) = \frac{D(s,q_{2D})}{\pi}\delta B_{2D}^2 \ell_{2D} \frac{(k_\perp \ell_{2D})^{q_{2D}}}{\left[1+(k_\perp \ell_{2D})^2\right]^{(q_{2D}+s)/2}}, \tag{2.107}$$

where

$$D(s,q) = \frac{\Gamma\left(\frac{s+q}{2}\right)}{\Gamma\left(\frac{s-1}{2}\right)\Gamma\left(\frac{q+1}{2}\right)}. \tag{2.108}$$

In these formulae, $\Gamma(z)$ denotes the Gamma function and $D(s,q)$ is a normalization factor derived from the constraint that $\delta B^2_{\text{slab/2D}} = \int P_{\text{slab/2D}}(\mathbf{k})dk^3$, under the restriction that $s > 1$ and $q > -1$. The exponents s and q denote the spectral indexes of the inertial and energy range, respectively. This can be understood by realising that the spectra (2.106) and (2.107) scale like $\sim k^{-s}$ for $k \geq \ell^{-1}_{\text{slab/2D}}$ and $\sim k^q$ for $k < \ell^{-1}_{\text{slab/2D}}$. As explained above, it is usual to assume $s = 5/3$, whereas the value of q is often chosen equal to zero for slab turbulence ($q_{\text{slab}} = 0$), corresponding to a flat spectrum, and larger than unity for pure 2D turbulence ($q_{2D} > 1$), corresponding to an increasing spectrum in the energy range (see Shalchi & Weinhorst, 2009, for a discussion). The condition $q_{2D} > 1$ is necessary to obtain a spectrum of the 2D modes that has a finite correlation length and a finite ultra-scale[20] (Matthaeus et al., 2007).

2.7 Quasi-linear theory

In this section, an expression will be derived for the turbulence term $(\delta\mathscr{F}/\delta t)_{\text{turb}}$ in Eq. (2.81), under the assumptions of QLT. Analogous discussions can be found in e.g., Schlickeiser (2002) and Zank (2014). In QLT, the effect of turbulence on the particle distribution function is assumed to be of perturbative nature, with a zero ensemble-average, i.e.,

$$\mathscr{F} = \mathscr{F}_0 + \delta\mathscr{F}, \quad \text{with} \quad \langle\delta\mathscr{F}\rangle = 0. \tag{2.109}$$

Taking the ensemble average of Eq. (2.80) gives then[21]

$$\frac{\partial\mathscr{F}_0}{\partial t} + \frac{d\zeta_0^i}{dt}\frac{\partial\mathscr{F}_0}{\partial\zeta^i} = -\frac{1}{p^2}\left\langle\frac{\partial}{\partial\zeta^i}\left(p^2\frac{d\zeta_\delta^i}{dt}\chi\delta\mathscr{F}\right)\right\rangle, \tag{2.110}$$

where $\zeta^i = (\mathbf{X}, p, \mu, \phi)$, and $\chi := \left(1 + \mathbf{U}\cdot v/c^2\right)$. Subtracting this equation from Eq. (2.80) gives

$$\frac{\partial\delta\mathscr{F}}{\partial t} + \frac{d\zeta_0^i}{dt}\frac{\partial\delta\mathscr{F}}{\partial\zeta^i} = -\frac{d\zeta_\delta^i}{dt}\frac{\partial\mathscr{F}_0}{\partial\zeta^i} + \delta\mathscr{S}, \tag{2.111}$$

[20] The ultra-scale corresponds to the length-scale of turbulent closed 2D structures (Matthaeus et al., 1999).

[21] To obtain this result, one can use Eq. (2.40) and Eq. (2.47). Moreover, note that $\delta\mathcal{F} = \chi\delta\mathscr{F}$, and that $\chi = \gamma/\tilde{\gamma}$.

where

$$\delta\mathscr{S} = \left\langle \frac{d\zeta^i_\delta}{dt}\frac{\partial\delta\mathscr{F}}{\partial\zeta^i}\right\rangle - \frac{d\zeta^i_\delta}{dt}\frac{\partial\delta\mathscr{F}}{\partial\zeta^i} \tag{2.112}$$

represent the non-linear second order terms in $\delta\zeta^i_\delta$, and $\delta\mathscr{F}$. In QLT, these terms are neglected such that Eq (2.111) becomes

$$\frac{\partial\delta\mathscr{F}}{\partial t} + \frac{d\zeta^i_0}{dt}\frac{\partial\delta\mathscr{F}}{\partial\zeta^i} = -\frac{d\zeta^i_\delta}{dt}\frac{\partial\mathscr{F}_0}{\partial\zeta^i}, \tag{2.113}$$

which can be solved by the method of characteristics. The characteristic curves are the unperturbed phase space trajectories described by $d\zeta^i_0/dt$ (Eqs. (2.64), (2.68), (2.72), and (2.78)). The solution to Eq. (2.113) is thus given by the following integral

$$\delta\mathscr{F} = -\int_0^t \left(\dot{\zeta}^i_\delta\frac{\partial\mathscr{F}_0}{\partial\zeta^i}\right)_{\text{char}} d\hat{t} + \delta\mathscr{F}(t=0), \tag{2.114}$$

where the over-dot notation is used to denote the time derivative and the integration is performed along characteristic curves.

To proceed, it is assumed that the derivatives of $\mathscr{F}_0$ can be brought outside the integral, and that the integration can be extended to infinity, i.e.,

$$\delta\mathscr{F} = -\frac{\partial\mathscr{F}_0}{\partial\zeta^i}\int_0^\infty \left(\dot{\zeta}^i_\delta\right)_{\text{char}} d\hat{t} + \delta\mathscr{F}(t=0). \tag{2.115}$$

As explained by e.g., Zank (2014), these assumption are justified when the characteristic time scale of the particle interaction with the turbulence fluctuations, i.e., the particle correlation time τ_c, is much smaller than the time scale on which a particle's orbit gets significantly distorted, i.e., the diffusion time scale τ_{diff}. In that case, the perturbative terms in the integrands in Eq. (2.115) only contribute on the time scale τ_c, after which they go to zero, which explains why the integration can be extended to infinity. On the other hand, $\mathscr{F}_0$ is typically close to gyrotropy and thus independent of the gyrophase, implying that $\mathscr{F}_0$ varies only on the much longer time scale τ_{diff}. This means that the derivatives of $\mathscr{F}_0$ are essentially constant on the time scale τ_c and can therefore be moved outside the integral.

Substituting expression (2.115) for $\delta\mathscr{F}$ in the right-hand side of Eq. (2.110) gives then[22]

$$\frac{\partial\mathscr{F}_0}{\partial t} + \frac{d\zeta^i_0}{dt}\frac{\partial\mathscr{F}_0}{\partial\zeta^i} = \frac{1}{p^2}\frac{\partial}{\partial\zeta^i}\left(p^2 D_{\zeta_i\zeta_j}\frac{\partial\mathscr{F}_0}{\partial\zeta^j}\right), \tag{2.117}$$

[22] To obtain this result, it is used that

$$\left\langle \frac{d\zeta^i_\delta}{dt}\frac{\partial}{\partial\zeta^i}\delta\mathscr{F}(t=0)\right\rangle = 0, \tag{2.116}$$

which is valid for times larger than the particle decorrelation time scale τ_c.

with

$$D_{\zeta_i\zeta_j} = \int_0^\infty \left\langle \dot{\zeta}^i_\delta(t)\dot{\zeta}^j_\delta(t+\hat{t})\right\rangle d\hat{t}. \tag{2.118}$$

Under the assumptions of QLT, we find thus that the turbulence term in Eq. (2.81) equals

$$\left(\frac{\delta\mathscr{F}}{\delta t}\right)_{\text{turb}} = \frac{1}{p^2}\frac{\partial}{\partial\zeta^i}\left(p^2 D_{\zeta_i\zeta_j}\frac{\partial\mathscr{F}}{\partial\zeta^j}\right), \tag{2.119}$$

where we have omitted the subscript "0" from the particle distribution function. The evolution of the particle distribution function is thus described by a convection–diffusion equation in phase space. There are 25 different diffusion coefficients[23] which are in general all different from zero. Furthermore, upon substituting the gyro-average of (2.119) into Eq. (2.82), the FTE transforms into a KBE with 16 different diffusion processes. By utilising instead Eq. (2.83), the FTE becomes a KFE.

In the next sections, expressions for the different diffusion coefficients will be derived by assuming the slab/2D composite turbulence model, which allows to solve Eq. (2.118) analytically. However, this will illustrate some problems associated with QLT, which are essentially the result of performing the integration in Eq. (2.118) along the unperturbed phase space trajectories. Looking back at the derivation presented above, it is seen that this assumption comes from neglecting the term $\delta\mathscr{S}$ in Eq. (2.111). The derivation presented above can be repeated without equating $\delta\mathscr{S}$ to zero, which again leads to Eq. (2.117) and expressions (2.118) for the diffusion coefficients. The main difference is that the integration in Eq. (2.118) is now performed along the perturbed and hence stochastic particle phase space trajectories. In essence, this is the starting point of the non-linear diffusion theories (see also Eq. (2.134)).

2.7.1 Pitch-angle diffusion

In this section, we derive the pitch-angle diffusion coefficients $D_{\mu\mu}$ under the assumptions of QLT and magnetostatic slab turbulence. The resulting pitch-angle diffusion coefficient was first derived by Jokipii (1966) and Hasselmann & Wibberenz (1968), and has since then been applied in many CR and SEP studies.

Equation (2.118) gives the general form for the diffusion coefficient in the framework of QLT. Ignoring fluctuations of the electric field, Eq (2.73) can be substituted into Eq. (2.118) to find[24]

$$D_{\mu\mu} = \left(1-\mu^2\right)\left(\frac{\Omega}{B_0}\right)^2 \int_0^\infty \cos(\Omega t) R_{xx} dt. \tag{2.120}$$

[23] Note that $dZ_\delta/dt = d\zeta^3_\delta/dt = 0$, such that $D_{\zeta_i\zeta_j} = 0$ if $i = 3$ or $j = 3$.

[24] We use here a Cartesian reference triad $\{\mathbf{e}_x, \mathbf{e}_y, \mathbf{b}\}$.

To obtain this expression, a couple of assumptions were made. Firstly, $\phi(t_0) = \pi/2$ was assumed in Eq. (2.118), which can be done without loss of generality in axisymmetric turbulence. Next, it was assumed that μ is constant in time while performing the integration in Eq. (2.118). Since in QLT this integration is performed along unperturbed particle trajectories, a constant μ implies that a constant background magnetic field is assumed, and thus $\phi(t) = \Omega t$, with Ω the gyrofrequency. Moreover, the correlation terms R_{xy}, R_{yx}, and R_{yy} in Eq. (2.120) were eliminated by using the properties of pure slab turbulence.

By considering the Fourier transform of R_{xx} and using Eqs. (2.98), (2.102), and (2.104), Eq. (2.120) can be written as

$$D_{\mu\mu} = 2\pi\left(1-\mu^2\right)\left(\frac{\Omega}{B_0}\right)^2 \int_0^\infty \int_{-\infty}^\infty \left[\cos(\Omega t) g_{\text{slab}}(k_\parallel) e^{izk_\parallel}\right] dk_\parallel dt.$$

Since QLT assumes that particles stream unperturbed along IMF lines, we have that $z = v\mu t$. Hence, upon using a complex notation for the cosine, we can write

$$\begin{aligned} D_{\mu\mu} &= \pi\left(1-\mu^2\right)\left(\frac{\Omega}{B_0}\right)^2 \int_0^\infty \int_{-\infty}^\infty g_{\text{slab}}(k_\parallel) e^{i\mu v k_\parallel t}\left(e^{i\Omega t} + e^{-i\Omega t}\right) dk_\parallel dt \\ &= \pi^2\left(1-\mu^2\right)\left(\frac{\Omega}{B_0}\right)^2 \int_{-\infty}^\infty g_{\text{slab}}(k_\parallel)\left[\delta(\mu v k_\parallel + \Omega) + \delta(\mu v k_\parallel - \Omega)\right] dk_\parallel \qquad (2.121) \\ &= 2\pi^2 \frac{\left(1-\mu^2\right)}{\mu v}\left(\frac{\Omega}{B_0}\right)^2 g_{\text{slab}}\left(k_\parallel = \frac{\Omega}{|\mu| v}\right). \end{aligned}$$

This result illustrates that pitch-angle diffusion in slab turbulence follows from the scattering of particles with waves that satisfy the resonance condition $k_\parallel = \Omega/\mu v$. For slab turbulence with a wave spectrum given by Eq. (2.106), the diffusion coefficient $D_{\mu\mu}$ can be written in terms of the dimensionless parameter $R := v\Omega^{-1}/\ell_{\text{slab}}$ as (Shalchi et al., 2004)

$$D_{\mu\mu} = \frac{\pi v D(s, q_{\text{slab}})}{\ell_{\text{slab}}} \frac{\delta B^2_{\text{slab}}}{B_0^2}\left(1-\mu^2\right)|\mu|^{s-1} R^{s-2}\left[1+\mu^2 R^2\right]^{-(q_{\text{slab}}+s)/2} \qquad (2.122)$$

To use this functional form of $D_{\mu\mu}$ when modelling energetic particle transport in the heliosphere, δB^2_{slab} and ℓ_{slab} need to be prescribed. Both quantities are poorly constraint for the solar wind plasma, and are believed to vary as a function of space and to be different in the slow and fast solar wind (e.g., Bruno & Carbone, 2005; Bruno et al., 2009). One way to circumvent this problem, is by instead prescribing the parallel mean free path $\lambda_\parallel$ of the energetic particles. This quantity can be regarded as the average distance travelled by a particle along the background magnetic field before it's parallel

velocity has changed significantly due to scattering processes. The parallel mean free path can be estimated from the time that particles need to reach an observer after the occurrence of a solar eruption. Hasselmann & Wibberenz (1970) derived that

$$\lambda_{\parallel} = \frac{3}{8} v \int_{-1}^{1} \frac{\left(1-\mu^2\right)^2}{D_{\mu\mu}} d\mu, \tag{2.123}$$

by assuming a particle distribution function that is close to an isotropic equilibrium with respect to the pitch-angle. Following the findings of Bieber et al. (1994), a common assumption when modelling SEPs is to assume a constant radial mean free path $\lambda_{\parallel}^{r} = \lambda_{\parallel}/b_r^2$, which corresponds to assuming that $\delta B_{\rm slab}^2/\ell_{\rm slab} \propto B_r^2$ in Eq. (2.122). In a nominal solar wind, this translates to turbulence that reduces in strength with increasing distance from the Sun.

One of the problems of QLT is that Eq. (2.122) becomes zero when $\mu = 0$. This is the well-known resonance gap or 90°-scattering problem (Klimas & Sandri, 1971, 1973; Kaiser et al., 1973; Earl, 1973; Völk, 1973), and implies that particles cannot reverse their propagation direction through scattering. The 90°-scattering problem follows from the assumption of QLT that particles propagate along unperturbed orbits in a uniform background magnetic field, which implies that particles satisfying the resonance condition $k_{\parallel} = \Omega/\mu v$ for a certain wave number $k_{\parallel}$, will do so indefinitely. Particles with $\mu \to 0$ can thus only resonate with wave numbers $k \to \infty$, for which the wave spectrum vanishes. In reality, a particle trajectory will, with time, increasingly deviate from its original unperturbed helical path, such that the sharp resonance function $\delta(\mu v k_{\parallel} \pm \Omega)$ in Eq. (2.121) is not valid.

This resonance problem can be solved in different manners. For example, one can calculate corrections to the unperturbed particle orbits used in standard QLT, leading to a second-order QLT (Shalchi, 2005; Tautz et al., 2008; Shalchi et al., 2009). Another approach is to include the effects of propagating plasma waves of different polarization states and travel directions, or to include wave damping (Schlickeiser, 2002). Furthermore, by considering turbulence with a dynamical correlation function $\Gamma(\mathbf{k}, t)$ that has an exponential time-dependence, the sharp resonance function of QLT is replaced by a smoother function like a Breit–Wigner or a Gaussian function, leading to a non-zero $D_{\mu\mu}(\mu = 0)$ (Bieber et al., 1994). For a more in-depth review of the 90°-scattering problem, we refer to Shalchi (2009).

Finally, in this section we derived $D_{\mu\mu}$ assuming pure slab turbulence. It can be shown (Shalchi, 2009) that for pure 2D turbulence, the diffusion coefficient $D_{\mu\mu}$ becomes zero, such that the parallel mean free path is infinite. In composite turbulence, where both slab and pure 2D turbulence are present, the pitch-angle diffusion is thus entirely controlled by the slab component.

2.7.2 Cross-field diffusion: field line random walk

In this section, the coefficients for the spatial diffusion processes appearing in the FTE (2.117) are computed, under the assumptions of QLT. Moreover, any electric field perturbations are ignored, such that Eq. (2.65) becomes

$$\dot{\mathbf{X}}_\delta = \mu v \left(\frac{\delta B_x}{B} \mathbf{e}_x + \frac{\delta B_y}{B} \mathbf{e}_y \right) - \frac{\delta B_z}{B} \left(v_x \mathbf{e}_x + v_y \mathbf{e}_y \right), \tag{2.124}$$

where we note that the first term scales with the particle speed along the magnetic field, i.e., μv, whereas the second term scales with the particle speed perpendicular to the magnetic field, i.e., $\sqrt{1-\mu^2} v$. Assuming incompressible turbulence, i.e., $\delta B_z = 0$, we find that

$$\dot{\mathbf{X}}_\delta = \mu v \frac{\delta \mathbf{B}}{B}, \tag{2.125}$$

which together with Eq. (2.64) describes that the GCs follow the perturbed magnetic field lines, while drifting across the background magnetic field. In other words, the diffusive spread of a particle population across the mean magnetic field is governed by the spread of the fluctuating magnetic field lines.

Using Eq. (2.118) of QLT, and assuming axisymmetric turbulence one finds that

$$D_{xx} = D_{yy} = \frac{\mu^2 v^2}{B^2} \int_0^\infty \langle \delta B_x(0) \delta B_x(t) \rangle \, dt, \tag{2.126}$$

where the integration is performed over unperturbed particle orbits. For a constant background magnetic field, the time coordinate t in Eq. (2.126) can be replaced by $z/|\mu| v$. For pure slab turbulence, one then finds upon substituting Eq. (2.104) in Eq. (2.126) that

$$\begin{aligned} D_{xx} =& \frac{|\mu| v}{B^2} \int_0^\infty \langle \delta B_x(0) \delta B_x(z) \rangle \, dz \\ =& 2\pi \frac{|\mu| v}{B^2} \int_0^\infty \int_{-\infty}^\infty g_{\text{slab}}(k_\parallel) e^{i z k_\parallel} dk_\parallel dz \\ =& 2\pi^2 \frac{|\mu| v}{B^2} g_{\text{slab}}(k_\parallel = 0). \end{aligned} \tag{2.127}$$

For a wave spectrum given in (2.106), we get $D_{xx} = 0$ if $q_{\text{slab}} > 0$ and $D_{xx} = \infty$ if $q_{\text{slab}} < 0$, which can be interpreted as sub- and superdiffusion, respectively. Only for $q_{\text{slab}} = 0$ we obtain normal Markovian diffusion with coefficient

$$D_{xx} = \pi |\mu| v \kappa_{FL}^{\text{slab}}, \tag{2.128}$$

where

$$\kappa_{FL}^{\text{slab}} = \pi D(s, 0) \ell_{\text{slab}} \frac{\delta B_{\text{slab}}^2}{B^2} \tag{2.129}$$

is the field line diffusion coefficient. This result is the famous FLRW limit, derived firstly in the pioneering work of Jokipii (1966) by directly evaluating the Fokker-Planck diffusion coefficients. Here we have thus illustrated how the FLRW limit naturally arises in the FTE under the assumptions of QLT. Important to note is that the FLRW only appears in the FTE because of the transformation to GC coordinates.

The diffusive behaviour predicted by QLT for pure slab turbulence is at odds with the findings of studies using full-orbit test particle simulations (Giacalone & Jokipii, 1999; Qin et al., 2002a,b). These studies have shown that when pure slab turbulence is considered, the particles mean square displacement across the average magnetic field scales with the root of time, i.e., $\left\langle (\Delta x_\perp)^2 \right\rangle \sim \sqrt{t}$, which corresponds to sub-diffusive behaviour. Hence, the QLT result for cross-field diffusion in pure slab turbulence is incorrect (see also Shalchi, 2008, for a discussion).

If instead of pure slab turbulence, pure 2D turbulence is assumed, one finds upon substituting Eq. (2.105) in Eq. (2.126) that

$$D_{xx} = \frac{\mu^2 v^2}{B^2} \int_0^\infty dt \int_0^\infty dk_\perp g(k_\perp) \int_0^{2\pi} d\psi \sin^2(\psi) e^{ik_\perp r_L(\cos(\phi(t)+\pi/2-\psi)}, \tag{2.130}$$

where $r_L = \sqrt{1-\mu^2} v/\Omega$ is the Larmor radius and we assumed without loss of generality that $\phi(t=0) = \pi/2$. Similarly, we have that

$$D_{yy} = \frac{\mu^2 v^2}{B^2} \int_0^\infty dt \int_0^\infty dk_\perp g(k_\perp) \int_0^{2\pi} d\psi \sin^2(\psi) e^{ik_\perp r_L(\cos(\phi(t)+\pi/2-\psi)}. \tag{2.131}$$

Using the identity

$$e^{ix\cos(\xi)} = \sum_{n=-\infty}^{\infty} J_n(x) e^{in(\xi+\pi/2)}, \tag{2.132}$$

where J_n is a Bessel function of the first kind, we can write the perpendicular diffusion coefficient $D_\perp = D_{xx} + D_{yy}$ as

$$\begin{aligned} D_\perp =& \frac{\mu^2 v^2}{B^2} \int_0^\infty dt \int_0^\infty dk_\perp g(k_\perp) \sum_{n=-\infty}^{\infty} J_n(k_\perp r_L) \int_0^{2\pi} d\psi e^{in(\phi(t)-\psi)} \\ =& 2\pi \frac{\mu^2 v^2}{B^2} \int_0^\infty dt \int_0^\infty dk_\perp g(k_\perp) J_0(k_\perp r_L) \\ =& +\infty. \end{aligned} \tag{2.133}$$

This infinite diffusion coefficient implies that under QLT and pure 2D magnetostatic turbulence, particle transport perpendicular to the magnetic field is not diffusive. In fact, it can be shown (Shalchi, 2009) that under these assumptions $\left\langle (\Delta x_\perp)^2 \right\rangle \sim t^2$, corresponding to a ballistic motion of the particles. Moreover, the infinite diffusion

coefficient for pure 2D turbulence implies that the diffusion coefficient for the composite slab/2D turbulence model is also infinite. However, full-orbit test particle simulations have shown that particles behave diffusively in pure 2D or composite turbulence (Giacalone & Jokipii, 1999; Qin et al., 2002a). The QLT result for cross-field diffusion in pure 2D or composite turbulence is therefore incorrect.

The disagreement between QLT and test-particle simulations can be attributed to the observation that perpendicular diffusion is in general a non-linear process, hence invalidating a first-order perturbation based approach. This realisation has led to the development of more sophisticated non-linear cross-field diffusion theories, which are discussed in the next section.

2.8 Non-linear cross-field diffusion theories

Non-linear diffusion theories start from the assumption that the effect of turbulence on the energetic particle distribution is diffusive in nature. Within these theories, the evolution of the particle distribution is thus still modelled by the FTE as formulated in e.g., Eq. (2.82), but with the *assumption* that the turbulence term consists of a set of diffusion processes, like in Eq. (2.119). It should however be noted that it is in principle possible that the effect of turbulence on the particle distribution leads to anomalous diffusion, in which case Eq. (2.119) does not hold. In anomalous diffusion regimes, it is possible to generalize the FTE by replacing the Laplacian operators that describe the diffusion processes with a diffusion operator of fractional order (e.g., Effenberger, 2014, and citations therein). In this work, only normal diffusion regimes will be considered.

Within non-linear diffusion theories, the Taylor–Green–Kubo (TGK) formula is often used to calculate the diffusion coefficients (Taylor, 1922; Green, 1951; Kubo, 1957). This approach utilises the particles' equations of motion in a fluctuating electromagnetic field to compute the momentum and spatial diffusion coefficients using the following formula:

$$D_{\zeta_i\zeta_j} = \int_0^\infty \left\langle \dot{\zeta}_i(0)\dot{\zeta}_j(t) \right\rangle dt. \tag{2.134}$$

Notice the similarity between the TGK formulation and the QLT formulation, i.e., Eq. (2.118). The main difference is that in the latter formulation the time integration is performed along unperturbed particle trajectories whereas in the former formulation the particle phase space coordinates are treated as random variables. However, as discussed at the end of Section 2.7, if the second-order term $\delta\mathscr{S}$ in Eq. (2.111) is not neglected in QLT, the integration in Eq. (2.118) has to be performed along the perturbed particle phase space trajectories. In that case Eqs. (2.118) and (2.134) become equivalent. Following this reasoning, one can thus state that a sufficient condition for a particle population to behave diffusively is obtained if the corresponding distribution function

can be written as in Eq. (2.109), where $\mathscr{F}_0$ varies on a diffusive time scale $\tau_{\rm diff}$ which is significantly longer than the particle decorrelation time scale τ_c.

In the next section, one of the most promising non-linear cross-field diffusion theories, i.e., the non-linear GC theory (NLGC; Matthaeus et al., 2003) is discussed, together with some of its extensions and improvements.

2.8.1 Non-linear guiding centre theory

In the original formulation of the NLGC theory by Matthaeus et al. (2003), the particle's GC velocity across the mean magnetic field is assumed to be:

$$\dot{\mathbf{X}}_\delta = a\mu v \frac{\delta \mathbf{B}}{B_0}, \tag{2.135}$$

with a being a free parameter that measures how well particles follow the magnetic field lines. For $a = 1$, we recover Eq. (2.125), which states that particles stream along the perturbed field lines. Moreover, Qin & Shalchi (2016) argued using a numerical approach that $a = 1$ is the only correct option, even though the best agreement between the NLGC theory and test particle simulations is found for $a = 1/\sqrt{3}$ (Matthaeus et al., 2003).

Substituting Eq. (2.135) into the TGK formula (2.134) gives then

$$D_\perp = \frac{a^2}{B^2} \int_0^\infty \langle v_z(0) v_z(t) \delta B_x \left[\mathbf{X}(0)\right] \delta B_x \left[\mathbf{X}(t)\right] \rangle \, dt, \tag{2.136}$$

where $v_z = \mu v$. The important difference with QLT is that the phase space coordinates v_z and $\mathbf{X}$ are treated as random variables, which means that the integrand of Eq. (2.136) consists of a fourth-order correlation function. To proceed, Matthaeus et al. (2003) assumed that the local magnetic field vector is not correlated with the particle velocities, such that Eq. (2.136) can be simplified to

$$D_\perp = \frac{a^2}{B^2} \int_0^\infty \langle v_z(0) v_z(t) \rangle \langle \delta B_x \left[\mathbf{X}(0)\right] \delta B_x \left[\mathbf{X}(t)\right] \rangle \, dt. \tag{2.137}$$

Qin & Shalchi (2016) illustrated that the fourth-order correlation can indeed be replaced by a product of second-order correlations, under the condition that the turbulence is dominated by the pure 2D component, which is the case for the solar wind (Bieber et al., 1996).

In a next step, Matthaeus et al. (2003) assumed an isotropic exponential model for the parallel velocity correlation, i.e.,

$$\langle v_z(0) v_z(t) \rangle = \frac{v^2}{3} e^{-vt/\lambda_\parallel}. \tag{2.138}$$

Such a correlation function is however only valid under strong isotropic scattering conditions (Shalchi, 2011).

To calculate the magnetic correlation function in Eq. (2.137), Corrsin's independence hypothesis is utilised, which states that the distributions of the particle's displacement and the velocity become statistically independent after a sufficient amount of time (Corrsin, 1951). This gives for homogeneous turbulence that

$$\langle \delta B_x \left[\mathbf{X}(0)\right] \delta B_x \left[\mathbf{X}(t)\right] \rangle = \int \left\langle \delta B_x^2(\mathbf{k},t) e^{i\mathbf{k}\cdot\Delta\mathbf{X}} \right\rangle dk^3 \tag{2.139}$$

$$\approx \int \left\langle \delta B_x^2(\mathbf{k},t) \right\rangle \left\langle e^{i\mathbf{k}\cdot\Delta\mathbf{X}} \right\rangle dk^3. \tag{2.140}$$

To proceed, it is assumed that the components $\Delta\mathbf{X}$ of the GC trajectory have uncorrelated axisymmetric Gaussian distributions and that both the parallel and the perpendicular displacements behave diffusively for all times, i.e., $\langle \Delta X \rangle^2 = 2tD_\perp$ and $\langle \Delta Z \rangle^2 = 2tD_\parallel$. Under these assumptions, we have

$$\left\langle e^{i\mathbf{k}\cdot\Delta\mathbf{X}} \right\rangle = e^{-k_\perp^2 D_\perp t - k_\parallel^2 D_\parallel t}, \tag{2.141}$$

and, hence,

$$D_\perp = \frac{a^2 v^2}{3B^2} \int d^3k \int_0^\infty dt P_{xx}(\mathbf{k},t) e^{-k_\perp^2 D_\perp t - k_\parallel^2 D_\parallel t - vt/\lambda_\parallel}. \tag{2.142}$$

In the original NLGC theory formulation, Matthaeus et al. (2003) assumed a dynamical correlation function (Eq. (2.100)) of the form $\Gamma(\mathbf{k},t) = e^{-\gamma(\mathbf{k})t}$, which leads to the following perpendicular diffusion coefficient

$$D_\perp = \frac{a^2 v^2}{B^2} \int d^3k \frac{P_{xx}(\mathbf{k})}{v/\lambda_\parallel + k_\perp^2 D_\perp t + k_\parallel^2 D_\parallel + \gamma(\mathbf{k})}. \tag{2.143}$$

This is a non-linear integral equation, since $D_\perp$ appears at both sides of the equality sign. Moreover, except for assuming spatial homogeneity, no other assumption was made regarding the magnetostatic correlation tensor $P_{xx}(\mathbf{k})$. Hence, Eq. (2.143) can be used for the slab/2D composite turbulence model, as well as for fully 3D turbulence models.

For pure slab turbulence, it is straightforward to show that Eq. (2.143) gives a finite diffusion coefficient, corresponding thus to normal diffusion. As explained in the previous section, this is at odds with the results of full-orbit test particle simulations, which show subdiffusive particle motion in pure slab turbulence. To accommodate for this, an extended NLGC (ENLGC) theory was developed by Shalchi (2006), in which the subdiffusive behaviour of the slab contribution is obtained. For composite turbulence, the perpendicular diffusion coefficient is assumed to be solely due to the

2D component of the turbulence and hence

$$D_\perp = \frac{a^2 v^2}{B^2} \int d^3k \frac{P_{xx}^{2D}(\mathbf{k})}{v/\lambda_\parallel + k_\perp^2 \kappa_\perp t + \gamma(\mathbf{k})}. \tag{2.144}$$

Note that $\lambda_\parallel$ still appears in the denominator of Eq. (2.144), connecting the parallel diffusion with the perpendicular diffusion. Since the slab component of the turbulence influences $\lambda_\parallel$ strongly, $D_\perp$ is still indirectly affected by the slab contribution. Because the ENLGC theory can only be used for a two-component turbulence model, Shalchi (2010) derived a more general model called the Unified Non-linear Transport (UNLT) theory, which is also valid for 3D turbulence models. Like the ENLGC theory, the UNLT theory predicts that the slab component does not contribute explicitly to the perpendicular diffusion coefficient. The UNLT theory uses a KBE similar to the FTE to determine a more accurate velocity correlation function than Eq. (2.142). As discussed in the next section, this also allows to derive the pitch-angle dependence of the cross-field diffusion coefficient under certain additional assumptions.

For the incorporation of the NLGC theory into a numerical particle transport model, it is useful to have analytical approximations of the non-linear integral equation Eq. (2.144). For the wave spectrum (2.107) and for magnetostatic turbulence (i.e., $\gamma(\mathbf{k}) = 0$), such analytical approximations were provided by Shalchi et al. (2010) for a whole set of different parameter regimes. Here, we only provide the approximations that are considered relevant for the solar wind regime, which corresponds to $\lambda_\parallel \lambda_\perp \ll 3\ell_{2D}^2$ (see also Shalchi et al., 2004). Depending on the spectral index q of the energy range, one finds in terms of the perpendicular mean free path $\lambda_\perp = 3D_\perp/v$ that (Shalchi et al., 2010)

$$\lambda_\perp \approx \begin{cases} \left[3^{(q+1)/2} a^2 D(s,q) \frac{\delta B_{2D}^2}{B^2} \ell_{2D}^{q+1} \Gamma\left(\frac{1+q}{2}\right) \Gamma\left(\frac{1-q}{2}\right)\right]^{2/(q+3)} \lambda_\parallel^{(1-q)/(3+q)} & \text{if } q < 1 \\ \sqrt{\frac{3(s-1)}{2(q-1)}} a \ell_{2D} \frac{\delta B_{2D}}{B} & \text{if } q > 1, \end{cases} \tag{2.145}$$

where $\Gamma(z)$ denotes the Gamma function.

2.8.2 Pitch-angle dependent cross-field diffusion

The isotropy assumption for the velocity correlation (2.138) implies that the underlying particle distribution function is independent of the pitch-angle coordinate. As a result, the obtained cross-field diffusion coefficient is also independent of μ, the cosine of the pitch angle. These conditions are often not applicable for SEPs, where focussing and anisotropic scattering produce particle distribution functions that are characterised by strong first-order parallel anisotropies, especially at the onset of an SEP event. Moreover, by using a numerical particle transport model with various

cross-field diffusion coefficients that have a different μ dependency, Strauss & Fichtner (2015) showed that the resulting SEP distributions can be significantly different in the heliosphere, even when the diffusion coefficients are identical after averaging over μ. This illustrates the importance of deriving the pitch-angle dependence of the cross-field diffusion coefficient.

Starting from the UNLT theory, Qin & Shalchi (2014) derived several asymptotic solutions for the pitch-angle dependent cross-field diffusion coefficient in 2D dominated turbulence, while assuming the wave spectrum (2.107). For the case where cross-field diffusion dominates parallel diffusion, the authors found the following FLRW limit

$$D_{\perp}(\mu) = av|\mu|\kappa_{\rm FL}^{\rm 2D}, \tag{2.146}$$

where the field line diffusion coefficient is given by (Shalchi & Weinhorst, 2009)

$$\kappa_{FL}^{\rm 2D} = \sqrt{\frac{s-1}{2(q_{\rm 2D}-1)}}\ell_{\rm 2D}\frac{\delta B_{\rm 2D}}{B}, \tag{2.147}$$

if the spectral index of the turbulence energy range satisfies $q_{\rm 2D} > 1$. For $q_{\rm 2D} \leq 1$, the diffusion coefficient $\kappa_{\rm FL}$ becomes infinite, which corresponds to superdiffusive behaviour. Note the similarity between Eq. (2.146) and the FLRW obtained for slab turbulence under the assumption of QLT, i.e., Eq. (2.128). Both diffusion coefficients scale like $|\mu|$, which originates from the streaming of the particles along the perturbed magnetic field lines.

For the limiting case where parallel diffusion dominates cross-field diffusion, Qin & Shalchi (2014) found the following diffusion coefficient:

$$D_{\perp}(\mu) = \frac{a^2v^2\mu^2}{4D}\frac{\delta B^2}{B^2}, \tag{2.148}$$

with $q_{\rm slab} = 0$ in (2.106) and where isotropic particle scattering conditions were assumed by using $D_{\mu\mu} = D(1-\mu^2)$, with D a constant.

In an alternative approach, Fraschetti (2016) suggested that cross-field diffusion results from gradient and curvature drifts induced by fluctuations associated with the inertial range of the turbulence, and derived a diffusion coefficient which scales as $D_{\perp} \sim (1-\mu^2)^2$. Furthermore, Webb et al. (2001) used yet another method to derive a cross-field diffusion coefficient $D_{\perp} \sim (1-\mu^2)$. Their method is based on solving a Bhatnagar–Gross–Krook (BGK) Boltzmann equation for the phase space distribution function that depends both on the particle's pitch angle and gyrophase. Finally, Engelbrecht (2019) recently suggested to replace the assumed isotropic velocity correlation (2.138) by

$$\langle v_z(0)v_z(t)\rangle = v^2\,\langle\mu(0)\mu(t)\rangle = v^2(\alpha\mu^2+\beta)\exp(-t/\tau), \tag{2.149}$$

where α and β are positive constants, and τ is some decorrelation time scale. Upon substituting Eq. (2.149) into Eq. (2.142), a diffusion coefficient that scales as $D_\perp \sim \alpha\mu^2 + \beta$ is obtained.

The various μ dependencies obtained for $D_\perp(\mu)$ illustrate the complexity of the underlying problem, both from a mathematical and physical viewpoint. Finding an accurate description of the pitch-angle dependence of the cross-field diffusion coefficient is however important, given the sensitivity of SEP transport models to the utilised cross-field diffusion coefficient. One way to address this problem is by performing multiple full-orbit test particle simulations under different turbulence conditions, and deduce the pitch-angle dependence of the cross-field diffusion coefficients from the simulation results.

2.9 Phenomenological approaches to cross-field diffusion

The discussion above illustrated that there are still many unresolved issues with the existing non-linear cross-field diffusion theories. In addition, various parameters of the turbulence models are still poorly constrained, like the bend over scale $\ell_{\mathrm{slab/2D}}$ and the spatial evolution of the turbulence amplitude δB^2 .

Given the uncertainties clouding the turbulence and non-linear cross-field diffusion theories, some authors have instead opted for a more phenomenological approach when prescribing the cross-field diffusion coefficient in particle transport models. For example, Dröge et al. (2010) suggested a perpendicular mean free path that is proportional to the Larmor radius r_L and the particle mean free path, giving

$$\lambda_\perp(\mu) = \alpha r_L \lambda_\parallel = \alpha \sqrt{1-\mu^2}\frac{p}{qB}\lambda_\parallel, \tag{2.150}$$

where α is a free parameters determining the strength of the cross-field diffusion. By averaging Eq. (2.150) over the pitch-angle, one obtains

$$\lambda_\perp = \frac{\alpha\pi}{4}\frac{p}{qB}\lambda_\parallel. \tag{2.151}$$

In Dröge et al. (2014), such a perpendicular mean free path is used to model a multi-spacecraft solar electron event reasonably well.

Another cross field diffusion model that is sometimes used in SEP modelling is (e.g., Zhang, 1999; Zhang et al., 2009; Wang et al., 2012; Wang & Qin, 2015)

$$\kappa_\perp = \kappa_0 \left(\frac{v}{c}\right)\left(\frac{p}{p_0}\right)^\beta \left(\frac{B_0}{B}\right), \tag{2.152}$$

where κ_0 and β are free parameters, whereas p_0 and B_0 are a reference momentum and magnetic field magnitude, respectively. This model was originally proposed and used in the context of cosmic ray modulation (e.g., Potgieter & Moraal, 1985; Potgieter et al., 1997).

2.10 Momentum and mixed diffusion coefficients

Until now, only the spatial and pitch-angle diffusion processes have been considered. However, as shown in Eq. (2.117), there are in fact 16 different diffusion processes appearing in the FTE. Of special interest is the diffusion process with coefficient D_{pp}, which is commonly referred to as second-order Fermi acceleration or stochastic acceleration (Fermi, 1949). From Eqs. (2.118) and (2.69), it is seen that D_{pp} is only non-zero if $\delta\mathbf{E}$ is non-zero. However, for MHD turbulence, the fluctuating electric fields are often much smaller than the fluctuating magnetic fields and as a result the diffusion processes described by D_{pp} and $D_{\mu p}$ are often negligible compared to the pitch-angle diffusion process. This can be understood from Eqs. (2.73) and (2.69), which give that that $d\mu_\delta/dt \sim q\delta B/m$ and $dp_\delta/dt \sim q\delta E$. For Alfvénic turbulence, the induction law gives $\delta E = V_A \delta B$, with V_A the Alfvén speed. Hence it is found that $D_{pp} \sim p^2(V_A/v)^2 D_{\mu\mu}$ and $D_{\mu p} \sim p(V_A/v)D_{\mu\mu}$. The characteristic time-scales τ_{ij} associated to the different diffusion processes can be defined as $\tau_{\mu\mu}^{-1} = D_{\mu\mu}$, $\tau_{\mu p}^{-1} = D_{\mu p}/p = (V_A/v)D_{\mu\mu}$, and $\tau_{pp}^{-1} = D_{pp}/p^2 = (V_A/v)^2 D_{\mu\mu}$, and hence we have that $\tau_{\mu\mu} \ll \tau_{\mu p} \ll \tau_{pp}$ if $V_A \ll v$. Neglecting the diffusion processes associated with $D_{\mu p}$ and D_{pp} corresponds thus to approximations that are valid to first and second order in V_A/v, respectively (Schlickeiser, 1989). This may be a reasonable assumption in most parts of the inner heliosphere, yet it has been suggested that stochastic acceleration may play an important role in the acceleration of low energy (< 100 keV) particles within turbulent solar wind structures like corotating interaction regions (e.g., Schwadron et al., 1996; Richardson, 2018, and references therein).

Finally, for incompressible axisymmetric turbulence with $\delta E = 0$, it can be shown that the diffusion coefficients $D_{X_i\mu} = D_{\mu X_i} = 0$ (e.g., Schlickeiser, 2011).

2.11 Summary and discussion

In this chapter we have presented a derivation of the FTE and discussed its diffusion coefficients. As noted in the introduction of this chapter, the FTE has been used by various authors under different assumptions, often without detailing its derivation. In this chapter, we have assumed a general background plasma and have included relativistic effects for a flat spacetime. Although we focus in this work on the inner

heliosphere, the FTE can be used to model energetic particle populations residing in any collisionless plasma, as long as the test particle approach is applicable. Examples of such environments include, among others, the solar corona, the magnetospheres of Earth and the gas giants, and interstellar space. Moreover, since we derived the FTE up to first order in U/c, it can also be used to model energetic particles propagating in astrophysical plasmas that are "mildly" relativistic, like some SNe. For more exotic objects, like pulsar winds or astrophysical jets, the fully relativistic version of the FTE has to be utilised. As explained in Section 2.2.2, it is important to define the mixed phase space distribution precisely for relativistic plasmas, since the usage of two reference frames introduces two different time coordinates.

For heliospheric plasmas, a good approximation is to neglect the terms of $O(U/c)$ in the FTE, since the typical bulk plasma speeds are low compared to the speed of light. As noted in Section 2.2.4 and 2.5, such approximation does not put any restriction on the applicability of the FTE in describing relativistic particle transport. This is because neglecting the $O(U/c)$ terms only puts restrictions on the speed of the background plasma, and not on the speed of the energetic particles. Evidently, when calculating the speed or kinetic energy of near-relativistic particles, their Lorentz factor γ needs to be taken into account.

One of the important results of this chapter is that a transformation to the GC coordinates before averaging over gyrophase leads to the inclusion of the GC drifts in the spatial part of the FTE. In Section 2.5 and Appendix B, we illustrated that the gyro-averaged drift term $\langle \mathbf{V}_d \rangle_\phi$ does not only contain the drifts due to the magnetic field's curvature and gradient, but also the polarization drift and drifts due to time-varying magnetic fields. Moreover, as illustrated in Section 2.7.2, the perturbation of the GC drift term introduces a spatial cross-field diffusion process in the FTE under the assumptions of QLT, suggesting that cross-field diffusion can at least partly be caused by the non-vanishing GC drifts. A similar result was derived by Zhang (2006) in the non-relativistic limit, and by Schlickeiser & Jenko (2010), for an isotropic particle distribution in a weakly non-uniform magnetic field.

This result can be overlooked by gyro-averaging the FTE without transforming to GC coordinates. In that case, information on the drift motion of the particles is lost, since the spatial part of the FTE, i.e., Eq (2.84), is obtained without the drift term. This has previously led to the statement (e.g., le Roux et al., 2004; Zank, 2014) that the assumption of a gyrotropicy rules out any contributions of the GC drifts to the spatial part of the FTE. A spatial cross-field diffusion process can then only appear in the FTE when the distribution is assumed to be nearly isotropic in pitch-angle. In that case, an expansion in terms of Legendre polynomials $P_n(\mu)$ can be truncated in first order to yield a spatial diffusion process, both parallel and perpendicular to the magnetic field (e.g., Zank, 2014). However, in this chapter, the statement that gyrotropicy rules out any contributions of the GC drifts in the spatial part of the FTE is shown to be incorrect. The particle distribution function can be independent of gyrophase, even when particle

drifts are important. In addition, we have illustrated that cross-field diffusion processes can appear in the FTE, without having to assume an isotropic pitch-angle distribution (PAD).

As explained in Appendix A, averaging the transport equation over the gyrophase has a different interpretation when using the GC coordinates $\mathbf{X}$ instead of the particle's exact coordinate $\mathbf{x}$. In the former case, the gyro-average is an average over particles that have the same GC, but are therefore located at different positions in space, whereas in the latter case the gyro-average is an average over particles that are all located at the exact same position in space, and have therefore different GCs.

An example where averaging the FTE over gyrophase is not possible when using GC coordinates, is found near current sheets (CS). At a CS, the magnetic field reverses direction and hence also the particle's magnetic moment and its direction of gyration reverses. As a consequence, a point located within a Larmor radius of the CS cannot be the GC of a particle population uniformly distributed in the 2π domain of the momentum gyrophase angle[25], such that the averaging operator A.1 is not well defined. Moreover, when crossing the CS, the pitch-angle coordinate θ of a particle jumps to $180° - \theta$ (or, equivalently, $\mu \mapsto -\mu$). Hence, the particle distribution across the CS can only be a continuous function of μ if the PAD is symmetric around $\mu = 0$. In Burger et al. (1985), an expression is derived for the GC drift along a CS, under the assumption that the particle distribution function is isotropic both in pitch-angle and gyrophase.

In Section 2.7, it was discussed how under the assumptions of QLT the effect of turbulence on the particle distribution function appears as a set of diffusion processes in the FTE. In particular, we used QLT to re-derive the pitch-angle diffusion coefficient $D_{\mu\mu}$ obtained by Hasselmann & Wibberenz (1968), and we briefly discussed the associated 90°-scattering problem. Next, we derived the diffusion coefficient of the cross-field diffusion process, which appears in the FTE due to our usage of GC coordinates. However, QLT predicts diffusive particle motion in pure slab turbulence and superdiffusion in pure 2D or composite slab/2D turbulence. This is at odds with the results of full-orbit particle simulations which predict subdiffusion and normal diffusion in pure slab and 2D turbulence, respectively. Hence, QLT is not applicable for cross-field diffusion and instead a non-linear approach is necessary.

In Section 2.8.1 we discussed some of the most promising approaches to cross-field diffusion, including the NLGC theory, the ENLGC theory, and the UNLT theory. However, several other cross-field diffusion theories exist, and we refer to Shalchi (2009) for an overview. A major unresolved question in particle diffusion theory is the pitch-angle dependence of the corresponding diffusion coefficients. This is especially

[25] For example, assume an infinitely thin and flat CS with a uniform magnetic field of opposite polarity on both sides of the CS. A point located a distance $\rho < r_L$ away from the CS, will be the instantaneous GC of particles on both side of the CS with a momentum phase-angle $\phi \in]-\arcsin(\rho/r_L), \pi + \arcsin(\rho/r_L)[$ (where $\phi = 0$ is assumed to correspond to a momentum vector perpendicular to the CS).

important to understand the spreading of SEP events, which are often characterised by an anisotropic PAD. Finally, we remark that both QLT and the non-linear diffusion theories assume a uniform background magnetic field, out of simplicity. In conclusion, the diffusive motion of energetic charged particles through a magnetized turbulent plasma remains thus a far from resolved fundamental physical problem.

Chapter 3

PARADISE

"What hath night to do with sleep?"
– John Milton (Paradise Lost)

Abstract. In this chapter, we present the notion of SDEs and briefly explain how these equations can be solved numerically using methods from Itô calculus. The FTE is then reformulated as a set of equivalent Itô SDEs, which can be done in both a time-forward and a time-backward manner. Next, we introduce our new model PARADISE, which solves the FTE in a stochastic manner by propagating pseudo-particles in a solar wind generated by a 3D MHD model. We discuss the numerical methods employed by PARADISE, and an overview is given of the different diffusion theories that are implemented in the model.

Section 3.3 of this chapter is partly based on Wijsen et al. (2019a).

3.1 Introduction

In the previous chapter, it was illustrated how the evolution of the distribution function of energetic particles propagating in a collisionless plasma can be described by the FTE, which can be formulated both as a KFE or a KBE. In this Chapter, it is discussed how the FTE can be solved by integrating an equivalent set of Itô SDEs either backward or forward in time. Furthermore, the *Particle Radiation Asset Directed at Interplanetary*

Space Exploration (PARADISE) model is introduced. This model applies Itô calculus to solve the FTE in complex background plasma configurations, which can for example be generated with a 3D time dependent MHD model.

The chapter is structured as follows. Section 3.2.1 provides a brief introduction on SDEs, and their relation to the Kolmogorov forward and backward equations. Section 3.2.2 discusses the Euler-Maruyama (EM) method, which is a numerical scheme that can be used to integrate SDEs in time. Section 3.2.3 illustrates how the Itô SDEs that are equivalent to the FTE are obtained. This leads to the introduction of pseudo-particles, whose exact meaning is discussed in Section 3.2.4. Sections 3.2.5 and 3.2.6 discuss how the differential intensity of energetic particles can be sampled by integrating SDEs forward in time for many pseudo-particles, hereby taking into account the boundary and initial conditions of the FTE. Finally, in Section 3.3, the PARADISE model is introduced and all its implementation details are specified.

3.2 Itô stochastic differential equations

3.2.1 Itô calculus

Just as the name suggests, SDEs are differential equations that contain stochastic terms, hence making their solution essentially non-deterministic. Itô calculus is a field in mathematics that addresses how the methods of (normal) calculus can be extended to solve such SDEs. This section provides a brief overview of some of the concepts and terminology of Itô calculus that will be used extensively in the remainder of this chapter. It should be noted that Itô calculus covers much more than what is introduced in this section. An in-depth introduction to the field of stochastic calculus can be found in e.g., Gardiner (2004) or Øksendal (2003).

In this work, we are only concerned with SDEs that can be formulated as

$$d\boldsymbol{\zeta}(t) = \mathbf{A}\left(\boldsymbol{\zeta}, t\right) dt + \mathbf{B}\left(\boldsymbol{\zeta}, t\right) \cdot d\mathbf{W}, \quad \boldsymbol{\zeta}(t = 0) = \boldsymbol{\zeta}^0, \tag{3.1}$$

where $\boldsymbol{\zeta}$ is an n-dimensional vector with initial state $\boldsymbol{\zeta}^0$, and $\mathbf{W}$ is a vector of n independent Wiener processes[1]. The vector function $\mathbf{A}$ is deterministic, and is often called the drift function of the SDE, although we will refrain from using this terminology to avoid confusion with the GC drifts of the energetic particles. Finally,

[1] Another name for a Wiener process is a Brownian motion. It is defined as a random variable $W(t)$ that is continuous in an interval $t \in [0, T]$ and satisfies the following three conditions: (i) $W(0) = 0$ with probability one, (ii) $\Delta W = W(t_2) - W(t_1) \sim \mathcal{N}(0, t_2 - t_1)$, where $0 \leq t_1 \leq t_2 \leq T$ and $\mathcal{N}(\mu, \sigma^2)$ a normal distribution with mean μ and standard deviation σ, (iii) For $0 \leq t_1 \leq t_2 \leq t_3 \leq t_4 \leq T$, the increments $W(t_2) - W(t_1)$ and $W(t_4) - W(t_3)$ are independent of each other.

the $n \times n$ matrix function B is also deterministic and is referred to as the volatility matrix.

To define the precise meaning of Eq. (3.1) in a mathematically rigorous manner, the following integral equation is considered

$$\boldsymbol{\zeta}(t) = \boldsymbol{\zeta}^0 + \int_0^t \mathbf{A}(\boldsymbol{\zeta}, s)\, ds + \int_0^t \mathbf{B}(\boldsymbol{\zeta}, s) \cdot d\mathbf{W}. \tag{3.2}$$

In this equation, the first integral is a deterministic integral which is well-defined using, for example, the rules of Lebesgue integration, hereby assuming that $\mathbf{A}$ is a measurable function. In contrast, the second integral is of stochastic nature, and can be defined in different non-equivalent manners. In the *Itô interpretation*, the stochastic integral is defined as

$$\int_0^t \mathbf{B}(\boldsymbol{\zeta}, s)\, d\mathbf{W} = \lim_{\Delta t \to 0} \sum_{k=0}^{K-1} \mathbf{B}(\boldsymbol{\zeta}, t_k) \cdot \Delta \mathbf{W}^k, \tag{3.3}$$

where the integration interval $[0, t]$ is divided into K subintervals of width Δt, such that $t = K\Delta t$, $t^k = k\Delta t$ and $\Delta \mathbf{W}^k = \mathbf{W}(t^{k+1}) - \mathbf{W}(t^k)$. It can be shown that the limit on the right-hand side converges in probability if $\mathbf{B}$ is a locally bounded, right-continuous, and non-anticipating[2] function (Kallenberg, 2002). Important in the Itô interpretation is that the integrand $\mathbf{B}(\boldsymbol{\zeta}, s)$ is evaluated at time t^k, i.e., the begin point of the interval $[t^k, t^{k+1}]$. In other words, the Itô interpretation only uses information that is known at the start of $[t^k, t^{k+1}]$ to approximate the integral in this interval, which is in accordance with the causality principle. In contrast, in the *Stratnovich interpretation* of the stochastic integral, the integrand $\mathbf{B}(\boldsymbol{\zeta}, s)$ is evaluated at the midpoints $(t^k + t^{k+1})/2$, in which case the stochastic integral will converge to a value different from the Itô interpretation. This is in sharp contrast to the deterministic Riemann or Lebesgue integral, which converge to the same value independent of the points in which the integrand is evaluated. In this work, we will always work with the Itô interpretation.

It is now possible to give a precise meaning to equation (3.1). It is a purely formal notation, which acts as a shorthand for the more rigorous integral equation (3.2), where the Itô interpretation (3.3) is assumed for the stochastic integral. We therefore also refer to Eq. (3.1) as an Itô SDE.

An important result from Itô calculus is that the probability distribution function, f, of the stochastic variable $\boldsymbol{\zeta}$ satisfies the following KFE (see Appendix C):

$$\frac{\partial f(\boldsymbol{\zeta}, t)}{\partial t} = -\frac{\partial}{\partial \zeta_i}\left[\mathsf{A}_i(\boldsymbol{\zeta}, t) f(\boldsymbol{\zeta}, t)\right] + \frac{\partial^2}{\partial \zeta_i \partial \zeta_j}\left[D_{ij}(\boldsymbol{\zeta}, t) f(\boldsymbol{\zeta}, t)\right], \tag{3.4}$$

[2] A function $\mathsf{B}(t)$ is non-anticipating with respect to $W(t)$ if $\mathsf{B}(t)$ is stochastically independent of $W(s) - W(t)$ for all $s > t$. Intuitively, this means that B cannot look into the future. A more formal definition can be found in Kallenberg (2002).

where Einstein's summation convention was used and where the diffusion tensor $\mathbf{D}$ satisfies

$$D_{ij}(\boldsymbol{\zeta}, t) = \frac{1}{2}\mathsf{B}_{ik}(\boldsymbol{\zeta}, t)\mathsf{B}_{jk}(\boldsymbol{\zeta}, t). \tag{3.5}$$

In these equations, $f(\boldsymbol{\zeta}, t)$ is actually the conditional probability function $f(\boldsymbol{\zeta}, t \,|\, \boldsymbol{\zeta}^0, t = 0)$, which describes the transition from the initial state $\boldsymbol{\zeta}^0$ to a new state $\boldsymbol{\zeta}(t)$.

Analogously, one can define the conditional probability function $f(\boldsymbol{\zeta}, t \,|\, \boldsymbol{\zeta}^T, t = T)$, where T is some final time, that is, $t < T$, and $\boldsymbol{\zeta}^T = \boldsymbol{\zeta}(t = T)$. In this case, $f(\boldsymbol{\zeta}, t \,|\, \boldsymbol{\zeta}^T, t = T)$ describes the transition from a state $\boldsymbol{\zeta}(t)$ to a final given state $\boldsymbol{\zeta}(T)$. Associated with $f(\boldsymbol{\zeta}, t \,|\, \boldsymbol{\zeta}^T, t = T)$ is a backward Itô SDE, which integrates the stochastic variable $\boldsymbol{\zeta}$ backwards in time starting from the final state $\boldsymbol{\zeta}^T$, that is,

$$d\boldsymbol{\zeta} = \tilde{\mathbf{A}}(\boldsymbol{\zeta}, s)\, ds + \tilde{\mathbf{B}}(\boldsymbol{\zeta}, s) \cdot d\mathbf{W}, \quad \boldsymbol{\zeta}(s = 0) = \boldsymbol{\zeta}^T, \tag{3.6}$$

where the backward time $s = T - t$ is introduced. In this case, the probability distribution f of stochastic variable $\boldsymbol{\zeta}$ satisfies the following KBE

$$-\frac{\partial f(\boldsymbol{\zeta}, s)}{\partial s} = \tilde{\mathsf{A}}_i(\boldsymbol{\zeta}, s)\frac{\partial f(\boldsymbol{\zeta}, s)}{\partial \zeta_i} + \tilde{D}_{ij}(\boldsymbol{\zeta}, s)\frac{\partial^2 f(\boldsymbol{\zeta}, s)}{\partial \zeta_i \partial \zeta_j}, \tag{3.7}$$

where like before $\tilde{\mathbf{D}} = \frac{1}{2}\tilde{\boldsymbol{B}}\tilde{\boldsymbol{B}}^{\mathsf{T}}$.

3.2.2 Numerical integration of SDEs

Given a grid of points $\{0, t^1, \ldots, t^K\}$ that partition the interval $[0, t]$, the exact value of the stochastic variable $\boldsymbol{\zeta}$ at time t^{k+1} is given by (see Eq. (3.2))

$$\boldsymbol{\zeta}(t^{k+1}) = \boldsymbol{\zeta}(t^k) + \int_{t^k}^{t^{k+1}} \mathbf{A}(\boldsymbol{\zeta}, s)\, ds + \int_{t^k}^{t^{k+1}} \mathbf{B}(\boldsymbol{\zeta}, s) \cdot d\mathbf{W}. \tag{3.8}$$

The most straightforward approach to solve this equation numerically, is by using the EM scheme, that is,

$$\boldsymbol{\zeta}^{k+1} = \boldsymbol{\zeta}^k + \mathbf{A}\left(\boldsymbol{\zeta}^k\right)\Delta t^k + \mathbf{B}\left(\boldsymbol{\zeta}^k\right) \cdot \Delta\mathbf{W}^k, \tag{3.9}$$

where $\Delta t^k = t^{k+1} - t^k$ is the numerical time step, and $\Delta\mathbf{W}^k$ is a vector of increments of Wiener processes, which are per definition Gaussian distributed with zero mean and variance Δt^k, i.e., $\Delta W_i^k \sim \mathcal{N}(0, \Delta t^k)$. Note that the EM method is in accordance with the Itô interpretation of the stochastic integral. Furthermore, for numerical purposes it is more natural to formulate the EM method as

$$\boldsymbol{\zeta}^{k+1} = \boldsymbol{\zeta}^k + \mathbf{A}\left(\boldsymbol{\zeta}^k\right)\Delta t^k + \sqrt{\Delta t^k}\mathbf{B}\left(\boldsymbol{\zeta}^k\right) \cdot \boldsymbol{\Lambda}^k, \tag{3.10}$$

where $\Lambda_i^k \sim \mathcal{N}(0,1)$. By using the prescribed initial state[3], $\boldsymbol{\zeta}^0$, and consequentially applying formula (3.10) for $k = 1 \ldots K$, an approximate solution to the SDE is found on the entire time grid $\{0, t^1, \ldots, t^K\}$.

Since the Λ_i^k are random numbers, each time the EM method is applied to integrate the SDE, a different solution is obtained. Hence, integrating the SDE N times gives a set of N different solutions $\{\boldsymbol{\zeta}_1, \boldsymbol{\zeta}_2, \ldots, \boldsymbol{\zeta}_N\}$. If N is large enough, it becomes eventually possible to derive the distribution function of the stochastic vector $\boldsymbol{\zeta}$, by sampling the obtained solutions in an n-dimensional histogram[4]. How this is done in practice will be discussed in detail in Section 3.2.6.

In contrast to deterministic methods, the stochastic nature of SDEs implies that it is only possible to make statistical statements about the convergence properties of numerical integration schemes. Many non-equivalent definitions for the convergence of a sequence of random variables exist and depending on the aim of the application a different convergence criterion is important. For our goals, i.e., solving the FTE numerically, a relevant criterion is the *weak convergence*. To define this notion precisely, the *weak error* needs to be introduced:

$$e_{\Delta t}^{\text{weak}} = \sup_{0 \leq t^k \leq T} \left| \left\langle \psi \left[\boldsymbol{\zeta}^k \right] \right\rangle - \left\langle \psi \left[\boldsymbol{\zeta}(t = t^k) \right] \right\rangle \right|, \tag{3.11}$$

where $\boldsymbol{\zeta}(t = t^k)$ represents an exact solution of the SDEs at time t^k, the operator $\langle \cdot \rangle$ denotes the expectation value, and ψ can be any function in an appropriate function class. The weak error $e_{\Delta t}^{\text{weak}}$ gives thus the error in the expectation of a certain function ψ. It can be shown that for the EM method, $e_{\Delta t}^{\text{weak}} \propto \Delta t$, such that the EM method is said to have a weak convergence of order one (Kloeden & Platen, 1992).

A related but different notion of convergence is the *strong convergence*. Given an exact solution $\boldsymbol{\zeta}(t)$ with a completely specified associated Wiener process $\mathbf{W}(t)$, the strong convergence quantifies how well a single numerical solution $\boldsymbol{\zeta}^k$ approximates the exact solution $\boldsymbol{\zeta}(t)$. In that case, $d\mathbf{W}^k$ in Eq. (3.10) needs to be obtained from the given Wiener process $\mathbf{W}(t)$. It can be shown that the EM method has a strong convergence of order $\sqrt{\Delta t}$. However, in many applications one is interested in functions of an ensemble of generated stochastic solutions and not in the individual trajectories themselves. For example, upon using Itô calculus to solve the FTE, the associated individual trajectories $\boldsymbol{\zeta}(t)$ have only a limited physical significance (see discussion in Section 3.2.4). Hence, the relevant notion of convergence is the weak and not the strong convergence.

The EM method can be regarded as a straightforward generalisation of the Euler method for ordinary differential equations (ODEs). Similar to ODE, there exist numerical

[3] If a time-backward SDE is solved, it is more appropriate to speak about the final state, denoted by $\boldsymbol{\zeta}_T$. However, in terms of the backward time coordinate s, as defined below Eq. (3.6), it can also be regarded as the initial condition and hence no distinction will be made between $\boldsymbol{\zeta}_0$ and $\boldsymbol{\zeta}_T$.

[4] We recall that $\boldsymbol{\zeta}$ is an n-dimensional vector.

methods that have a higher order of weak and/or strong convergence than the EM method. Examples include the Milstein scheme and the order 2.0 weak/strong Taylor scheme (see Kloeden & Platen, 1992, and references therein). However, the higher order schemes increase quickly in complexity, requiring the computation of additional terms that involve the derivatives of the A and B functions, as well as multiple independent random numbers. These terms can be computationally expensive to compute such that the higher order schemes are not necessarily more efficient than the EM method. In this work, we will therefore only consider the EM method and we refer to Wawrzynczak et al. (2015) and Van den Berg (2019) for a discussion and comparison of higher order integration schemes applied in the context of energetic particle transport in the heliosphere.

Finally, it can be shown that a one-step stochastic scheme like the EM method is unconditionally stable if the functions $\mathsf{A}(\boldsymbol{\zeta}, t)$ and $\mathsf{B}(\boldsymbol{\zeta}, t)$ are sufficiently regular and smooth functions (Kloeden & Platen, 1992). Sufficient conditions include that $\mathsf{A}(\boldsymbol{\zeta}, t)$ and $\mathsf{B}(\boldsymbol{\zeta}, t)$ are, for all times $t \in [0, T]$, Lipschitz continuous in the $\boldsymbol{\zeta}$ coordinate and linearly bounded in growth, that is, $\sim O(\zeta_i)$ for $\zeta_i \to \infty$. We refer to Kloeden & Platen (1992) for an extensive introduction and overview of the many numerical recipes of stochastic calculus.

3.2.3 The FTE as a set of forward or backward SDEs

In Chapter 2 it was illustrated how the FTE can be formulated either as a KBE (see Eq. (2.82)) or as a KFE (see Eq. (2.83)), under the assumption that the effect of the turbulence on the energetic particle population is diffusive (e.g., Eq. (2.119)). To make these versions of the FTE fully comparable to Eqs. (3.4) and (3.7), the diffusion terms in the FTE need to be rewritten. By doing so for Eq. (2.82), the following KBE is obtained

$$\frac{\partial \mathscr{F}}{\partial t} + \frac{d\mathbf{x}}{dt} \cdot \nabla \mathscr{F} + \frac{d\mu}{dt}\frac{\partial \mathscr{F}}{\partial \mu} + \frac{dp}{dt}\frac{\partial \mathscr{F}}{\partial p} = \mathbf{D}_{\perp} : \nabla\nabla \mathscr{F} + D_{\mu\mu}\frac{\partial^2 \mathscr{F}}{\partial \mu^2}, \tag{3.12}$$

with

$$\frac{d\mathbf{x}}{dt} = \mathbf{U} + \left(1 - \frac{\mu v \mathbf{U}\cdot\mathbf{b}}{c^2}\right)(\mu v\mathbf{b} + \mathbf{V}_d) + \nabla\cdot\mathbf{D}_\perp, \tag{3.13}$$

$$\frac{d\mu}{dt} = \frac{1-\mu^2}{2}\left[\frac{v\mathbf{U}}{c^2}\cdot\frac{\partial\mathbf{b}}{\partial t} + v\left(1 - \frac{\mu v\mathbf{U}\cdot\mathbf{b}}{c^2}\right)\nabla\cdot\mathbf{b} + \mu\nabla\cdot\mathbf{U} - 3\mu\mathbf{bb}:\nabla\mathbf{U} - \frac{2}{v}\mathbf{b}\cdot\frac{d\mathbf{U}}{dt}\right] + \frac{\partial D_{\mu\mu}}{\partial\mu}, \tag{3.14}$$

$$\frac{dp}{dt} = \left(\frac{1-3\mu^2}{2}\mathbf{bb}:\nabla\mathbf{U} - \frac{1-\mu^2}{2}\nabla\cdot\mathbf{U} - \frac{\mu}{v}\mathbf{b}\cdot\frac{d\mathbf{U}}{dt}\right)p. \tag{3.15}$$

where the dyadic product $\nabla\nabla$ equals the Hessian operator. Following the discussion in Section 2.10, only the pitch-angle diffusion and the cross-field diffusion are assumed to be non-zero. However, it is straightforward to include the other diffusion processes in these equations.

By comparing Eq. (3.12) with (3.7), it can be seen that $\mathscr{F}$ is proportional to the conditional probability density of the stochastic vector $\boldsymbol{\zeta} = (\mathbf{x}, \mu, p)^T$, which satisfies the following set of backward SDEs:

$$d\mathbf{x} = -\frac{d\mathbf{x}}{dt}dt + \mathbf{B}\cdot d\mathbf{W}_\mathbf{x}, \tag{3.16}$$

$$d\mu = -\frac{d\mu}{dt}dt + \sqrt{2D_{\mu\mu}}dW_\mu, \tag{3.17}$$

$$dp = -\frac{dp}{dt}dt, \tag{3.18}$$

where $\mathbf{W}_\mathbf{x}$ and W_μ are, respectively, three- and one-dimensional Wiener processes and $\mathbf{B}$ is a 3×3 matrix that satisfies $\mathbf{BB}^T = 2\mathbf{D}_\perp$. Moreover, t should be identified with the backward time coordinate s in Eqs. (3.16) – (3.18).

Likewise, Eq. (2.83) can be formulated in the same format as Eq. (3.4), giving the following KFE

$$\frac{\partial\mathcal{J}}{\partial t} + \nabla\cdot\left(\frac{d\mathbf{x}}{dt}\mathcal{J}\right) + \frac{\partial}{\partial\mu}\left(\frac{d\mu}{dt}\mathcal{J}\right) + \frac{\partial}{\partial p}\left(\frac{dp}{dt}\mathcal{J}\right) = \nabla\nabla:(\mathbf{D}_\perp\mathcal{J}) + \frac{\partial^2}{\partial\mu^2}\left(D_{\mu\mu}\mathcal{J}\right), \tag{3.19}$$

with $d\mathbf{x}/dt$, $d\mu/dt$, and, dp/dt given by Eqs. (3.13) – (3.15), respectively. In this case, it can be seen by comparing Eq. (3.12) with (3.7) that $\mathcal{J}$ is proportional to the conditional probability density of the stochastic vector $\boldsymbol{\zeta} = (\mathbf{x}, \mu, p)^T$, which satisfies the following

set of forward SDEs

$$d\mathbf{x} = \frac{d\mathbf{x}}{dt}dt + \mathbf{B} \cdot d\mathbf{W}_{\mathbf{x}}, \tag{3.20}$$

$$d\mu = \frac{d\mu}{dt}dt + \sqrt{2D_{\mu\mu}}dW_{\mu}, \tag{3.21}$$

$$dp = \frac{dp}{dt}dt, \tag{3.22}$$

where $\mathbf{W}_{\mathbf{x}}$, W_{μ}, and $\mathbf{B}$ have the same meaning as in Eqs. (3.16) – (3.18). However, in contrast to the latter equations, t is the forward running time coordinate in Eqs. (3.16) – (3.18).

To solve the FTE, the SDEs (3.20) – (3.22) or (3.16) – (3.18) have to be integrated repeatedly forward or backward in time, respectively. Each time an integration is performed, a five-dimensional (5D) trajectory $\boldsymbol{\zeta}(t)$ in phase space is obtained. These trajectories are typically referred to as the trajectories of *quasi-particles* or *pseudo-particles*. In the next section, it will be shown that these trajectories do not represent real particle trajectories nor do they represent the GC trajectories (see also Kopp et al., 2012; Strauss & Effenberger, 2017, for a discussion).

By sampling many pseudo-particles, their corresponding distribution functions can be obtained. The precise way this is done and how the initial and boundary conditions are taken into account is explained in sections 3.2.5 and 3.2.6. In the following, we limit ourselves to discussing the forward integration method, as this is the method that is used in the next chapters to study energetic particles in the heliosphere. For an in-depth discussion on the backwards integration method, we refer to Strauss & Effenberger (2017).

3.2.4 Pseudo-particles

A trajectory $\boldsymbol{\zeta}(t) = [\mathbf{x}(t), \mu(t), p(t)]^T$ of a pseudo-particle, obtained by integrating SDEs (3.20) – (3.22), should not be confused with the trajectory of a real particle or its GC through phase space. This can be understood by realising that the phase space trajectory of a real particle satisfies Eqs. (2.63), (2.67), (2.71), and (2.77), which are the Newton-Lorentz equations expressed in mixed coordinates. Even the non-stochastic part of the SDEs, i.e., Eqs. (3.13) – (3.15), are not equivalent to the Lorentz-Newton equation in the average background electromagnetic field, since they contain the additional terms $\partial D_{\mu\mu}/\partial\mu$ and $\nabla \cdot \mathbf{D}_{\perp}$, which do not appear in Eqs. (2.64) and (2.72). The pseudo-particle trajectories can thus also not be regarded as the particle or GC trajectories in the average background magnetic field with super-imposed Brownian noise. Only in the trivial

case when there is no turbulence and hence no diffusion, the SDEs reduce to a set of ODEs which describe the particle's equation of motion.

In Strauss & Effenberger (2017) it is argued that, if no sources or sinks are present in the FTE, a single pseudo-particle can be regarded as an ensemble of real particles. Therefore, a more appropriate name for a pseudo-particle would be *a phase space density element*. This can be understood by realising that the distribution function of the pseudo-particles remains constant along their trajectories through phase space, which can be regarded as a generalization of Liouville's theorem in the presence of collisions.

3.2.5 Injecting the pseudo-particles

In order to solve the FTE as formulated in Eq. (3.19), the differential intensity $\mathcal{J}_b$ at the boundaries of the domain and the initial differential intensity $\mathcal{J}_i$ need to be specified. When using the forward SDE integration method, the pseudo-particles are injected according to these initial and boundary conditions, since the differential intensity is proportional to the distributions of the pseudo-particles (see Section 3.2.3). How this is done in practice is illustrated below with some example cases encountered in heliophysics.

Injection from a boundary

During an impulsive solar eruptive event, SEPs are accelerated to high energies in the solar corona, after which they escape into the heliosphere. If we aim at modelling only the transport of these SEPs in interplanetary space, the inner boundary of the computational domain can be chosen as a spherical shell with a large enough radius such that it encapsulates the corona. The outer boundary of the computational domain can be chosen as a spherical shell several AUs away from the inner boundary, such that it has no influence on the simulations. In such a setting, the SEPs that enter the heliosphere after being accelerated in the corona will translate into a time dependent differential intensity at the inner boundary of the computational domain. Since the production of SEPs in the corona occurs only during a limited amount of time and in a limited region, $\mathcal{J}_b$ will only be non-zero for a limited time range and a limited portion of the inner boundary. Furthermore, if the heliosphere is assumed to be depleted of SEPs at the start of the simulation, the initial condition is zero everywhere, i.e., $\mathcal{J}_i \equiv 0$.

To solve the FTE using the time-forward SDE method, the pseudo-particles need to be injected according to the differential intensity $\mathcal{J}_b$. This is because, as explained in Section 3.2.3, the differential intensity $\mathcal{J}$ is proportional to the density distribution of

the pseudo-particles. Generating a sample of pseudo-particles from $\mathcal{J}_b(\mathbf{x}, \mu, p, t)$ can be done in different ways:

- *Method 1:* The injection time t_i as well as the initial values $(\mathbf{x}_i, \mu_i, p_i)$ of each of the pseudo particles are determined by an inversion or a rejection sampling from the normalised $\mathcal{J}_b$ function. Each pseudo-particle gets a statistical weight $\alpha = 1/N$, with N denoting the total number of injected pseudo-particles.
- *Method 2:* The injection time t_i as well as the initial values $(\mathbf{x}_i, \mu_i, p_i)$ are generated from a uniform distribution, and each particle gets a statistical weight $\alpha = \mathcal{J}_b(\mathbf{x}_i, p_i, t_i)/N$. This weight is taken into account when sampling the pseudo-particles (see Eq. (3.24)).
- *Method 1+2:* If $\mathcal{J}_b(\mathbf{x}_i, p_i, t_i)$ consists of a product of functions that have no common variables, then any of both previous methods can be used for the separate functions. For example, if $\mathcal{J}_b(\mathbf{x}_i, p_i, t_i) = h(p_i)k(\mathbf{x}_i, \mu_i)g(t_i)$, then the p_i values can be generated e.g., by a rejection sampling from the normalised $f(p)$ function, whereas the injection time t_i as well as the initial values $\mathbf{x}_i$ and μ_i can e.g., be generated from a uniform distribution, and each pseudo-particle receives a statistical weight $\alpha = k(\mathbf{x}_i, \mu_i)g(t_i)/N$.

Method 2 can be useful to generate the p_i values of the pseudo-particles. This is because the energy dependence of the injection function is often assumed to be a power law that can span one or two orders of magnitude. Consequently, if method 1 is applied to generate the initial momentum coordinate, almost all the pseudo-particles will have a p_i at the low end of the spectrum and only very few will have a p_i at the high end of the spectrum. When sampling the pseudo-particles to obtain $\mathcal{J}$ (see Section 3.2.6), this will translate into a small statistical error at low energies but a large statistical error at high energies. To increase the statistics at high energies, more pseudo-particles can be injected, yet these will also mostly improve the statistics at low energies even further. Hence, a lot of computational effort needs to be wasted to get reasonable statistics at high energies. In contrast, with method 2, all energies have the same statistical weight upon injection, such that the computational effort is equally distributed.

In contrast to the momentum value p_i, it may often be better to use method 1 to generate the pseudo-particles' injection times t_i, as explained in the following. The time profile of an impulsive event typically consists of a rapid increase of several orders of magnitude followed by an exponential decrease at later times. The pitch-angle scattering of particles in the heliosphere will eventually result in a diffusive motion of the particles along the magnetic field lines. By the time that the pseudo-particles originating from the exponential decay phase are injected, the pseudo-particles injected around the time of the intensity peak will have spread diffusively along the field line. The contribution of the former pseudo-particles to the overall pseudo-particle

distribution will therefore be negligible compared to the contribution of the latter. In other words, the diffusive motion of the pseudo-particles eventually erases the time injection history. Therefore, it is unnecessary to use method 2 to get better statistics for the pseudo-particles injected at later times, since their contribution to $\mathcal{J}$ is negligible anywhere in space. We note that the above argument only holds if the particles' mean free path is not too large. More precisely, the scattering time scale $\lambda_{\parallel}/v$ should be significantly small compared to the characteristic time scale of $\mathcal{J}_b$.

Finally, CRs can be modelled by using a similar set-up as the one discussed above for impulsive SEP events. In the case of CRs, the pseudo-particles are injected at the outer boundary instead of the inner boundary. The outer boundary can e.g., be placed at the heliopause in which case the energy dependence of $\mathcal{J}_b$ is given by the local interstellar spectrum (see e.g., Strauss et al., 2013).

Injection from an initial distribution

In the previous section, it was discussed how the FTE can be solved for time dependent boundary conditions in a computational domain that is initially depleted of energetic particles. Similarly, one can envision a problem where the intensity at the boundaries is zero, i.e., $\mathcal{J}_b = 0$, but an initial non-zero differential intensity $\mathcal{J}_i$ is provided inside the computational domain, e.g., describing the suprathermal tail of the solar wind. In that case, the pseudo-particles have to be sampled from the normalised $\mathcal{J}_i$, which can be done with the same methods that were discussed in previous section, with the difference that $t_i = 0$ for all pseudo particles. Furthermore, the situation where both $\mathcal{J}_i \neq 0$ and $\mathcal{J}_b \neq 0$ is a straightforward generalization of the previous two cases.

3.2.6 Sampling the differential intensity $\mathcal{J}$

In Sections 3.2.3 it was explained that the differential intensity $\mathcal{J}$ can be considered proportional to the distribution density of the pseudo-particles that satisfy Eqs. (3.20)–(3.20). Hence, one can write

$$\mathcal{J} \propto \frac{dN_{\mathrm{pp}}}{d\mu dp d\mathbf{x}}, \tag{3.23}$$

where dN_{pp} is the number of weighted pseudo-particles in the infinitesimal $d\mu dp d\mathbf{x}$ on time t. The term "weighted" means that every particle contributes only its statistical weight to dN_{pp}, that is,

$$dN_{\mathrm{pp}} = \sum_k \alpha_k, \tag{3.24}$$

where the summation runs over the pseudo-particles located in the infinitesimal $d\mu dp d\mathbf{x}$.

In practice, the infinitesimal $d\mu dp d\mathbf{x}$ will be replaced by a 5D sampling box $\Delta\mu\Delta p\Delta\mathbf{x}$, and the pseudo-particles will be counted during a binning time step Δt (see Section 3.3). The differential intensity $\mathcal{J}$ is thus estimated by sampling the pseudo-particles in a 5D histogram. Evidently, the more pseudo-particles are integrated, the better this sampling distribution will converge to the real solution.

Finally, an important simplification occurs if the background plasma is stationary, since the differential intensity can then be obtained from a convolution of the Green's function with the boundary and the initial conditions (Webb & Gleeson, 1977). This Green function is the sampling distribution obtained after a delta injection of the pseudo-particles in phase space.

3.3 The PARADISE model

In this section, we introduce a new model named PARADISE, which solves the FTE by integrating the equivalent set of Itô SDEs forward in time for many pseudo-particles. PARADISE is written in C++ and uses the Message Passing Interface (MPI), to distribute the pseudo-particles over different threads. This is straightforward since the different pseudo-particles behave as test-particles, that is, they do not interact with each other, such that the SDE method represents an embarrassingly parallel problem. The discussion provided in this section is partly adapted from sections 2 and 3 of Wijsen et al. (2019a).

3.3.1 The SDEs in spherical coordinates

PARADISE solves the FTE using spherical coordinates for the spatial coordinate. By denoting the spherical coordinates with (r, ϑ, φ), the corresponding FTE can be written as a KFE as follows

$$\begin{aligned}
&\frac{\partial\tilde{\mathcal{J}}}{\partial t} + \frac{\partial}{\partial r}\left(\frac{dr}{dt}\tilde{\mathcal{J}}\right) + \frac{\partial}{\partial \vartheta}\left(\frac{d\vartheta}{dt}\tilde{\mathcal{J}}\right) + \frac{\partial}{\partial \varphi}\left(\frac{d\varphi}{dt}\tilde{\mathcal{J}}\right) \frac{\partial}{\partial \mu}\left(\frac{d\mu}{dt}\tilde{\mathcal{J}}\right) + \frac{\partial}{\partial p}\left(\frac{dp}{dt}\tilde{\mathcal{J}}\right) \\
&\quad = \frac{\partial^2}{\partial r^2}\left(D^{\perp}_{rr}\tilde{\mathcal{J}}\right) + \frac{\partial^2}{\partial \vartheta^2}\left(\frac{D^{\perp}_{\vartheta\vartheta}}{r^2}\tilde{\mathcal{J}}\right) + \frac{\partial^2}{\partial \varphi^2}\left(\frac{D^{\perp}_{\varphi\varphi}}{r^2\sin^2\vartheta}\tilde{\mathcal{J}}\right) \\
&\quad + \frac{\partial^2}{\partial r\partial \vartheta}\left(\frac{D^{\perp}_{r\vartheta} + D^{\perp}_{\vartheta r}}{r}\tilde{\mathcal{J}}\right) + \frac{\partial^2}{\partial r\partial \varphi}\left(\frac{D^{\perp}_{r\varphi} + D^{\perp}_{\varphi r}}{r\sin\vartheta}\tilde{\mathcal{J}}\right) + \frac{\partial^2}{\partial \vartheta\partial \varphi}\left(\frac{D^{\perp}_{\vartheta\varphi} + D^{\perp}_{\varphi\vartheta}}{r^2\sin\vartheta}\tilde{\mathcal{J}}\right) \\
&\quad + \frac{\partial^2}{\partial \mu^2}\left(D_{\mu\mu}\tilde{\mathcal{J}}\right),
\end{aligned} \tag{3.25}$$

with $\tilde{\mathcal{J}} = r^2 \sin\vartheta \mathcal{J}$ and

$$\frac{dr}{dt} = \left[U_r + \chi\left(\mu v b_r + V_{d,r}\right) + \frac{1}{r^2}\frac{\partial r^2 D^{\perp}_{rr}}{\partial r} + \frac{1}{r\sin\vartheta}\left(\frac{\partial}{\partial\vartheta}\left(\sin\vartheta D^{\perp}_{r\vartheta}\right) + \frac{\partial D^{\perp}_{r\varphi}}{\partial\varphi}\right)\right], \quad (3.26)$$

$$\frac{d\vartheta}{dt} = \frac{1}{r}\left[U_\vartheta + \chi\left(\mu v b_\vartheta + V_{d,\vartheta}\right) + \frac{1}{r}\frac{\partial r D^{\perp}_{\vartheta r}}{\partial r} + \frac{1}{r\sin\vartheta}\left(\frac{\partial}{\partial\vartheta}\left(\sin\vartheta D^{\perp}_{\vartheta\vartheta}\right) + \frac{\partial D^{\perp}_{\vartheta\varphi}}{\partial\varphi}\right)\right], \quad (3.27)$$

$$\frac{d\varphi}{dt} = \frac{1}{r\sin\vartheta}\left[U_\varphi + \chi\left(\mu v b_\vartheta + V_{d,\varphi}\right) + \frac{1}{r}\left(\frac{\partial r D^{\perp}_{\varphi r}}{\partial r} + \frac{\partial D^{\perp}_{\varphi\vartheta}}{\partial\vartheta} + \frac{1}{\sin\vartheta}\frac{\partial D^{\perp}_{\varphi\varphi}}{\partial\varphi}\right)\right], \quad (3.28)$$

where $\chi = (1 - \mathbf{b}\cdot\mathbf{U}/c^2)$. The equations for $d\mu/dt$ and dp/dt are given by Eqs. (3.14) and (3.15), respectively. Using the EM method, PARADISE integrates the SDEs forward in time, that is,

$$r^{k+1} = r^k + \left.\frac{dr}{dt}\right|_{t=t^k}\Delta t^k + \Delta r^{k+1}_{\perp}, \quad (3.29)$$

$$\vartheta^{k+1} = \vartheta^k + \left.\frac{d\vartheta}{dt}\right|_{t=t^k}\Delta t^k + \Delta \vartheta^{k+1}_{\perp}, \quad (3.30)$$

$$\varphi^{k+1} = \varphi^k + \left.\frac{d\varphi}{dt}\right|_{t=t^k}\Delta t + \Delta \varphi^{k+1}_{\perp}, \quad (3.31)$$

$$\mu^{k+1} = \mu^k + \frac{d\mu}{dt}|_{t=t^k}\Delta t^k + \sqrt{2D_{\mu\mu}\Delta t^k}\Lambda^k_\mu \quad (3.32)$$

$$p^{k+1} = p^k + \left.\frac{dp}{dt}\right|_{t=t^k}\Delta t^k, \quad (3.33)$$

where Λ^k_μ is a random number drawn from a standard normal distribution. In PARADISE, these random numbers are generated using the Mersenne Twister pseudo-random number generator (Matsumoto & Nishimura, 1998), which is included in the Boost C++ library[5]. The quantities $\Delta r^{k+1}_{\perp}$, $\Delta\vartheta^{k+1}_{\perp}$, and $\Delta\varphi^{k+1}_{\perp}$ account for the stochastic variations associated with the cross-field diffusion and are given in the next section. Furthermore, as explained in Section 3.3.8, PARADISE has an alternative method to compute μ^{k+1}.

[5] www.boost.org

3.3.2 Cross-field diffusion

The most straightforward manner to prescribe $\Delta r_\perp^{k+1}$, $\Delta\vartheta_\perp^{k+1}$, and $\Delta\varphi_\perp^{k+1}$ would be by using the standard SDE approach, that is,

$$\Delta r_\perp^{k+1} = \left[\mathsf{B}\cdot\mathbf{\Lambda}^k\right]_r \sqrt{\Delta t^k}, \tag{3.34}$$

$$\Delta\vartheta_\perp^{k+1} = \left[\mathsf{B}\cdot\mathbf{\Lambda}^k\right]_\vartheta \sqrt{\Delta t^k}, \tag{3.35}$$

$$\Delta\varphi_\perp^{k+1} = \left[\mathsf{B}\cdot\mathbf{\Lambda}^k\right]_\varphi \sqrt{\Delta t^k}, \tag{3.36}$$

where the vector $\mathbf{\Lambda}$ consists of three standard normal distributed random variables and B satisfies

$$\mathsf{B}\mathsf{B}^T = 2\begin{pmatrix} D_{rr}^\perp & \frac{D_{r\vartheta}^\perp}{r} & \frac{D_{r\varphi}^\perp}{r\sin\vartheta} \\ \frac{D_{r\vartheta}^\perp}{r} & \frac{D_{\vartheta\vartheta}^\perp}{r^2} & \frac{D_{\vartheta\varphi}^\perp}{r^2\sin\vartheta} \\ \frac{D_{r\varphi}^\perp}{r\sin\vartheta} & \frac{D_{\vartheta\varphi}^\perp}{r^2\sin\vartheta} & \frac{D_{\varphi\varphi}^\perp}{r^2\sin^2\vartheta} \end{pmatrix}, \tag{3.37}$$

where it was assumed here that $D_{r\vartheta} = D_{\vartheta r}$, $D_{r\varphi} = D_{\varphi r}$, and $D_{\vartheta\varphi} = D_{\varphi\vartheta}$, which is valid for axisymmetric turbulence. However, finding a matrix B that satisfies Eq. (3.37) can be challenging. One of the reasons is that the cross-field diffusion tensor is only positive semi-definite instead of positive definite[6]. This can be easily seen by expressing the cross-field diffusion tensor in an orthonormal basis of the form $\{\tilde{\mathbf{e}}_x, \tilde{\mathbf{e}}_y, \mathbf{b}\}$:

$$\mathbf{D}_\perp = D_\perp(\mathbb{I} - \mathbf{bb}) = \begin{pmatrix} D_\perp & 0 & 0 \\ 0 & D_\perp & 0 \\ 0 & 0 & 0 \end{pmatrix}, \tag{3.38}$$

where $D_\perp$ is the perpendicular diffusion coefficient, $\mathbb{I}$ is the identity matrix, and $\mathbf{bb}$ is the dyadic product of the unit magnetic field vector. Equation (3.38) illustrates that $\mathbf{D}_\perp$ is only a positive semi-definite matrix because there is no spatial diffusion along the magnetic field line, that is, $D_{33} = D_\parallel = 0$.

Using the reference triad $\{\tilde{\mathbf{e}}_x, \tilde{\mathbf{e}}_y, \mathbf{b}\}$, an evident choice for the volatile matrix B is

$$\mathsf{B} = \begin{pmatrix} \sqrt{2D_\perp} & 0 & 0 \\ 0 & \sqrt{2D_\perp} & 0 \\ 0 & 0 & 0 \end{pmatrix}. \tag{3.39}$$

Denoting with $\tilde{x}, \tilde{y}$, and $\tilde{z}$ the Cartesian coordinates of a pseudo-particle in an inertial reference frame which has its axis aligned with $\{\tilde{\mathbf{e}}_x, \tilde{\mathbf{e}}_y, \mathbf{b}\}$, the stochastic part of the EM

[6] For a positive definite matrix, one can use the Cholesky decomposition to directly obtain a B.

scheme can be formulated as

$$\Delta\tilde{x}_\perp^{k+1} := \tilde{x}_\perp^{k+1} - \tilde{x}^k = \sqrt{2D_\perp \Delta t}\Lambda_{\tilde{x}}, \tag{3.40}$$

$$\Delta\tilde{y}_\perp^{k+1} := \tilde{y}_\perp^{k+1} - \tilde{y}^k = \sqrt{2D_\perp \Delta t}\Lambda_{\tilde{y}}, \tag{3.41}$$

$$\Delta\tilde{z}_\perp^{k+1} := \tilde{z}_\perp^{k+1} - \tilde{z}^k = 0, \tag{3.42}$$

where $\Lambda_i \sim \mathcal{N}(0,1)$. Expressing the displacement vector $\Delta\tilde{\mathbf{x}}_\perp^{k+1}$ in the Cartesian frame associated with the spherical coordinate system used by PARADISE gives

$$\Delta\mathbf{x}_\perp^{k+1} = R\Delta\tilde{\mathbf{x}}_\perp^{k+1}, \tag{3.43}$$

where the matrix R can be obtained using Rodrigues' rotation formula, which gives

$$R = \begin{pmatrix} 1 - b_x^2(1-b_z)/(b_x^2+b_y^2) & -b_x b_y(1-b_z)/(b_x^2+b_y^2) & b_x \\ -b_x b_y(1-b_z)/(b_x^2+b_y^2) & 1 - b_y^2(1-b_z)/(b_x^2+b_y^2) & b_y \\ -b_x & -b_y & b_z \end{pmatrix}. \tag{3.44}$$

This matrix describes the rotation of the Cartesian coordinate frame $\{\tilde{\mathbf{e}}_x, \tilde{\mathbf{e}}_y, \mathbf{b}\}$ over an angle $\arccos(b_z)$ and with the axis of rotation along $(b_y, -b_x, 0)^T$. In these expressions, the magnetic unit vector $\mathbf{b}$ is expressed in the Cartesian frame $\{\mathbf{e}_x, \mathbf{e}_y, \mathbf{e}_z\}$. By denoting with $\mathbf{x}^k$ the pseudo-particle's position vector in the Cartesian frame, we can define $\mathbf{x}_\perp^{k+1} := \mathbf{x}^k + \Delta\mathbf{x}_\perp^{k+1}$. If we now express $\mathbf{x}_\perp^{k+1}$ in spherical coordinates $(r_\perp^{k+1}, \vartheta_\perp^{k+1}, \varphi_\perp^{k+1})$, we find

$$\Delta r_\perp^{k+1} := r_\perp^{k+1} - r^k, \tag{3.45}$$

$$\Delta\vartheta_\perp^{k+1} := \vartheta_\perp^{k+1} - \vartheta^k, \tag{3.46}$$

$$\Delta\varphi_\perp^{k+1} := \varphi_\perp^{k+1} - \varphi^k, \tag{3.47}$$

which can be substituted into Eqs. (3.29) – (3.31).

3.3.3 The time step

PARADISE utilises an adaptive time step Δt^k when integrating the pseudo-particles forward in time. The time step is chosen such that the first and second moment of the SDE are limited by the characteristic scales of the system (Strauss & Effenberger, 2017). To do so, we introduce the variable s which satisfies

$$ds = dt\sqrt{\left(\frac{dr}{dt}\right)^2 + \left(r\frac{d\vartheta}{dt}\right)^2 + \left(r\sin\vartheta\frac{d\varphi}{dt}\right)^2},$$

where the time derivatives are given by Eqs. (3.26) – (3.28). The time step is then calculated as

$$\Delta t^k = \min\left\{\frac{s_0}{ds/dt}, \frac{\mu_0}{|d\mu/dt|}, \frac{p_0}{|dp/dt|}, \frac{\mu_0^2}{2D_{\mu\mu}}, \frac{s_0^2}{2D^{\perp}},\right\}, \tag{3.48}$$

with $d\mu/dt$ and dp/dt given by Eqs. (3.14) and (3.15), respectively. The time-derivatives and the diffusion coefficients appearing in Eq. (3.48) are evaluated at time t^k. The quantities s_0, μ_0 and p_0 are the characteristic scales of the corresponding variables that need to be resolved. These scales can be chosen as a fraction of the sampling box (see below), or they can be related to a typical scale derived from the background plasma.

3.3.4 Injecting the pseudo-particles

In PARADISE, pseudo-particles can be injected into the computational domain according to any of the methods given in Section 3.2.5. A pseudo-particle's initial state $(r_i, \vartheta_i, \varphi_i, \mu_i, p_i)$ and injection time t_i can thus directly be sampled from the given injection function, or can be sampled from a uniform distribution upon which the injection function attributes a statistical weight α_i to the pseudo particle. Depending on the form of the injection distribution, combinations of these two methods are also possible. Moreover, in PARADISE the injection distributions are handled in a modular fashion in separate files, such that one can easily add new functions.

3.3.5 Boundary conditions

When one of the phase space coordinates of a pseudo-particle reaches a boundary of the computational domain, the corresponding boundary conditions have to be taken into account. For the spatial domain, PARADISE can accommodate for reflecting, absorbing and periodic boundary conditions. In Strauss & Effenberger (2017), it is explained how these boundary conditions are handled with SDEs. When the pseudo-particle reaches an absorbing boundary, the pseudo-particle leaves the computational domain and is no longer propagated any further. With periodic boundary conditions, the pseudo-particle re-appears in the computational domain at the other side of the periodic boundary. The azimuthal coordinate $\varphi \in [0, 2\pi[$ is treated as such. When the pseudo-particle reaches a reflective boundary, the pseudo-particle gets reflected similar to how a hard sphere reflects off a planar surface. For example, when a pseudo-particle crosses a reflective inner boundary located at a radial coordinate R_i, its radial and μ coordinate are changed as

$$r \mapsto 2R_i - r \quad \text{and} \quad \mu \mapsto -\mu. \tag{3.49}$$

Finally, since μ is the cosine of the pitch-angle, its value is restricted to the interval $[-1, 1]$. If Eq. (3.32) produces a $|\mu^{k+1}| > 1$, then a reflective boundary condition[7] is assumed to ensure $\mu^{k+1} \in [-1, 1]$.

3.3.6 Sampling the pseudo-particles

To obtain the differential intensity, the pseudo particles are sampled in a 5D histogram. For a certain point $(r, \vartheta, \varphi, \mu, E)$ in phase space, the corresponding bins of the histogram are defined as $[r - \Delta/2, r + \Delta/2] \times [\vartheta - \Delta\vartheta/2, \vartheta + \Delta\vartheta/2] \times [\varphi - \Delta\varphi/2, \varphi + \Delta\varphi/2] \times [\mu - \Delta\mu/2, \mu + \Delta\mu/2] \times [E - \Delta E/2, E + \Delta E/2]$, where E represents the kinetic energy. To improve the sampling statistics, we average over a fixed time interval $[t^k - \Delta t/2, t^k + \Delta t/2]$, where $\Delta t = \sum_{i=0}^{n} \Delta t^k$, for a certain integer n. Hence, the differential intensity, $\mathcal{J}$, is computed as follows[8]

$$\begin{aligned}\mathcal{J}(r, \vartheta, \varphi, E, \mu, t^k) &= \frac{\tilde{\mathcal{J}}(r, \vartheta, \varphi, \mu, E, t^k)}{r^2 \sin\vartheta} \\ &\approx \frac{1}{\Delta t} \int_{t^k - \Delta t/2}^{t^k + \Delta t/2} \frac{dN^i_{pp}}{2\pi r^2 \sin\vartheta dr d\vartheta d\varphi d\mu dE/v} dt \\ &\approx \frac{1}{\Delta t} \sum_{i=0}^{n} \frac{vN^i_{pp}}{2\pi r^2 \sin\vartheta \Delta r \Delta\vartheta \Delta\varphi \Delta E \Delta\mu} \Delta t^{k+i} \end{aligned} \tag{3.50}$$

where N^i_{pp} gives the weighted number of pseudo-particles in the 5D sampling volume at time $t^k - \Delta t/2 + \sum_{l=0}^{i} \Delta t^{k+l}$. As explained in Section 3.2.6, the term "weighted" refers here to the fact that each pseudo-particle only contributes its statistical weight α_i to total number dN^i_{pp}. Furthermore, the division by 2π is performed to follow the standard definition of the differential intensity and originates from the gyrotropic assumption (Appendix A). From Eq. (3.50) it is also clear that pseudo-particles can be sampled in any volume element $dV = r^2 \sin\vartheta dr d\vartheta d\varphi$, independent of the coordinate type. It is thus also possible to use e.g., Cartesian or cylindrical sampling boxes, even when the SDEs are integrated in spherical coordinates.

In PARADISE, the user can provide a list of individual spatial locations where the pseudo-particles need to be sampled, for example, corresponding to certain spacecraft locations. Alternatively, the user can prescribe an entire grid of sampling boxes covering large parts of the spatial domain, which allows to model in detail the spatial

[7] This condition will lead to $d\mathcal{J}/d\mu = 0$ at $\mu = \pm 1$, which is not how real solutions behave. This artificial effect can be mitigated If the time step is small enough near $\mu = \pm 1$, such that pseudo-particles always remain in the last μ-bin after the reflection (R. Vainio, private communication). The small-angle scattering method described in Section 3.3.8 does not suffer from this restriction.

[8] We use here that $dE = vdp$.

and temporal evolution of the differential intensity $\mathcal{J}$ in large regions of the heliosphere, but can be very memory consuming. For the energy coordinate E, PARADISE can accommodate energy bins that are spaced according to a constant size ΔE or according to a constant $\log_{10} \Delta E$. Finally, the domain of the pitch-angle cosine μ, that is, $[-1, 1]$, is typically divided into 20 bins of equal width $\Delta\mu = 0.1$, although other resolutions are possible.

3.3.7 The background plasma

To solve the FTE, the flow velocity and the magnetic field of the background plasma need to be specified. These plasma variables can be calculated from an analytical model or from a model that solves the ideal MHD equations. PARADISE requires the variables of the background plasma to be specified on a 3D spherical grid. For a time-dependent MHD simulation, snapshots of the gridded plasma variables need to be provided. The maximal time step between two consecutive snapshots depends on how fast the background plasma evolves in time. PARADISE does not require the time step between two snapshots to be constant, and hence a higher snapshot cadence can be used when the plasma is going through a very dynamic phase.

Since the pseudo-particles are not constrained to a numerical grid, the plasma variables need to be interpolated to the precise position of the pseudo-particles. After locating the grid-cell in which the pseudo particle resides, this is done by using a standard trilinear interpolation in space. Moreover, the FTE contains multiple terms with derivatives of the magnetic (unit) vector and the plasma velocity. These derivatives are calculated on the corners of the grid cell that the pseudo-particle occupies and are subsequently also interpolated to the position of the pseudo particle. The derivatives are calculated using a fourth order central difference scheme. For a temporally variable plasma, a linear interpolation is performed between two consecutive MHD snapshots, and the time-derivatives are calculated using a first order finite difference scheme.

When simulating the solar wind in the inner heliosphere, a common assumption is that the solar wind is stationary in a reference frame corotating with the Sun (when no CMEs are present). Given the solar rotation rate $\Omega_\odot$, a single snapshot is then sufficient to know the entire time evolution of the background plasma. In PARADISE, a plasma that is stationary in a rotating frame can be handled by uploading a single snapshot at the start of the simulation. It is hereby assumed that the rotation axis is aligned with the polar axis of the spherical coordinate system, such that the rotation occurs as a function of the azimuthal angle φ. In that case, the rotation of the snapshot is taken into account by using the longitudinal coordinate $\varphi - \Omega_\odot t$ when determining in which grid-cell of the background plasma the pseudo-particle is residing. Moreover, the Eulerian time

derivatives in the FTE are computed using

$$\frac{\partial}{\partial t} = -\Omega_{\odot}\frac{\partial}{\partial \varphi}, \tag{3.51}$$

where $\Omega_{\odot}$ is assumed to be positive if the plasma rotates in the direction of increasing azimuthal angle φ.

EUHFORIA

The model used in this work to describe the solar wind is the *EUropean Heliospheric FORecasting Information Asset* (EUHFORIA; Pomoell & Poedts, 2018), and will be described briefly in the following.

EUHFORIA consists of a data-driven coronal model and a 3D time-dependent MHD model of the heliosphere. The coronal part uses observations of the photospheric magnetic field to construct a model of the coronal large-scale magnetic field, which, in turn, is used to obtain solar wind plasma parameters at 0.1 AU by employing a set of empirical relations. The heliospheric model utilises these plasma parameters as boundary conditions to solve the ideal MHD equations on a spherical 3D grid up to a prescribed outer boundary, which can be placed at several AU. Alternatively, the heliospheric part of EUHFORIA can also be used by prescribing synthetic boundary conditions, that is, boundary conditions that are not provided by the coronal model. The MHD equations are integrated using a finite volume method together with a constrained transport approach for advancing the magnetic field in a divergence-free manner.

Furthermore, EUHFORIA also allows the injection of CMEs in the ambient solar wind of the heliospheric model. Different CME models are implemented in EUHFORIA, including the hydrodynamic cone model (Odstrčil & Pizzo, 1999) and a linear force-free spheromak model (Verbeke et al., 2019). For further details on the implementation of EUHFORIA, we refer to Pomoell & Poedts (2018).

3.3.8 The diffusion coefficients

Turbulence

PARADISE contains a separate module in which the characteristics of the plasma turbulence are provided. This turbulence module is used by some of the modules that describe a pitch-angle or a cross-field diffusion coefficient, as explained in the next sections. Currently, PARADISE contains the slab/2D composite magnetostatic turbulence model introduced in Section 2.6.3. This composite model incorporates the pure slab turbulence model and the pure 2D turbulence model. Moreover, the assumed

wave spectra of the slab and 2D components are given by Eqs. (2.106) and (2.107), respectively.

Pitch-angle diffusion

The pitch-angle diffusion appearing in the FTE can be handled with two different methods in PARADISE. The first approach follows the standard SDE procedure, and updates the time step according to Eq. (3.32). The other method is based on the exact solution of a diffusion equation and is explained in the next section.

The diffusion coefficients are treated in a modular fashion, such that it is straightforward to incorporate new functional forms for $D_{\mu\mu}$. Currently, PARADISE has three different pitch-angle diffusion coefficients implemented, which are all derived from magnetostatic QLT (see Section 2.7.1), that is,

$$D_{\mu\mu} = 2\pi^2 \frac{\left(1-\mu^2\right)}{|\mu| v} \left(\frac{\Omega}{B}\right)^2 g_{\text{slab}}\left(k_{\parallel} = \frac{\Omega}{|\mu| v}\right), \tag{3.52}$$

$$D_{\mu\mu} = D_0 \left(\frac{|Q|}{\gamma m}\right)^{2-s} v^{s-1} \left(|\mu|^{s-1} + H\right)\left(1-\mu^2\right), \tag{3.53}$$

$$D_{\mu\mu} = \frac{\nu_0}{2} \left(\frac{|Q|}{\gamma m}\right)^{2-s} v^{s-1} \left(\frac{|\mu|}{1+|\mu|} + \epsilon\right)\left(1-\mu^2\right), \tag{3.54}$$

where Ω denotes the gyrofrequency, Q the particle charge, m the particle mass, and s the spectral index of the wave spectrum of the inertial range of slab turbulence. The meaning of the parameters D_0, H, ν_0 and ϵ is explained below.

The diffusion coefficient (3.52) follows directly from (2.121), with g_{slab} the wave spectrum of the slab component of the turbulence[9]. In PARADISE, this wave spectrum is described in the turbulence module. For example, for the wave spectrum (2.106), the diffusion coefficient $D_{\mu\mu}$ becomes equal to Eq. (2.122).

The diffusion coefficient (3.53) follows from (3.52), by assuming $g_{\text{slab}}(k_{\parallel}) \sim k_{\parallel}^{-s}$. In addition, the 90° scattering problem of QLT (see Section 2.7.1) is addressed by introducing the parameter H, which provides a non-zero value for $D_{\mu\mu}$ at $\mu = 0$ (Beeck & Wibberenz, 1986). The parameter D_0 is derived by assuming a constant (radial) mean free path for a reference particle species with a prescribed fixed energy. By using Eq. (2.123), D_0 is thus calculated as

$$D_0 = \frac{3}{4} v_{\text{ref}}^{2-s} \frac{1}{(\lambda_{\parallel})_{\text{ref}}} \left(\frac{|Q_{\text{ref}}|}{\gamma_{\text{ref}} m_{\text{ref}}}\right)^{2-s} \int_0^1 \frac{1-\mu^2}{|\mu|^{s-1} + H} d\mu. \tag{3.55}$$

[9] Recall from Section 2.7.1 that, under the assumptions of QLT, pure 2D turbulence has $D_{\mu\mu} = 0$, such that only the slab component contributes to the pitch-angle diffusion.

If the radial mean free path is assumed to be constant instead of the mean free path, then $(\lambda_\parallel)_{\rm ref}$ has to replaced by $\left(\lambda_\parallel^r\right)_{\rm ref}/b_r^2$ in this equation. The diffusion coefficient (3.53) is thus not coupled to any turbulence module, but requires prescribed values for H, $m_{\rm ref}$, $Q_{\rm ref}$, $v_{\rm ref}$ and $(\lambda_\parallel)_{\rm ref}$ or $(\lambda_\parallel^r)_{\rm ref}$.

When using a $D_{\mu\mu}$ like (3.53) or (2.122) in numerical applications, caution is needed since $\partial D_{\mu\mu}/\partial\mu$ has a pole at $\mu = 0$. This pole needs to be treated carefully in order to obtain correct PADs, and to prevent the time step (3.48) from becoming too small. In practice, it turns out to be sufficient to set $\partial D_{\mu\mu}/\partial\mu$ equal to zero in an interval, $[-\varepsilon, \varepsilon]$. As discussed in Van den Berg (2019), a possible choice for the small parameter ε can be derived from

$$\left.\frac{\partial D_{\mu\mu}}{\partial\mu}\right|_{\mu=\varepsilon} = 4\left.\frac{\partial D_{\mu\mu}}{\partial\mu}\right|_{\mu=1}.$$

Alternatively, expression (3.54) can be used to describe the pitch-angle diffusion. This functional form was proposed by Agueda et al. (2008) and has the advantage that $\partial D_{\mu\mu}/\partial\mu$ is bounded for $\mu \in [-1, 1]$. Agueda & Vainio (2013) illustrated that the diffusion coefficients defined in (3.53) and (3.54) closely match when the parameter ϵ is chosen carefully. In addition, the functional form (3.54) for the pitch-angle diffusion coefficient allows for a more efficient implementation of the pitch-angle diffusion, as explained in the next section and in Agueda et al. (2008).

The parameter ν_0 in (3.54) can be determined by assuming a constant (radial) mean free path for a reference particle species with a prescribed fixed energy. Under this assumption, Eq. (2.123) can be used to obtain (see Agueda et al., 2008)

$$\nu_0 = v_{\rm ref}^{2-s}\frac{1}{(\lambda_\parallel)_{\rm ref}}\left(\frac{|Q_{\rm ref}|}{\gamma_{\rm ref}m_{\rm ref}}\right)^{2-s}\psi(\epsilon), \tag{3.56}$$

where

$$\psi(\epsilon) = \frac{3}{2}\int_0^1 \frac{1-\mu^2}{\frac{\mu}{1+\mu}+\epsilon}d\mu = \frac{1}{1+\epsilon^4}\left[4\epsilon^3 + 15\epsilon^2 + 12\epsilon + 1 + 6(1+2\epsilon)\ln\left(\frac{1+2\epsilon}{\epsilon}\right)\right].$$

The coefficient ν_0 is called the *scattering frequency*, for reasons explained in the next section.

Pitch-angle scattering

In this section we introduce an alternative, more efficient approach to update the μ coordinate of the pseudo-particles. The method was first introduced by Torsti et al. (1996) for isotropic pitch-angle scattering and later extended by Kocharov et al. (1997) and Agueda et al. (2008) to accommodate for anisotropic scattering as well. This

approach, which we will refer to as the "small-angle scattering" (SAS) approach, is based on the exact solution of a diffusion equation for a small-angle isotropic scattering process, that is,

$$\frac{\partial F}{\partial t} = \frac{\nu}{2\sin\tilde{\theta}}\frac{\partial}{\partial\tilde{\theta}}\sin\tilde{\theta}\frac{\partial F}{\partial\tilde{\theta}} \approx \frac{\nu}{2\tilde{\theta}}\frac{\partial}{\partial\tilde{\theta}}\tilde{\theta}\frac{\partial F}{\partial\tilde{\theta}}, \tag{3.57}$$

where ν is a constant scattering frequency and $\tilde{\theta}$ is the angle between the propagation directions of the unscattered and scattered particle trajectory. The second equality in Eq. (3.57) is valid when the scattering angle $\tilde{\theta}$ is small, which holds for times $\delta t \ll \nu^{-1}$. A solution of Eq. (3.57) after a time δt is then given by

$$F(\tilde{\theta},\tilde{\phi},\delta t)d\tilde{\theta}d\tilde{\phi} = \frac{1}{2\pi}\left[\frac{1}{2\nu\delta t}\exp\left(-\frac{\tilde{\theta}^2}{2\nu\delta t}\right)d\tilde{\theta}^2\right]d\tilde{\phi}, \tag{3.58}$$

where $\tilde{\phi}$ is the phase angle around the scattering axis (see Fig. 4.1 of Vainio, 1998). Equation (3.58) states thus that after a time δt, the phase angle $\tilde{\phi} \sim \mathcal{U}[0, 2\pi)$, where $\mathcal{U}$ is a uniform distribution, and the square angle $\tilde{\theta}^2 \sim \mathcal{E}(2\nu\delta t)$, where $\mathcal{E}$ denotes the exponential distribution.

Following Eq. (3.58), the new cosine of the pitch-angle, $\mu_{\rm new}$, is then related to the pitch-angle cosine $\mu_{\rm old}$ from before the scattering process through (Vainio, 1998)

$$\mu_{\rm new} = \mu_{\rm old}\cos\tilde{\theta} + \sqrt{1-\mu_{\rm old}^2}\sin\tilde{\theta}\cos\tilde{\phi}, \tag{3.59}$$

where $\tilde{\theta}$ and $\tilde{\phi}$ are random numbers generated from their corresponding distributions.

To proceed, we remark that the diffusion coefficient (3.54) can be written as the sum of two separate diffusion processes, that is,

$$D_{\mu\mu} = D_{\mu\mu}^{\rm iso} + D_{\mu\mu}^{\rm aniso},$$

where $D_{\mu\mu}^{\rm iso}$ describes an isotropic[10] scattering process with scattering frequency[11] $\epsilon\nu$, that is,

$$D_{\mu\mu}^{\rm iso} = \frac{\epsilon\nu}{2}\left(1-\mu^2\right), \tag{3.60}$$

and $D_{\mu\mu}^{\rm aniso}$ describes the following anisotropic pitch-angle scattering process

$$D_{\mu\mu}^{\rm aniso} = \frac{\nu}{2}\left(1-\mu^2\right)\left(\frac{|\mu|}{1+|\mu|}\right). \tag{3.61}$$

[10] To understand why Eq. (3.60) represents a isotropic pitch-angle scattering process, note that $D_{\mu\mu} = (1-\mu^2)D_{\theta\theta}$, where θ is the particle pitch-angle.

[11] $\nu := \nu_0\left(\frac{|Q|}{\gamma m}\right)^{2-s} v^{s-1}$.

However, this anisotropic scattering process can be made isotropic by performing the following coordinate transformation (Agueda et al., 2008)

$$\eta : [-1,1] \to [-1,1] : \mu \mapsto \eta(\mu) = \begin{cases} 2\mu - 1 & \mu \geq 0 \\ 2\mu + 1 & \mu < 0, \end{cases} \tag{3.62}$$

for which

$$D_{\eta\eta} = \left(\frac{d\eta}{d\mu}\right)^2 D_{\mu\mu}^{\text{aniso}} = \frac{1}{2}\nu\left(1-\eta^2\right). \tag{3.63}$$

Hence, the pitch-angle diffusion coefficient (3.54) can be treated by means of two subsequent isotropic scattering processes, one in the μ variable with frequency $\epsilon\nu$, and one in the η variable with frequency ν.

Within the SAS approach, the μ coordinate is thus updated according to

$$\mu^{k+1} = \mu^k + \left.\frac{d\mu}{dt}\right|_{t=t^k} \Delta t^k + \Delta\mu_{\text{scattering}}, \tag{3.64}$$

where $\Delta\mu_{\text{scattering}}$ is obtained from the two scattering processes described above, and $d\mu/dt$ is now given by Eq. (2.85), which is different from Eq. (3.14) appearing in the SDE (3.21).

As discussed by Vainio (1998) and Agueda & Vainio (2013), a main advantage of the SAS approach with respect to the standard SDE approach is that it allows for larger time steps when integrating the pseudo-particles' trajectories. The reason behind this efficiency increase can be understood intuitively by realising that the SAS approach uses the exact solution of the small-angle diffusion equation, and hence it does not need to resolve the small pitch-angle changes leading to this solution. In contrast, the standard Itô approach needs a much smaller time step because it needs to resolve these small-angle scattering processes properly in order to obtain the correct PADs.

Cross-field diffusion

Various cross-field diffusion models are implemented in PARADISE, including the ENLGC (see Eq. (2.145)), the FLRW limit of the UNLT theory (see Eq. (2.146)), and the three phenomenological approaches given by Eqs. (2.150) – (2.152). The parameters appearing in the non-linear diffusion theories follow from the pure 2D component[12] of the turbulence and are thus specified in the turbulence module of PARADISE. The phenomenological approaches are not derived from any turbulence model and are thus not dependent on the turbulence module. The free parameters of these cross-field diffusion models have thus to be prescribed by the user.

[12] As explained in Section 2.7.2, the slab component of turbulence produces subdiffusion.

Chapter 4

Modelling the transport of SEPs in a CIR

"The cure for boredom is curiosity. There is no cure for curiosity."
– Dorothy Parker

Abstract. In this chapter, the PARADISE model is verified by reproducing the results of Dröge et al. (2010). In addition, we study how different solar wind speeds affect the energy of protons while they travel in a nominal Parker spiral. This is done by injecting 4 MeV protons impulsively and uniformly from a region of limited spatial extent located at the inner boundary of the computational domain. Thereafter, we study the propagation of such protons in a solar wind containing a corotating interaction region (CIR), which was generated with EUHFORIA.

We find that the protons undergo considerable deceleration in a nominal solar wind, especially if the solar wind speed is high. In the solar wind containing a CIR, we observe proton acceleration at the compression and shock waves bounding the CIR. These waves also act as magnetic mirrors, producing long-lasting high particle intensities in the inner heliosphere. It is also illustrated that the compressed magnetic field inside a CIR can enhance the effect of cross-field diffusion. In addition, in our simulations cross-field diffusion leads to the formation of accelerated particle populations centred on the forward shock wave at larger radial distances, despite the lack of magnetic

connection between the particle injection region and this shock wave.

This chapter is entirely based on Wijsen et al. (2019a).

4.1 Introduction

Occasionally, particle monitors on board spacecraft will register sudden strong increases in particle fluxes over a wide range of energies. The origin of these particles typically lies in eruptive events occurring at the Sun, and they are therefore commonly known as SEPs. The majority of these SEPs are expected to have gained high energies either by means of stochastic acceleration mechanisms in a parent flare region or by means of first order Fermi acceleration at shock waves driven by CMEs. Apart from solar eruptive events, corotating interaction regions (CIRs; Smith & Wolfe, 1976) are considered an important source of energetic particles in the heliosphere (Richardson, 2004). At larger heliocentric distances, these CIRs are typically bounded by a forward shock wave propagating in the slow solar wind, and a reverse shock wave propagating in the fast solar wind (see e.g., Richardson, 2018). Like the shock wave in front of a CME, the shock waves associated with a CIR can potentially also accelerate particles to high energies (Fisk & Lee, 1980; Classen et al., 1998).

Once particles escape from their acceleration site, they travel through the heliosphere, spiralling around the IMF lines. During their journey, particles interact with small-scale magnetic turbulence omni-present in the solar wind. This turbulence can scatter the particles, and hence determines the particles' mean free path. A large number of studies have been conducted that focus on quantifying the amount of magnetic turbulence in the solar wind, and studying the effect of different mean free paths on particle events (e.g., Beeck & Sanderson, 1989; Kunow et al., 1991; Bieber et al., 1994, and references therein). This has typically been done by assuming a Parker solar wind configuration (Parker, 1958) and describing the effect of turbulence on particle transport through diffusive processes in the particle's spatial coordinate or pitch-angle. Aside from the characteristics of small-scale magnetic field turbulence, energetic particle transport, and hence SEP events, can also strongly be affected by the global solar wind configuration. The latter is seldom described well by a steady-state Parker configuration, since the characteristics of solar wind source regions, like coronal streamers and coronal holes, are very different from one another, leading to varying solar wind speeds and densities. Apart from that, transient solar eruptive events strongly affect the conditions in interplanetary (IP) space. Therefore, it is important to include these varying solar wind conditions in SEP transport models, in order to achieve a better understanding of SEP events.

In this chapter, we use PARADISE to model the transport and energy changes of SEPs

in the inner heliosphere by solving the FTE. We first briefly illustrate the transport effects for protons travelling in a nominal slow or fast Parker solar wind configuration, and compare the obtained intensity profiles to the results of Dröge et al. (2010). Next, we study in detail SEP transport in a EUHFORIA-generated slow solar wind with an embedded fast solar wind stream, forming a CIR at large heliospheric radial distances ($r \gtrsim 1.5$ AU). Giacalone et al. (2002) introduced an analytical model for a CIR at small radial distances ($r \sim 1$ AU), i.e., where the forward and reverse shocks have not yet formed, to study its effect on interstellar pickup-ions. This analytical model was later-on used by e.g., Kocharov et al. (2003, 2008b) to illustrate that corotating compression regions can modify the time-intensity profiles, anisotropies and energy spectra of SEP events. Both Giacalone et al. (2002) and Kocharov et al. (2003) also illustrated that a forward or reverse compression wave can act as a magnetic mirror, temporarily trapping energetic particles at small radial distances. The analytical CIR model of Giacalone et al. (2002) has however its limitations, since it includes either a forward or a reverse compression wave, but not both. Therefore, in their model, only IMF lines of the slow (fast) solar wind can intersect the forward (reverse) compression wave, and as a result, the inner structure of the CIR is relatively simple, resembling a compressed Parker spiral magnetic field. However, in reality, there will often be both a forward and reverse compression or shock wave bounding the CIR. In between those waves, magnetic field lines converge to a SI, which separates the compressed fast and slow solar wind plasmas, and which may have a non-negligible influence on energetic particle transport (see e.g., Intriligator et al., 2001). Such a CIR-structure is captured by our MHD simulation, and we show that it can have significant effects on the time-intensity and anisotropy profiles of SEP events. In addition to the above, we study how the magnetic field configuration inside the CIR can amplify the efficiency of cross-field diffusion, without requiring high levels of turbulence.

The structure of this chapter is as follows. In Section 4.2 we specify the equations and diffusion coefficients that PARADISE uses to describe the pitch-angle dependent transport of energetic particles in the heliosphere. Section 4.3 presents the performance of the model when describing the transport of protons under nominal slow and fast solar wind conditions, as a verification test of PARADISE. The effects of different solar wind speeds on the particle distributions are discussed. In Section 4.4 we present the results when propagating protons in a solar wind containing a CIR with different cross-field diffusion conditions. Finally, in Section 4.5 we summarise the results presented in this chapter and give the conclusions.

4.2 Particle transport model

As explained in Chapter 2, the evolution of the gyrotropic differential particle intensity $j(\mathbf{x}, p, \mu, t)$ can be described by the FTE, which can be formulated for the non-relativistic

solar wind as (see Section 2.5)

$$\frac{\partial j}{\partial t} + \nabla \cdot \left[\left(\frac{d\mathbf{x}}{dt} + \nabla \cdot \boldsymbol{\kappa}_{\perp} \right) j \right] + \frac{\partial}{\partial \mu} \left[\left(\frac{d\mu}{dt} + \frac{\partial D_{\mu\mu}}{\partial \mu} \right) j \right] + \frac{\partial}{\partial p} \left(\frac{dp}{dt} j \right) = \frac{\partial^2}{\partial \mu^2} \left[D_{\mu\mu} j \right] + \nabla\nabla : (\boldsymbol{\kappa}_{\perp} j), \tag{4.1}$$

with

$$\frac{d\mathbf{x}}{dt} = \mathbf{V}_{\mathrm{sw}} + \mathbf{V}_{gd} + \mu v \mathbf{b} \tag{4.2}$$

$$\frac{d\mu}{dt} = \frac{1-\mu^2}{2} \left(v \nabla \cdot \mathbf{b} + \mu \nabla \cdot \mathbf{V}_{\mathrm{sw}} - 3\mu \mathbf{bb} : \nabla \mathbf{V}_{\mathrm{sw}} - \frac{2}{v} \mathbf{b} \cdot \frac{d\mathbf{V}_{\mathrm{sw}}}{dt} \right) \tag{4.3}$$

$$\frac{dp}{dt} = \left(\frac{1-3\mu^2}{2} (\mathbf{bb} : \nabla \mathbf{V}_{\mathrm{sw}}) - \frac{1-\mu^2}{2} \nabla \cdot \mathbf{V}_{\mathrm{sw}} - \frac{\mu}{v} \mathbf{b} \cdot \frac{d\mathbf{V}_{\mathrm{sw}}}{dt} \right) p. \tag{4.4}$$

Here $\mathbf{x}$ is the spatial coordinate, p the momentum, v the speed, μ the pitch-angle cosine, $\mathbf{V}_{\mathrm{sw}}$ is the solar wind velocity, and $\mathbf{b}$ the unit vector in the direction of the mean magnetic field. $D_{\mu\mu}$ is the pitch-angle diffusion coefficient, $\boldsymbol{\kappa}_{\perp}$ the spatial cross-field diffusion tensor, and $\mathbf{V}_{gd}$ the particle drift due to the gradient and curvature of the mean magnetic field. The effects of the polarization drift are thus not taken into account; Dalla et al. (2013) illustrated that this drift is significantly smaller than the sum of the gradient and curvature drifts.

We recall from Chapter 2 that the FTE is written in mixed coordinates, which means that the spatial coordinate is measured in the observer's fixed inertial frame, whereas the momentum and pitch-angle cosine are measured in a reference frame co-moving with the solar wind. In the latter frame, the motional electric field equals zero, leaving the Lorentz force only capable of changing the propagation direction of the particle and not its energy. However, the co-moving frame is not inertial, and fictitious forces will therefore act on the particle, altering its energy and pitch-angle. This results in a monotonic decrease of the particle's momentum in the co-moving frame when travelling in the expanding solar wind. This constant loss of energy is often termed adiabatic deceleration, yet if the particle travels in a converging flow e.g., at shocks or compression regions, the particle will accelerate instead of decelerate. Furthermore, Dalla et al. (2015) have shown that magnetic gradient and curvature drifts can also lead to a substantial deceleration of SEPs, especially at high energies and high latitude. These drift-induced energy losses are included in the momentum terms Eq. (4.3) and Eq. (4.4) of the FTE, as shown by le Roux et al. (2007).

For the pitch-angle diffusion coefficient, we use the functional from (3.54), which we restate here for referential convenience:

$$D_{\mu\mu} = \frac{\nu_0}{2}\left(\frac{|Q|}{m}\right)^{2-q} v^{q-1}\left(\frac{|\mu|}{1+|\mu|}+\epsilon\right)\left(1-\mu^2\right). \tag{4.5}$$

Moreover, we use the SAS method of PARADISE to compute the evolution of the pitch-angle coordinate of the pseudo-particles (see Section 3.3.8). Similar to Dröge et al. (2010), we assume throughout this chapter a constant radial mean free path of 0.3 AU for 4 MeV protons. We recall from Section 3.3.8 that the radial mean free path is defined as $\lambda_\parallel^r = \lambda_\parallel \cos^2\psi = \lambda_\parallel b_r^2$, where $\lambda_\parallel$ is the normal parallel mean free path and ψ is the angle between the radial unit vector and the IMF.

For the cross-field diffusion, we use the phenomenological approach introduced by Dröge et al. (2010), which was also introduced at the end of Section 2.7.2. We recall that in this approach, the perpendicular mean free path is assumed to scale with the gyroradius of the particle and the parallel mean free path. Averaging over the pitch-angle gives then the following diffusion coefficient (see also Eq. (2.151))

$$\boldsymbol{\kappa}_\perp = \frac{\pi}{12}\frac{\alpha v \lambda_\parallel^r}{b_r^2}\frac{B_0}{B}\left(\mathbb{I}-\mathbf{bb}\right), \tag{4.6}$$

where $\mathbb{I}$ is the unit tensor, $\mathbf{bb}$ is a dyadic product, and α is a free parameter that determines the ratio between the parallel and perpendicular mean free path at a reference magnetic field strength B_0.

The numerical procedures used by PARADISE to solve the FTE are explained in detail in Section 3.3. In particular, the sampling procedure of the integrated pseudo-particles is specified in Section 3.3.6. In this work, the pseudo-particles are sampled in Cartesian sampling boxes of size $\Delta x = \Delta y = \Delta z = 0.025$ AU. The bin size of the energy channels is chosen to be constant and equal to $\Delta E = 0.4$ MeV. The energy channels that we consider in this work are listed in Table 4.1 and in the following, we simply refer to the arithmetic mean $\langle E \rangle$ when discussing a specific energy channel.

The μ-coordinate of the pseudo-particles is sampled in bins of size $\Delta\mu = 0.1$ and the binning of the pseudo-particles is performed during time intervals of $\Delta t = 10$ minutes. Finally, we note that we use reflective inner and absorptive outer boundary conditions. The outer boundary is placed at sufficiently large radial distance such that it does not affect the simulation results.

4.3 SEP propagation in uniform wind conditions

As a verification test of PARADISE, we present in this section the results obtained when propagating particles in a nominal IMF for slow (400 km/s) and fast (700 km/s) solar

$E_{\mathrm{min}} - E_{\mathrm{max}}$	$\langle E \rangle$
2.0 – 2.4	2.2
2.4 – 2.8	2.6
2.8 – 3.2	3.0
3.2 – 3.6	3.4
3.6 – 4.0	3.8
4.0 – 4.4	4.2
4.4 – 4.8	4.6

Table 4.1: Energy channels and their arithmetic mean $\langle E \rangle$ in MeV.

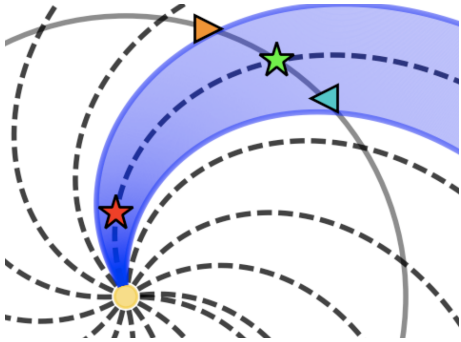

Figure 4.1: Diagram of the ecliptic illustrating the particle streaming zone (blue) for an injection over an azimuthal range of 30°. The markers represent the different observers introduced in the text. The triangles are stationary observers A (cyan) and B (orange), whereas the stars are the corotating observers C (red) and D (green). The dashed lines represent magnetic field lines.

wind configurations. Both solar winds are computed assuming a constant sidereal solar rotation period of 25.4 days. Similar to Dröge et al. (2010), we consider an impulsive event of 4 MeV protons, injected uniformly at the solar equator over a longitudinal range of 30 degrees and at a radial distance of 0.05 AU. For each simulation presented in this section, we propagated 10^6 particles.

As illustrated in the diagram shown in Fig. 4.1, we place four different observers in the solar equatorial plane. The two observers marked by triangles are stationary. Observer A (cyan triangle) is initially located in the SEP streaming zone, close to the eastern boundary, while observer B (orange triangle) is initially located outside the SEP streaming zone, near the western boundary. Eventually, the corotation of the particles with the magnetic field leaves observer A outside the SEP streaming zone, whereas observer B moves into the SEP streaming zone. The two remaining observers, C (red star) and D (green star), are corotating with the centre of the particle streaming zone

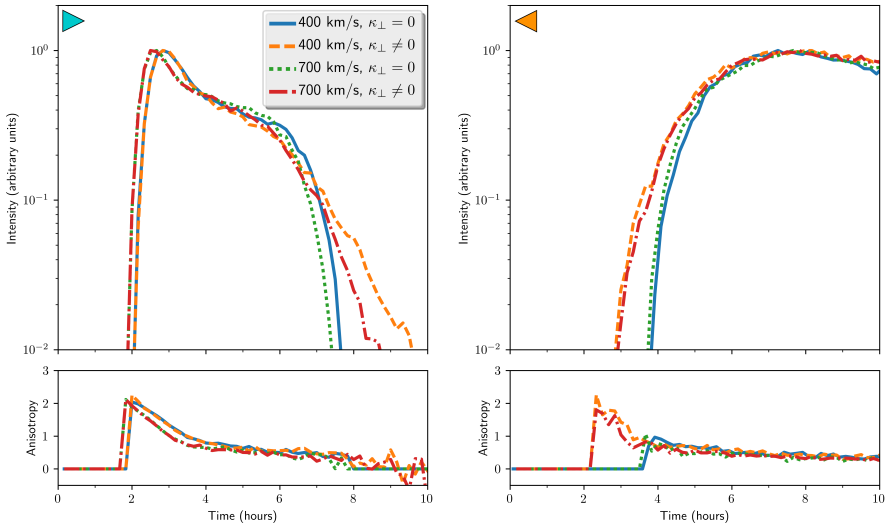

Figure 4.2: Intensity and anisotropy time profiles of 4 MeV protons propagating in fast and slow solar wind configurations, with and without cross-field diffusion as detailed in the legend. The left (right) panel shows the results for observer A (B) indicated by the cyan (orange) triangle marker as in Fig. 4.1. Adiabatic deceleration and solar wind convection are neglected, with the exception of accounting for corotation.

and located at heliocentric radial distances of 0.3 AU and 1 AU, respectively.

As a first test, we transport particles considering neither energy changes nor particle drifts. The particles retain thus their original 4.0 MeV injection energy throughout the entire simulation. We also neglect solar wind convection, but include the corotation effect. Similar assumptions were made by Dröge et al. (2010), and their results are used here to verify the results of PARADISE. With this aim, we assume $\epsilon = 0.048$ in Eq. (4.5), to characterise $D_{\mu\mu}$. This value was obtained from minimizing the sum of the squared differences between (4.5) and (3.53) for $H = 0.05$, as this latter value was used by Dröge et al. (2010). We assume a constant radial mean free path, $\lambda_\parallel^r = 0.3$ AU, and perform simulations both with and without spatial cross-field diffusion. For the cases with cross-field diffusion, we assume $\alpha = 10^{-4}$ in Eq. (4.6), which corresponds to a rather small perpendicular mean free path. Note that e.g., Dröge et al. (2016), Qin & Wang (2015), and Strauss et al. (2017) use a $\kappa_\perp$ of the order of $\sim 0.01\kappa_\parallel$, i.e., about 100 times larger than the value we assume.

Figure 4.2 shows the omni-directional intensity, i.e.,

$$I = \int_{-1}^{1} j(\mu) d\mu, \tag{4.7}$$

and the first order parallel anisotropy, i.e.,

$$A = \frac{\int_{-1}^{1} \mu j(\mu) d\mu}{\int_{-1}^{1} j(\mu) d\mu}, \tag{4.8}$$

measured by the two stationary observers described above. The intensity profiles depicted in the left panel of this figure (observer A), for the cases where particles travel in the slow solar wind (blue and orange curves), reproduce the profiles shown in the right panel of Fig. 8 of Dröge et al. (2010). The effects of cross-field diffusion are seen when observers A and B respectively leave and enter the particle streaming zone. For observer A and for both solar winds, the cut-off in the particle intensity observed after ~7 h becomes more gradual due to cross-field diffusion. For observer B (right panel of Fig. 4.2), the effect of cross-field diffusion is to shift the particle onset to an earlier time.

The effect of the different solar wind speeds is rather small for these simulations, and merely reflect the difference in the IMF curvature of the solar wind configuration, i.e., the distance a particle needs to travel to reach 1 AU reduces for larger values of the solar wind speed.

In contrast, the effect of the solar wind speed becomes much more pronounced when all terms of the FTE are included in the simulations. Particle intensity-time profiles and anisotropies obtained from such simulations are shown in Fig. 4.3 for the same observers and different energy channels, in the range of 2.2 – 4.0 MeV. Panel A of Fig. 4.3 shows the results for observer A when located in the slow solar wind. Recalling that all particles were injected with the same initial energy of 4.0 MeV, the effect of adiabatic deceleration becomes very clear. During the first 1.5 h after the particle onset time, the main contribution to the total intensities is due to particles from the highest energy channel, which subsequently falls off rapidly by several orders of magnitude, leaving 3.4 MeV as the most populated energy channel. The latter remains the main contributor to the total intensity until the observer leaves the particle streaming zone, and all intensities drop to zero.

Panel B of Fig 4.3 shows the particle intensities for observer A, but this time for the fast solar wind case. A comparison between panels A and B shows that adiabatic deceleration is much stronger in the fast solar wind. In this latter case, most particles have already decelerated out of the highest energy channel upon reaching 1 AU. At a time of 5 h, the 3.0 MeV channel becomes the most populated energy channel, a transition that does not occur for the intensities measured in the slow solar wind case.

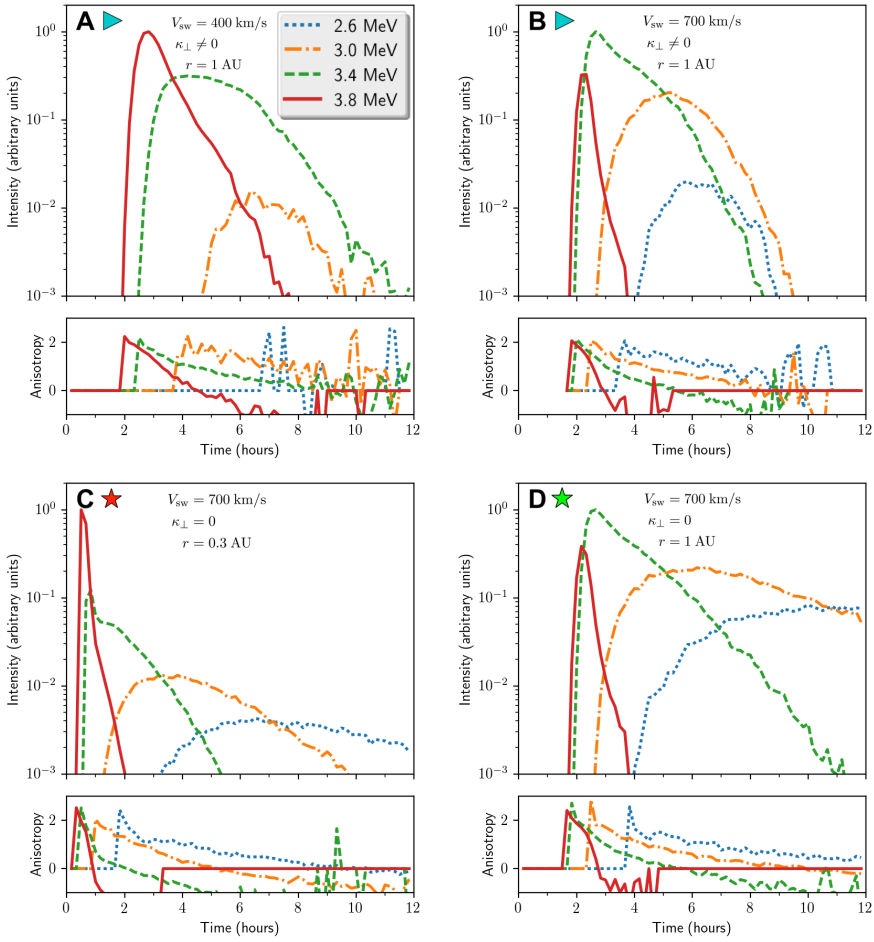

Figure 4.3: Intensity and anisotropy time profiles for different energy channels of protons injected with an initial energy of 4 MeV. All the effects of the FTE are included. The first row shows the profiles for observer A located in the slow (panel A) and fast (panel B) solar wind. The last row shows the profiles for corotating observers C (panel C) and D (panel D).

In addition, a considerable number of particles are registered in the 2.6 MeV channel in the fast solar wind case, whereas this channel is only scarcely populated in the slow solar wind simulation. The strong dependence of adiabatic deceleration on the solar wind speed can be understood by writing Eq. (4.4) for the case of a constant radial velocity, giving $dp/dt \propto V_{sw}$ (see, e.g., Ruffolo, 1995).

The bottom panels of Fig 4.3 show the intensity and anisotropy time profiles for the two corotating observers. At 0.3 AU (panel C), the event onset is characterised by a sharp peak of SEPs populating the highest energy channel (red curve). This peak reflects the impulsive mono-energetic delta injection and corresponds to the particles that have not yet scattered significantly on their path from 0.05 to 0.3 AU. Moreover, it is seen that the intensity of the highest energy channel shows a kink around ~1 h, corresponding to the time at which most of the particles start coming from the anti-sunward direction, as indicated by the change of sign seen in the corresponding anisotropy time profile. The intensity and anisotropy profiles for the corotating observer located at 1 AU (Panel D) show similar features to those in Panel B, with the exception that after ~11 h the lowest depicted energy channel becomes the most populated one because the corotating observer remains in the particle streaming zone. In addition to the effects of adiabatic deceleration, the qualitative differences between the intensity profiles for the corotating observers at 0.3 AU and 1.0 AU are partly due to the fact that particles with the highest energy have the hardest time travelling back in the sunward direction due the magnetic mirroring effect, which is proportional to both the speed of the particle and the magnetic field magnitude. Therefore, at 0.3 AU, the strong focusing/mirroring effect drives particles of higher energy more effectively towards large radial distances than particles of low energy. This explains why the transition from energy channel 3.0. MeV to 2.6. MeV as being the most populated channel occurs earlier in panel C than in panel D.

4.4 SEP propagation in mixed solar wind conditions

4.4.1 A corotating interaction region

We now study the propagation of SEPs in a non-nominal solar wind configuration computed by EUHFORIA. We demonstrate the performance of the coupling of PARADISE with the EUHFORIA model by propagating particles in a synthetically generated solar wind. In particular, we simulate a fast solar wind stream embedded in a slow solar wind. Such a configuration is obtained by prescribing a solar wind with a speed of 330 km s^{-1} everywhere at the inner boundary of the heliospheric model of EUHFORIA, except for the points with longitude and latitude satisfying

$$(\text{longitude} - 75^\circ)^2 + (\text{latitude} - 5^\circ)^2 < 20^\circ, \tag{4.9}$$

where we prescribe a faster solar wind with a speed of $v_{\mathrm{fsw}} = 660$ km s^{-1}. To some extent, this is reminiscent to a coronal hole located close to the solar equatorial plane. The fast solar wind region described by (4.9) is surrounded by a transition region of an angular width of 6°, in which the speed changes linearly from the slow to the fast solar wind speed. EUHFORIA also requires the prescription of the polarity of the magnetic field at the inner boundary. We choose a dipolar polarity structure, with the CS tilted by 40° with respect to the solar equatorial plane, intersecting the latter at longitudes 165° and 345°. In this configuration, the fast solar wind stream is completely embedded in a magnetic field of positive polarity. As described in Pomoell & Poedts (2018), the number density n, and the magnetic field vector are prescribed at the inner boundary $R_b = 0.1$ AU, so that a constant kinetic energy density is obtained. This is done by choosing these variables as follows

$$\left(B_r, B_\vartheta, B_\varphi\right) = \left(\mathrm{sgn}(B_{\mathrm{dp}})B_{\mathrm{fsw}}v_r/v_{\mathrm{fsw}}, 0, -(B_r/v_r)R_b\Omega_\odot \sin\vartheta\right)$$

$$n = n_{\mathrm{fsw}}(v_{\mathrm{fsw}}/v_r)^2,$$

where $n_{\mathrm{fsw}} = 300\,\mathrm{cm}^{-3}$ and $B_{\mathrm{fsw}} = 300$ nT are, respectively, the number density and magnetic field strength of the fast solar wind. $\mathrm{sgn}(B_{\mathrm{dp}})$ is the sign of the magnetic dipolar structure described above. Finally, the plasma thermal pressure on the inner boundary is chosen to be constant and equal to $P = 3.3$ nPa.

The EUHFORIA simulation is performed with a radial resolution of $1.03\,\mathrm{R}_\odot$, and an angular resolution of 1° for both longitude and colatitude, resulting in a numerical grid consisting of $1024 \times 120 \times 360$ cells. The simulation is started by performing a relaxation in which the MHD equations are advanced in time until a fully steady-state solar wind is obtained in the corotating frame.

Figure 4.4 displays snapshots of the solar wind simulation showing the radial velocity (left panel) and the scaled magnetic field magnitude, rB, (right panel), in the solar equatorial plane. Despite the simple inner boundary conditions, the generated solar wind contains a non-trivial structure. The substantial difference between the prescribed speeds of the slow and fast winds, combined with a relatively narrow transition region, results in the formation of a CIR from relatively small radial distances outwards ($r > 1.1$ AU). This CIR is bounded by a forward shock wave moving into the slow solar wind and a reverse shock wave moving into the fast solar wind and the rarefaction region behind the fast solar wind. Due to the finite resolution of the simulation, the width of the shock wave in the simulation is larger than it would be for a real interplanetary CIR shock. This makes it difficult to exactly pinpoint where the boundaries of the CIR evolve from a large amplitude compression wave to a fully formed shock wave. To estimate the location of the shock formation, we searched for strong jumps in radial and longitudinal profiles of various MHD quantities. As an example, Fig. 4.5 shows, from top to bottom, the longitudinal profiles of the radial velocity, the scaled thermal pressure, and the scaled magnetic field magnitude at different radial distances (colour

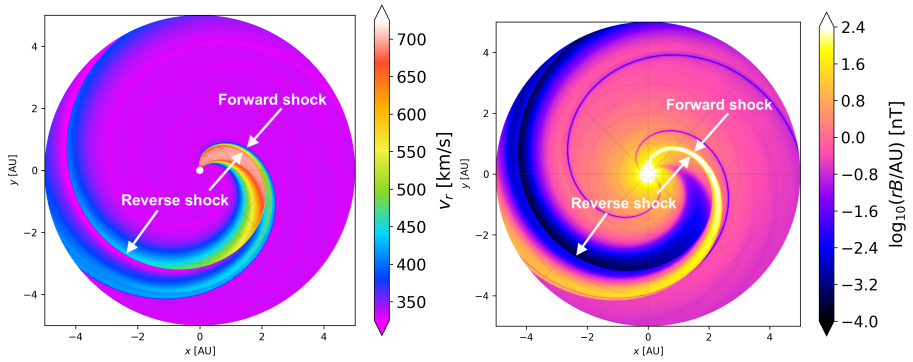

Figure 4.4: Snapshot from the EUHFORIA simulation in the heliographic equatorial plane. The left panel shows the radial speed, while the right panel shows the logarithm of the scaled magnetic field magnitude, rB.

coded as indicated in the inset). By examining the top panel and following the curves in the direction of decreasing longitude, we see that at 1 AU (blue curve) the increase in the radial speed profile is still relatively smooth. From 2 AU outward, the increase splits into two steps, indicating the formation of the forward-reverse pair of shocks between 1 and 2 AU, that become increasingly clearly separated at larger radial distances. The second increase in solar wind speed is simultaneously seen with a decrease in both the solar wind pressure and IMF profiles, as respectively shown in the middle and bottom panels of Fig. 4.5, indicating the presence of a reverse shock. Although at 1 AU the longitudinal profile of the radial velocity does not show a separation between the forward and the reverse shock, the pressure profile does exhibit a clear two-step transition, indicating that the shocks are starting to form.

Both the forward and reverse shock locations become apparent in Fig. 4.4. The forward shock wave is seen in the radial speed contours (left panel) as sudden colour jumps from purple to blue, and from pinkish to yellow in the scaled magnetic field (right panel). In this forward shock, the slow solar wind plasma is accelerated, compressed, and also the magnetic field magnitude increases significantly in the downstream region. We remark that the CS, indicated as a dip in the magnetic field intensity, crosses the forward shock at ~3 AU (see the right panel of Fig. 4.4).

At small radial distances ($r < 2.5$ AU), the reverse shock is observed as colour jumps from yellow to reddish orange in both left and right panels of Fig. 4.4. At larger radial distances, the reverse shock becomes clearer as indicated by the sharp colour transitions from purple to blue (left panel) and from blue to black (right panel). The reverse shock decelerates and compresses the fast solar wind and increases the magnetic field in the shocked plasma. At large radial distances, the reverse shock is in fact travelling into

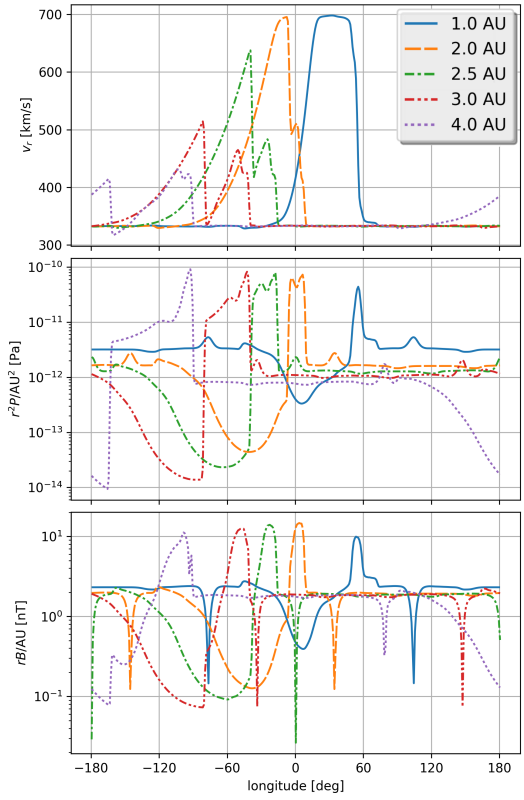

Figure 4.5: Longitudinal profiles of the radial velocity (top panel), scaled thermal pressure (middle panel), and scaled magnetic field magnitude (bottom panel) at different radial distances.

the rarefaction region behind the fast solar wind stream. This is due to the relatively small size of the source region of the fast solar wind.

As illustrated in Fig 4.6, the SI is characterised by a reversal of the longitudinal solar wind flow angle (see the yellow stripe separating the blue and reddish bands), since the shock waves and the interaction between the two shocked plasmas deflect the solar wind in different directions. Figure 4.6 also shows how the IMF converges towards the SI inside the CIR; thus embedding the SI in a strong magnetic field. In addition, although not shown here, the SI is characterised by a relatively abrupt change in plasma density. As discussed below, the different properties of the shocked fast and slow solar wind plasmas, and their SI may have a non-negligible effect on the energy changes of energetic particles.

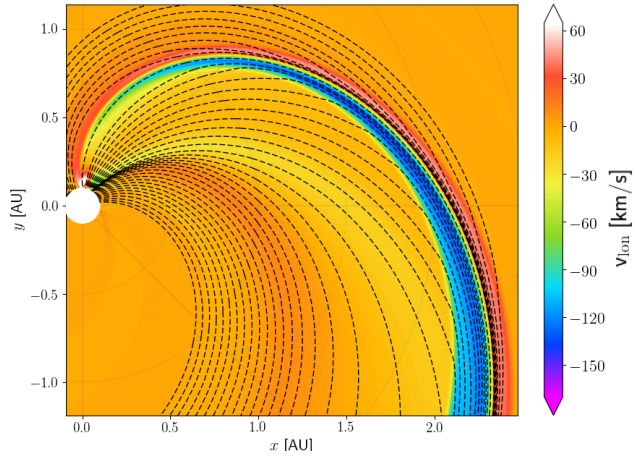

Figure 4.6: Longitudinal velocity profile of the solar wind in the heliographic equatorial plane, illustrating the streaming interface (the yellow stripe separating the blue and reddish bands). The black dashed lines are magnetic field lines, drawn with a constant longitudinal separation of 3.5° at $r = 1$ AU.

4.4.2 SEP transport in the heliosphere

We consider a delta injection in time of 10^8 protons with an energy of 4 MeV, an isotropic pitch-angle distribution, and uniformly distributed over a spatial region described by

$$(\text{longitude}, \text{latitude}) \in [75°, 105°] \times [-5°, 5°] \tag{4.10}$$

at the inner boundary of the heliospheric model. Comparing to the source of the fast solar wind (see Eq. (4.9)), the particle injection region covers a small part of the slow solar wind, the transition zone and a significant part of the fast solar wind. Such a configuration, in which energetic particles are impulsively injected near the boundary of a coronal hole, may especially be representative for ^{3}He-rich SEP events (see e.g., Wang et al., 2006; Kocharov et al., 2008a; Bučík et al., 2018).

The choice of our injection region also ensures that the particles do not interact with the CS during the 16 h that we propagate the particles. The effects of the CS on the particle distributions near a CIR is left for future work.

Using a mono-energetic particle injection allows us to study the energy changes of the particles more easily and to compare the results with those obtained in Section 4.3. As in Section 4.3, we assume a constant radial mean free path $\lambda_\parallel^r = 0.3$ AU for 4 MeV protons throughout the entire heliosphere. Since we are using a constant radial mean free path, the actual parallel mean free path will vary according to $\lambda_\parallel = \lambda_\parallel^r / b_r^2$. At a

fixed radial distance, b_r is larger in the fast solar wind than in the slow solar wind, such that the parallel mean free path is larger in the former as compared to the latter. In the CIR, the parallel mean free path will have values between those of the fast and slow solar wind. Observations have shown that the parallel mean free path in the fast solar wind is typically smaller than in the slow solar wind (see, e.g., Erdos et al., 1999). Nevertheless, we remark that the particles' mean free path might vary rather strongly across solar wind regimes with different flow speed (see, e.g., Pacheco et al., 2017), and hence our assumption of a constant $\lambda_{\parallel}^{r}$ might underestimate this variation.

We perform simulations both with and without cross-field diffusion. The simulations without cross-field diffusion do however include the effect of particle drifts, and hence there is a possibility for the particle to move perpendicular to the IMF. To characterise $\kappa_{\perp}$ we assume as in Section 4.3 that $\alpha = 10^{-4}$ in Eq. (4.6). Moreover, we choose the reference magnetic field magnitude B_0 to be the maximum magnetic field strength at 1 AU, i.e., $B_0 = \max_{r=1\,\mathrm{AU}} B = 9.7\,\mathrm{nT}$. This maximum is obtained in the compressed shocked slow solar wind, and hence the cross-field diffusion is the smallest there. In contrast, the shocked fast solar wind contains a magnetic field ($\sim$2 nT) that is significantly smaller than the one of the shocked slow solar wind. This means that the cross-field diffusion will be stronger in the shocked fast solar wind. The SI separates these plasma populations and therefore also acts as a boundary across which almost no particle can diffuse in our simulations. This is clearly seen in our simulations when injecting particles only in the fast solar wind regime (not shown here). Since our injection region is connected to magnetic field lines at both sides of the SI, we do not see a sudden dip in the overall particle intensity near the SI, something that is often observed in energetic particle events related to CIRs (see e.g., Strauss et al., 2016; Dwyer et al., 1997). However, as described in Section 4.4.4, near the SI we do see a decrease in intensity of the high-energy channels, since the magnetic field lines immediately on either side of the SI originate from the transition region itself. These IMF lines therefore do not intersect the compression or shock waves bounding the CIR, where the particles may accelerate or reflect. In our simulations, the SI acts as a diffusion barrier because of the increase in magnetic field strength in the shocked slow solar wind. However, Strauss et al. (2016) argue that the reduction in cross-field diffusion near the SI is due to strong damping of magnetic field fluctuations perpendicular to the SI, leading to an anisotropic cross-field diffusion.

Finally, we note that at 1 AU the ratio of the perpendicular mean free path to the parallel mean free path in the CIR is, in our simulations, at most $\lambda_{\perp}/\lambda_{\parallel} = 3.81 \times 10^{-4}$. This is small compared to the values obtained by Dwyer et al. (1997), who find ratios of the order of unity for three CIRs using data from the Wind spacecraft. However, in our results below we show that the magnetic field topology inside a CIR may increase the effect of the cross-field diffusion, without necessitating increased amounts of turbulence or large values of $\lambda_{\perp}/\lambda_{\parallel}$.

Figure 4.7 shows the total particle density drawn in grey shades on top of the radial

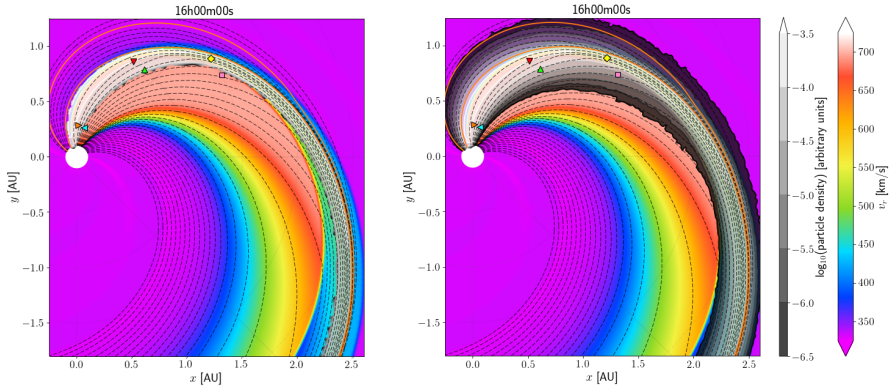

Figure 4.7: Particle densities drawn in grey shades on top of the radial velocity profile of the background solar wind, 16 h after the particle injection. The left and right panels correspond to the cases without and with perpendicular diffusion, respectively. The solid orange and dashed black lines represent magnetic field lines, drawn with a constant longitudinal separation of 3.5° at $r = 1$ AU. The markers correspond to the location of the different observers discussed in the text.

velocity profile of the background solar wind in the solar equatorial plane, 16 h after the particle injection. The left panel of Fig. 4.7 corresponds to the simulation assuming $\kappa_\perp = 0$, while the right panel corresponds to the simulation with $\kappa_\perp \neq 0$. In contrast to the cases discussed in Section 4.3 with a Parker solar wind configuration, the difference between the simulations is significant. At 1 AU, the longitudinal extent of the particle zone for the case with cross-field diffusion is more than twice that of the case without cross-field diffusion, although this extended area shows a particle density two-orders of magnitude smaller than in the main streaming zone. We also performed a simulation where we injected particles only in the slow solar wind of the EUHFORIA simulation and obtained similar results as for the simulations shown in Section 4.3, i.e., the cross-field diffusion had only a weak effect. The reason why the cross-field diffusion becomes more effective in the CIR is because the CIR contains compressed IMF lines that are widely separated in the unperturbed solar wind (see Fig. 4.7). An example of such magnetic field lines is the pair of orange lines in Fig. 4.7. Even a very small cross-field motion in the CIR can transport a particle across these magnetic field lines. This results in a significant angular spread of the particle density for $r \lesssim 2$ AU, when particles return from the CIR to the unperturbed fast or slow solar wind. Such a reversal in the propagation direction of particles travelling inside the CIR is facilitated due to the IMF lines converging towards the SI, hence acting as a magnetic mirror. Apart from the SI, the forward and reverse shock waves may also mirror the particles. As a consequence of the existence of these three magnetic mirrors, there is a significant amount of sunward propagating particles and particle densities remain high at small

radial distances for a prolonged amount of time, as shown in Section 4.4.4.

4.4.3 Particle acceleration

The FTE contains the necessary physics[1] for modelling the acceleration of particles travelling in, e.g., converging or accelerated flows. The different mechanisms that alter the particle's energy can be more easily understood by rewriting Eq. (4.4) in the following form (le Roux & Webb, 2012):

$$\frac{1}{p}\frac{dp}{dt} = -\frac{1}{3}\nabla \cdot \mathbf{V_{sw}} + \frac{1}{2}(1-3\mu^2)\mathbf{bb} : \boldsymbol{\sigma} - \frac{\mu}{v}\mathbf{b}\cdot\frac{d\mathbf{V}_{\mathrm{sw}}}{dt}, \tag{4.11}$$

where $\boldsymbol{\sigma}$ denotes the shear tensor given by

$$\sigma_{ij} = \frac{1}{2}\left(\frac{\partial V_{\mathrm{sw,i}}}{\partial x_j} + \frac{\partial V_{\mathrm{sw,j}}}{\partial x_i} - \frac{2}{3}\frac{\partial V_{\mathrm{sw,i}}}{\partial x_i}\delta_{ij}\right). \tag{4.12}$$

The first term on the right hand side of Eq. (4.11) illustrates the effect of converging or diverging flows on the particle's energy. A particularly important example of a converging flow is found at a shock wave, where the plasma flow has a negative divergence. Each time the particles cross the shock they will therefore accelerate, a mechanism known as diffusive shock acceleration or first order Fermi acceleration. As discussed in Section 4.4.1, the EUHFORIA simulation contains two separate shock waves bounding the CIR which, as shown below, accelerate particles. Such diffusive particle acceleration at the forward and reverse CIR shock waves is considered as a likely mechanism to explain the particle intensity peaks often measured at CIRs (see e.g., Richardson, 2004, and references therein). As already noted before, the finite resolution of the MHD simulation will unavoidably smear out the shocks over a spatial region larger than the width of real CIR shocks, making the terminology "shock acceleration" not strictly applicable to our results. However, also in large amplitude compression waves, particles will gain energy due to their motion and scattering in the converging flows, similar to what happens during first order Fermi shock acceleration. This mechanism was proposed by Giacalone et al. (2002) as the main acceleration mechanism in CIRs, producing energetic particle populations at smaller radial distances, before the forward and reverse shocks are formed.

In our simulation, IMF lines to which the majority of the particles are injected are initially diverging while residing in the unperturbed slow or fast solar wind, and converging once entering the transition zone or CIR at larger radial distances. Hence, particles injected on those IMF lines will initially lose energy due to adiabatic deceleration, and later, gain energy due to adiabatic acceleration. In addition, there are

[1] At least, when the test-particle approach is an appropriate approximation (see also Section 1.5.2).

also particles injected in the transition zone itself, that therefore follow IMF lines that never cross any compression or shock wave and that are immediately adjacent to the SI in the CIR. Due to the lack of any compression or shock wave crossings, these particles will not experience any substantial acceleration. However, inside the CIR the flows are slowly converging towards the SI, which may result in weak adiabatic acceleration.

The other two mechanisms contained in Equation (4.4) that alter the momentum of the particle are the flow shearing and flow acceleration, respectively represented in the last two terms on the right hand side of Eq. (4.11). These terms are non-zero at the shock waves, and it is the cosine of the pitch-angle which determines whether the particle gains or loses energy upon crossing the shock. For example, the acceleration (deceleration) of the solar wind across the forward (reverse) shock, will increase (decrease) the particle's energy when it travels from the downstream to the upstream region, and vice-versa. There is also flow shear in the CIR, especially at the streaming interface, where the shocked decelerated fast solar wind meets the shocked accelerated slow solar wind. Figure 4.8 shows, at $t = 12$ h, the particle density of protons accelerated above their initial energy, registered in two energy channels: 4.2 MeV (top row) and 4.6 MeV (bottom row). The left (right) column shows the results for the simulation without (with) cross-field diffusion. The background in the top and bottom row depict, respectively, the radial velocity and the scaled pressure, r^2P, of the solar wind. The four panels of Fig. 4.8 clearly show the existence of an accelerated particle population centred on the reverse shock wave. As seen in the temporal evolution of this particle population (available as a movie in the web version of Wijsen et al., 2019a), the 4.2 MeV channel starts being populated 2 h and 40 min after the injection, and at a radial distance of ~1.2 AU, while the 4.6 MeV channel starts getting populated about 1 h and 40 min later, at a slightly larger radial distance (~1.35 AU).

By calculating the length of the field line on which the first accelerated particles appear, a particle of 4 MeV would need ~2.2 h to reach the acceleration zone if it were to travel scatter-free. When travelling towards the reverse shock, the particles will however lose momentum due to adiabatic deceleration, and hence it will arrive at the shock wave with an energy lower than 4.0 MeV. As shown in Section 4.3, this energy loss can be significant, especially since the particles are travelling in a fast solar wind during their journey towards the reverse shock wave. Therefore, the particles may need more than one shock crossing to reach energies above 4.0 MeV. Multiple shock wave crossings are facilitated due to the focusing/mirroring effect at both sides of the shock. When travelling in the sunward direction, the particle will eventually be mirrored and focused in the direction of the shock because of the converging magnetic field lines near the Sun. After crossing the shock wave, the particle will propagate in the CIR where the magnetic field lines are converging towards the SI, and hence the particle is likely to eventually get mirrored and focussed back towards the shock. Apart from particle mirroring due to the mean magnetic field, scattering of the particles due to turbulence will also facilitate multiple shock crossings.

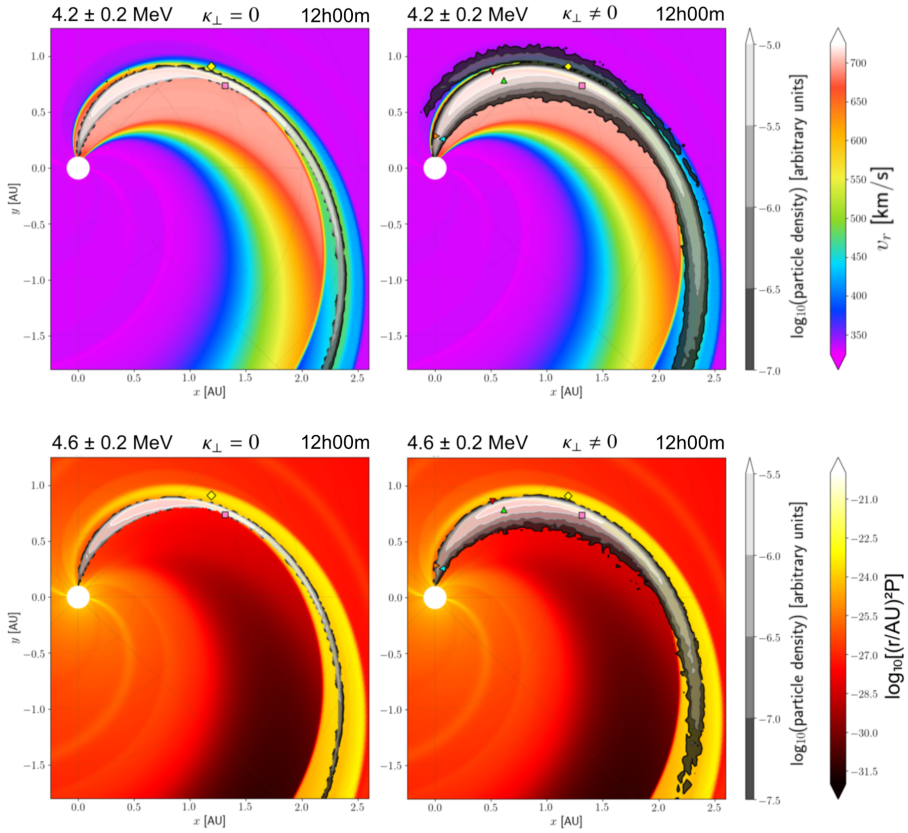

Figure 4.8: Top row shows particle intensities of energy channel 4.2 MeV drawn in grey shades on top of the radial velocity profile of the solar wind. The bottom row shows particle intensities of energy channel 4.6 MeV drawn in grey shades on top of scaled pressure profile of the solar wind. The right and left columns correspond, respectively, to the simulations with and without perpendicular diffusion. The entire temporal evolution is available as an movie in the web version of Wijsen et al. (2019a).

A notable difference between the simulations with and without cross-field diffusion is the existence of a second population of accelerated particles for the former case. Centred on the forward shock of the CIR, this population is only visible in the 4.2 MeV energy channel (see the top right panel of Fig. 4.8) and from ∼6 h after the particle injection, at a radial distance of ∼1.6 AU. The IMF lines originating from the injection zone do not traverse the forward shock at these large radial distances, and hence these particles are there as a result of cross-field motions inside the shocked slow solar wind. Remark that both populations of accelerated particles are separated by the SI. The existence of this additional population of accelerated particles illustrates that a weak cross-field diffusion can have noticeable effects on energetic particle populations when the particles are travelling in a non-nominal solar wind configuration.

4.4.4 Proton fluxes measured by virtual observers

We now analyse the proton intensities and anisotropies measured by a fleet of virtual observers located in the solar equatorial plane, covering the entire zone where energetic particles travel during the first 16 h after their injection. We have studied 47 stationary observers positioned at radial distances of 0.28 AU, 1 AU, 1.5 AU and 2 AU from the Sun. In order to illustrate the richness and variety of different time profiles encountered, even when looking at observers located relatively close to each other, we have selected six observers to be discussed. These observers are indicated by the various markers in Fig. 4.7. All the intensities are normalised to the maximum intensity measured at 1 AU in the 3.8 MeV energy channel by the observer located at 56.11° in longitude (not shown here). In this section, we mainly focus on the simulations done with cross-field diffusion, except for the observers located at 1.5 AU, for which we also discuss the case $\kappa_\perp = 0$.

Figure 4.9 shows 2.0 − 4.8 MeV proton intensity-time profiles (top panels) and anisotropy time profiles (bottom panels) gathered by two observers located at a radial distance of 0.28 AU, which corresponds to the closest planned perihelion for Solar Orbiter. The left panel of Fig. 4.9 shows the results for the observer located at a longitude of 76.5° represented by the cyan left facing triangle in Fig. 4.7. This observer is positioned in the fast solar wind during the entire simulation. Initially, at $t = 0$ h, the observer is magnetically connected to the reverse shock at $r \sim 1.2$ AU, yet this connection point moves towards larger radial distances due to the antisunward propagation of the reverse shock. The early sharp intensity peak of the 3.8 MeV energy channel (solid purple curve) reflects the mono-energetic delta time injection of the 4 MeV protons. However, the 3.4 MeV energy channel (dot-dashed red curve) and even the lower energy channels are quickly populated due to efficient adiabatic deceleration, since particles travel in a fast wind stream.

A particularly interesting feature is that the intensity of the 3.8 energy channel switches

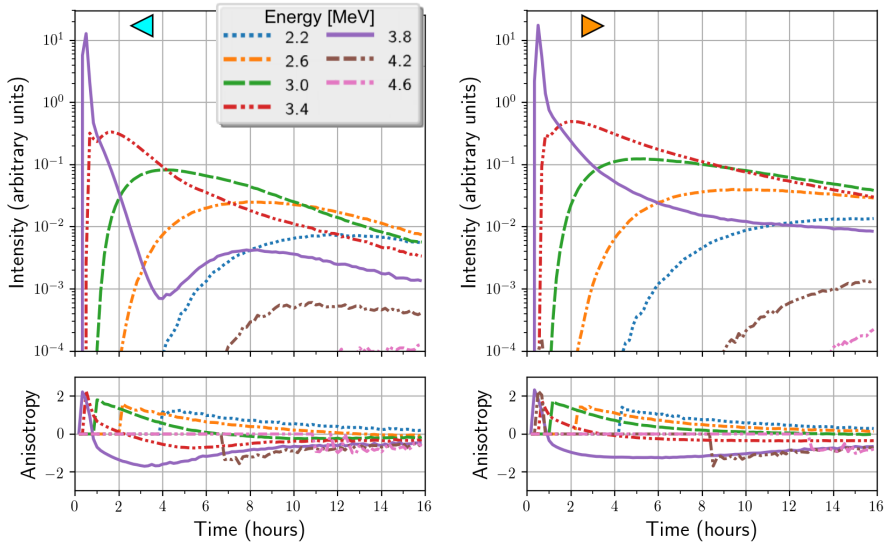

Figure 4.9: Proton intensities (top panels) and anisotropies (bottom panels) measured in the solar equatorial plane at a heliocentric radial distance of 0.28 AU and at longitudes of 76.5° (left panel) and 87.5° (right panel).

from rapidly decreasing to gradually increasing after ~4 h. This increase is due to particles that got mirrored at the reverse shock. The reason why these particles have not yet adiabatically decelerated to lower energy channels is because they have gained energy at the reverse shock, counteracting the energy losses they suffer when travelling in the fast solar wind.

The right panel of Fig. 4.9 shows the intensity and anisotropy profiles for an observer located at a longitude of 87.5°. Like in the previous instance, this observer is positioned in the fast solar wind, but this time close to the transition region towards the slow solar wind (see the right facing orange triangle in Fig. 4.7). The main difference with respect to the former observer is that the intensity profile of the 3.8 MeV protons does not show this double peaked structure, but instead it monotonically decreases after onset. This is because the IMF lines connecting the observer move already at small radial distances (< 1 AU) into the transition zone between the fast and slow solar wind, and hence the magnetic mirrors are much closer to the observer. At these distances, the forward and reverse shock waves are not yet formed and hence there is no significant acceleration of particles. Despite the absence of a real shock wave, the particles may adiabatically gain energy upon crossing the compression wave between the fast solar wind and the transition zone, keeping the 3.8 MeV energy channel populated. In addition, the enhanced magnetic field strength in the compression waves will again act as a particle

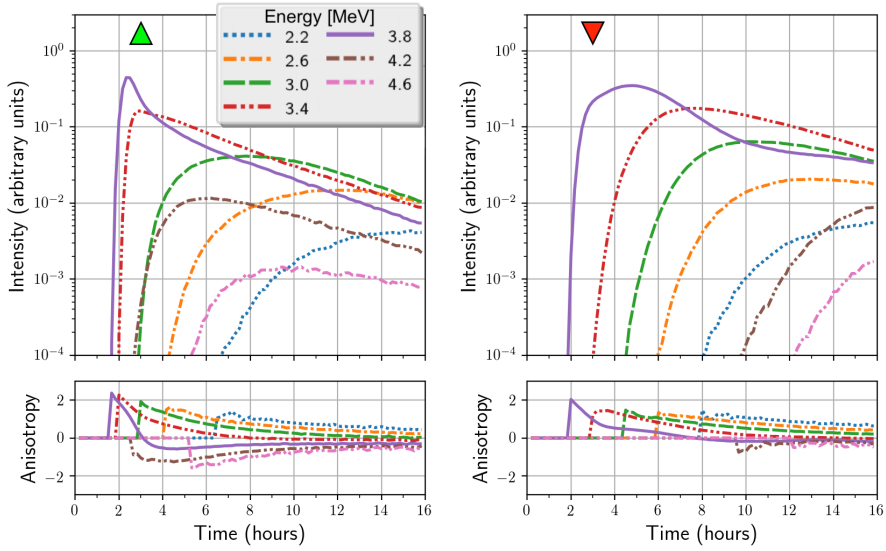

Figure 4.10: Proton intensities (top panels) and anisotropies (bottom panels) measured in the solar equatorial plane at a heliocentric radial distance of 1 AU and at longitudes of 52° (left panel) and 59.3° (right panel).

mirror. We conclude thus that the combination of acceleration and mirroring at the compression/shock waves explains why, for both observers at 0.28 AU, the intensities in all energy channels remain high throughout the simulation, which is in sharp contrast with the intensity profiles shown in the lower left panel of Fig. 4.3 for an observer in a Parker spiral at a similar radial distance.

Next we consider two observers located at a radial distance of 1 AU. The first of these observers is located at a longitude of 52° (green upward triangle in the right panel of Fig. 4.7). The proton intensity and anisotropy profiles for this observer are shown in the left panel of Fig. 4.10. As for the observers at 0.28 AU, particles propagate towards this observer in the fast solar wind and hence low-energy channels close to 4 MeV are populated rapidly due to adiabatic deceleration. During the entire simulation, the IMF lines passing through the stationary observer cross the reverse shock at a radial distance around 1.3 AU. The observer is thus constantly closely connected to the reverse shock at the location where the first population of accelerated particles generated (see Section 4.4.3). As a consequence, this observer measures relatively high particle intensities in the 4.2 MeV (brown curve) and 4.6 MeV (pink curve) energy channels, which are populated by those shock-accelerated particles. Since the observer is connected to the reverse shock at a radial distance larger than 1 AU, and the magnetic field is pointing anti-sunward, the anisotropies of the accelerated

particles are all negative. After ~3 h, the anisotropy for the 3.8 MeV channel (purple curve) is negative, suggesting that this channel is also mainly populated by particles that interacted with the shock. This explains the slow decrease of the 3.8 MeV proton intensities after ~3 h which is in sharp contrast to the intensity profiles discussed in Section 4.3 for particles travelling in a Parker solar wind (see e.g., the lower right panel of Fig. 4.3 for a comparison).

The second observer at 1 AU is located at a longitude of 59.3° (see the downward facing red triangle in the right panel of Fig. 4.7). Initially, this observer is positioned on the compression wave between the slow solar wind and the transition region. Later on, the transition region rotates past the observer until it crosses, near the end of the simulation, the boundary between the transition region and the fast solar wind. The intensity and anisotropy profiles for this observer are shown in the right panel of Fig. 4.10. The most remarkable feature is the distinct shape of the 3.8 MeV energy channel, and the relatively big time gap between the arrival of particles of energy channels 3.8 MeV and 3.4 MeV, as compared to the first observer at 1 AU (see the left panel of Fig. 4.10). These features can be explained as a consequence of the interplay between adiabatic acceleration and deceleration as follows. The first particles reaching the observer at ~2 h are following IMF lines that start in the slow solar wind, and hence they are adiabatically decelerated during the first part of their journey. However, as explained in Section 4.3, this adiabatic deceleration will be only limited due to the slow wind speed (~330 km s^{-1}). Before reaching the observer, the particles leave the slow solar wind and cross the compression wave bounding the transition zone, where they may accelerate to some extent. The net result is that more particles remain in their initial 3.8 MeV energy channel. After ~5 h, the intensity of the 3.8 MeV energy channel starts decreasing more rapidly until ~10 h. During that decrease, the observer is connected to IMF lines that are (almost) entirely inside the transition region at small radial distances and at larger radial distances they lie adjacent to the SI. Hence, as explained in Section 4.4.3, due to the lack of converging flows, the particles following these field lines will mostly adiabatically decelerate. In addition, these particles do not experience the magnetic mirroring effect of the compression or shock waves. Later on, at ~10 h, the intensity of the 3.8 MeV energy channel starts decreasing more gradually, since the observer becomes connected to IMF lines that cross the compression wave between the fast solar wind and the transition zone, where the particles may accelerate. Near ~12 h, the observer enters the fast solar wind and establishes connection with IMF lines crossing the reverse shock at radial distances larger than 1 AU. However, it is seen that the observer already measures particles with energies above 4 MeV before 12 h. These particles are there solely due to cross-field diffusion, since they are not observed in the simulations with zero cross-field diffusion (not shown here).

For the two observers located at 1.5 AU, we discuss the resulting profiles for both the simulations with and without cross-field diffusion. The first observer we consider (pink square in Fig. 4.7) is located at a longitude of 29.8°. The top (bottom) graphs in the left

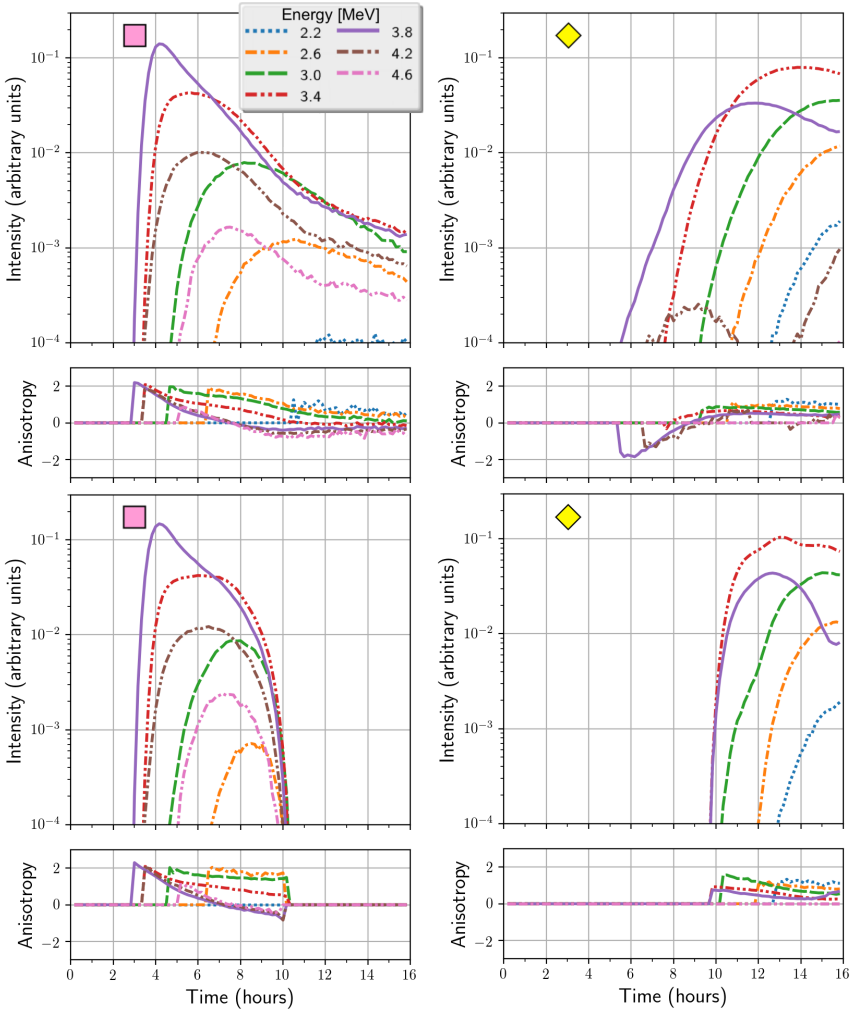

Figure 4.11: Intensities and anisotropies measured in the solar equatorial plane at a heliocentric radial distance of 1.5 AU and at longitudes of 29.8° (left column) and 37.54° (right column). The top and bottom rows correspond, respectively, to the simulations with and without perpendicular diffusion.

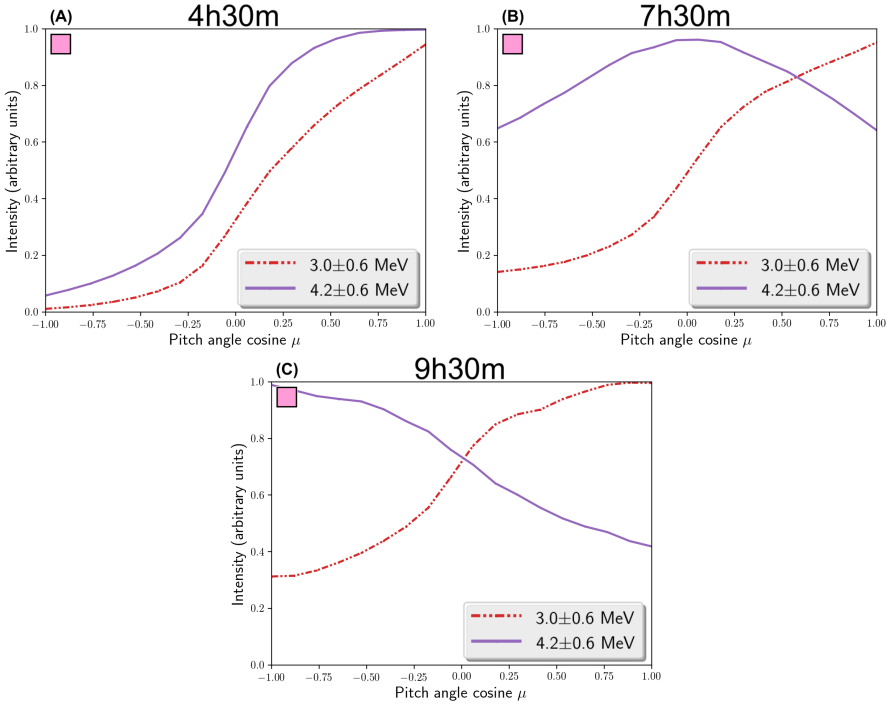

Figure 4.12: Pitch-angle distribution functions at three different time instances for an observer located at 1.5 AU and at longitude of 29.8°. See top left panel of Fig. 4.11 for the intensities and anisotropies of this observer.

column of Fig. 4.11 respectively show the particles' intensity and anisotropy profiles seen by this observer for the case with (without) cross-field diffusion. This observer is in particular interesting because it crosses the particle acceleration site at the reverse shock, at ~7.5 h. This is indicated by the anisotropies of the energy channels containing accelerated particles which switch sign around that time. This becomes clear after inspecting the PADs. Figure 4.12 shows, for the case with cross-field diffusion, the proton PADs at three time instances for two different energy channels, 4.2 ± 0.6 MeV (purple curves) and 3.0 ± 0.6 MeV (red curves). Panel A corresponds to 4.5 h after the injection, when the shock is between the Sun and the observer, whereas Panel C shows the PADs at 9.5 h, when the observer is located between the Sun and the shock. Panel B shows the intermediate situation, i.e., when the observer is located on the shock. The 4.2 ± 0.6 MeV channel is mainly populated with shock-accelerated particles and hence, the corresponding PAD (purple curves) turns over during the shock passage, i.e., the PAD evolves from an increasing to a decreasing function of μ. At the shock passage, the PAD becomes more horizontal, reflecting the less anisotropic conditions there. In

contrast, the 3.0 ± 0.6 MeV channel is mostly populated by particles adiabatically decelerated at smaller radial distances. Therefore, the PAD of this energy channel remains an increasing function of μ during and after the observer crossing the shock.

Note also that in Fig. 4.11, the 2.2 MeV channel is almost completely depleted of any particles for this observer. This contrasts with what is observed at 0.28 AU and at 1 AU, where this energy channel shows significant intensities. This difference can be attributed to the combined effect of shock acceleration and adiabatic compression in the CIR occurring at radial distances larger than 1 AU.

The drop in intensities after ∼10 h is because the observer moves out of the particle streaming zone due to the corotation effect, as is clearly seen in the case without cross-field diffusion (bottom left panel of Fig. 4.11). At the same time, the top panel of Fig. 4.11 shows that the cross-field diffusion has a stronger effect compared to the cases discussed in Section 4.3.

The second observer at 1.5 AU is located at a longitude of 37.54° (yellow diamond in Fig. 4.7). This observer is initially positioned in the slow solar wind outside the particles' streaming zone, and only enters this zone after > 6 h due to the corotation of the particles with the IMF, as shown by the intensity and anisotropy time profiles in the right column of Fig. 4.11. Comparing the cases with (top panel) and without (bottom panel) cross-field diffusion, the onset of the particle event occurs about 4 h earlier in the former case. For this case, the first observed particles are all high-energy particles (channel 3.8 MeV) showing a negative anisotropy. This agrees with the finding above that the cross-field diffusion is more effective at large radial distances in the CIR, such that high-energy particles are initially affected more strongly because they travel faster to those distances. This also explains the time-gap between the arrival of particles populating the 3.8 MeV and 3.4 MeV channels. The negative anisotropy is again an indication of the mirroring effects of the CIR.

Interesting is also the first small bump of 4.2 MeV protons seen only in the simulation with cross-field diffusion, around 9 h. This bump is due to particles accelerated by the forward shock, and it corresponds to the second accelerated particle population discussed in Section 4.4.3 that reached those IMF lines due to cross-field motions. At the end of the particle event, this observer detects a second increase of intensity in the 4.2 MeV channel for the case with cross-field diffusion, since the observer approaches the reverse shock wave.

For the simulation assuming $\kappa_\perp = 0$ (see the bottom right panel of Fig. 4.11), after a prompt onset, the 3.8 MeV proton intensity-time profile shows a rounded plateau-shape similar to that obtained for the observer at 1 AU depicted in the right panel of Fig. 4.10. This shape can again be attributed to the non-trivial interplay between acceleration/deceleration processes occurring in the slow solar wind, the transition zone and the forward shock. The sharp decrease between 13 and 15 h is again due to

the passage of the SI and its adjacent magnetic field lines, i.e., the field lines that do not cross any shock/compression wave where the particles can accelerate and mirror.

4.5 Summary and conclusions

In this chapter, we presented the verification and the first results of the PARADISE model, which solves the FTE to obtain the energetic particle distribution function in the inner heliosphere. In Section 4.3 we tested PARADISE by propagating particles in a nominal IMF for slow and fast solar wind configurations. We started with presenting the results of simulations both with and without cross-field diffusion, yet neglecting particle convection and adiabatic energy losses in the solar wind. These simulations illustrated how cross-field diffusion can make sharp cut-offs in particle intensities more gradual, a result previously shown by Dröge et al. (2010). Next we included all terms of the FTE, and illustrated how particles are considerably more adiabatically decelerated in the fast solar wind than in the slow solar wind. For a fixed source of particles near the Sun, Ruffolo (1995) and Kocharov et al. (1998) quantified the decay rate of proton intensities for 1 AU observers due to adiabatic deceleration. We have shown instead the substantial energy loss of particles in the fast solar wind by depicting how the 4 MeV injected protons populated lower-energy channels in the case of observers located at two different radial distances. Comparing for those observers, the most populated energy channels at every time instance, revealed differences that reflect the dependence of magnetic focusing on the particle's velocity and on the radially decreasing magnetic field strength.

In the second part of the chapter we propagated particles in a solar wind generated by EUHFORIA. A slow solar wind configuration with an embedded fast solar wind stream was modelled. The substantial difference between the slow and fast solar wind speeds resulted in the formation of a CIR bounded by a forward and a reverse shock at relatively small radial distances (~1.5 AU onwards). Hence, unlike previous simulations of impulsive SEP events in CIRs (Giacalone et al., 2002; Kocharov et al., 2008b), we use a 3D MHD simulation that includes both the forward and reverse shock waves in the same set-up, which allows a more complete description of the particles' intensity-time profiles obtained by virtual observers placed at different locations in the ecliptic plane. We considered an impulsive injection of 4 MeV protons at the inner boundary of EUHFORIA, uniformly spread over a region covering a small part of the slow solar wind and a substantial part of the fast solar wind stream. The particles were propagated both with and without cross-field diffusion. Despite using a small perpendicular mean free path, the differences between both cases were substantial. When cross-field diffusion was switched on, particles spread over a much larger region in the heliosphere, more than doubling its longitudinal extent in the solar equatorial plane. In contrast, this feature was not observed in the simulations using a simple

Parker solar wind, despite using a similar cross-field diffusion. Therefore, the increase of efficiency of the cross-field diffusion in the simulation containing the embedded fast solar wind stream, can be attributed to the more complex magnetic field configuration found in the CIR. In particular, inside the CIR, magnetic field lines are converging such that small cross-field motions can transport particles to magnetic field lines that are widely separated in the unperturbed solar wind. This increase of efficiency of cross-field diffusion at the boundary between a slow and fast solar wind stream could potentially help explain some of the actual measured particle events that show a large angular spread in the heliosphere.

We note that we are using a rather simplified model for the cross-field diffusion. However since we use a very weak cross-field diffusion, which is in addition minimal at the CIR shocks and at the SI due to its inverse scaling with the magnetic field strength, it is likely that a more realistic treatment of the cross-field motions will influence the particle densities in the heliosphere in a similar or even stronger way.

Our simulations also showed the formation of an accelerated particle population centred on the reverse shock of the CIR. In particular, the acceleration site of the particles was mainly situated at a radial distance of ~1.5 AU, yet this location merely reflects the magnetic connection between the reverse shock and the particles injection region. There are also field lines originating from the particle injection region that cross the boundary between the slow or fast solar wind and the transition zone at small radial distances, i.e., before the compression waves have steepened into shock waves. The particles following these field lines show already signatures of strongly reduced adiabatic deceleration and even adiabatic acceleration. This is exemplified by the plateau-shape in the 3.8 MeV energy channel during the first hour of the particle event (see, e.g., the right panel of Fig. 4.10).

A second population of accelerated particles, centred on the forward shock near ~1.6 AU, appeared in the case of the simulation with cross-field diffusion. This population of accelerated particles was not present in the case without cross-field diffusion, since no magnetic field lines connected the particle injection region with the forward shock at those larger radial distances. Remark that these forward shock accelerated particles were injected in the slow solar wind, since particles injected in the fast solar wind cannot reach the forward shock due to the SI acting as a diffusion barrier. The formation of an extra population of accelerated particles solely because of cross-field diffusion illustrates again how a weak cross-field motion can significantly alter the particle population in the heliosphere when the solar wind is more complex than a simple Parker configuration. This is important since in reality, a Parker configuration is relatively rare, and can most of the time only be found during solar minimum.

We conclude that the more complex magnetic field configuration of the CIR produced particle time-intensity profiles that differ strongly in shape from the ones obtained when using a nominal IMF. By placing virtual observers at different locations in the

heliosphere, we illustrated that the intensity profiles can largely vary from one to the other, even for observers located close to each other, i.e., separated $< 10^{\circ}$ in longitude. These differences can only be attributed to the varying solar wind conditions since the particles were injected uniformly over the selected region at the inner boundary of EUHFORIA. Hence, the background solar wind can have a major influence on the particle transport, which illustrates the necessity of using more realistic background solar wind configurations when studying SEP events. MHD codes like EUHFORIA can, to some extent, provide such realistic background winds.

Chapter 5

The interplanetary spread of SEPs near a CIR

"If you think you are too small to make a difference, try sleeping with a mosquito."
– Dalai Lama

Abstract. This chapter extends the study of Chapter 4, by investigating how a corotating interaction region (CIR) influences the spread of solar energetic protons in space. PARADISE is used to model the transport of 4 MeV protons, which are injected uniformly from four different regions located at 0.1 AU in a solar wind containing a CIR. The source regions have the same size and shape, yet are shifted in longitude and are therefore magnetically connected to different solar wind regions.

The intensity and anisotropy profiles measured along a selection of interplanetary magnetic (IMF) lines are found to vary strongly according to the solar wind conditions. IMF lines that cross the CIR shocks show the formation of accelerated particle populations, with the reverse shock wave being the more efficient particle accelerator. Furthermore, it is shown that the longitudinal width of the particle distribution can increase, decrease, or remain constant with increasing heliocentric radial distance, depending on the underlying IMF structure. Cross-field diffusion increases this longitudinal width, but does not alter its increasing or decreasing behaviour as a function of radial distance.

Finally, it is shown that the deflection and compression of the IMF in the CIR deforms the three-dimensional shape of the particle distribution, such that the original shape of the injection profile is lost.

This chapter is entirely based on Wijsen et al. (2019b).

5.1 Introduction

Understanding the spatial variation of SEP intensities has been the subject of several multi-spacecraft studies (e.g., Dresing et al., 2012; Lario et al., 2013; Dresing et al., 2014; Wiedenbeck et al., 2013; Richardson et al., 2014; Klassen et al., 2016; Lario et al., 2017, to cite a few amongst the more recent works). These studies have illustrated that the spatial dependence of intensity distributions can vary from nominal Gaussian-like shapes (e.g., Richardson et al., 2014; Wiedenbeck et al., 2013; Lario et al., 2013) to more complex and non-symmetric profiles (e.g., Klassen et al., 2016). In addition, the longitudinal extent of SEP events in space has been observed to vary significantly, with some events even being circumsolar (e.g., Gómez-Herrero et al., 2015). The onset times of SEP events have also been shown to vary strongly across multiple spacecraft, with the nominally best connected spacecraft to the parent particle source not always showing the earliest onset (e.g., Klassen et al., 2015).

Various scenarios have been proposed to explain these observations, ranging from processes occurring in the corona, like e.g., strongly tilted non-radial magnetic fields (e.g., Klein et al., 2008; Klassen et al., 2018) or asymmetric coronal shock waves (e.g., Lario et al., 2014), to processes occurring in the interplanetary medium like e.g., cross-magnetic field diffusion (e.g., Dröge et al., 2010; Laitinen et al., 2013; Dröge et al., 2014) and/or different pitch-angle scattering conditions along particle paths residing in different solar wind streams (e.g., Pacheco et al., 2017). In addition, the IMF can deviate strongly from the nominal Parker spiral due to e.g., CMEs or CIRs, which will also significantly alter the characteristics of SEP events, and hence contribute to the spatial variations observed across SEP events.

The solar wind often contains plasma streams of varying speeds, which may evolve into CIRs if a fast stream follows a slow stream. Hence, understanding energetic particle transport in such conditions has received much attention in recent years (see, e.g., Giacalone et al., 2002; Kocharov et al., 2003; Wu et al., 2014; Mason et al., 2012a). In previous chapter, we used EUHFORIA (Pomoell & Poedts, 2018) to model a localised fast wind stream embedded in an ambient slow solar wind, resulting in a self-consistently generated CIR bounded by forward and reverse shock waves (see Section 4.4). Using PARADISE, the transport of protons in a CIR was modelled by impulsively injecting 4 MeV SEPs. Using a fleet of virtual satellites distributed in the

solar equatorial plane, it was shown how the time-intensity profiles of SEP events can strongly vary from one observer to the other, even when they are located close to each other, that is, separated by less than 10° in longitude. These differences could only be attributed to the varying solar wind conditions, since the particles were uniformly injected from a source region, situated at the inner boundary of EUHFORIA which is located at a heliocentric radial distance of 0.1 AU. Due to the non-nominal IMF topology, nearby located observers can magnetically be connected to solar wind regions with very different properties, and hence sample different particle distributions.

The strong dependence of the modelled time-intensity profiles on the position of the observer suggests that the location and size of the particle source region can also have a considerable effect on the SEP distributions in the heliosphere. In a non-nominal solar wind, small shifts in longitude or latitude can connect the particle source region magnetically to parts of the solar wind with considerably different characteristics. Hence, any shifts in the location of the source region can alter the energy spectrum, the duration, and the spatial spread of energetic particle events. To get better insight on the importance of this effect, in this work, we model the transport of particles injected from four different source regions located also at 0.1 AU from the Sun, that is, at the inner boundary of our solar wind model. These particle source regions are chosen identical in size and shape, but shifted in longitude and hence magnetically connected to different solar wind conditions. We use the same EUHFORIA solar wind configuration as in previous chapter. Our results illustrate how the location of the particle source region and hence the IMF topology can strongly alter the resulting particle distributions in all three spatial dimensions of the heliosphere.

The chapter is structured as follows. Section 5.2 provides the set-up of the PARADISE simulations considered in this chapter. Section 5.3 discusses the results of the simulations. It is shown how the particle intensities and anisotropies along selected magnetic field lines strongly depend on the solar wind properties encountered by the IMF line. Moreover, it is illustrated how the longitudinal intensity and anisotropy profiles are modulated by the CIR structure, and how the radial evolution of the longitudinal width of the particle intensity distributions reflects the IMF topology in the solar equatorial plane. This is analysed by using simulations both with and without cross-field diffusion. It is also illustrated that the particle intensities have a strong latitudinal dependence as well. A summary is given in Section 5.4.

5.2 Simulation set-up

In Chapter 4, we used EUHFORIA to model a solar wind with an embedded fast solar wind stream, generating a corotating interaction region bounded by a forward and a reverse shock wave. In this work, we use the same solar wind model, yet we inject

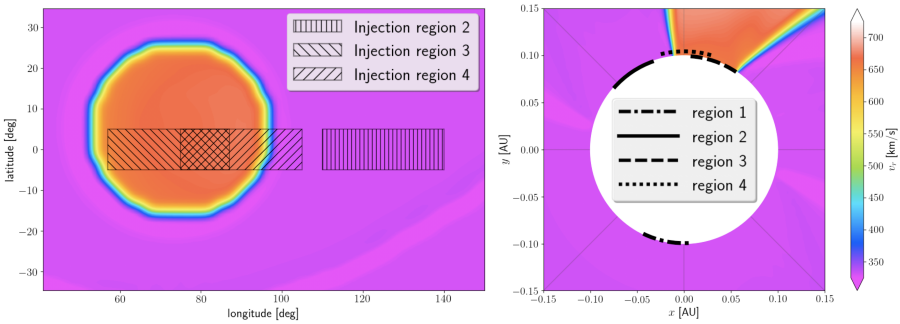

Figure 5.1: Snapshot of the solar wind radial velocity showing a part of the $r = 0.1$ AU inner boundary (left panel) and a part of the solar equatorial plane (right panel). Indicated on both panels are the different particle injection regions.

protons uniformly in the four different injection regions as illustrated in Fig. 5.1. These four injection regions are all centred around the solar equatorial plane and have a longitudinal width of 30° and a latitudinal width of 10°. This rectangular shape makes it straightforward to quantify the latitudinal and longitudinal deformation of the particle streaming zone due to a non-nominal IMF, since in a Parker spiral the longitudinal and latitudinal width remain constant and hence, the rectangular shape is exactly preserved. For the first case, the injection region is located in the slow solar wind (see the right panel of Fig. 5.1), far enough from the CIR such that the particles travel in a nominal slow solar wind. For case 2, the injection region is located in the slow solar wind in front of the CIR in such a way that magnetic field lines connect this injection region with the forward shock of the CIR. In contrast, injection region 3 is entirely located in the fast solar wind stream and magnetically connected to the reverse shock of the CIR. Finally, the injection region of case 4 is the same injection region as discussed in Chapter 4, being located partly in the slow solar wind and partly in the fast solar wind.

Like in Chapter 4, we inject protons impulsively (i.e., a delta injection in time) and with an initial energy of 4 MeV to facilitate the tracking of the energy changes of the particles in the solar wind. We assume the same scattering conditions as in Chapter 4 which are summarised as follows. The pitch-angle diffusion coefficient is characterised by Eq. (4.5), and we take the proton radial mean free path constant and equal to $\lambda_{\parallel}^{r} = 0.3$ AU for 4 MeV protons. The values of the parameters characterising the cross-field diffusion coefficient (Eq 4.6) are $\alpha = 10^{-4}$ and $B_0 = \max B(r = 1\,\text{AU}) = 9.7\,\text{nT}$. As explained in Chapter 4, this maximum value of the magnetic field is obtained in the compressed shocked slow solar wind, where the cross-field diffusion is minimal. In our simulations, the ratio of the perpendicular mean free path to the parallel mean free path inside the CIR and at 1 AU is at most $\lambda_{\perp}/\lambda_{\parallel} = 3.81 \times 10^{-4}$. This is small compared to the values obtained by Dwyer et al. (1997), who find ratios of the order of unity for

three CIRs using 44 – 313 keV/nuc Helium measurements from the Wind spacecraft. Therefore, we expect that the effects of the cross-field diffusion near the CIR found in the results below are likely to be enhanced with a more realistic treatment of the cross-field motions.

Moreover, in the simulations presented below, the same resolution for the pseudo-particle sampling histogram is assumed as in Chapter 4, and the utilised energy channels are listed in Table 4.1.

Finally, we would like to note that the finite resolution of our MHD simulation produces shock waves that are wider than real interplanetary CIR shocks. Therefore, as explained in Chapter 4, one can argue that the terminology "particle shock acceleration" is not strictly applicable for particle acceleration near the strong compression waves in our simulations. However, the particles will gain energy due to their motion and scattering in converging flows characterising these compression waves, which is analogous to what happens during first-order Fermi shock acceleration (see also Giacalone et al., 2002, for a discussion).

5.3 Results

5.3.1 Particle intensities along a magnetic field line

In this section, we analyse the particle intensities and anisotropies measured along four corotating magnetic field lines, which originate from the centre of the different injection regions. The results are shown in Figs. 5.2 and 5.3 for the simulations with non-zero cross-field diffusion. The panels showing the anisotropy profiles indicate the particle propagation direction, since the magnetic field polarity in the unperturbed solar wind and near the fast solar wind stream is different (see Section 4.4.1).

Panel 3a of Fig. 5.2 depicts the corotating IMF line for case 1, together with the energy-integrated omni-directional particle intensity at 12 h 30 min. Panels 1a and 2a show that the lower energy channels are quickly populated by the particles, as a result of adiabatic deceleration. For example, after ~4 h, the 3.4 MeV energy channel shows already intensities of the same order of magnitude as the 3.8 MeV energy channel. Owing to our mono-energetic injection of 4 MeV particles and the nominal solar wind conditions, the 3.8 MeV energy channel can only lose particles, since it cannot get replenished through adiabatic deceleration of protons with energies above 4 MeV or through proton acceleration. The 3.8 MeV protons remaining a prolonged time close to the Sun move quickly to a lower energy channel, since adiabatic deceleration is most efficient at small radial distances ($\nabla \cdot \mathbf{V}_{\rm sw} \propto V_{\rm sw}/r$ in a Parker solar wind). Hence, protons only remain in the 3.8 MeV channel if they propagate quickly, and

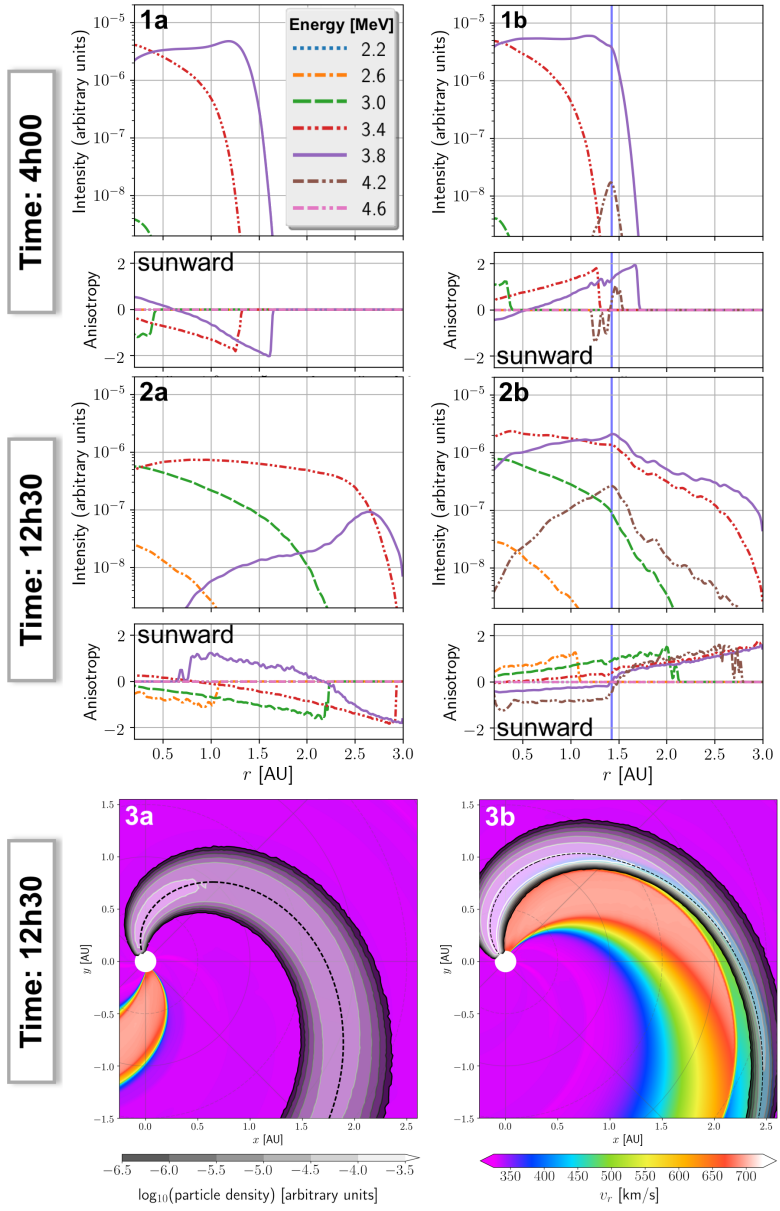

Figure 5.2: Rows 1 and 2 show snapshots of the particle intensities and anisotropies of, respectively, cases 1 and 2 along the selected IMF line. This IMF line is indicated by a dashed line in the figures of row 3, which also show the particle densities drawn in grey shades on top of the radial velocity profile of the solar wind. The blue vertical line in row 2 indicates the forward shock.

thus with a pitch angle close to 180°, to larger radial distances where the adiabatic deceleration is weaker. This, combined with the focusing effect, explains the high anti-sunward anisotropies of the 3.8 MeV energy channel at the start of the event. After the bulk of 3.8 MeV protons has passed, the intensity of these particles drops and the anisotropies switch sign, as is shown in panel 2a around $r \sim 2.25$ AU. For $r < 2.25$ AU, the measured sunward-streaming protons have reversed their propagation direction through scattering, after having travelled to large radial distances where the adiabatic deceleration is weaker. However, if they continue propagating in the sunward direction, they will eventually populate a lower energy channel. The combined high efficiency of adiabatic deceleration and focusing at small radial distances also explains why the lower energy channels typically show strong anti-sunward anisotropies, even 12.5 h after the delta injection (see e.g. the 3.0 MeV channel in panel 2a). This is because close to the Sun, adiabatic deceleration continuously and efficiently decelerates particles to these lower energy channels, and focusing increases $|\mu|$; thus, resembling the effect of a time-extended particle injection in those channels.

In addition, our simulations also show relatively strong anisotropies because we use a rather fine energy resolution , i.e., $\Delta E = 0.4$ MeV. If we were to consider, for example, a 3.0 ± 1.0 MeV energy channel instead, then the anisotropy in Panels 1b would be relatively small for $r < 1.5$ AU, since it would be modulated by the energy channel with highest intensity, i.e., the 3.4 MeV channel. This means however that we would lose all information about the behaviour of particles with energies outside the 3.4 MeV channel. Finally, we note that high anisotropies obtained with corresponding low intensities are not very significant when comparing with in-situ observations, since these anisotropies would likely be mitigated by an isotropic background of energetic particles.

Next, we look at a magnetic field line originating from the centre of injection region 2, which is illustrated in Panel 3b of Fig. 5.2. This IMF line crosses the forward shock wave of the CIR at a heliocentric radial distance of $r \sim 1.4$ AU. This is reflected in the intensity profiles of the snapshot at 4 h (Panel 1b), through the appearance of particles in the energy channel 4.2 MeV, centred on the forward shock (indicated by the blue vertical line in Panels 1b and 2b). Apart from this, the intensities of case 2 at 4 h are not very different as compared to case 1. This changes when examining the intensity profiles after 12.5 h (Panel 2b), since more particles have had time to interact with the forward shock and to travel inside the CIR. The 4.2 MeV energy channel, peaking at the forward shock, is now substantially populated. The 3.8 MeV energy channel, which in nominal conditions (case 1) only loses particles, gets now replenished through particle acceleration at the shock. In addition, the 3.8 MeV energy channel receives particles away from the shock, through the adiabatic deceleration of the 4.2 MeV particles. Together, this explains why the 3.8 MeV energy channel shows high intensities along the entire field line, in sharp contrast to case 1. Finally, it is seen that the anisotropy profiles in Panel 2b have also been strongly altered in comparison to Panel 2a. Especially the sign-switch of the anisotropies of energy channels 3.8 MeV

and 4.2 MeV at the forward shock is notable, and is a consequence of the accelerated particles streaming away from the shock in both sunward and anti-sunward direction.

The first column of Fig. 5.3 shows the particle intensity and anisotropy profiles along a field line originating from the centre of injection region 3. As for case 2, the field line enters the CIR at a heliospheric radial distance of $r \sim 1.4$ AU. However, for case 3 the IMF line originates in the fast solar wind and crosses the reverse instead of the forward shock. The snapshot at 4 h (Panel 1a) is considerably different from the two previous snapshots, since the IMF line resides in the fast solar wind for $r < 1.4$ AU, instead of the slow solar wind. As a consequence, the particles experience considerably more adiabatic deceleration since the divergence of the solar wind velocity is larger in the fast than in the slow solar wind (see Chapter 4). This explains why the 3.8 MeV energy channel is quickly depleted of particles close to the Sun, whereas the lower energy channels show much higher intensities compared to the previous two cases. It is also seen that the 4.2 MeV energy channel starts to get populated with particles at the reverse shock wave, which is indicated by the red vertical line. The snapshot after 12.5 h (Panel 2a) is strongly different from case 1 and 2, reflecting the interplay between strong adiabatic deceleration at small radial distances ($r < 1.4$ AU) and acceleration at the reverse shock. Comparing with the snapshot after 4 h illustrates that the reverse shock has repopulated the 3.8 MeV energy channel at small radial distances. In addition, acceleration at the reverse shock has filled both the 4.2 MeV and the 4.6 MeV energy channels with particles. We remark that the 4.6 MeV energy channel was not populated for the IMF line of case 2, which crossed the forward shock at the same radial distance. The reverse shock is thus a more efficient particle accelerator in our simulations. Apart from this, we find again that the anisotropies of the highest energy channels, this time including the 3.4 MeV channel, switch sign near the shock.

Finally, we look at a magnetic field line originating from the centre of injection region 4, as illustrated in Panel 3b of Fig. 5.3. At a small heliocentric radial distance (~0.6 AU), this IMF line enters the CIR by crossing the compression wave that steepens into the reverse shock wave at larger radial distances. The compression wave is not yet strong enough to accelerate particles into the 4.2 MeV energy channel, yet it contributes by counteracting to some extent the adiabatic deceleration that the particles undergo while travelling in the fast solar wind. This can be seen by noting that the 3.8 MeV energy channel remains substantially populated at 12.5 h, which contrasts with case 1 (e.g. Panel 1b of Fig. 5.3). On the other hand, particles residing for some time in the fast solar wind are considerably decelerated. As a result, the 3.0 MeV and the 2.6 MeV energy channels show intensities similar to the case 3, which are much higher than for cases 1 and 2. Panel 2b of Fig. 5.3 shows the presence of a small population of accelerated particles in the 4.2 MeV channel. These particles are not seen for the simulation done with zero cross-field diffusion (not shown here), and they originate thus from adjacent field lines that cross the reverse shock wave at ~1.4 AU, as indicated by the anisotropy sign switch around this distance.

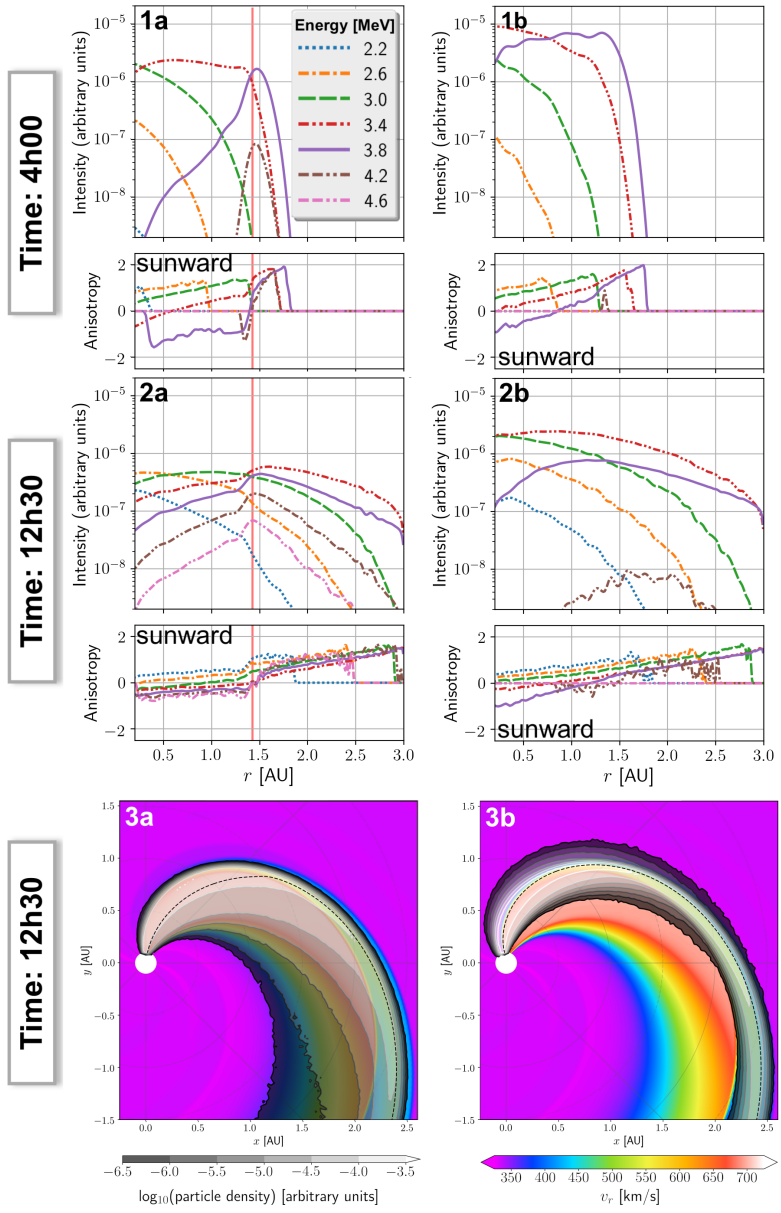

Figure 5.3: Same as Fig. 5.3, but for case 3 (left column) and case 4 (right column). The red vertical line in the row 1 indicates the reverse shock.

Case	$\Delta\varphi_i^0$	$\Delta\varphi_i^\perp$	$\Delta\varphi_{\mathrm{L},i}$	$\Delta\varphi_{\mathrm{U},i}$	$\Delta\varphi_i^\perp$ / $\Delta\varphi_i^0$
1	30°	66°	17.9°	18.1°	2.2
2	11.1°	36.1°	5.1°	19.9°	3.2
3	47.3°	75.8°	23.8°	4.7°	1.6
4	5.6°	41.2°	15.4°	20.1°	7.3

Table 5.1: The longitudinal widths of the particle intensities and the longitudinal increases due to cross-field diffusion. The numbers are for a heliocentric radial distance r = 1.5 AU in the solar equatorial plane.

5.3.2 Longitudinal intensity profiles

In this section, we examine the variation of the particle intensity and anisotropy profiles in the solar equatorial plane at a fixed heliocentric radial distance of 1.5 AU. For the four different cases, we study the intensities and anisotropies as a function of the longitude separation from the centre of the injection region, $\varphi - \varphi_c$. Here, φ denotes the counterclockwise measured longitude coordinate and φ_c represents the longitude of the point at 1.5 AU that connects magnetically to the centre of the injection region at 0.1 AU. Moreover, the figures discussed below are obtained 15.5 h after the particle injection, and both the results for simulations with (Panels A) and without (Panels B) cross-field diffusion are shown.

In order to quantify the longitudinal width of the particle intensity distributions, we define $\Delta\varphi_i^{0,\perp}$ as the longitudinal width of the region where the omnidirectional intensity, integrated over all energies, is larger than 10^{-9} in our simulations. The subscript i denotes the case number, whereas the superscripts 0 and $\perp$ indicate whether we are considering a simulation with or without cross-field diffusion, respectively. By denoting the longitudes of the lower and upper longitudinal edges of the particle intensity distribution with $\varphi_{\mathrm{L},i}$ and $\varphi_{\mathrm{U},i}$, respectively, we can write $\Delta\varphi_i^{0,\perp} = \varphi_{\mathrm{U},i}^{0,\perp} - \varphi_{\mathrm{L},i}^{0,\perp}$. The edge-longitudes $\varphi_{\mathrm{L},i}$ and $\varphi_{\mathrm{U},i}$ also allow to measure the longitudinal width increase due to cross-field diffusion of the intensity distribution by considering $\Delta\varphi_{\mathrm{L},i} = \varphi_{\mathrm{L},i}^0 - \varphi_{\mathrm{L},i}^\perp$ and $\Delta\varphi_{\mathrm{U},i} = \varphi_{\mathrm{U},i}^\perp - \varphi_{\mathrm{U},i}^0$. Table 5.1 summarizes for the four different cases the longitudinal widths $\Delta\varphi_i^{0,\perp}$ of the particle intensities, and the longitudinal width increases $\Delta\varphi_{\mathrm{L},i}$ and $\Delta\varphi_{\mathrm{U},i}$. In the following, these quantities are discussed together with the corresponding figures.

Figure 5.4 shows the longitudinal profiles for case 1, for which particles propagate in a nominal solar wind. Consequently, the longitudinal intensity profiles are symmetric around the centre of the particle streaming zone, and the sharp intensity cut-offs at the edges for the case without cross-field diffusion (reflecting the sharp transition in the spatial injection profile) are smoothed for the case with cross-field diffusion. It is seen that cross-field diffusion spreads the 3.4 MeV protons more in longitude than

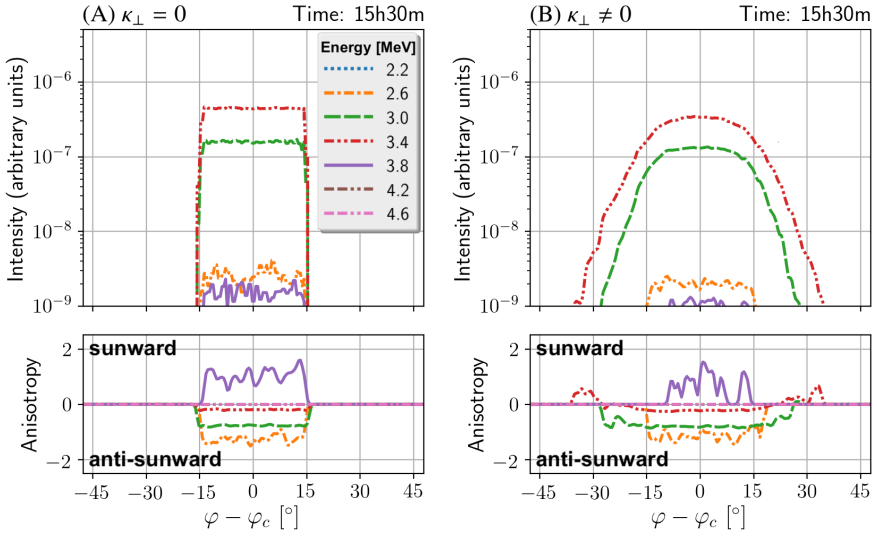

Figure 5.4: Snapshot of the intensities (top panels) and anisotropies (bottom panels) of protons originating from injection region 1, at time 15h30, both for the case without (left panel) and with (right panel) cross-field diffusion. The profiles are measured in the solar equatorial plane at a heliocentric radial distance of 1.5 AU, and as a function of longitudinal separation from the centre of the injection region.

than, for example, the 2.6 MeV protons. This is partly because the cross-field diffusion increases with the speed of the particles [1], but also because the 3.4 MeV channel gets populated before the 2.6 MeV energy channel, and hence the particles have more time to diffuse across the magnetic field. From Table 5.1, it is seen that $\Delta\varphi^0 = 30°$, which means that the longitudinal width of the particle intensity distribution remains equal to the width of the injection zone, as expected for a nominal IMF configuration. Finally, we point out that the wiggles in energy channels 3.8 MeV and 2.6 MeV are due to the low statistics at those low intensities.

Contrary to case 1, Fig. 5.5 shows that for case 2 the intensity profiles are strongly asymmetric around the centre of the particle streaming zone. For $\varphi - \varphi_c \lesssim 2°$, particles are travelling in the highly compressed region downstream of the forward shock. Moreover, the intensities peak around the forward shock, where particles get accelerated. Because of this shock acceleration, the 3.8 MeV energy channel shows high intensities, which is in sharp contrast to case 1. Table 5.1 shows that the width of the particle streaming zone $\Delta\varphi_2^0$ is less than half the width of the previous case, and

[1] We have that $\lambda_\parallel^r \propto v^{2-q}$, where $q = 5/3$ denotes the exponent of the power spectrum of the magnetic turbulence. Equation (4.6) then gives that $\kappa_\perp \propto v^{3-q}$.

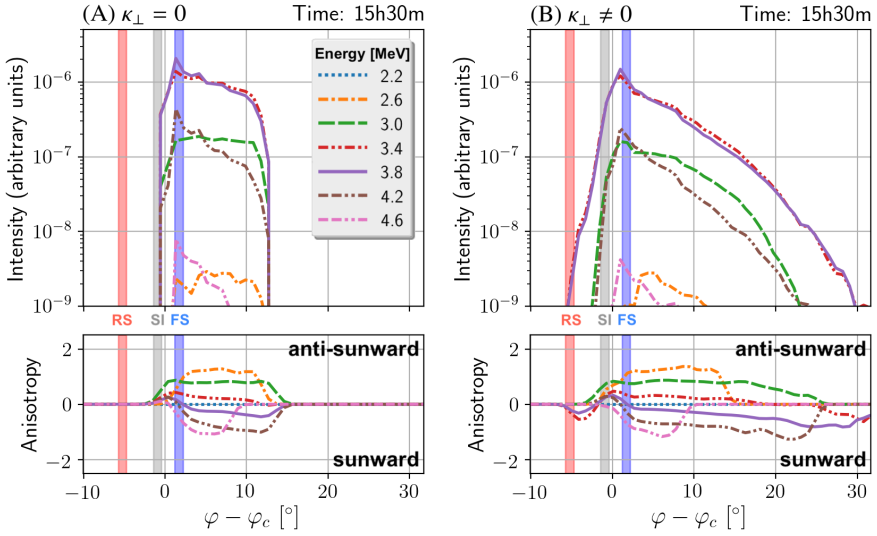

Figure 5.5: Same as Fig. 5.4, but for protons originating from injection region 2. The grey, red, and blue bands are centred on the SI, the reverse shock (RS), and the forward shock (FS), respectively.

thus also less than half the longitudinal width of the injection region. This decrease in width is due to particles following IMF lines that cross the forward shock, where the magnetic field is compressed. This also explains why the peak intensities in Fig. 5.5 are higher than those in Fig. 5.4. When looking at Panel B of Fig. 5.5, it is noticeable that, in contrast to case 1, the effect of cross-field diffusion on the intensity profiles is asymmetric. This can also be seen from Table 5.1, which shows that $\Delta\varphi_{\mathrm{L},2} \ll \Delta\varphi_{\mathrm{U},2}$. The reason for this asymmetry is that, near $\varphi - \varphi_c \sim 0$, the particles encounter the SI, which is characterised by a strong magnetic field, and hence a weaker cross-field diffusion according to Eq. (4.6). Finally, we remark that the cross-field diffusion has a larger effect on the longitudinal spread for case 2 than for case 1, when comparing $\Delta\varphi_1^\perp / \Delta\varphi_1^0 = 2.2$ with $\Delta\varphi_2^\perp / \Delta\varphi_2^0 = 3.2$ (see Table 5.1). Despite the increased magnetic field in the shocked slow solar wind, the cross-field diffusion can thus still be important since magnetic field lines that are significantly separated in the unperturbed solar wind are closely compressed in the CIR. Hence a small cross-field diffusion in the CIR is sufficient to transport the particles across these IMF lines, and if afterwards the particles return to the unperturbed solar wind, they produce a wide particle streaming region.

The longitudinal intensity and anisotropy profiles for case 3 are illustrated in Fig. 5.6. We see that the intensities for this case peak around the reverse shock, which also shows the presence of accelerated particles populating the 4.2 MeV and 4.6 MeV

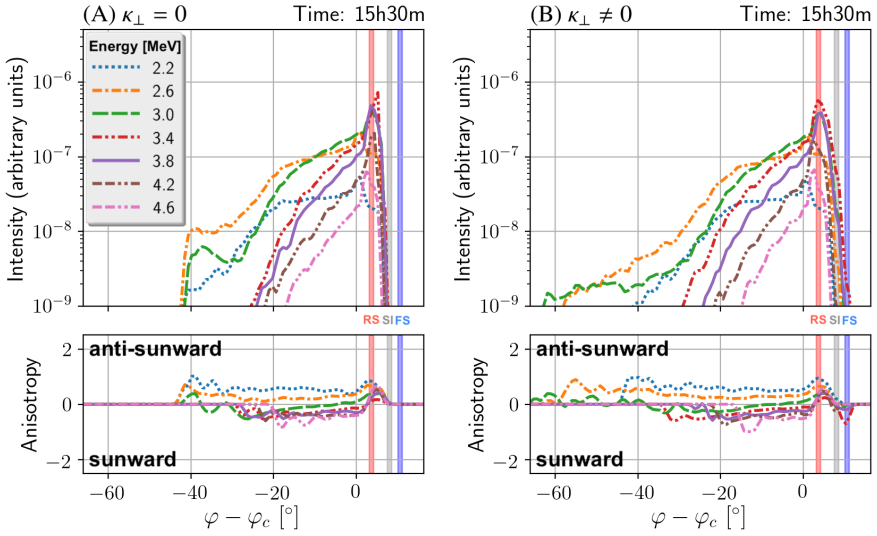

Figure 5.6: Same as Figs. 5.4 and 5.5, but for protons originating from injection region 3.

energy channels. Like case 2, the intensity profiles are strongly asymmetric around the centre of the particle streaming zone. This is because for $\varphi - \varphi_c \gtrsim 5°$ particles are travelling in the highly compressed region downstream of the reverse shock, whereas for $\varphi - \varphi_c \lesssim -30°$ particles are travelling in the rarefaction region behind the fast solar wind stream. It is seen in Table 5.1 that $\Delta\varphi_3^0 > 30°$, that is, the longitudinal width of the particle intensity distribution at 1.5 AU is larger than the original width of the injection region, even without cross-field diffusion. This can be attributed to the rarefaction region behind the fast solar wind stream. In addition, $\Delta\varphi_3^0$ would have even been much larger if it were not for the compressed IMF in the CIR at the upper longitude edge of case 3.

Looking at Panel B of Fig. 5.6, we see that similar to case 2, the cross-field diffusion has a clear asymmetric effect on the intensity profiles. This asymmetry is also evident from Table 5.1, showing $\Delta\varphi_{\mathrm{L},3} \gg \Delta\varphi_{\mathrm{U},3}$, and can be attributed to the proximity of the SI to the upper boundary of the particle longitudinal spread. In the CIR, only few particles diffuse through the SI and hence the SI is characterised by a steep drop in intensities. We remark that $\Delta\varphi_3^\perp \,/\, \Delta\varphi_3^0 \sim 1.6$ (see Table 5.1) is smaller than for the previous two cases, even though the cross-field diffusion is maximal in the fast stream and the rarefaction region owing to the weak IMF in these regions. The latter is confirmed in Table 5.1 by noting that $\Delta\varphi_{\mathrm{L},3}$ is the largest of all $\Delta\varphi_{\mathrm{L},i}$ and $\Delta\varphi_{\mathrm{U},i}$.

The longitudinal particle intensity and anisotropy profiles for case 4 are shown in

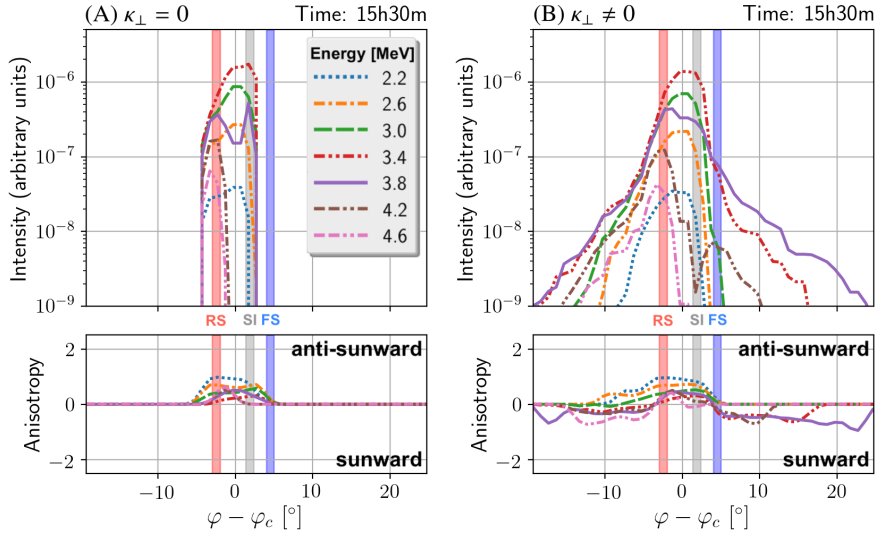

Figure 5.7: Same as Figs. 5.4 and 5.5, but for protons originating from injection region 4.

Fig. 5.7. Panel A of this figure illustrates that the streaming zone is much narrower compared to the previous cases, reflecting the highly compressed IMF inside the CIR. By looking at Table 5.1, we see that $\Delta\varphi_4^0 = 5.6$, that is, the longitudinal width of the intensity distribution is more than five times smaller than the width of the injection region. Comparing Panel A with Panel B of Fig. 5.7, illustrates that cross-field diffusion has brought particles to field lines that only enter the CIR at larger radial distances. This can be seen by noting that cross-field diffusion has produced substantial particle intensities to the left of the red band, which denotes the reverse shock, and to the right of the blue band, which denotes the forward shock. These intensities correspond to particles that have moved to field lines that are outside the CIR at 1.5 AU, since the two shocks are the boundaries of the CIR. These field lines eventually enter the CIR at larger radial distances as a consequence of the propagation of the reverse shock into the fast solar wind and the forward shock into the slow solar wind.

Among the four cases studied, case 4 is the most influenced by cross-field diffusion since the increase of the longitudinal width because of perpendicular diffusion is the largest, i.e., $\Delta\varphi_4^\perp/\Delta\varphi_4^0 = 7.3$ (see Table 5.1). That is, the longitudinal width of the particle spread is more than seven times wider than the width when only parallel transport is considered. Similar to case 2, this can again be attributed to small cross-field motions inside the CIR, bringing particles to IMF lines that are closely compressed inside the CIR but significantly separated outside the CIR.

Furthermore, Fig. 5.7 shows that the case without cross-field diffusion (Panel A) results in an accelerated particle population only at the reverse shock, whereas the case with cross-field diffusion (Panel B) shows the formation of accelerated particle populations centred on the forward shock and on the reverse shock (see also Chapter 4); the SI separates both populations and exhibits a depressed level of the intensity (brown curve). Such an intensity dip of the CIR-accelerated energetic particles situated near the SI is a feature regularly observed (see e.g., Mason et al., 1997; Dwyer et al., 1997; Strauss et al., 2016). The reason for this phenomenon is likely that the SI acts as a diffusion barrier, keeping the energetic particles accelerated at the forward shock separated from those accelerated at the reverse shock.

To conclude this section, we would like to remark that by defining $\Delta\varphi_i^{0,\perp}$ as the longitudinal width of the energy integrated intensities, we lost information on the energy dependence of the longitudinal widths. However, by looking at Figs. 5.4–5.7 we see that different energy channels have different longitudinal widths, and that the energy channel that determines the total longitudinal width, $\Delta\varphi_i^{0,\perp}$, changes across the different cases. We find a similar behaviour for the variables $\Delta\varphi_{\mathrm{L},i}$ and $\Delta\varphi_{\mathrm{U},i}$, which measure the longitudinal increase of the energy integrated intensities due to cross-field diffusion. A comparison of Figs. 5.4–5.7 illustrates again that the cross-field diffusion does not affect all energy channels in the same manner, which is partly due to the dependence of the cross-field diffusion on the particle speed (see footnote 1). The variation of $\Delta\varphi_i^{0,\perp}$ and $\Delta\varphi_{\mathrm{L,U,i}}$ with energy is also influenced by our choice for a mono-energetic impulsive injection. For example, in our simulations, the evolution of the longitudinal width of the 2.6 MeV energy channel depends on how fast and where this channel gets populated through adiabatic deceleration, which depends on the specific solar wind conditions that are different for the four cases. If we would consider a mono-energetic delta injection of 2.8 MeV protons instead of 4 MeV protons, the spreading of the protons populating the 2.6 MeV energy channel would be altered as compared to our current simulations. This is because this energy channel would now be populated from the very start of the simulation. Hence, in order to further investigate the energy dependence of the particle spreading in the heliosphere, we need to consider a particle source injection with an energy spectrum covering a wide range of energies. This task will be addressed in a future work.

5.3.3 Radial evolution of the longitudinal width

In the previous section, we examined how the total longitudinal width $\Delta\varphi_i$ of the particle streaming zone at 1.5 AU varies across the four different cases. We now study how $\Delta\varphi_i$ varies as a function of radial distance in the solar equatorial plane, 15.5 h after particle injection. The radial dependence of $\Delta\varphi_i$ is illustrated in the left panel of Fig. 5.8, for the four injection cases, both without (dashed curves) and with (solid

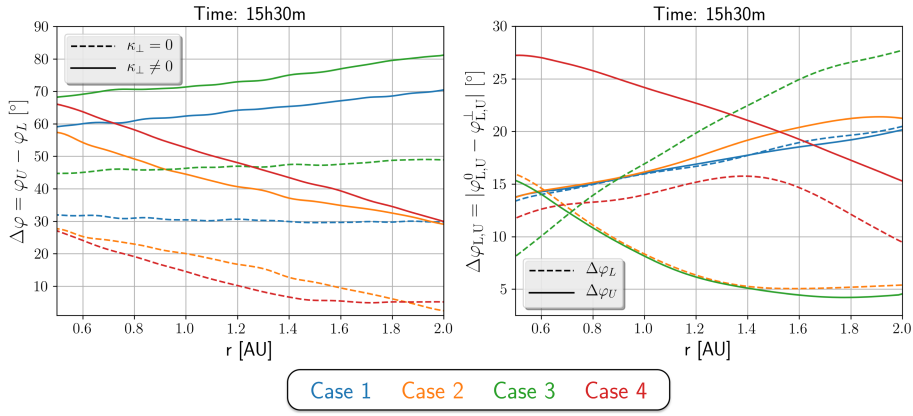

Figure 5.8: *Left panel:* longitudinal width of the particle streaming zone for the simulations without (dashed lines) and with (solid lines) cross-field diffusion, 15.5 h after particle injection. *Right panel:* the longitudinal increase of the particle streaming zone at the lower (dashed) and upper (solid) longitude boundaries, 15.5 h after particle injection.

curves) cross-field diffusion. The right panel of Fig. 5.8 shows the radial dependence of $\Delta\varphi_{\mathrm{L},i}$ (dashed curves) and $\Delta\varphi_{\mathrm{U},i}$ (solid curves) for the four different cases.

For case 1 (blue lines), we see that $\Delta\varphi_1^0$ is constant and equal to ~30°, i.e., the width of the injection zone, which is expected for a nominal IMF. In contrast, $\Delta\varphi_1^\perp$ increases with the heliocentric radial distance which is because cross-field diffusion in our simulations, as in others (e.g., Zhang et al., 2009; Dröge et al., 2010; Dröge et al., 2014), is stronger at larger radial distances because of the decreasing magnetic field strength. From the lower panel of Fig. 5.8, we see that the increase in width of the streaming zone is the same at both sides of the streaming zone.

For case 2, the evolution of $\Delta\varphi_2$ is illustrated by the orange lines in Fig. 5.8. In contrast to case 1, the longitudinal width of the particle intensity distribution is monotonically decreasing with radial distance in the heliospheric equatorial plane, both for the simulations without and with cross-field diffusion. This is because the magnetic field lines bounding injection region 2 enter the CIR, where they are compressed and, once inside the CIR, the field lines further converge towards the SI therefore decreasing the width of the streaming zone monotonically. Looking at the right panel of Fig. 5.8, it is seen that there is a strong difference between the change of the width at the lower and upper longitudinal edges of the streaming zone. The field line bounding the lower longitudinal side of the injection region enters the CIR at ~1.3 AU, i.e., around the location where $\Delta\varphi_{\mathrm{L},i}$ becomes constant and equal to ~5°.

As noted before, any cross-field transport inside the CIR can bring the particles on IMF lines that are closely adjacent in the CIR, but significantly separated outside the CIR. Hence, we expect to see the effect of cross-field diffusion happening inside the CIR more clearly outside the CIR, that is, before the IMF lines enter the CIR. At the lower longitudinal edge, cross-field transport in the direction of the SI is only visible at small radial distances, since the particles move on field lines that are everywhere closely adjacent to each other except at very small radial distances when they reside in the unperturbed solar wind. This explains why $\Delta\varphi_{\mathrm{L},2}$ is slightly larger than $\Delta\varphi_{\mathrm{L},1}$ below 0.6 AU. For the same reason, $\Delta\varphi_{\mathrm{U},2} > \Delta\varphi_{\mathrm{U},1}$, since cross-field transport in the opposite direction of the SI moves particles near the upper longitude edge on field lines that enter the CIR at larger radial distances. In this latter case, the effect of the cross-field transport needs time to be particularly notable, since particles have to travel to large radial distances, diffuse across the magnetic field, and subsequently return towards the inner heliosphere. For this reason, $\Delta\varphi_{\mathrm{U},2} \approx \Delta\varphi_{\mathrm{U},1}$ for $r < 1$ AU at 15.5 h.

For case 3, $\Delta\varphi_3^0$ is slowly increasing instead of remaining constant like case 1 or decreasing like case 2. Most of the IMF lines originating from injection region 3 enter the CIR at large radial distances where they are compressed. However some of the IMF lines enter the rarefaction region behind the fast solar wind stream, where IMF lines are strongly diverging. This explains the larger longitudinal width $\Delta\varphi_3$ as compared to the other cases. Such large extent of the particles is also clearly observed by comparing the particle density map of the panels in the last rows of Figs. 5.2 and 5.3. The behaviours of $\Delta\varphi_{\mathrm{L},3}$ and $\Delta\varphi_{\mathrm{U},3}$ are analogous yet mirrored when compared to the corresponding variables of case 2, since the upper longitudinal edge is now close to the SI. At the lower edge, $\Delta\varphi_{\mathrm{L},3} > \Delta\varphi_{\mathrm{L},1}$ for $r > 1$ AU, indicating that cross-field diffusion is more efficient in the rarefaction region than in the slow solar wind. This is because of the lower magnetic field strength in the rarefaction region that translates into a stronger cross-field diffusion (see Eq. (4.6)).

For case 4, $\Delta\varphi_4^0$ and $\Delta\varphi_4^\perp$ both decrease, similar to case 2. The behaviour of $\Delta\varphi_4^0$ is largely determined by the lower longitudinal edge, since the field line bounding the upper longitudinal edge quickly enters the CIR and converges towards the SI. Around ~1.4 AU, the field line bounding the lower longitudinal edge enters the CIR, explaining the kink in $\Delta\varphi_4^0$ at this distance. In contrast to the IMF in the shocked slow solar wind, the IMF in the shocked fast solar wind converges only very slowly in the direction of the SI, explaining why $\Delta\varphi_4^0$ remains approximately constant for $r > 1.4$ AU. Figure 5.8 also illustrates that the strong increase of $\Delta\varphi_4^\perp$ with decreasing radial distance is largely determined by $\Delta\varphi_{\mathrm{U},4}$, i.e., by the cross-field motion of particles in the shocked slow solar wind. As for case 2, this motion bring particles on IMF lines that enter the CIR from the slow solar wind at much larger radial distances than the IMF lines bounding the particle streaming zone in the case with null cross-field diffusion (see the red solid line in the lower panel of Fig. 5.8). The large curvature of the IMF in the slow solar wind then explains the strong increase in $\Delta\varphi_{\mathrm{U},4}$ towards the Sun.

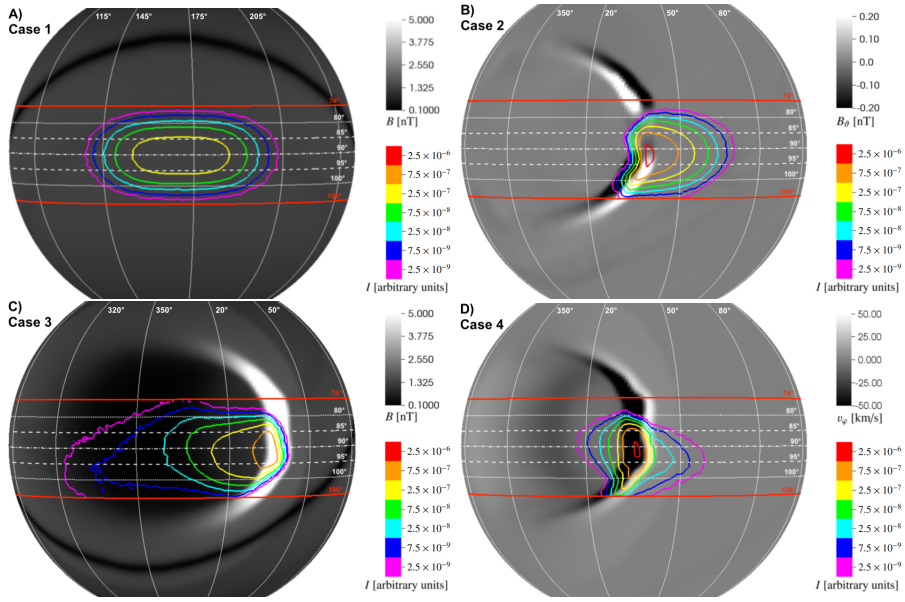

Figure 5.9: Contour plots of the particle intensity at $r = 1.5$ AU, drawn on top of different MHD solar wind variables, 15.5 h after particle injection and for the simulations with cross-field diffusion. The red parallels indicate the borders of the sampling region. *Upper left panel:* intensities of case 1 drawn on top of the magnetic field magnitude. *Upper right panel:* intensities of case 2 drawn on top of the magnetic field colatitude component. *Lower left panel:* intensities of case 3 drawn on top of the magnetic field magnitude. *Lower right panel:* intensities of case 4 drawn on top of the longitudinal velocity component.

5.3.4 Latitudinal variation of particle intensity

In the following, we examine the energy-integrated particle intensity variations both in longitude and colatitude, at the fixed heliocentric radial distance of $r = 1.5$ AU and 15.5 h after particle injection. Figure 5.9 shows such spherical surfaces for the four different cases with the SEP intensity levels depicted as contour lines on top of different solar wind variables. All particle intensity contours represent the simulations with cross-field diffusion.

Panel A of Fig. 5.9 corresponds to case 1, where the elliptical shape of the intensity contours reflects the rectangular shape of the particle injection region (see Fig. 5.1). Although not shown in this figure, the intensity contours for the simulation with zero cross-field diffusion, are all coincident and rectangular like the source region,

as expected in a Parker spiral magnetic field. In contrast, the shapes of the intensity contours for case 2 (Panel B Fig. 5.9) are no longer similar to the original source region. Inside the CIR, particles are transported southward owing to the deflection of the IMF upon crossing the forward shock, as indicated by the magnetic field colatitude component B_ϑ drawn in the background of the panel (see also e.g., Pizzo, 1991). Panel C of Fig. 5.9 shows the intensity contours for case 3, drawn on top of the magnetic field strength. We see that the particles are spread in a large region in the rarefaction zone behind the CIR, characterised by a weak magnetic field. The peak of the intensities occurs at the reverse shock and the corresponding downstream region, where the magnetic field is compressed. Finally, the intensity contours for case 4 (Panel D of Fig. 5.9) are drawn on top of the longitudinal solar wind velocity component v_φ, which clearly indicates the location of the SI. Similar to case 2, it is seen that the intensity contours are peaking towards the south in the shocked slow solar wind, as a result of the deflection of the IMF at the forward shock. In contrast, the particles do not propagate towards the northern hemisphere, due to the northward location of the coronal hole centre with respect to the location of the injection region (see the left panel of Fig. 5.1). The deformation of the particle intensity contours both in longitude and latitude makes the original shape of the injection region no longer easily discernible, unless the IMF structure between the Sun and the observer is known accurately.

5.4 Summary

In this chapter we extended the study of Chapter 4 by injecting 4 MeV protons from four different source regions into a solar wind containing a CIR. When examining the particle intensities, the four cases differed significantly from one another, reflecting the different underlying IMF configurations encountered by the particles. Measuring the intensity and anisotropy along four different magnetic field lines illustrated the important effect of the solar wind speed on the energy content of the initial injected particle population. The three IMF lines that were connected to the CIR showed significant differences from the IMF line located in the unperturbed slow solar wind. The intensity and anisotropy profiles along the IMF lines crossing the forward and reverse shocks demonstrated how accelerated particle populations formed centred on these shock waves, because of the presence of converging plasma flows.

Furthermore, by studying the longitudinal intensity and anisotropy profiles at $r = 1.5$ AU, it was illustrated how the solar wind configuration completely alters the observed profiles across the different cases. Whereas the longitudinal profile in a nominal solar wind is symmetric, the longitudinal profiles measured near the CIR were highly asymmetric. In the latter cases, the intensities reached their peak values at the shocks bounding the CIR because of the compressed magnetic flux tubes there. For

cases 2 and 3 we saw a sharp drop in intensities near the SI, as the corresponding injection regions were not crossing the transition region between the fast and slow solar wind at the inner boundary. Cross-field diffusion smoothed this drop only slightly, since the SI is characterised by a strong IMF and hence a weak cross-field diffusion. The effect of the SI on the particle intensities was also clearly reflected in the intensity profile of the 4.2 MeV energy channel for case 4 with cross-field diffusion. This energy channel is populated by two proton populations accelerated in the CIR shocks, and the SI separates both populations. Although the effect of the SI has been predicted by simulations accounting for cross-field diffusion processes (Strauss et al., 2016), our model is for the first time able to show with detail the acceleration of protons at both shocks of the CIR and reproduce the observed dip of particle intensities (e.g., Dwyer et al., 1997).

Studying the width of the particle streaming zone as a function of heliocentric radial distance revealed that the different solar wind configurations produce completely different dependencies. For a nominal solar wind without cross-field diffusion, the width remains constant whereas in non-nominal conditions, the width can either increase or decrease away from the Sun. Moreover, whereas cross-field diffusion widens the particle streaming zone, it does not significantly influence the behaviour of the width as a function of radial distance. We suggest therefore that the IMF topology might play an important role in contributing to the occurrence of widespread and narrow SEP events. In addition, the latitudinal spreading of the particles were analysed, by showing the particle distributions on a spherical surface at a heliocentric radial distance of 1.5 AU. It was illustrated that the IMF structure of the CIR alters the shape of the intensity distribution, such that the shape of the original injection region is no longer obvious.

Finally, we want to point out that large SEP events simultaneously observed by e.g., the Solar Terrestrial Relations Observatory (STEREO) and by near-Earth spacecraft might develop under different background solar wind conditions (on top of observed CME propagation), as detected by each spacecraft (e.g. see the events analysed by Lario et al., 2014, 2016). The modelling presented in this work suggests that a non-nominal structured solar wind may significantly affect both the spatial extent and energy spectrum of SEP events. How the SEP spatial distribution is affected by the solar wind also depends on the relative location of the particle source with respect to any large-scale plasma structure. Therefore, models such as ours may contribute towards gaining insights in understanding the observed multi-spacecraft SEP event intensities.

Chapter 6

Spreading protons in the heliosphere: a note on cross-field diffusion effects

"Wanderer, there is no path
the path is forged as you wander."
– Antonio Machado

Abstract. This chapter extends the studies presented in chapters 4 and 5 by varying the protons' perpendicular mean free path. We address thus the question on how different values for the cross-field diffusion coefficient may affect the energetic particle spread and intensity profiles near a corotating interaction region (CIR). We find that both a strong cross-field diffusion and a solar wind rarefaction region are capable of dispersing SEPs efficiently, producing overall low particle intensities which can in some cases prevent the SEPs from being detected in-situ, since their intensity may drop below the detected pre-event intensity levels. We also discuss how accelerated particle populations form on the reverse and forward shock waves, separated by the stream interface (SI) inside the CIR. Under strong levels of cross-field diffusion, particles cross the SI and both accelerated particle populations merge together.

This chapter is entirely based on Wijsen et al. (2019c).

6.1 Introduction

In Chapter 5, it was illustrated how a CIR can strongly affect the spread of SEPs in the inner heliosphere. It was shown that the azimuthal width of the particle intensity distribution can increase, remain constant, or decrease as a function of heliocentric radial distance. Moreover, by performing simulations both with and without cross-field diffusion, it was illustrated that a moderate cross-field diffusion process increases the azimuthal width of the particles distribution, but does not alter its qualitative behaviour as a function of radial distance. The latter is entirely determined by the underlying IMF topology. In this work, we study how the results of the previous chapters are modified when considering stronger cross-field diffusion processes, for which the particles have thus a larger perpendicular mean free path.

Several CIRs have been observed with signatures of energetic particle populations residing in the proximity of the associated reverse and forward compression or shock waves, such that the measured intensity profiles have a characteristic double peak structure (e.g., Barnes & Simpson, 1976; Decker et al., 1981; Tsurutani et al., 1982; Dwyer et al., 1997; Mason & Sanderson, 1999). Furthermore, the minimum proton intensity found between the two intensity maxima is observed to be correlated with the maximal magnetic field strength of the CIR (Tsurutani et al., 1982), and coincides typically with the SI where the shocked slow and fast solar wind plasmas meet each other (see e.g., Strauss et al., 2016, for a discussion). This intensity dip can persist for several solar rotations (Tsurutani et al., 1982), which suggests that the SI acts as an efficient barrier across which perpendicular particle transport is largely inhibited. In Chapter 5, it was illustrated that in our simulations the protons accelerated above their initial injection energy of 4 MeV are also characterised by an intensity profile with a double peak structure and an intensity dip coinciding with the SI (see the brown curve in Panel B of Fig. 5.7). In this work, we investigate how this result is affected when considering different levels of cross-field diffusion.

This chapter is structured as follows. After detailing the set-up of our simulations in Section 6.2, we show how the longitudinal width of the particle intensity distribution varies as a function of radial distance, time, and level of cross-field diffusion (Section 6.3). Next, we investigate how the different levels of cross-field diffusion used in our simulations affect the particle acceleration at the shock waves bounding the CIR (Section 6.4). We end in Section 6.5 with a summary and discussion of the obtained results.

6.2 Simulation of SEP transport within a CIR

In this chapter, a similar solar wind configuration as in Chapters 4 and 5 is considered. That is, EUHFORIA is used to model a slow solar wind with an embedded fast solar wind stream, which leads to the formation of a CIR bounded by a forward and a reverse shock wave. We recall from Section 4.4.1 that this solar wind configuration is generated by prescribing a solar wind speed of 330 km/s everywhere at the inner boundary of EUHFORIA, except for a region satisfying $(\text{longitude} - 75°)^2 + (\text{latitude} - 5°)^2 < (20°)^2$, where a solar wind of speed 660 km/s is prescribed. This high-speed region is surrounded by a transition zone of width 6° (see also Fig. 5.1). As discussed in Chapter 4, the precise location where the large-amplitude compression waves bounding the transition region evolve into shock waves, and hence marking the formation of the CIR, is difficult to pinpoint. This is because the finite resolution of our MHD simulation produces inevitably shock waves that are wider than observed interplanetary CIR shocks. However, in our simulations particles start to get accelerated above their injecting energy from a heliocentric radial distance of ~1.3 AU onward, indicating that the large-amplitude compression waves have steepened sufficiently to allow for efficient particle acceleration counteracting the adiabatic deceleration occurring elsewhere in the expanding solar wind.

In contrast to the EUHFORIA simulation used in Chapters 4 and 5, we assume in the current study a monopolar positive magnetic field at the inner boundary of the model, such that there is no CS present in the simulated solar wind. This is done to avoid any effects of the CS on the simulated particle intensities, which is necessary due to the larger spread of the particles in this work compared to the simulations performed in previous chapters. As discussed in Section 2.11, the standard guiding centre approximation used in the FTE breaks down near a CS (see also Speiser, 1965; Burger et al., 1985). Apart from the magnetic field polarity, all other MHD variables prescribed at the inner boundary of the model are the same as the ones described in Section 4.4.1.

We consider the same particle injection region as in Chapter 4 and in case 4 of Chapter 5 (see Fig. 5.1). We recall that this injection region is located at the inner boundary of the model, at a heliocentric radial distance of 0.1 AU, and centred around the solar equatorial plane with a latitudinal width of 10°. The source region has a longitudinal width of 30°, such that it covers a region extending from the slow to the fast solar wind. As a consequence, it is magnetically connected to both the forward and reverse compression/shock waves, hence also encompassing the SI inside the CIR, where the shocked slow and fast solar wind plasma meet.

Like in the previous chapters, we consider a mono-energetic injection of 4 MeV protons, allowing us to easily track the energy changes of the particles during their propagation in the solar wind. Unlike Chapters 4 and 5, we inject the protons according to a

Reid-Axford time profile (Reid, 1964) in order to mimic a prompt flare-like injection of particles, i.e.,

$$j(t) \propto \frac{1}{t} \exp\left(-\frac{\beta}{t} - \frac{t}{\tau}\right),$$

where j denotes the differential intensity, $\beta = 1.5$ h and $\tau = 0.2$ h (like in Lario et al., 2007).

The particle scattering conditions are determined by the pitch-angle diffusion coefficient $D_{\mu\mu}$ and the cross-field diffusion tensor $\boldsymbol{\kappa}_\perp$. As detailed in Section 4.2, we use quasi-linear theory to prescribe the functional form of $D_{\mu\mu}$. The strength of the magnetic turbulence acting as pitch-angle scattering centres is quantified by assuming a constant radial mean free path $\lambda_r^{\parallel} = 0.3$ AU for 4 MeV protons. We assume the same cross-field diffusion tensor as in Chapters 4 and 5, which we restate here for referential convenience (see also Eq. (2.151)):

$$\boldsymbol{\kappa}_\perp = \alpha \frac{\pi}{12} v \lambda_\parallel \frac{B_0}{B} (\mathbb{I} - \mathbf{bb}), \tag{6.1}$$

where $\mathbb{I}$ is the unit tensor, $\mathbf{bb}$ the dyadic product of the magnetic unit vector, and $\lambda_\parallel$ the parallel mean free path. B_0 is a reference magnetic field strength value fixed to the maximum value of B at 1 AU, $B_0 = 9.7$ nT, which is attained in the shocked slow solar wind, adjacent to the SI.

We note that we use rather simple functional forms for the pitch-angle and cross-field diffusion coefficients. However, the significant uncertainties regarding the turbulent conditions and hence the particle diffusion properties in large scale plasma structures like CIRs, make it difficult to establish more realistic assumptions for the particle diffusion coefficients (Kota & Jokipii, 1991; Horbury & Schmidt, 1999; Crooker et al., 1999). Nonetheless, it was demonstrated in Chapters 4 and 5 how our choice for the pitch-angle and the cross-field diffusion coefficients can reproduce different features of the energetic particle intensity profiles associated with CIRs, like the particle acceleration near the shock waves and the intensity dip near the SI. This is also discussed in more detail in Section 6.5 of this chapter. In reality, the parallel and perpendicular mean free path of the particles might vary rather strongly across the CIR due to the presence of different turbulent regimes (Horbury & Schmidt, 1999). The increase in turbulence near the CIR shocks (see e.g., Tsurutani et al., 1995, and Section 6.5 for a discussion) would most likely decrease the parallel mean free path and therefore amplify some of the effects that we describe in this work. A smaller radial mean free path would imply that the particles will scatter across the CIR shock waves more often, resulting in more particle acceleration. On the other hand, using a large constant radial mean free path everywhere in our simulations allows us to more easily trace the effects of the underlying non-nominal IMF topology and the different levels of cross-field diffusion. In addition, more advanced theories of cross-field diffusion, such as the non-linear guiding centre theory (see e.g., Matthaeus et al., 2003; Shalchi,

2009, or Section 2.7.2), require the specification of the magnetic turbulence level δB^2 among other parameters. For nominal solar wind conditions, one typically assumes that this quantity decreases as a power-law with radial distance from the Sun (e.g., Mason et al., 2012b; Zhao et al., 2016; Hu et al., 2017). However, such a singular dependence on the radial coordinate is not valid in a solar wind containing a CIR, as the turbulent conditions in a CIR are significantly different from those encountered in the fast or slow solar wind (e.g., Horbury & Schmidt, 1999; Crooker et al., 1999; Richardson, 2018). Therefore, since the behaviour of the turbulence in a CIR is not well understood, we instead adopt the phenomenological form (6.1) for the cross-field diffusion, as its effects are more easily traceable in the simulations.

Since the perpendicular mean free path satisfies $\lambda_\perp = 3\kappa_\perp/v$, it is seen from Eq. (6.1) that the parameter α determines the ratio $\lambda_\perp/\lambda_\parallel$ at 1 AU up to a factor of order unity. We consider three different values for the parameter α, namely 2×10^{-4}, 2×10^{-3}, and 2×10^{-2}. In the remainder of the text, we will refer to the simulations performed with these different values of α as case 1, case 2 and case 3, respectively. These values of α help us to classify the 'level' or 'strength' of the cross-field diffusion employed in our simulations. In this way, the case with the strongest cross-field diffusion corresponds to case 3 ($\alpha = 2 \times 10^{-2}$).

6.3 The spread of SEPs in the solar equatorial plane

In this section, we analyse how the different levels of cross-field diffusion affect the longitudinal width of the particle intensity distributions in the solar equatorial plane. For this purpose, we define the particle streaming zone as the region where the omni-directional intensity, integrated over energy, is larger than the limiting value $10^{-8.5}$ (in arbitrary units). This threshold is set three orders of magnitude below the peak-intensity attained at 1 AU for a simulation without cross-field diffusion. Defining the longitudinal coordinate φ in anticlockwise direction, we obtain at each heliocentric radial distance, r, and time, t, the lower, $\varphi_L(t, r)$, and upper, $\varphi_U(t, r)$, edge longitudes of the particle streaming zone, such that we can define the longitudinal width of the particle streaming zone as $\Delta\varphi(r, t) = \varphi_U(t, r) - \varphi_L(t, r)$. The left column of Fig. 6.1 shows for the three cases the radial dependence of $\Delta\varphi(r, t)$ at different times. The right column of Fig. 6.1 shows for each case the corresponding snapshots of the particle intensities at 11.5 h. In these figures, the lower longitudinal boundary is indicated by a green line, whereas the upper longitudinal boundary is shown in blue.

From the first column of Fig. 6.1, we see that for all cases, $\Delta\varphi(r, t)$ generally decreases with increasing radial distance, reflecting the IMF compression at the shock waves

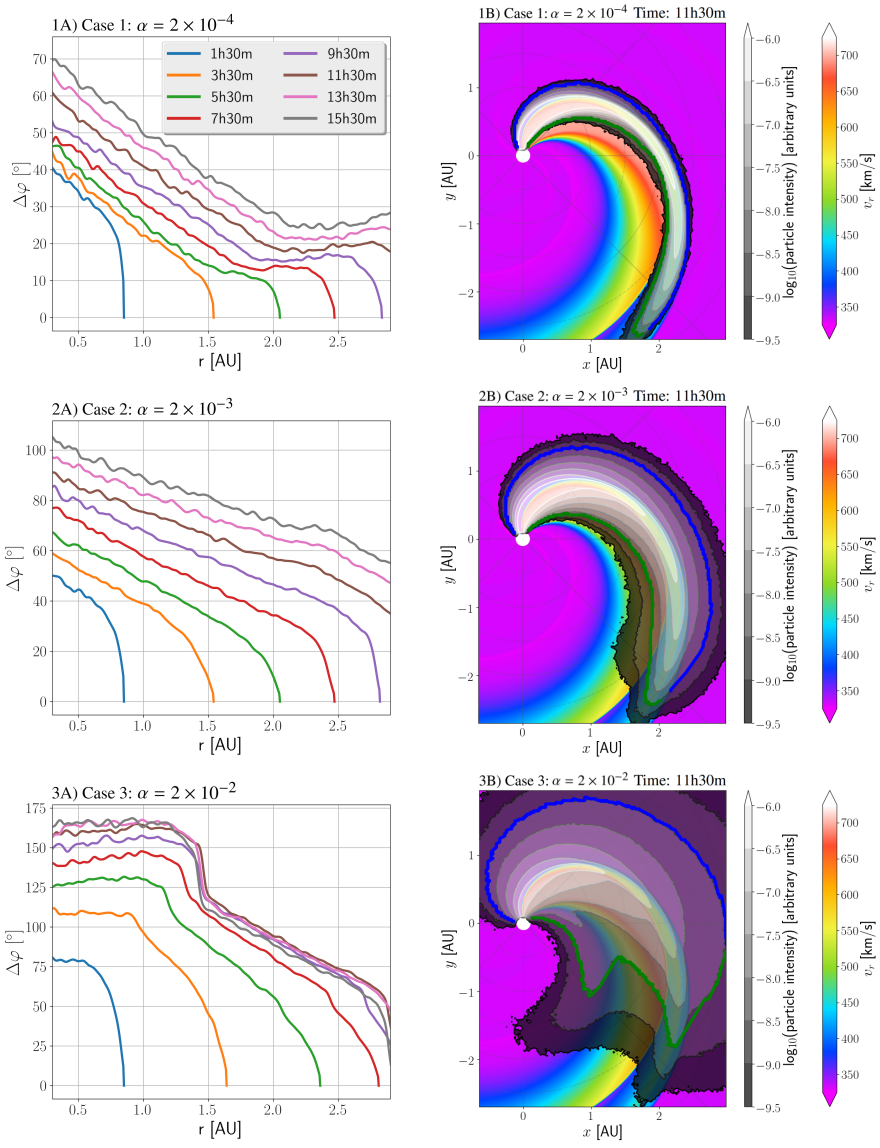

Figure 6.1: *Column A*: the longitudinal width of the omni-directional intensity distribution as a function of radial distance at different times. *Column B:* the energy-integrated particle intensities at 11.5 h, drawn in grey shades on top of the radial velocity profile of the solar wind. The green and blue curves represent, respectively, the lower and upper longitudinal edges of the particle streaming zone, as determined by the prescribed intensity threshold (see text). The first row is for case 1, the second for case 2, and the third for case 3.

bounding the CIR. However, apart from this common decreasing trend, there are several differences between the radial evolution of $\Delta\phi$ when comparing the different cases.

For case 1, it is seen from Panel 1A that at large radial distances ($r \gtrsim 2$ AU), the width of the particle streaming zone remains approximately constant and even starts to increase slightly. At these distances, the particle streaming zone is located entirely within the CIR, meaning that all the IMF lines on which particles are travelling have crossed the shock waves at distances $r < 2$ AU. In contrast, we see in Panel 2A that for case 2 the longitudinal width of the particle streaming zone does not become constant from $r = 2$ AU onward. This is because the stronger cross-field diffusion has brought particles to IMF lines that cross the shock waves at radial distances larger than 2 AU, and hence, contrary to case 1, there are still particles outside the CIR at these large radial distances. However, since the forward and reverse shock waves propagate into the slow and fast solar wind, respectively, we expect that from a certain radial distance onward, all particles will again reside inside the CIR, and hence the behaviour of the longitudinal width will become qualitatively similar to what is observed for case 1.

Panel 3A shows that the strong cross-field diffusion of case 3 introduces several features to the radial dependence of the longitudinal width that are not seen in the two other cases. At small radial distances, the width of the particle streaming zone remains approximately constant, and even increases slightly, which is because some particles have been transported to the unperturbed slow solar wind behind the high-speed stream. However, Panel 3A shows that the constant longitudinal width of the particle intensity distribution is followed by a sudden drop at larger radial distances. For times later than 9.5 h, this drop occurs at approximately the same radial distance of $r = 1.4$ AU. Looking at Panel 3B, we see that this decrease is because the omni-directional intensity drops below the $10^{-8.5}$ threshold in the rarefaction region behind the high-speed solar wind stream (the pronounced indent in the green intensity threshold contour in Panel 3B). This is a result of the strong expansion of magnetic flux tubes inside the rarefaction region, which causes the energetic particle density to get rarefied as well.

In addition, the large cross-field diffusion for case 3 spreads the energetic particles over a much larger region than for the two other cases, hence rarefying the particle densities everywhere in the heliosphere. This is especially true in the fast solar wind stream and the rarefaction region, since the low magnetic field strength implies a more efficient cross-field diffusion (see Eq. (6.1)). As a consequence, the intensities for case 3 are everywhere relatively low as compared to the other cases. These low intensities imply that a large part of the SEP event may go undetected if the pre-event intensity levels are high enough or the measuring instrument is not sensitive enough. In fact, such a situation is illustrated in Panel 3B, where we see that a large region is characterised by particle intensities below the $10^{-8.5}$ threshold, which is therefore not taken into account when determining the width of the intensity distributions. The low intensity values due to the efficient particle spreading also explains why in Panel 3A the longitudinal width does not increase any further after 9.5 h, and why for a radial distance larger than

1.5 AU, the longitudinal width at time 15.5 h is even smaller than at the three previous time instances.

From the first column of Fig. 6.1, it is seen that for all three cases the longitudinal width of the particle streaming zone at small radial distances and at 1.5 h is already significantly larger than the longitudinal width of the injection region, which was 30°. A rapid spread of particles at early times can be understood by considering the diffusive cross-field flux, which can, for small radial distances and in the solar equatorial plane, be approximated as (Strauss et al., 2017):

$$\left|F_{\perp}^{\mathrm{dif}}\right| \sim \kappa_{\perp} \left|\frac{\partial j}{\partial \varphi}\right|.$$

From this expression, we see that the cross-field diffusion will be more notable when large longitudinal gradients are present in the directional intensity function. Since our particles are injected with a uniform intensity from a source region of limited spatial extent, we have in fact that, upon injection, $|\partial j/\partial \varphi| \longrightarrow +\infty$ at the boundaries of our injection region in the solar equatorial plane. This infinite derivative does not produce numerical problems due to the stochastic nature of our model. However, it explains the efficient cross-field diffusion early on in the event (see also Strauss et al., 2017, for a discussion).

Moreover, the above argument is more generally valid at any location in the heliosphere when considering the gradient of the intensity in the direction perpendicular to the magnetic field. More specifically, for an isotropic $\boldsymbol{\kappa}_{\perp}$, the diffusive cross-field flux in the direction of a unit vector $\mathbf{e}_{\perp}$, with $\mathbf{e}_{\perp} \perp \mathbf{b}$, can be defined as

$$\left|F_{\perp}^{\mathrm{dif}}\right| \sim \kappa_{\perp} \left|\mathbf{e}_{\perp} \cdot \nabla j\right|. \tag{6.2}$$

Hence, cross-field diffusion will be most effective where $\kappa_{\perp}$ is large or where there are large particle intensity gradients perpendicular to the magnetic field. Such large gradients are induced by the IMF topology inside the CIR, where the magnetic field is compressed. As discussed above, this compression of the magnetic field lines leads to a compression of the particle intensity distribution, and hence a decreasing longitudinal width. However, the same compression will also produce larger particle intensity gradients perpendicular to the magnetic field, hence increasing the cross-field flux according to Eq. (6.2).

At the same time, we have that the inverse scaling of our cross-field diffusion with the magnetic field strength implies that the perpendicular mean free path decreases inside the CIR. However, as discussed in Chapters 4 and 5, a small cross-field motion of the particles inside the CIR where the IMF lines are closely compressed may transport the particles on field lines that are significantly separated outside the CIR, i.e., at smaller radial distances. The observed cross-field diffusion in our simulations results thus from a non-trivial interplay between the magnetic field dependence of the cross-field

diffusion tensor and the intensity gradients perpendicular to the magnetic field. Both mechanisms are strongly influenced by non-nominal solar wind conditions.

Finally, we remark that by adding the cross-field diffusion term in the spatial part of the FTE, the energetic particles are given an additional velocity component on top of their actual velocity v. As a consequence, particles with $\mu \sim 1$ might spread faster than their speed allows for, hence violating causality (Strauss & Fichtner, 2015). Following a similar procedure as in Strauss & Fichtner (2015) to estimate the impact of this effect in our simulations, we found it to be negligible since the intensities resulting from such particles are more than two orders of magnitude below the selected threshold value. This non-physical behaviour is a consequence of treating the motion of particles perpendicular to the mean magnetic field as a spatial diffusion process, and would not appear if one would instead e.g., model cross-field motions by stochastically varying only the propagation direction of the particles. Such an approach boils down to varying the magnetic unit vector, which is similar to the method implemented by Laitinen et al. (2013) to model the motion of particles along random-walking magnetic field lines.

6.4 The effect of cross-field diffusion on shock accelerated particle populations

We now examine the particle intensity and anisotropy profiles in the solar equatorial plane at a fixed heliocentric radial distance of 1 AU. We focus hereby on energy channels of width $\Delta E = 0.2$ MeV, which are above the initial 4 MeV injection energy of the particles, meaning that we only consider particles that have been accelerated at the shock waves bounding the CIR. The acceleration of protons and ions at shock waves depends on several factors, including the scattering conditions (e.g., Lee, 1983; Gordon et al., 1999; Vainio & Laitinen, 2007; Afanasiev et al., 2015), the shock strength (e.g., Lario et al., 1998; Rice et al., 2003; Rodríguez-Gasén et al., 2011, 2014; Prinsloo et al., 2019), and the shock obliquity (e.g., Zank et al., 2001, 2006; Battarbee et al., 2013), among others. In Section 6.5 we provide a discussion on these factors in the context of CIR shocks, and how they influence the results presented in this section.

Figure 6.2 shows snapshots at 11 h (left) and at 31 h (right) of the intensity and anisotropy profiles for case 1, as a function of $\varphi - \varphi_c$, where φ_c denotes the longitude of the point at 1 AU that connects magnetically to the centre of the particle injection region at 0.1 AU. The left panel of Fig. 6.2 shows two distinct intensity enhancements in the 4.1 ± 0.1 MeV energy channel, resulting from particle acceleration at the two shock waves bounding the CIR. The intensity enhancement at $\varphi - \varphi_c < 0$ is produced by particle acceleration at the reverse shock, whereas the intensity enhancement at $\varphi - \varphi_c > 0$ is produced by particle acceleration at the forward shock. The negative anisotropies in the lower panels of Fig. 6.2 indicate that the acceleration of the particles

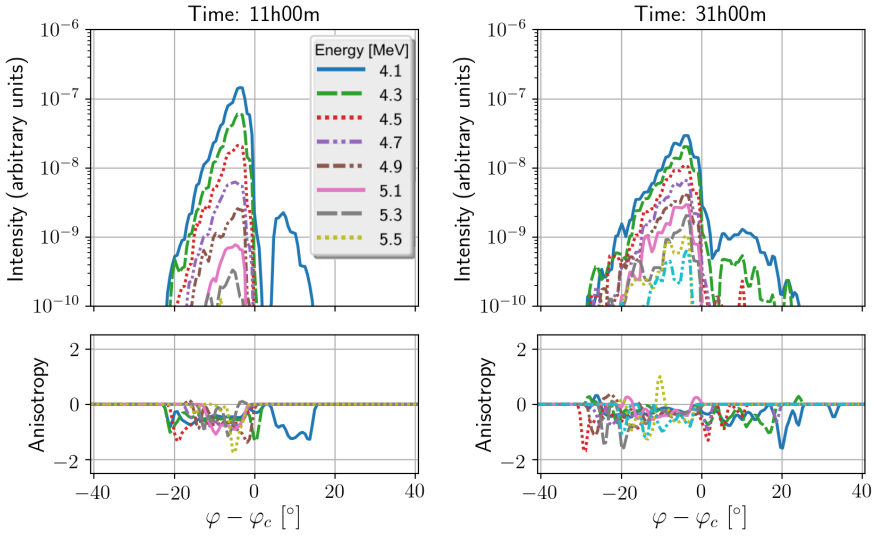

Figure 6.2: Snapshot of the proton intensities (upper panels) and anisotropies (lower panels) for case 1 at 11.0 h (left) and 31.0 h (right). The profiles are measured in the solar equatorial plane at a fixed heliocentric radial distance of 1 AU and shown as a function of the longitudinal separation from the centre of the injection region.

occurs at radial distances larger than 1 AU. This is in accordance with the findings of Chapter 4, where we observed the generation of accelerated particles at the shocks for $r \gtrsim 1.3$ AU. In our simulations, the reverse shock is a considerably more efficient particle accelerator than the forward shock. For the former, we see that after 11 h there are particles accelerated up to ~1.0 MeV above their initial energy, whereas the latter only accelerates particles slightly above 4 MeV.

The two intensity enhancements in the left panel of Fig. 6.2 can co-exist without merging because the SI separating them is characterised by a strong magnetic field, and hence by a weak cross-field diffusion since the latter scales inversely proportional to the magnetic field strength (see Eq.(6.1)). However, since the cross-field diffusion is not exactly zero at the SI, the separation between the two intensity enhancements will slowly diffuse away. The latter might be aided by the large particle intensity gradients perpendicular to the magnetic field observed at the SI. The right panel of Fig. 6.2, which shows the intensity and anisotropy profiles of case 1 at 31.0 h, shows that the intensity dip has indeed increased to a higher intensity level. At this time, the reverse shock has accelerated protons above 5.3 MeV, although the intensities and hence the statistics for these particles are low.

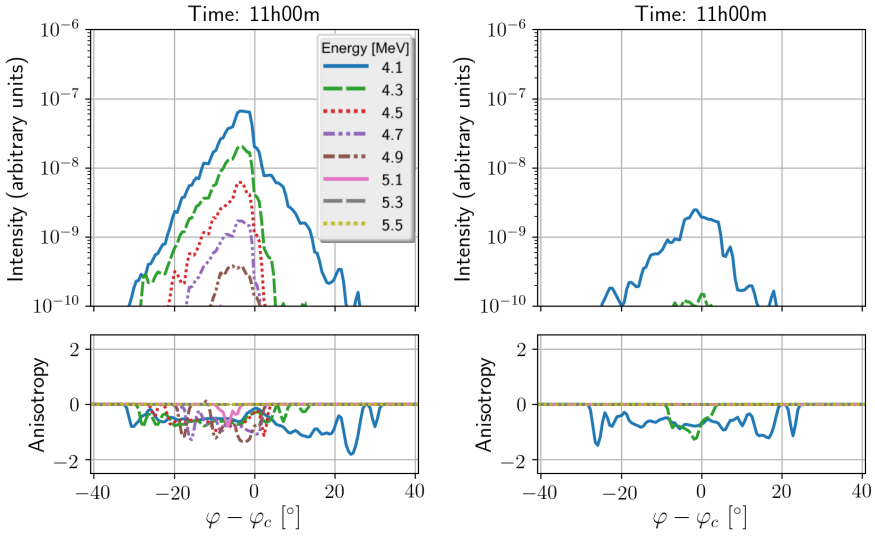

Figure 6.3: Snapshot of the proton intensities (upper panels) and anisotropies (lower panels) at time 11.0 h for case 2 (left) and case 3 (right). The profiles are measured in the solar equatorial plane at a fixed heliocentric radial distance of 1 AU and shown as a function of the longitudinal separation from the centre of the injection region.

Figure. 6.3 shows the longitudinal intensity and anisotropy profiles at 1 AU for case 2 and 3 at 11.0 h. Focusing on the left panel of Fig. 6.3, we see that the stronger cross-field diffusion of case 2 has merged the two 4.1 ± 0.1 MeV intensity enhancements of case 1 into one wide enhancement. Moreover, we see that there is less particle acceleration when compared to the previous case, since the 5.1 ± 0.1 MeV and 5.3 ± 0.1 MeV energy channels are no longer populated by particles. The peak intensities of the other channels have also decreased, yet these channels cover now a larger longitudinal range. The drop in accelerated particle intensities with increasing cross-field diffusion is even more notable when looking at the right panel of Fig. 6.3, which shows the intensity profiles for case 3. This panel illustrates that the large cross-field diffusion assumed in case 3 leads to low intensity levels of accelerated particles. This is because the cross-field diffusion efficiently disperses the particles by transporting them to IMF lines that either cross the shock wave at much larger radial distances, or that enter the CIR before the shock waves have formed.

6.5 Summary and discussion

In this work, we have extended the studies presented in Chapters 4 and 5. Like in those chapters, we considered a slow solar wind configuration containing a high-speed solar wind stream that eventually evolves into a CIR. Furthermore, we injected 4 MeV protons at the inner boundary of our model, from a source region that extends both in the slow and fast solar wind regimes, hence also covering the transition region between both plasma environments. Assuming a cross-field diffusion coefficient that scales inversely proportional to the magnetic field strength, we performed simulations with three different levels of cross-field diffusion. This allowed us to study how the strength of cross-field diffusion may alter the particles spread and the energy content of SEPs in a solar wind that deviates from a nominal solar wind configuration, under the assumptions of our model.

From our simulations, we found that the longitudinal widths of the particle intensity distributions show a general decreasing trend with increasing radial distance, reflecting the underlying IMF topology near and within the CIR. Such a decreasing width is in contrast with what is observed in nominal solar wind configurations, where the width of the particle intensity distribution remains constant in the absence of cross-field diffusion or increases with radial distance if cross-field diffusion is present (see Chapter 5). Although our three simulations with different levels of cross-field diffusion showed overall a similar decreasing trend, there were some notable differences. For the case with the strongest cross-field diffusion, there was a sudden drop in the longitudinal width of the particle intensity distributions at ~1.4 AU, because the particle intensity falls below our prescribed threshold. This intensity drop occurred in the rarefaction region behind the high-speed solar wind stream, where the magnetic flux tubes are strongly expanding, hence rarefying the SEP densities. In addition, the strong cross-field diffusion in our simulation dispersed particles over such a large region in the heliosphere that the intensities decreased everywhere significantly in comparison with the simulations that use a weaker cross-field diffusion. As a consequence, a substantial number of particles resided in regions of the solar wind showing intensities below our prescribed threshold, and were therefore not taken into account when calculating the longitudinal width. A similar situation may happen with actual in-situ observed SEP events, i.e., when particles propagate either under strong diffusive transport conditions or in solar wind rarefaction regions, they might be dispersed efficiently such that their intensities drop below the background level measured by a given particle instrument, as similarly noticed by Pacheco et al. (2019) for electron events simulated under diffusive parallel transport conditions.

Similar to what Strauss et al. (2017) obtained for electron propagation in a nominal IMF, we find that the cross-field diffusion is very effective early in the event, when large intensity gradients are present. However, in contrast to a Parker solar wind, the

compressed IMF topology inside the CIR also gives rise to large intensity gradients perpendicular to the magnetic field, increasing the effectiveness of cross-field diffusion. In contrast, the strongly diverging magnetic field topology in the rarefaction region might produce very low particle intensity gradients, hence decreasing the diffusive cross-field flux as defined in Eq. (6.2). We find thus that for a cross-field diffusion coefficient that scales inversely proportional to the magnetic field strength, the effectiveness of the cross-field diffusion is determined by an intricate interplay between the variations in the magnetic field strength and the particle intensity gradients, both modulated by the IMF topology and hence by the converging or diverging properties of the solar wind flow.

In Section 6.4, we showed the intensity profiles of the shock-accelerated particles at 1 AU, as a function of longitude. For case 1, i.e., the case with the weakest cross-field diffusion, two separate intensity enhancements were visible, reflecting the particle acceleration occurring at the two different shock waves. The negative anisotropies indicate that the acceleration of the particles happens at larger radial distances, where the shocks have formed. This agrees with in-situ observations at 1 AU, showing that the flow of energetic ions accelerated at a CIR shock is typically towards the Sun (Marshall & Stone, 1978).

Moreover, the double structure in the intensity profiles is a feature that is also commonly detected with in-situ observations at different radial distances from the Sun (Barnes & Simpson, 1976; Decker et al., 1981; Tsurutani et al., 1982; Dwyer et al., 1997; Mason & Sanderson, 1999). Like in our simulations, observations measure typically more accelerated particle fluxes originating from the reverse shock than from the forward shock (Tsurutani et al., 1982; Desai et al., 1998; Mason et al., 1999). This difference might be partly due to the fact that the relative speed difference between the unperturbed solar wind and the shock is higher for the reverse shock than for the forward shock, since the reverse shock propagates radially inwards in the solar wind frame (see also Kocharov et al., 2003).

Another important factor that might contribute to the observed differences in accelerated particle fluxes originating from the different shocks is the angle between the shock normal and the upstream magnetic field, i.e., the shock angle, θ_{Bn}. In our simulation, the reverse shock of the CIR is more oblique than the forward shock, which follows from the difference in speed between the fast and slow solar wind. Tsurutani et al. (1982) demonstrated that proton fluxes near CIRs are correlated with the shock angle, with the most intense proton events occurring for shocks that are quasi-perpendicular. This is in accordance with the results obtained by Zank et al. (2006), which illustrated that perpendicular shocks can be very efficient particle accelerators given that there is a sufficient amount of turbulence present in the solar wind to diffuse the particles across magnetic field lines. Interesting to note is that CIR shocks are indeed typically characterised by increased amounts of turbulence (e.g., Horbury & Schmidt, 1999) as compared to the unperturbed solar wind, despite the fact that wave excitation by the

streaming instability is quenched for highly oblique shocks. The latter is a consequence of the proportionality of the wave growth to the shock angle (Gordon et al., 1999; Li et al., 2003; Rice et al., 2003).

The dip between the two intensity enhancements at the reverse and forward shocks coincides with the SI, and can be explained by noting that the field lines adjacent to the SI do not cross the reverse shock wave, nor the forward shock wave. Hence the only way for shock-accelerated particles to reach these field-lines is through cross-field transport. Using observations made by the Pioneer 10 and 11 spacecraft of a CIR lasting for 14 rotations, Tsurutani et al. (1982) showed that the intensity dip increases with a factor of 10 over 11 solar rotations, likely due to cross-field diffusion. Similarly, we see in the simulations of case 1 that the intensity minimum increases in time. Figure 6.2 illustrated that the dip increased by a similar factor of ~10, yet in only 20 h, i.e., much faster than the observations in Tsurutani et al. (1982). This difference can have various causes, as discussed in the following. It may suggest that the cross-field diffusion used in case 1, for which $\lambda_\perp/\lambda_\parallel \sim 10^{-4}$ at 1 AU, might still be too strong inside a CIR. However, Dwyer et al. (1997) obtained values for $\lambda_\perp/\lambda_\parallel$ of the order of unity for three CIRs using 44 – 313 keV/nucleon helium measurements from the Wind spacecraft. Important to note here is that the results of Tsurutani et al. (1982) regarding the increase in the intensity dip near the SI were done when the Pioneer 10 and 11 spacecraft were at a radial distance of ~4.4 and 4.9 AU, whereas the Wind spacecraft is located at ~1 AU, and hence the properties of the solar wind turbulence might be different.

Other non-negligible factors that affect the acceleration of particles and hence also the evolution of the intensity dip are the shock compression ratio (Drury & Voelk, 1981), the obliquity of the shock (Jokipii, 1987), and the shock speed (Prinsloo et al., 2019). In fact, Desai et al. (1998) showed that the proton intensity at CIRs is well correlated with the compression ratio, even if there is no shock present, at least when the particle seed remains constant. In our simulations the particles accelerated at the CIR shocks originate from a flare-like impulsive event, with the particle source region magnetically connected to a limited part of the CIR shocks. However, studies have shown that the seed particle population of most CIR events is likely the supra-thermal tail of the solar wind (see e.g., Chotoo et al., 2000; Mason et al., 2012). This means that the seed population consists of charged particles with energies around ~10 keV/nucleon, i.e., much lower than the 4 MeV injection energy that we consider. Pitch-angle scattering, cross-field diffusion and the acceleration processes in these non-nominal solar wind conditions are dependent on the momentum of the particles. A continuous reservoir of low-energy seed particles at the CIR shocks may thus also help explaining the differences observed between our model and the observations in Tsurutani et al. (1982). However, the observation that CIRs accompanied by the largest energetic particle enhancements are often associated with quasi-perpendicular shocks (Tsurutani et al., 1982), raises the question how low energy protons would overcome the associated injection problem (Jokipii, 1987; Zank et al., 1996). Possible explanations

can be found in the high levels of turbulence found near CIR shocks, or by considering a seed population originating from the supra-thermal tail of the shock-heated solar wind plasma. Prinsloo et al. (2019) illustrated that the prior heating of the solar wind distribution is important in reproducing the intensities of typical energetic storm particle events observed at shock waves driven by CMEs, especially when the injection energy is high like is typically the case for quasi-perpendicular shocks (Tylka et al., 2005; Zank et al., 2006). A similar conclusion may hold for the shock waves bounding the CIR. In our simulations, we avoid any injection problem by only considering protons of sufficiently high energy. We leave it for future work to study how our results change when e.g., continuously injecting the low-energy particles from the supra-thermal tail of the solar wind.

The double-enhancement intensity structure never forms at 1 AU in our case 2 and 3 simulations, where we use a cross-field diffusion magnitude comparable to that of Dwyer et al. (1997). This may be due to strong turbulence variations near and within the CIR that are not captured by our cross-field diffusion model. More specifically, the plasma near the reverse shock is often characterised by significant magnetic fluctuations (Tsurutani et al., 1995; Horbury & Schmidt, 1999), while inside the CIR, the turbulent fluctuation of the magnetic field typically decreases towards the SI (Tsurutani et al., 1982; Dwyer et al., 1997). More recently, Strauss et al. (2016) showed the decrease in turbulence at the SI by computing the variance of the in-situ measured magnetic field components for a CIR. In addition, these authors argue that a tangential magnetic discontinuity like the SI may produce an anisotropic cross-field diffusion tensor, by strongly damping magnetic field fluctuations in the direction perpendicular to the discontinuity. As a consequence, the SI would act as an efficient diffusion barrier, while still allowing for strong cross-field diffusion near the CIR boundaries. Hence, the model proposed by Strauss et al. (2016) seems to explain both the slow increase of the intensity dip in the CIR shown in Tsurutani et al. (1982) and the large values of $\lambda_\perp/\lambda_\parallel$ reported in Dwyer et al. (1997) near the reverse shock. In our simulations, a strong cross-field diffusion near the shocks leads to less particle acceleration, owing to the efficiency of the cross-field diffusion at spreading particles away from the shock wave.

As mentioned above, in addition to different shock properties, this apparent inconsistency between our simulation results and in-situ observations may be due to the fact that we are considering 4 MeV protons, whereas Dwyer et al. (1997) obtain their results for helium with lower energies per nucleon. The ion parallel mean free path typically decreases with decreasing rigidity (Dröge, 2000, 2003), and therefore low-energy particles would be more efficiently trapped near the shock waves. In addition, the strong levels of turbulence observed near CIR shocks might reduce the parallel mean free path of the particles significantly, hence both increasing $\lambda_\perp/\lambda_\parallel$ and facilitating multiple shock encounters. Moreover, cross-field diffusion might have a non-negligible pitch-angle dependence, as discussed in Strauss & Fichtner (2015), which could also influence the scattering of the particles near the shock waves. Further investigation

of these issues is required, as it will eventually lead to a better understanding of particle transport in the complex turbulent environments that characterise large scale interplanetary structures like CIRs. The strongly changing turbulence properties found in the different parts of a CIR, and the possibility to have in-situ measurements of these regions, make CIRs the ideal laboratories to study the transport of particles perpendicular to the mean magnetic field.

Chapter 7

The effect of drifts on the decay phase of SEP events

"But still try, for who knows what is possible?"
– Michael Faraday

Abstract. In this chapter, we study the effect of the magnetic gradient and curvature drifts on the pitch-angle dependent transport of solar energetic particles (SEPs), for ∼3 – 36 MeV protons. We focus on the decay phase of SEP events during which a temporal invariant spectrum and disappearing spatial intensity gradients are often observed; a phenomenon known as the 'reservoir effect' or the 'SEPs flood'. Using PARADISE, we model the effects of drifts in a Parker solar wind, and in a solar wind containing a corotating interaction region (CIR).

It is illustrated that observers magnetically connected close to the edges of the particle injection site measure as a result of drifts a sudden drop in the particle intensities. This drop occurs at different times for different energies, preventing the SEP flood phenomenon to form. In the CIR wind, the drift effects are enhanced due to the presence of large magnetic field gradients. Furthermore, it is also shown that cross-field diffusion can mitigate the drift effects to some extent. We conclude that particle drifts can in some cases substantially modify the decay phase of SEP events, especially if the solar wind contains compression regions or shock waves where the drifts are enhanced. For the SEP flood

phenomenon to establish, it is thus necessary to mitigate the effect of drifts.

This chapter is entirely based on Wijsen et al. (2020).

7.1 Introduction

When SEPs are released from their acceleration site, they commence a journey through the inner heliosphere and beyond. Being charged particles, SEPs are subject to the Lorentz-force, gyrating along the IMF lines embedded in the solar wind. The IMF contains turbulent fluctuations that scatter energetic particles and possibly transport them perpendicular to the magnetic field. In addition, gradients in the IMF and the curvature of the IMF lines induce particle drifts, moving particles across IMF lines.

Recently, Marsh et al. (2013) and Dalla et al. (2015, 2017) used full-orbit test particle simulations to model particle propagation in interplanetary space. These authors illustrate that drifts can have a major effect on the distribution of SEPs in the heliosphere, especially when considering high-energy particles (> 100 MeV protons) or ions with a high mass-to-charge ratio. The importance of drifts also increases towards higher heliocentric latitudes as discussed analytically, for example, by Dalla et al. (2013). In addition, Dalla et al. (2015) show how drifts in the opposite direction of the convective electric field in the solar wind result in the deceleration of energetic particles. This process has also been discussed previously by le Roux et al. (2007) and le Roux & Webb (2009), by using instead a kinetic transport equation approach.

In the past, the effect of particle drifts has mainly been studied in the context of CRs as drifts provide a natural explanation for the observed heliospheric CR modulation over the solar cycle (Jokipii et al., 1977) and for different features in the energy spectrum of cosmic-rays, such as the first and second knees (Ptuskin et al., 1993). Modelling CR transport in space is typically done by solving the Parker equation (Parker, 1965), which describes the evolution of an isotropic distribution function. The spatial evolution is described through a diffusion process, in which the effects of particle drifts enter via the off-diagonal elements of the corresponding diffusion tensor. However, in order to explain the observations of CR modulation using the Parker equation approach, the effects of particle drifts are often too strong and hence have to be reduced (e.g., Potgieter et al., 1989). Full-orbit test particle simulations in a prescribed turbulent magnetic field configuration have indeed illustrated that the drift coefficients in the Parker equation can be suppressed if the level of turbulence is high enough (e.g., Giacalone & Jokipii, 1999; Candia & Roulet, 2004; Minnie et al., 2007; Tautz & Shalchi, 2012; Engelbrecht et al., 2017). However, it is important to note that the Parker equation is only valid for isotropic particle distributions, which is not necessarily valid for SEPs as they are often characterised by strong anisotropies (e.g., Heras et al., 1994). For such

events, the FTE is more appropriate to describe the particle distributions. It is not clear how the results on drift reduction translate to the situation of a pitch-angle dependent distribution function, especially because the particle drifts are in that case also pitch-angle dependent. Assuming a large-scale Parker spiral magnetic field configuration (Parker, 1958), Marsh et al. (2013) used their full-orbit test particle model to show that the scattering conditions have only a weak effect on the particle drifts. However, it is not clear if this is due to the high energies they considered, the relatively large parallel mean free paths, or the way their model treats the effects of turbulence through random scattering events that are Poisson-distributed in time.

Aside from the work mentioned above, particle drifts have been largely ignored when modelling SEP transport in the inner heliosphere. Instead, much more attention has been devoted to cross-field diffusion, as it is perceived as an efficient manner to spread particles in the heliosphere. In several cross-field diffusion models, the perpendicular transport of energetic particles is a result of particles diffusing along magnetic field lines that undergo a random walk (see e.g., Shalchi, 2009, and references therein). Cross-field diffusion is most effective where there are large particle intensity gradients perpendicular to the magnetic field (see e.g., (6.2)), hence, reducing these intensity gradients. Therefore, cross-field diffusion provides a tentative explanation for multi-spacecraft observations that have shown that particle intensities measured in the decay phase of large SEP events by widely separated spacecraft often evolve similarly in time (McKibben, 1972). In addition, the decay phases of these SEP events often have energy spectra that are invariant both in space and time (e.g., Reames et al., 1997a,b). Roelof et al. (1992) suggested that diffusion barriers produced by CMEs and interplanetary shocks may be the responsible mechanism and, hence, they coined the term 'reservoir phenomenon'. Reames et al. (1996) proposed that the formation of the reservoir is based on the trapping of particles in a slowly expanding bottle behind a CME. However, it has been noted by authors such as Wang & Qin (2015) that such an expanding magnetic bottle model would still need cross-field diffusion to reduce the spatial gradients of SEP fluxes. In addition, for some SEP events, CMEs are not directly observed by the spacecraft, yet the reservoir phenomenon is still observed (Dalla et al., 2003) and in some cases, the reservoir phenomenon commences before the arrival of the CME (Reames, 1999; Wang & Qin, 2015). It is for these reasons, among others, that He & Wan (2016) renamed the reservoir phenomenon instead as the 'SEP flood'. In these studies on the reservoir or flood phenomenon, the effects of drifts appear to have been ignored. This despite the observation that during the decay phase particles will have had enough time to drift a substantial distance. In addition, large scale structures in the IMF, such as magnetic bottles, may produce enhanced particle drifts due to, for example, the presence of strong magnetic field gradients.

In Chapter 2, it was illustrated that the spatial term of the FTE contains the GC drift term (see Section 2.3), if a transformation to GC coordinates is made before gyro-averaging the transport equation. In this chapter, we use PARADISE to study the

effect of particle drifts due to the gradient and curvature of the magnetic field on the energy spectra and decay rates of SEP time-intensity profiles measured by observers located at different positions in the inner heliosphere. We assume different solar wind configurations, including nominal Parker solar winds of 300 km s^{-1} and 700 km s^{-1} and a solar wind containing a CIR, modelled with EUHFORIA (Pomoell & Poedts, 2018). Particles are propagated under different scattering conditions and assuming different injection profiles. We find that the energy dependence of drifts might have a substantial effect in some cases, especially for observers magnetically connected to the edges of the SEP injection sites. Moreover, the magnetic bottle that is naturally formed in a solar wind containing a CIR, produces strong drifts making particle intensities measured in different energy channels to decay at different rates.

The chapter is structured as follows. In Section 7.2, we briefly describe our particle transport model. In Sections 7.3.1 and 7.3.2, we study the effect of drifts on the intensity-time profiles measured by observers placed along different IMF lines in a Parker configuration with solar wind speeds of 300 km s^{-1} and 700 km s^{-1}. In Section 7.3.3, we compare the intensity decay rate of different energy channels. In Sections 7.3.4 and 7.3.5, we show how drifts affect the measured particle energy spectra, obtained from the peak intensities and the fluence, respectively. The effect of cross-field diffusion on our results is discussed in Section 7.3.6. In Section 7.3.7, we investigate the particle drifts in a solar wind containing a CIR. We conclude with a summary and discussion in Section 7.4.

7.2 Modelling SEP transport

Like in previous chapters, we use PARADISE to model the transport of SEP in the inner heliosphere. We recall from Chapter 3 that PARADISE solves the FTE as expressed in Eq. (3.25). Important for the study presented in this chapter is that the effect of the GC drifts is included in the spatial part of the FTE that we solve (see Section 2.5). In the following, it is assumed that the GC drifts are due to the curvature and the gradient of the magnetic field. Moroever, as llustrated in the appendix of le Roux & Webb (2009), the FTE also includes the effects of the gradient and curvature drift on the particle energy changes by the convective electric field. In addition, le Roux & Webb (2009) showed that by including the gradient and curvature drifts in the spatial term of the FTE, the equation becomes equivalent to the standard drift guiding kinetic equation (Littlejohn, 1983).

For the PARADISE simulations presented in this chapter, the pseudo-particles are sampled in the phase-space volume $2\pi r^2 \sin(\vartheta)\Delta\vartheta\Delta\varphi\Delta r\Delta E\Delta\mu$, where E is the particle energy and (r, ϑ, φ) are spherical coordinates associated with the inertial frame. We choose $\Delta r = 0.01$ AU, $\Delta\vartheta = \Delta\varphi = 0.5°$, $\Delta\mu = 0.1$, $\log_{10}(\Delta E) = 0.1068215$. The energy

$E_{\text{min}} - E_{\text{max}}$	$\langle E \rangle$
2.39 – 3.06	2.70
3.06 – 3.91	3.46
3.91 – 5.00	4.42
5.00 – 6.39	5.65
6.39 – 8.18	7.23
8.18 – 10.46	9.25
10.46 – 13.37	11.82
13.37 – 17.10	15.12
17.10 – 21.87	19.34
21.87 – 27.96	24.73
27.96 – 35.76	31.62

Table 7.1: Energy channels and their geometric mean $\langle E \rangle$ in MeV.

channels that we consider in this chapter are listed in Table 7.1 and in the following, when discussing a specific energy channel, we simply refer to the geometric mean $\langle E \rangle$ of the channel. Moreover, the sampled pseudo-particle distribution is averaged over time periods of $\Delta t = 5$ min, to obtain better statistics (see Section 3.3.6). Like in chapters 4, 5, and 6, we assume reflective inner boundary conditions. In contrast, the outer boundary condition is chosen absorptive, yet is placed at sufficiently large radial distance such that the pseudo-particles have no time to reach it within the simulation time.

All simulations discussed in this chapter are performed using 1.5×10^8 particles. To increase the statistics further, we average over a time period of 5 min.

To mimic a prompt injection of particles, the protons are injected according to a Reid-Axford time profile (Reid, 1964) and a power law in energy E:

$$j(t) \propto \frac{E^{-\gamma}}{t} \exp\left(-\frac{\beta}{t} - \frac{t}{\tau}\right), \tag{7.1}$$

where we choose the parameters of $\beta = 0.2$ h, $\tau = 1$ h and $\gamma = 3$, unless stated otherwise. We inject particles with an energy range between 2 and 60 MeV uniformly from a region that spans 5° in both longitude and latitude, located at 0.1 AU and centred on the solar equatorial plane. The upper energy of 60 MeV is 24.24 MeV above the highest energy channel considered in our simulations (see Table 7.1). This is done to prevent adiabatic deceleration from depleting the highest energy channel, hence allowing us to focus on the effects of drifts more easily. To obtain comparable statistics in all energy channels, our model injects particles uniformly between 2 and 60 MeV. However, upon injection all particles receive a statistical weight derived from the power law distribution, which is taken into account when sampling the particles.

The particle scattering conditions are determined by the pitch-angle diffusion coefficient $D_{\mu\mu}$, for which we use the same functional form as in previous chapters (see Section 4.2). The level of particle diffusion is quantified by assuming a constant radial mean free path $\lambda_{\parallel}^{r}$ (Bieber et al., 1994). In this chapter, we choose either $\lambda_{\parallel}^{r} = 0.3$ AU or $\lambda_{\parallel}^{r} = 0.08$ AU. We do not consider cross-field diffusion, that is, $\kappa_{\perp} = 0$, except in Section 7.3.6, where we describe the cross-field diffusion model. We inject particles in a Parker IMF of positive polarity for slow 300 km s^{-1} and fast 700 km s^{-1} solar wind configurations. Both solar winds are computed assuming a constant sidereal solar rotation period of 25.4 days and a radial magnetic field strength of 1.85 nT at 1.0 AU. In addition, we inject particles in a solar wind configuration containing a CIR, which is generated by a 3D ideal MHD model. The set-up of these latter simulations is discussed in more detail in Section 7.3.7.

Furthermore, in the results presented below, we focus on observers corotating with the IMF, since the effects of corotation have already been discussed thoroughly in previous studies (see e.g., Dröge et al., 2010; Giacalone & Jokipii, 2012; Wijsen et al., 2019a). Finally, in this work we focus on the effect of drifts in the latitudinal direction only since, close to the equatorial plane, the latitudinal component of the particle drift velocity is dominant with respect to the azimuthal component (e.g., Dalla et al., 2013). Therefore, in the following we consider observers at different latitudes, but all magnetically connected to the azimuthal centre of the injection region.

7.3 Results

7.3.1 Observers along IMF lines

In this section, we study the intensity-time profiles measured by observers placed at heliocentric radial distances of 0.3 AU, 1.0 AU, and 1.5 AU along two different IMF lines. One IMF line has its foot-point located in the centre of the particle injection region and is hence referred to as the central IMF line'. The other has its foot-point 3° more towards the south, that is, 0.5° south of the southernmost edge of the injection region and is therefore referred to as the southern IMF line'. The latter magnetic field line is not connected, thus, to the injection region at 0.1 AU and any particle intensities measured along this IMF line can solely be attributed to drifts since the cross-field diffusion is set to zero.

The results shown in Fig. 7.1 are for particles experiencing a constant radial mean free path of 0.3 AU in a 300 km s^{-1} Parker solar wind. The upper left panel of Fig. 7.1 shows the intensity-time profiles in three different energy channels for the observers located along the central IMF line. After the prompt onset, particle intensities evolve for the three observers identically, that is, the SEP flood phenomenon is reproduced. As

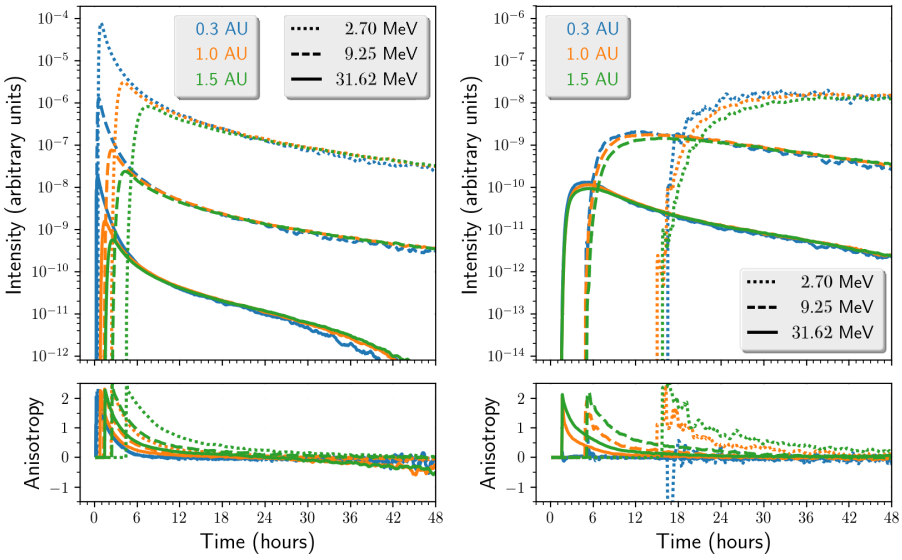

Figure 7.1: Intensity and anisotropy profiles for three observers located along an IMF line in a 300 km s^{-1} Parker solar wind rooted at 0.1 AU at 0° latitude (left panel) and at −3° latitude (right panel). Both panels show the profiles for observers at a heliocentric radial distance of 0.3 AU (blue), 1 AU (orange), and 1.5 AU (green), and for protons of 2.70 MeV (dotted curves), 9.25 MeV (dashed) and 31.62 MeV (solid).

can be seen, the corresponding anisotropies indicate at the onset of the particle event, a clear anti-sunward net-flux of particles, whereas during the decay phase, the particle distribution isotropizes.

The upper right panel of Fig. 7.1 shows the intensity-time profiles for observers along the IMF line not connected to the injection region. Since magnetic gradient and curvature drifts are both directed southwards in a Parker spiral of positive polarity (see e.g., Dalla et al., 2013), particles eventually reach this IMF line. However, this process requires time, explaining why the prompt phase of the particle event is not apparent in the intensity-time profiles. As can be seen, the onset time of the particle event and the attained intensities is approximately identical for the three observers. For the 2.70 MeV energy channel, the onset time is delayed up to ∼16 h. Meanwhile, at this time, the SEP flood phenomenon has already been established for a well-connected observer and, hence, it is also observed for the southwards drifting particles. This is the reason why the onset time and the attained intensities are approximately identical along the southern IMF line. The significant difference between the arrival time of particles residing in the different energy channels is due to the proportionality of the drifts to the

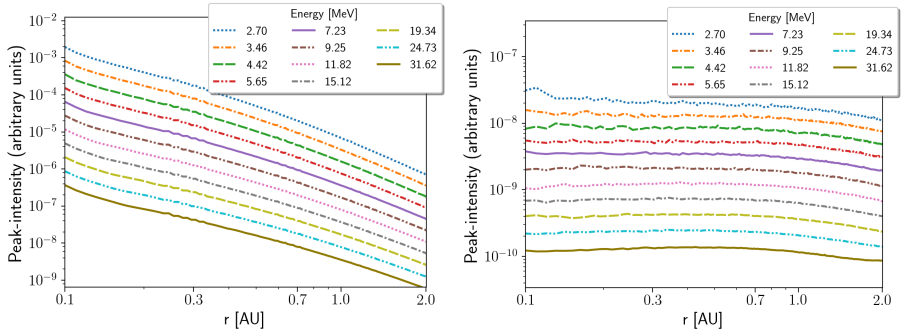

Figure 7.2: Peak-intensities of the simulated proton channels (colour coded) as a function of radial distance for an IMF line at 0° latitude (left panel) and at −3° latitude (right panel).

particle energy.

Finally, in looking at the anisotropies (see Eq. (4.8)), we see that at the onset time, the observers at 1.0 and 1.5 AU see strong positive anisotropies corresponding to anti-sunward streaming protons. This is the case even for the 2.70 MeV channel, which sees the particle onset only after 16 h. At this time, the anisotropies in this channel are much smaller for the same observers along the central IMF line. It is only for the observer at 0.3 AU that the particle distribution is already isotropic at the time of the onset.

Figure 7.2 shows the peak intensity along both IMF lines as a function of the heliocentric radial distance for various energy channels. For the well-connected IMF line, we see a decreasing trend resulting from the expanding magnetic flux tubes and particle scattering, as studied previously in, for example, Lario et al. (2007) and He et al. (2017). The peak intensities along this IMF line track the prompt phase of the particle event. For the southern IMF line, we see that the peak intensity is approximately constant with radial distance. This is because the peak intensities along the IMF line are not reached during the prompt phase of the particle event but during the decay phase when the SEP flood phenomenon is established.

To give a better idea of the effect of the solar wind speed on the particle drifts, we show in Fig. 7.3 the intensity-time profiles for the case of a solar wind of 700 km s^{-1} instead of 300 km s^{-1}. Panel A of the figure shows the intensity-time profiles for the observers along the southern IMF line, where we assumed the same scattering conditions as before (i.e., $\lambda_{\parallel}^{r} = 0.3$ AU). Thus, the only difference in the simulation parameters between this panel and the upper right panel of Fig. 7.1 is the solar wind speed. As can be seen, similar intensities are achieved in both cases, yet the decay rate

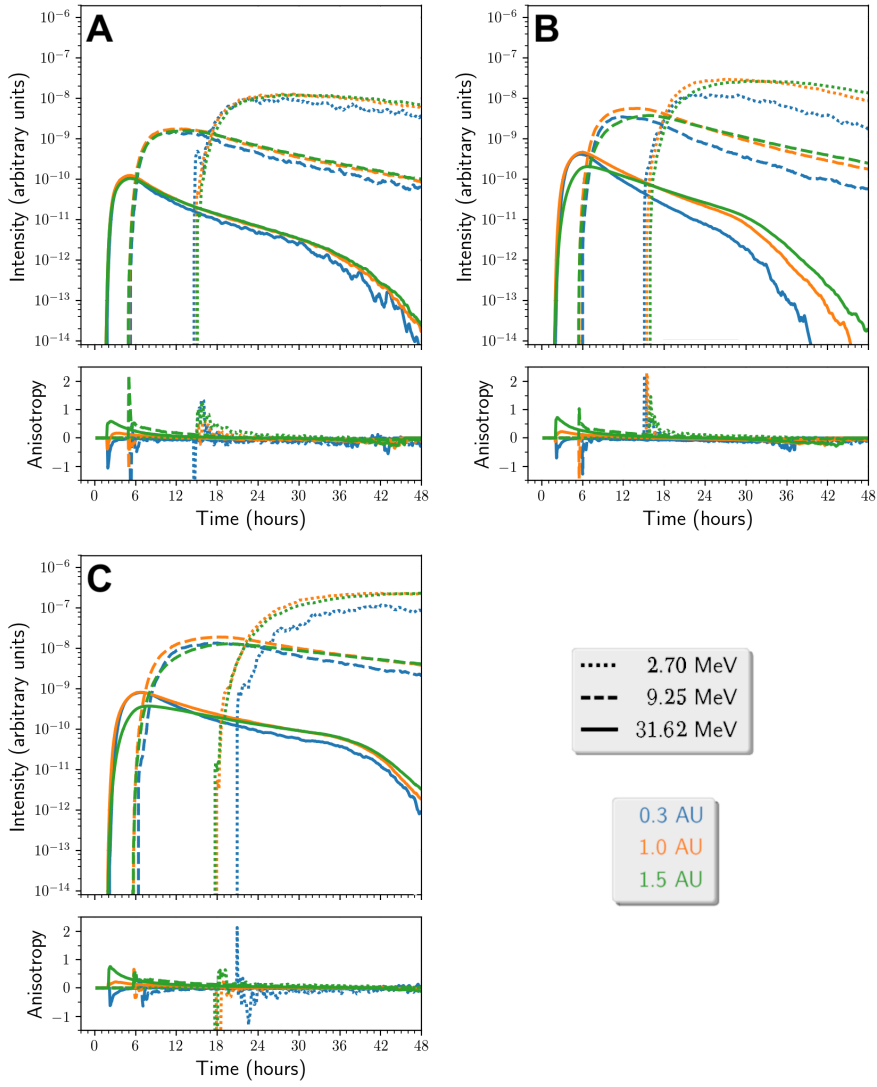

Figure 7.3: Intensity-time profiles for an observer at −3° latitude, in a 700 km s^{-1} Parker solar wind. Panel A: $\lambda_{\parallel}^{r}$ = 0.3 AU. Panel B: $\lambda_{\parallel}^{r}$ = 0.08 AU. Panel C: $\lambda_{\parallel}^{r}$ = 0.08 AU and with particle deceleration switched off.

of the 31.62 MeV channel is considerably higher in the 700 km s^{-1} case, especially towards the end of the simulation. Moreover, the flood phenomenon is not as well established in the 700 km s^{-1} solar wind since the observer at 0.3 AU measures slightly lower particle intensities than the observers at 1.0 and 1.5 AU. A remarkable difference between the slow and fast solar wind cases is that the anisotropies in the former are significantly larger during the first hours following the particle onset. In addition, in contrast to the slow solar wind case, both at 0.3 AU and 1.0 AU in the fast solar wind case, the observers measure negative anisotropies in the 9.25 MeV and the 31.62 MeV energy channels, indicating sunward streaming protons. From the expression of the drift velocities in a Parker spiral (see Eqs. (23) – (29) in Dalla et al., 2013), it can be derived that for the assumed solar wind configurations, the drifts in the latitudinal direction are larger in the fast than in the slow solar wind for heliocentric distances $r \gtrsim 0.8$ AU. In contrast, for $r \lesssim 0.8$ AU, the slow solar wind contains the larger particle latitudinal drift speeds. These radial dependencies of the drifts lead to the different anisotropies measured in both solar wind configurations.

Next, we examine the effect of the radial mean free path on the particle drifts. Panel B of Fig. 7.3 shows the intensity-time profiles for $\lambda_{\parallel}^{r} = 0.08$ AU. As can be seen, decreasing the radial mean free path increases the obtained intensities but also the decay rate, especially for the observer at 0.3 AU. Despite the smaller mean free path and hence the stronger diffusion along the IMF line, the flood phenomenon is less established compared to the previous simulation. This result can be attributed to the effects of particle deceleration. The smaller mean free path traps particles a longer time at small radial distances, where adiabatic deceleration is strongest. To illustrate this, we show in Panel C of Fig. 7.3 the intensity-time profiles for a simulation where the terms causing particle energy changes were switched off (i.e., $dp/dt = 0$). In this case, the different observers do obtain largely similar intensities in the corresponding energy channels. We also note that the onset of the particle intensities in the 2.70 MeV energy channel is delayed by about 2 h. This is because in the simulation including particle deceleration, particles with higher injection energy and hence larger initial drift velocity end up populating the 2.70 MeV energy channel, therefore, arriving earlier. This illustrates the important combined effect of particle deceleration and particle drifts.

Finally, it is worth noting that the peak-intensities of the drifted particles are larger for the smaller particle mean free path case. This in contrast to what is obtained for well-connected observers, where peak-intensities increase for larger mean free paths (Lario et al., 2007; Agueda et al., 2012). Transport under small mean free paths favours the spreading of particles via drifts, translating into enhanced particle intensity levels observed all along the southern IMF line, whereas in the case of the central IMF line, the less anisotropic streaming conditions of the particles translate into larger peak intensities for the observers closer to the Sun with respect to those attained at further distances (Lario et al., 2007).

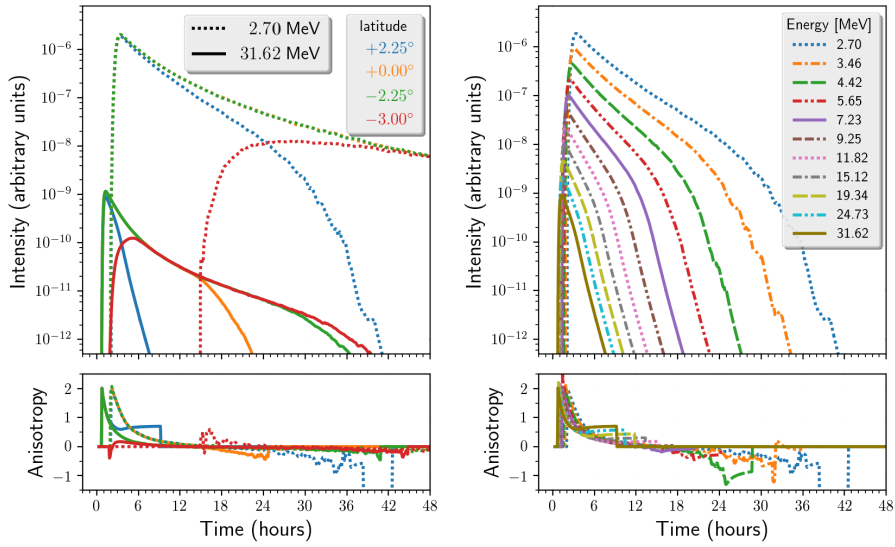

Figure 7.4: *Left panel:* 2.70 MeV and 31.62 MeV proton intensity-time profiles for observers located at 1.0 AU and at different latitudes, as indicated by the insets. *Right panel:* intensity-time profiles with a complete energy coverage for an observer located a 1.0 AU and 2.25° latitude (depicted by blue curves in the left panel).

7.3.2 Observers at different latitudes

In this section, we study in detail the intensity-time profiles of corotating observers located at 1.0 AU, but at different latitudes. Specifically, we consider observers at latitudes 2.25°, 0°, −2.25°, and −3°. These latitudes denote the centre of the corresponding sampling box, which has a latitudinal width $\Delta\vartheta = 0.5°$ (see Section 7.2). Only the first three observers are thus magnetically connected to the particle injection region. A 700 km s^{-1} solar wind and a $\lambda_{\parallel}^{r} = 0.3$ AU are assumed. The left panel of Fig. 7.4 shows the intensities and anisotropies for a high-energy (31.62 MeV) and a low-energy (2.70 MeV) channel. In these figures, the anisotropy is set to zero when the corresponding intensity drops below a threshold value of 10^{-13} to avoid spurious, non-significant fluctuations of the anisotropies. The intensity at high energy is observed to drop quickly for the observer located at 2.25° latitude (blue curves). This observer is connected to a point close to the northern edge of the injection region and since the particles experience drifts that are solely southward in a Parker IMF of positive polarity, particles are rapidly drained from this field line due to the drifts. The right panel of Fig. 7.4 displays the intensity-time profiles for all eleven energy channels for this same observer. In this panel we clearly see how the proportionality of the drifts with the

particles' energy makes the higher-energy channels drop to zero first.

It is important to note that the drops in intensity in Fig. 7.4 are influenced by the assumed spatial sampling resolution. If, for example, the latitudinal extent of the sampling box would be reduced, the southern edge of the sampling box would be shifted northward, (i.e., connected even closer to the northern edge of the injection region) and, hence, the drop-offs in intensity would occur earlier.

The solid orange curve in the left panel of Fig. 7.4 shows that for the observer located in the equatorial plane, the intensities in the highest energy channel eventually also drop to zero. However, this occurs later than for the 2.25° observer because during the first hours of the particle event, the observer at 0° latitude receives drifting particles that were injected north of the solar equatorial plane; the net southward particle flux due to drifts is thus initially zero. With time, all high-energy particles drift southwards of the observer and the in-flux of these particles drops to zero, resulting in the increased decay rate. This does not happen for the 2.70 MeV channel in the depicted time-range, since the particle drifts are much slower at the low energies. Similarly, for the observer located at −2.25° latitude (green curves in the left panel of Fig. 7.4), the increase in the decay rate of the 31.62 MeV channel is only seen after ∼28 h.

As discussed in the previous section, the observer located at −3° latitude (red curves in the left panel of Fig. 7.4) only receives particles due to drifts as it is not magnetically connected to the injection region. There is an increase in the decay rate after ∼32 h in the highest energy channel. This faster decay is not present when drifts are not included (see e.g. the left panel of Fig. 7.5 for an observer in the equatorial plane). Moreover, the intensities in the 2.70 MeV channel converge towards the intensities of the well-connected observers located at 0° and −2.25° latitude.

In considering all observers, we see that for the 31.62 MeV energy channel, the different observers never measure the same intensities, that is, the SEP flood phenomenon is not reproduced. When excluding the observer at 2.25° latitude, the flood phenomenon is reproduced during a short interval (between ∼4 and ∼14 h). However, in this interval, the reservoir effect is not present in the 2.70 MeV channel unless also the observer located at −3.0° latitude is excluded. We note that all well-connected observers would see the same intensity time-profiles if drifts were not present, since particles are injected uniformly from the injection region. Thus, these results clearly demonstrate that drifts prevent the SEP flood phenomenon to occur for observers with different magnetic connection to the particle source, at least when no other cross-field transport mechanisms are at work. This applies to the observers at different radial distances (not shown here).

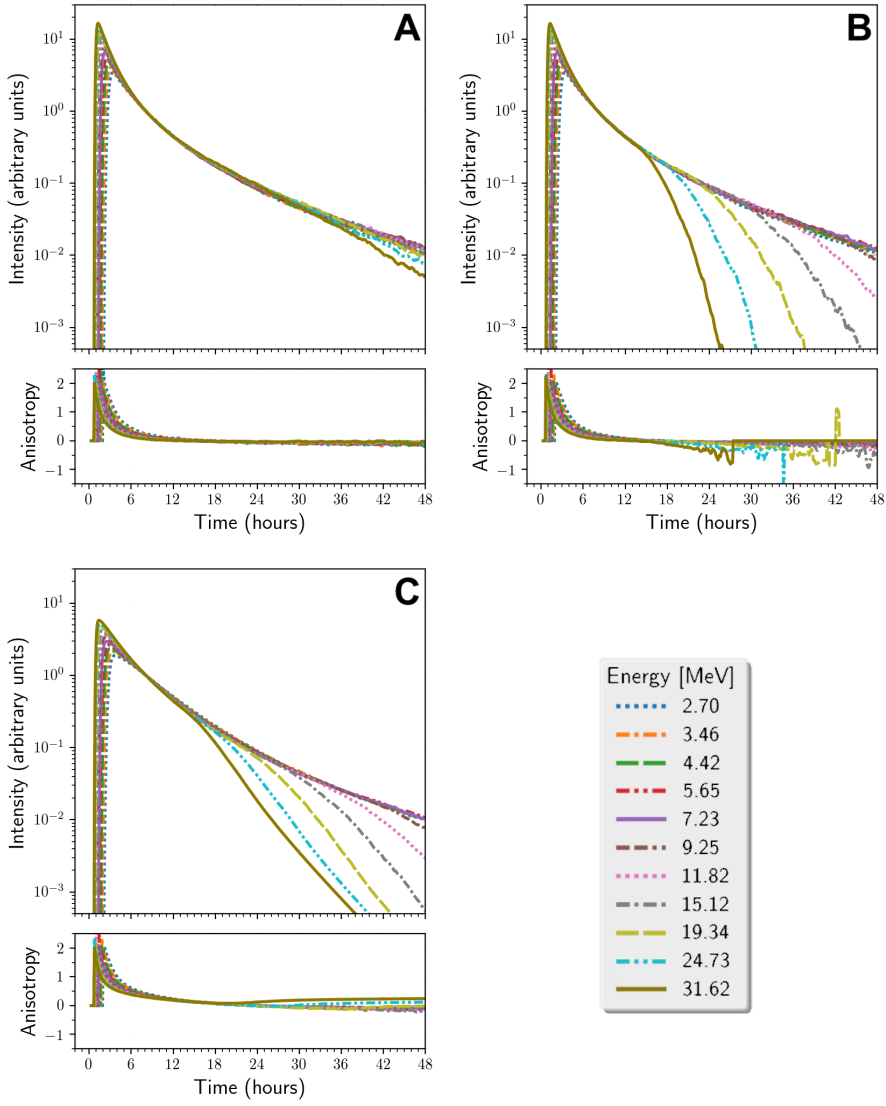

Figure 7.5: Normalised intensity-time profiles for observers at 0° latitude. Panel A is for simulations with no particle drifts, whereas Panel B includes drifts. In Panel C, particles are injected according to a Reid-Axford profile with a slower decay rate (see text).

7.3.3 The intensity decay rates

As noted in the introduction, the decay phase of SEP events is often characterised by disappearing spatial intensity gradients and by identical decay rates at different energy channels. In this section, we compare these decay rates by normalising the intensity time-profiles obtained for an observer located in the solar equatorial plane to their value attained at $t = 8$ h. As in the previous section, we consider a 700 km s^{-1} solar wind with $\lambda_{\parallel}^{r} = 0.3$ AU. Panel A of Fig. 7.5 shows the intensity-time profiles obtained when the particle drift $\mathbf{V}_d$ in Eqs. (3.26) – (3.28) is set to zero in the simulation. In this case, particle intensities measured in different energy channels decay at a similar rate until nearer to the end of the simulation where the highest energy channel starts decaying faster. Despite that particles have been injected up to 60 MeV, eventually the majority have decelerated to energies below 31.62 MeV and, consequently, this energy channel becomes depleted of particles. The depletion of intensity in the 31.62 MeV channel does not occur within the simulated 48 h when, instead, particles are injected up to, for example, 90 MeV, (not shown here). Panel B of Fig. 7.5 shows the intensity-time profiles when the drift term is included in Eqs. (3.26) – (3.28), illustrating that drifts cause a significant increase in the decay rate in the higher energy channels. Consequently, it is only approximately ten hours after the prompt phase that a similar decay rate is seen in all energy channels.

Finally, Panel C of Fig. 7.5 shows the intensity-time profiles when injecting particles according to a Reid-Axford profile with a much slower decay rate, that is, with $\beta = 0.2$ h $\tau = 8$ h in Eq. (7.1). Such a heavy-tailed injection time-profile mimics a prolonged injection of SEPs. As can be seen, the intensity drop-off in the high-energy channels due to drifts is much more gradual. However, different energy channels still show different decay rates.

7.3.4 Peak-intensity energy spectra

In this section, we study the effects of drifts on the energy spectrum measured during the peak-intensity in every energy channel for a 700 km s^{-1} solar wind. The peak-intensity energy spectrum is often used as a proxy for the particle energy spectrum dN/dE near the Sun, where dN denotes the number of particles in an infinitesimal phase-space element[1]. If particles were to travel scatter-free and without energy changes, the observed peak-intensity energy spectrum would correspond to the injected spectrum. In the present simulation setup, we would therefore obtain a peak intensity spectrum proportional to $E^{-3.5}$, since particles are injected according to $j \propto E^{-3}$ (or $dN/dE \propto E^{-3.5}$; see Section 2).

[1] The differential energy spectrum, $j(E)$ (often denoted as dJ/dE), is proportional to $v\,dN/dE$.

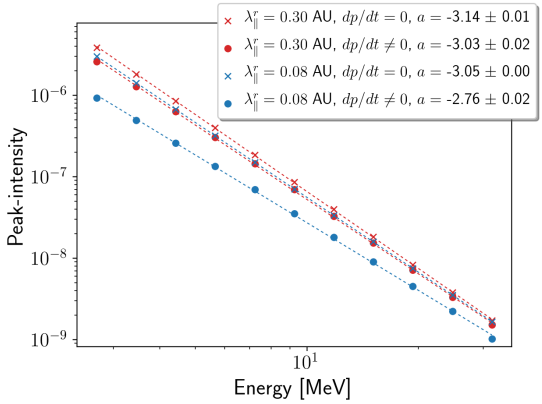

Figure 7.6: Peak-intensity spectra for simulations with $\mathbf{V}_d = 0$ in Eqs. (3.26) – (3.28) and for observers at 1.0 AU and 0° latitude in the 700 km s^{-1} solar wind. Dotted lines are linear fits with the slope a and the standard error given in the inset.

However, adiabatic deceleration and the (energy dependent) particle scattering will harden the spectrum. Figure 7.6 shows the energy spectra for four simulations without particle drifts, both with and without particle deceleration and for two different radial mean free paths. Denoting the slope of the linear (in log-log space) fit to the data in the figure by a, we see that all energy spectra are harder than the injected spectrum, that is, the absolute value of the slope is always smaller than 3.5. The energy dependence of the assumed diffusion coefficient $D_{\mu\mu}$ (see also Eq. (4.5)) implies that low-energy particles have a smaller mean free path than high-energy particles, therefore lowering the attained peak-intensity more for the former compared to the latter (Lario et al., 2007). As a result, the energy spectrum is hardened. The diffusion of the peak-intensities due to scattering also explains why in Fig. 7.6, the peak-intensities are lower for $\lambda_\parallel^r = 0.08$ AU than for $\lambda_\parallel^r = 0.3$ AU. Moreover, the smaller the mean free path, the more pronounced the effect of the energy dependence of the mean free path on the energy spectrum as it takes a longer time for the particles to reach the observer. In addition, the smaller mean free path for low-energy particles will keep these particles closer to the Sun for a prolonged time, where the adiabatic deceleration is largest, hence, further hardening the energy spectrum.

Apart from scattering and adiabatic deceleration, particle drifts can modify the observed peak-intensity energy spectrum, as drifts are energy dependent. Figure 7.7 shows the peak-intensity energy spectra for observers that are, as before, located at different radial distances along the same IMF line. This is done for three different IMF lines, where each IMF line's foot-point has a different latitude. The left and right panels of Fig. 7.7 shows results for the injection intensity $j(E) \propto E^{-1}$ and $j(E) \propto E^{-3}$, respectively. The

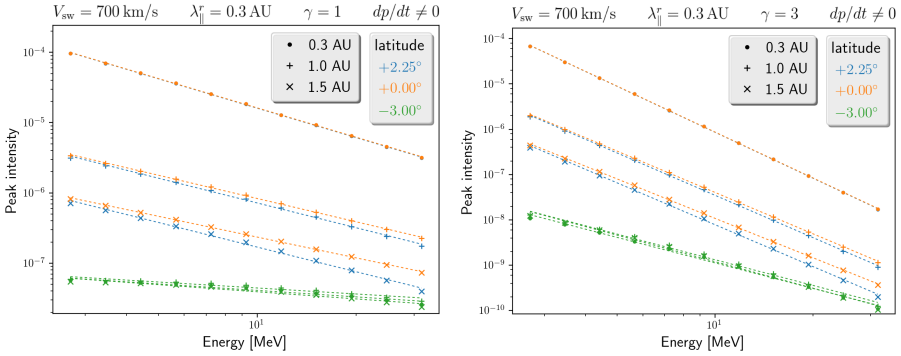

Figure 7.7: Peak-intensity spectra for simulations with the effect of drifts included and for observers in a 700 km s^{-1} solar wind, located at different radial distances and latitudes. Left and right panels are for injection intensities $j \propto E^{-1}$ and $j \propto E^{-3}$, respectively. The dotted curves are linear fits with the slope a and its standard error given in Table 7.2. We note that the orange line covers the blue line for the observers at 0.3 AU (dot symbols).

dotted lines are linear fits to the energy spectra, with the estimated slope a and the standard error given in Table 7.2.

For observers in the solar equatorial plane (orange curves) the energy spectra can be seen to harden with radial distance. In contrast, for the observer located at 2.25° latitude (blue curves), the energy spectra remain constant with radial distance. This is because by the time the particles reach 1.5 AU, some high-energy particles have already drifted significantly southward, counteracting the spectral hardening that would be otherwise observed. Consequently, an IMF line with foot-point closer to the northern edge of the injection region would show an energy spectrum that softens with radial distance. At small radial distances, the observers located at 0.3 AU with latitudes 2.25° and 0° measure identical peak-intensities. This is because these peak-intensities are obtained early in the simulation, before the effects of drifts become notable.

The green curves of Fig. 7.7 show that observers at latitude −3° have a much harder spectrum than the others. This is due to the proportionality of the drifts to the particle energy. In the left panel, depicting the case of $\gamma = 1$ in Eq. (7.1), we expect, therefore, to see a peak-intensity energy spectrum $E^{-0.5}$. However, as noted before, particle scattering and adiabatic deceleration will harden the spectrum even more, explaining the $a < 0.5$ slope that is obtained. Analogously for case of $\gamma = 3$, we expect to see a peak-intensity energy spectrum harder than $E^{-2.5}$, which is indeed the case. Finally, it is interesting to note that the energy spectrum of observers along the IMF line with latitude −3° is independent of radial distance. This is because the peak-intensity occurs

γ	lat [°]	r [AU]	slope a	standard error
1	2.25	0.3	−1.39	0.01
	2.25	1.0	−1.17	0.01
	2.25	1.5	−1.17	0.01
	0.00	0.3	−1.39	0.01
	0.00	1.0	−1.10	0.01
	0.00	1.5	−0.98	0.01
	−3.00	0.3	−0.33	0.03
	−3.00	1.0	−0.29	0.02
	−3.00	1.5	−0.34	0.03
3	2.25	0.3	−3.37	0.01
	2.25	1.0	−3.10	0.02
	2.25	1.5	−3.07	0.03
	0.00	0.3	−3.37	0.01
	0.00	1.0	−3.03	0.02
	0.00	1.5	−2.89	0.02
	−3.00	0.3	−1.94	0.05
	−3.00	1.0	−1.89	0.05
	−3.00	1.5	−1.94	0.04

Table 7.2: Linear Regression variables of Fig. 7.7.

during the decay phase of the SEP event when the SEP flood phenomenon is established along IMF lines (see Section 7.3.1).

7.3.5 Energy spectra of fluence

We now examine the energy spectrum obtained from computing the particle fluence for observers located at different latitudes at 1 AU. As for the case with the energy spectrum of the peak-intensities, the fluence energy spectrum can be used as a proxy for the energy spectrum dN/dE near the Sun, especially when the particle mean free path is large.

Since the particle drifts introduce changes on the timescale of hours, we divide the 48 simulated hours in three different time intervals, each 16 h long. Figure 7.8 shows the energy spectra for four different observers. In Panel A, we see that during the first 16 h interval, drifts soften the energy spectrum for the observer at 2.25° latitude with respect to the observer at 0°. For the observer at −3° latitude we see an energy spectrum with positive slope at low energies, again due to the energy dependence of the drifts (drifted low-energy protons have just started to reach the 1.0 AU observer within this period; see Panel A of Fig. 7.3). Panel B of Fig. 7.8 shows how a very soft energy spectrum

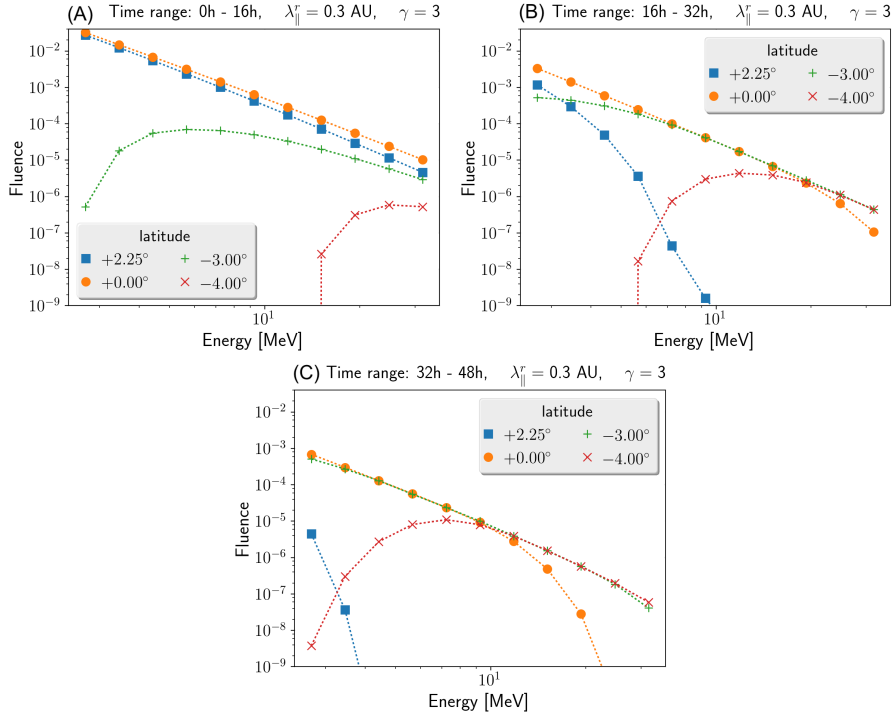

Figure 7.8: Fluence energy spectra for three different time intervals, as indicated above the figures. The energy spectra are for observers in a 700 km s^{-1} Parker wind located at different latitudes at 1 AU.

is observed at 2.25° latitude. In contrast, the energy spectra of the observers at −3° and −4° latitude converge towards the one of the observer in the solar equatorial plane, except at the high-energy end, where the equatorial observer starts seeing a softening of its energy spectra due to the particle drifts. This becomes even more pronounced in the last 16 h of the simulation, during which the energy spectrum of the 0° observer is formed by a power law and an exponential rollover at ∼10 MeV (see also panel B of Fig. 7.5).

7.3.6 The effect of cross-field diffusion

In the previous sections, we illustrate how drifts alter the modelled intensity-time profiles and energy spectra. It is shown that drifts can pose a challenge for the formation of the SEP flood phenomenon, if no other cross-field transport mechanisms are available.

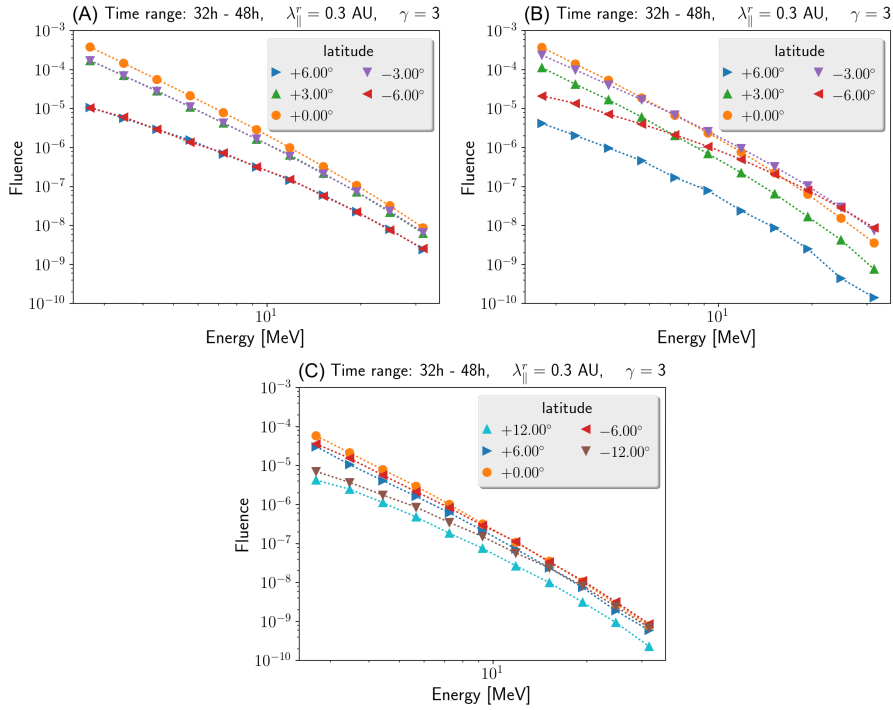

Figure 7.9: Fluence energy spectra for simulations with cross-field diffusion, measured between 32h and 48h. Panels A and B are for $\alpha = 10^{-4}$, whereas Panel C is for $\alpha = 10^{-3}$. Panel A is for simulations without particle drifts, whereas panels B and C include drifts.

The SEP flood or reservoir effect is, however, considered as an effect of spatial diffusion (e.g., Wang & Qin, 2015). In this section, we show how cross-field diffusion might alter the results of the previous sections. In order to do so, we perform simulations using an axisymmetric cross-field diffusion process, with the same diffusion coefficient as in chapters 4, 5 and 6, that is,

$$\kappa_\perp = \alpha \frac{\pi}{12} v \lambda_\parallel \frac{B_0}{B}, \tag{7.2}$$

where B_0 is the magnetic field strength at 1 AU, $\lambda_\parallel = \lambda_\parallel^r / b_r^2$ is the parallel mean free path, and the parameter α determines the strength of the cross-field diffusion. The simple functional form of $\kappa_\perp$ allows us to easily track the effects of cross-field diffusion in our simulations. We leave it to future work to study the effects of more advanced cross-field diffusion theories on the pitch-angle dependent drifts.

Panels A and B of Fig. 7.9 show the fluence energy spectra for different observers, measured between 32h and 48h and with a cross-field diffusion parameter $\alpha = 10^{-4}$. Panel A of the figure corresponds to simulations without particle drifts, whereas the Panel B includes the effects of particle drifts. A comparison of both panels illustrates that significant differences exist between the two simulations. The symmetry with respect to the solar equatorial plane is broken when drifts are present, with the observers in the southern hemisphere measuring a harder energy spectrum than the corresponding observers in the northern hemisphere. Since different observers measure a different energy spectrum, the SEP flood phenomenon is not reproduced. The slopes of the energy spectra of the different observers match more closely when no particle drifts are included, although they are not identical. This is because the cross-field diffusion model we use contains an energy-dependence, which counteracts the establishment of the reservoir phenomenon.

Panel C of Fig. 7.9 shows the same as Panel B, yet for a cross-field diffusion process that is ten times stronger ($\alpha = 10^{-3}$). As before, we see that the particle drifts can break the symmetry with respect to the solar equatorial plane. However, the difference between the observers at $\pm 6^\circ$ is considerably smaller than in Panel B, that is, cross-field diffusion mitigates the effect of the drifts. At larger latitudes and high energies, we still see a non-negligible difference between the northern and the corresponding southern observer.

7.3.7 A magnetic bottle

The reservoir phenomenon is usually attributed to the expansion of a magnetic bottle, typically in association with CMEs (Reames et al., 1996). Another solar wind configuration that also contains a magnetic bottle is a CIR. In this case, one end of the bottle is formed by the converging IMF lines near the Sun whereas the other end is formed at the CIR, where the plasma and IMF are compressed. In Section 4.4.1, we used EUHFORIA to generate a solar wind configuration containing a CIR. We recall that this was done by prescribing a slow solar wind of 330 km s^{-1} everywhere at the inner boundary, with the exception of a circular 660 km s^{-1} fast solar wind region with a 30° diameter and a midpoint located at 5° latitude. Between the slow and fast wind, a transition region exists in which the solar wind speed increases linearly. This transition region eventually evolves at larger radial distances into a corotating interaction region bounded by two MHD shock waves (see Fig. 4.4).

Figure 7.10 shows the logarithm of the magnetic field strength in the solar equatorial plane, as well as some magnetic field lines. From the inner boundary, we inject particles in a region located in the slow solar wind in front of the fast wind stream. The magnetic field lines bounding the injection region are denoted in green and, as before, the injection region is centred on the solar equatorial plane with a latitudinal width

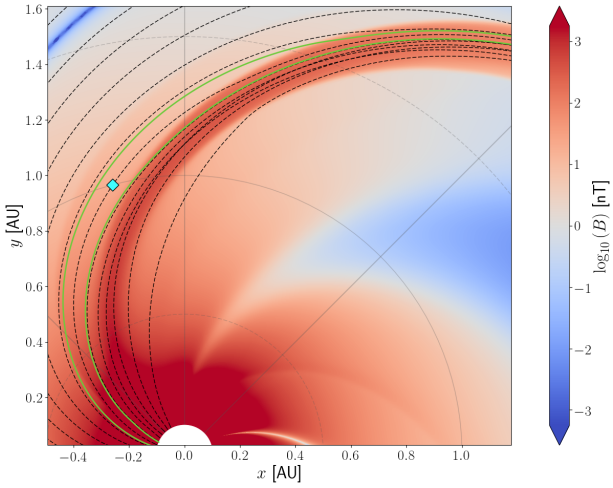

Figure 7.10: Magnetic field strength in the solar equatorial plane. Dashed lines represent some IMF lines with equally spaced foot-points. Green lines are the IMF lines at the edges of the particle injection region. The cyan diamond is the observer discussed in the text.

of 5°. The green IMF lines in Fig. 7.10 highlight the magnetic bottle structure that has formed. In addition, it is shown in Chapter 4 that the strong and sudden magnetic field enhancement at the forward shock or compression wave of the CIR is an effective particle mirror. Particles are injected as described in Section 7.2, with $\lambda_{\parallel}^{r} = 0.3$ AU and $\kappa_{\perp} = 0$. Moreover, we do both simulations with and without the inclusion of particle drifts in the spatial term of the FTE.

Panels A and B of Fig. 7.11 show the intensity-time profiles for the corotating observer indicated by a cyan diamond in Fig. 7.10, who is thus located in the solar equatorial plane. Panel A shows the results obtained for simulations when the GC drift $\mathbf{V}_d$ is neglected in Eqs. (3.26) – (3.28), whereas Panel B includes those particle drift effects. The time-intensity profiles in Panel A decay very slowly with time. For example, over a range of ∼48 h the intensities only drop by a factor of ∼3 for the lowest energy channel, which is much less than in a Parker spiral, where there is typically a decrease of several orders of magnitude (see e.g. Fig. 7.1). As we already alluded to previously, this is the effect of the magnetic bottle, trapping the particles between the Sun and the CIR.

In Panel B of Fig. 7.11, the time-intensity profiles are strongly altered when the effect of particle drifts are included. At the forward shock wave of the CIR, there is a strong magnetic gradient pointing sunward, which enhances the southward gradient drift motion of the particles. As a result, all energy channels are affected by the drifts. This

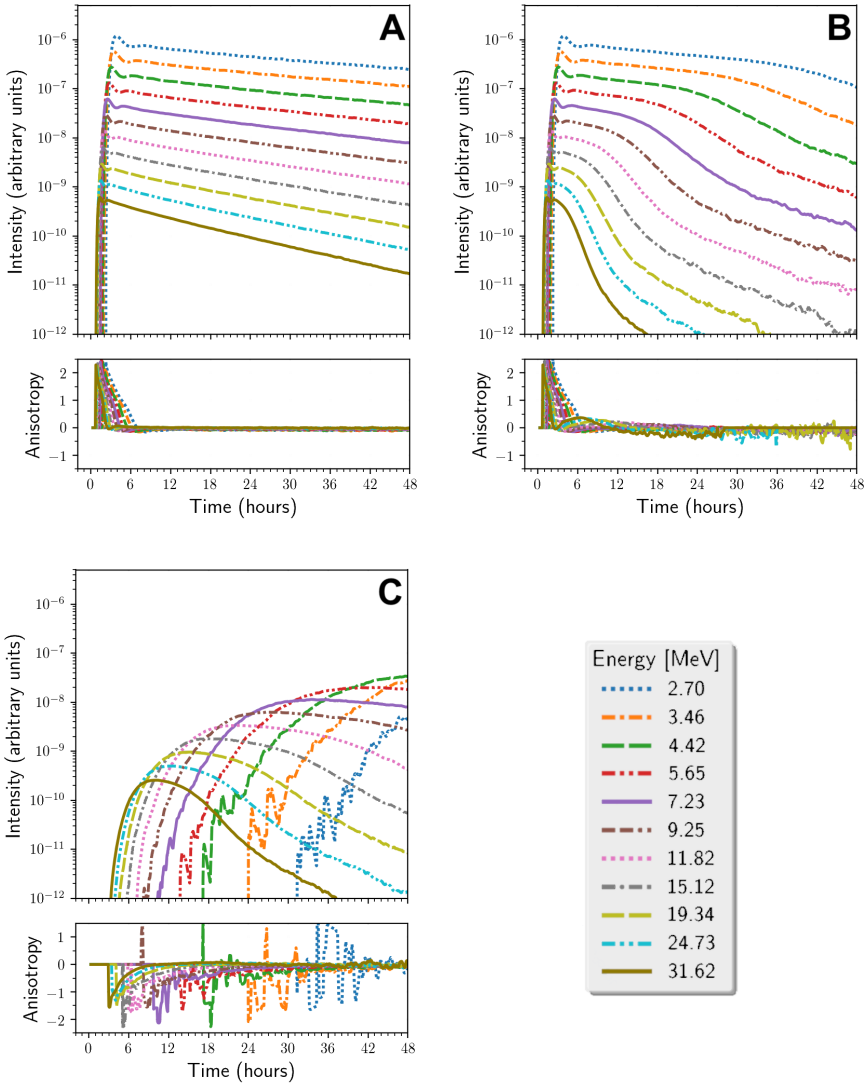

Figure 7.11: Panels A and B are the intensity-time profiles for the observer indicated by the cyan diamond in Fig. 7.10 for simulations without and with particle drifts, respectively. Panel C is for an observer at the same longitude as the other panels yet at a latitude of $-6.5°$ and with the effect of particle drifts included.

is in sharp contrast with the 300 km s^{-1} Parker solar wind case, where drifts had no effects on the intensity decay rates for a well-connected observer (see left panel of Fig. 7.1), and with the 700 km s^{-1} solar wind, where only the high energy channels were affected by drifts. Moreover, Panel B of Fig. 7.11 shows that different energy channels have different decay rates, with the higher energy channels decaying faster. No reservoir phenomenon is thus established, despite the presence of a magnetic bottle.

Panel C of Fig. 7.10 displays the intensities measured by an observer located at −6.5° in latitude. In the Parker spiral, this observer did not see any significant intensities, yet here we see that the observer detects intensities comparable and even higher than the intensities of a well-connected observer in the decay phase. The intensity in the 31.62 MeV channel is only a factor of ∼3 lower than the peak intensity of that channel for the well-connected observer. From the anisotropies, we see that most particles are streaming sunward, which is a result of the significant drifts and the mirroring that these particles undergo when reaching the forward shock wave bounding the CIR.

Figure 7.12 shows the 31.62 MeV intensities and anisotropies during the first 6 h of the simulation, when particles are instead injected as a delta function in time. The inset plots show three snapshots of the normalised pitch angle distributions (PADs). The first snapshot corresponds to the peak phase and shows a clear anti-sunward streaming particle distribution (i.e., a PAD with a positive slope). However, after ∼2 h, a second maximum in the intensity profiles appears. The corresponding PAD has a negative slope, indicating sunward streaming protons. These are particles that have been mirrored at the forward shock of the CIR. Afterwards, the simulation without drifts slowly decreases in intensity and becomes more isotropic (a vanishing anisotropy and a horizontal PAD). In contrast, the simulation that includes drifts shows a rapidly decreasing intensity profile with positive anisotropies and a PAD of positive slope, indicating anti-sunward streaming protons like at the peak phase of the event. This is because the particles not only undergo mirroring at the forward shock, but also strong southwards drifts, driving the particles to lower latitudes.

7.4 Summary and discussion

In this chapter, we have investigated how drifts may affect the intensity-time profiles of SEP events for protons with energies between 2.39 and 35.76 MeV. Since drifts are a relatively slow process compared to the streaming of the particles along the IMF lines, their effect is mainly manifested during the decay phase of SEP events.

When the effect of drifts is neglected in the spatial part of the FTE, the modelled intensity-time profiles for observers located at different radial distances along an IMF line typically show the same intensity fall-off after the prompt phase of the particle event. Moreover, the decay rate is similar for all energy channels. Both properties

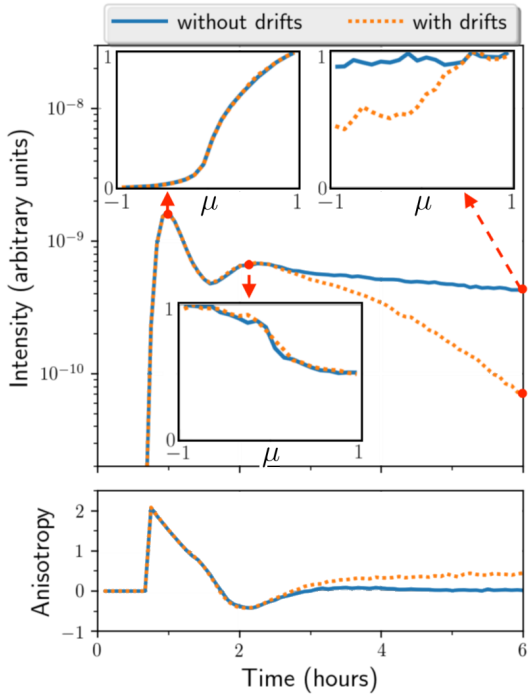

Figure 7.12: 31.62 MeV intensities and anisotropies for the observer indicated by the cyan diamond in Fig. 7.10. The three insets show the normalised pitch angle distributions, corresponding to the snapshots indicated by the red dots. Solid and dotted lines are for simulations without and with particle drifts.

are in accordance with the SEP flood or reservoir phenomenon and are expected in a diffusion-dominated system. When magnetic gradient and curvature drifts are modelled in a Parker spiral configuration of positive polarity, particles experience a southwards drift. As a result, an observer magnetically connected close to the northern edge of the particle injection region will see a prompt drop in the intensities. The proportionality of the drifts to energy leads to an intensity drop that occurs earlier for the more energetic particles. As a result, the intensity drop is different from the drop observed when a stationary observer leaves the particle streaming zone due to corotation (see e.g. Dröge et al. (2010); Wijsen et al. (2019a)). This latter intensity drop is more abrupt and occurs quasi-simultaneously for all energy channels, unless there is energy-dependent cross-field diffusion or significant particle drifts in the azimuthal direction.

Observers that have a magnetic connection south of the particle injection region detect the particle onset at later times when compared to a well-connected observer. For these

southern observers, the particle onset occurs during the decay phase of the SEP event seen by the well-connected observer and, hence, observers located along the same IMF line see similar intensities and onset times, irrespective of their radial distance from the Sun. In addition, because of the energy dependence of the drifts, the difference in the arrival times among particles of different energies is larger as compared to a well-connected event.

The effect of drifts on the different energy channels is enhanced by adiabatic deceleration since high-energy particles may drift significantly before decelerating to lower-energy channels, giving the false impression that the low-energy particles are drifting considerably. Such an impression is aided by assuming strong scattering conditions since a small mean free path keeps particles for a prolonged amount of time at smaller radial distances, where the adiabatic deceleration is strongest. This is especially true for a fast solar wind, since adiabatic deceleration scales with the solar wind velocity in a Parker solar wind.

Observers located south of the particle injection region measure a very hard energy spectrum when looking at the peak intensities. In contrast, observers magnetically connected to the northern edge of the particle injection region measure a much softer energy spectrum. A similar trend is observed when studying the energy spectra derived from particle fluences. An observer at positive latitude sees a very soft energy spectrum during the decay phase of the SEP event. In contrast, an observer south of the particle injection region measures an energy spectrum with a positive slope at lower energies for a prolonged amount of time. The observer located in the solar equatorial plane sees the energy spectrum evolving from a simple power law to a power law with an exponential rollover at high energies due to the combined effects of drifts and adiabatic deceleration (see also Fig. 7.5).

An evident way of reproducing the SEP flood phenomenon is to have strong spatial diffusion (McKibben, 1972), since diffusion tends to mitigate any gradients present in a physical system. If cross-field diffusion is responsible for the reservoir phenomenon, then particle drifts impose a lower limit on the strength of the needed cross-field diffusion. This is because the cross-field diffusion needs to be strong enough to mitigate any asymmetry introduced by the particle drifts. The cross-field diffusion used in Section 7.3.6 with $\alpha = 10^{-4}$ was not strong enough to wash away the drift effects on the particle distribution function. For a cross-field diffusion ten times stronger, i.e., $\alpha = 10^{-3}$, the asymmetry between the intensities in the northern and southern hemispheres is diminished. However, the efficiency of cross-field diffusion to mitigate the effect of particle drifts might strongly depend on the properties of the diffusion tensor as, for example, its dependence on the particle energy. Hence more simulations with different diffusion models are required to clarify this point.

Finally, the reservoir phenomenon has been explained in the past as the result of particle trapping in an expanding magnetic bottle (Reames et al., 1996). In Section 7.3.7, we

use a solar wind configuration with a CIR that naturally produces a magnetic bottle, although it is not expanding. When particle drifts were not included in the spatial part of the FTE, we observed a very slow decay in the different energy channels, but with a slightly different decay rate.

When including the effect of drifts in the simulations, the particle intensity-time profiles were strongly modified. In contrast to the cases in a Parker IMF, all energy channels are now affected by the particle drifts, even the lower ones. The reason is that particle drifts are strongly enhanced at the forward shock wave that bounds the CIR. The gradient drift introduced by this forward compression wave is mostly southward in the solar equatorial plane, hence, intensifying the drift present in a nominal Parker spiral of positive polarity. As a result, the asymmetry of the particle distribution as a function of latitude is strongly enhanced.

Although it is not modelled here, a magnetic bottle configuration behind a CME is also likely to be characterised by strong magnetic field gradients and, hence, strong particle drifts. Any model attempting to explain the reservoir phenomenon should take this into account, although significant cross-field diffusion might diminish or remove the effect of drifts. Full-orbit particle simulations indicate that the particle drift terms as appearing in the isotropic Parker equation can be quenched when strong turbulence is present (see e.g., Engelbrecht et al., 2017, and references therein). However, the results of these full-orbit simulations might be altered strongly near high amplitude compression waves or shock waves, where strong magnetic field gradients amplify the particle drifts. In addition, the level of turbulence near shock waves depends on the shock geometry, since, for example, the excitation of Alfvén waves due to particle streaming is proportional to the cosine of the angle between the upstream magnetic field and the shock normal direction (e.g., Tylka et al., 2005; Tylka & Lee, 2006, and references therein). Quasi-perpendicular shocks, such as the forward shock in our simulated CIR, might thus be characterised by reduced levels of turbulence such that the particle drifts are not quenched.

Finally, it is worth noting that the proportionality of drifts with energy will increase their effects on high-energy particles (e.g., Marsh et al., 2013) and that the solar wind often contains compression and rarefaction regions, as well as current sheets which modify the strength and the direction of drifts. Hence, more studies are required that include the effect of more realistic non-nominal solar wind configurations in order to better understand the effects that drifts might have on the observed intensity-time profiles of SEP events. In this respect, Parker Solar Probe and Solar Orbiter observations may help to disentangle all these effects.

Chapter 8

A gradual SEP event

"To be sure of hitting the target, shoot first, and call whatever you hit the target."
– Ashleigh Brilliant

Abstract. This chapter shows the first results of PARADISE simulations that model the acceleration and transport of low-energy protons in a nominal solar wind containing a coronal mass ejection (CME). The CME is modelled by using the hydrodynamic cone model of EUHFORIA, and we assume different particle scattering conditions at the shock wave driven by the CME. It is illustrated that the shock wave can accelerate protons and act as an efficient magnetic mirror, such that particles residing downstream of the shock are efficiently trapped. In addition, the trapping of particles can be strongly enhanced by prescribing a small mean free path inside the MHD shock wave. In that case, particles are closely tied to the solar wind plasma and have only a small probability of escaping upstream of the shock. As a result, most of the particles are advected to the downstream region. Furthermore, we study the particle anisotropies, intensities, and energy spectra measured by three stationary observers located at 1 AU. Due to their different magnetic connection to the CME shock, the observers measure different SEP intensity-time profiles, which show similarities to real in-situ observed events.

8.1 Introduction

Coronal mass ejections often propagate through the solar atmosphere and the inner heliosphere at speeds significantly higher than the ambient solar wind. Consequently, a compression wave is formed at the leading edge of the CME, which steepens into a collisionless shock wave if the speed of the CME is higher than the magnetosonic speed of the solar wind (Kallenrode, 2004). In these shock waves, energetic particles can be accelerated through first-order Fermi and shock-drift acceleration (Drury & Voelk, 1981; Decker, 1988). When this happens, spacecraft that are magnetically connected to the CME shock wave will measure elevated energetic particle intensities. These enhancements can last for several days, and are known as gradual SEP events (Desai & Giacalone, 2016; Reames, 2017).

Not every CME is accompanied by a gradual SEP event, and it is not yet fully understood why this is the case. Many different factors are believed to contribute to the (in)efficiency of a CME as a particle accelerator, such as the shock geometry, the shock speed, the turbulence at the shock wave, the existence of a suprathermal seed population (e.g., originating from a solar flare), and the presence of multiple CMEs. The seed population of particles that are injected into a shock acceleration mechanism might originate from the suprathermal tail of the solar wind, or alternatively from previous large or small-scale solar activity (e.g., Tylka et al., 2005; Cane et al., 2006; Kahler et al., 2017; Lario et al., 2019). The shock speed and geometry play an important role in determining the minimum energy that a seed particle needs in order to participate in the shock acceleration process (e.g., Battarbee et al., 2013). If the particle's speed is too low, it will be advected with the solar wind downstream of the shock, before it can undergo multiple shock crossings and gain energy. Since charged particles follow magnetic field lines, the injection energy is expected to be substantially higher at quasi-perpendicular[1] shocks than at quasi-parallel shocks. This means that particles can only get accelerated at quasi-perpendicular shocks if they are already sufficiently energetic, which is referred to as the *injection problem* (e.g., Jokipii, 1987). However, it was shown by Zank et al. (2006) that the injection energy at quasi-perpendicular shocks can be reduced significantly when the turbulent magnetic field has a significant transverse complexity. In that case, cross-field diffusion makes it possible for particles to undergo multiple shock-crossings and hence gain energy.

In quasi-parallel shocks, particles can undergo multiple shock crossings if they scatter and reverse their propagation direction after crossing the shock. As discussed in Section 2.7.1, the slab component of the magnetic turbulence gives rise to particle scattering processes, which follow from resonant wave-particle interactions. Hence, the

[1] A quasi-perpendicular shock is characterised by a shock angle that is close to 90°. The shock angle is defined as the angle between the upstream magnetic field and the normal to the shock front, and it is often denoted with θ_{Bn}. When θ_{Bn} is close to 0°, we speak of a quasi-parallel shock.

efficiency of particle acceleration near a quasi-parallel shock depends on the amount of slab turbulence, which can be strongly variable near shock waves. The latter is because the energized particles can excite additional waves through the streaming instability (e.g., Lee, 1983; Kennel et al., 1986; Vainio, 2003). Moreover, due to the interaction of the CME with a non-nominal solar wind, the shock will evolve dynamically. Consequently, regions of the shock that are quasi-parallel can evolve into quasi-perpendicular configurations, and vice-versa. This provides an alternative way to overcome the injection problem at quasi-perpendicular shocks, besides cross-field diffusion.

In summary, a gradual SEP event involves numerous physical processes that happen over a wide range of energy, length, and time scales. This makes modelling an entire gradual event very complicated, such that often numerous assumptions need to be made. A common simplification is to describe the shock front analytically, by assuming a planar or a semi-elliptical shock geometry. Other assumptions include a constant shock propagation speed, a radial or uniform background magnetic field, and a background plasma with a constant flow speed. To obtain a more accurate description of the dynamical evolution of the shock wave, a global MHD model can be utilised to simulate the CME propagation in a realistic background plasma. An energetic particle transport model can then be used to study how the obtained CME shock affects the transport and acceleration of particles. Such an approach was, for example, taken by Kozarev et al. (2013) and Schwadron et al. (2015) to model particle acceleration in the low corona, using the EPREM model (Schwadron et al., 2010, 2014). However, even with an MHD model, it is far from evident to obtain a realistic description of the evolution of a CME due to the numerous uncertainties related to the internal structure of the CME and the plasma through which it propagates.

In this Chapter, we use PARADISE to solve the FTE in a nominal solar wind containing a cone CME (e.g., Odstrčil & Pizzo, 1999). The solar wind and the CME are modelled using EUHFORIA, for which the inner boundary is located at 0.1 AU. Hence, we only model the interplanetary evolution of the CME, and we study to what extent low-energy protons (~100 keV) can be (re-)accelerated during this phase of a gradual SEP event, under simplified assumptions on the particle scattering conditions.

We recall from Section 4.4.3 that the FTE equation contains the necessary physics to describe particle acceleration in converging, accelerating, and shear flows (see also le Roux et al., 2007; le Roux & Webb, 2009). At compression and shock waves, acceleration due to the converging flows plays an important role (Axford et al., 1977; Bell, 1978; Giacalone et al., 2002). Moreover, as illustrated by e.g., le Roux et al. (2007), the momentum term of the FTE contains the energy changes due to the particle drifts along the motional electric field. In addition, the FTE as derived in Chapter 2 contains the GC drifts in the spatial part, such that it is also capable of modelling shock-drift acceleration.

When using a 3D MHD model such as EUHFORIA to simulate the evolution of a CME in the inner heliosphere, the shock wave generated in front of the CME will typically be much wider than a real interplanetary shock wave, due to the limited resolution of the numerical grid. In such MHD simulations, the shock wave in thus similar to a large amplitude compression wave, which can be characterised by the length scale (e.g., Vainio & Afanasiev, 2018)

$$L_C \sim U_n/|\nabla \cdot \mathbf{U}|. \tag{8.1}$$

Here, $\mathbf{U}$ denotes the velocity of the solar wind plasma measured in a reference frame co-moving with the shock wave, and the subscript "n" refers to the vector component measured along the shock normal. The efficiency of the particle acceleration near compression waves is related to the particle diffusion length, which can be defined as (e.g., Giacalone et al., 2002)

$$L_D = \frac{\kappa_{nn}}{U_n} = \frac{v\lambda_n}{3U_n}, \tag{8.2}$$

where κ_{nn} and λ_n denote the particles' spatial diffusion coefficient and the mean free path normal to the shock front, respectively. The latter is related to the particles' parallel and perpendicular mean free paths through

$$\lambda_n = \lambda_{\parallel} \cos^2 \theta_{Bn} + \lambda_{\perp} \sin^2 \theta_{Bn}. \tag{8.3}$$

If $L_D \gg L_C$, the particles can cross the compression wave multiple times and gain energy through first-order Fermi acceleration (e.g., Giacalone et al., 2002; Jokipii et al., 2003; Jokipii & Giacalone, 2007). For the latter acceleration process to happen, the diffusive length scale upstream and downstream of the compression wave cannot be too large either (e.g., compared to the focusing length $L_F = (\nabla \cdot \mathbf{b})^{-1}$), since otherwise particles will escape into the interplanetary medium (Battarbee et al., 2011; Vainio et al., 2014). In the other limiting case, when $L_D \ll L_C$, the particles will be closely tied to the scattering centres embedded in the solar wind and hence they are advected with the plasma flow through the compression wave[2]. As a result, the particles will gain energy in an adiabatic fashion (e.g., Giacalone et al., 2005; Vainio & Afanasiev, 2018; Schwadron et al., 2020).

In this chapter, we perform simulations with different values for the parallel mean free path at the simulated CME shock wave. We show that if $L_D \gg L_C$, particles can gain energy by crossing the shock multiple times. However, the acceleration in our simulations is limited due to the absence of a foreshock region, which can trap particles efficiently near the shock wave for parallel and oblique shock geometries (e.g., Beeck & Sanderson, 1989; Heras et al., 1992; Vainio & Laitinen, 2007; Vainio

[2] As seen from a frame co-moving with the shock or compression wave.

et al., 2014; Afanasiev et al., 2015). The simulations we have performed illustrate that when L_D becomes comparable or smaller than L_C, the majority of particles is advected downstream the shock, which causes the particle intensities to peak in the trailing edge of the shock wave. Since we only consider parallel transport (i.e., $\lambda_\perp = 0$), the shock angle θ_{B_n} plays an important role in determining the diffusive length scale L_D. Consequently, the ratio L_D/L_C and hence the particle acceleration conditions can be strongly different at the eastern and western flanks of the shock wave, even for equal parallel mean free paths.

The chapter is structured as follows. Section 8.2.1 describes the solar wind and the CME model used in this chapter. Section 8.2.2 provides the details on the injected energetic particle distribution and the assumed interplanetary scattering conditions. The results of the simulations are presented in Section 8.3. The chapter is concluded in Section 8.4 with a summary and a discussion.

8.2 Modelling set-up

8.2.1 A CME in a uniform solar wind

In this work, we utilise EUHFORIA to generate a Parker-like solar wind configuration. This is done by prescribing a monopolar uniform magnetic field and a constant radial plasma speed of 500 km/s at the inner boundary of the model, located at 0.1 AU. The standard inner boundary conditions from EUHFORIA are utilised to prescribe the other MHD variables (see Pomoell & Poedts, 2018, or Section 4.4.1). The MHD simulation is performed with a radial resolution of 0.82 solar radii and an angular resolution of 1°, resulting in a grid with $1024 \times 120 \times 360$ cells. The outer boundary is placed at 4 AU, to limit its influence on the energetic particles. Since a plasma with a polytropic index of 1.5 is assumed in EUHFORIA, the solar wind slightly accelerates while streaming away from the inner boundary (Pomoell & Vainio, 2012), such that the obtained configuration is different from an exact Parker spiral.

A cone CME is injected from the inner boundary, centred on the solar equatorial plane. This CME model consists of a hydrodynamical cloud that is characterised by a spherical shape and a constant pressure, density, and radial speed (e.g., Scolini et al., 2018). The injection speed is assumed to be 2000 km/s, the angular half-width 30°, the mass density 10^{-18} kg/m^3, and the temperature 0.8×10^6 K. The latter three variables are representative for an average CME event, whereas a 2000 km/s injection speed corresponds to a fast CME (Gopalswamy et al., 2014). In our simulations, it takes the leading edge of the CME about 25 h to reach 1 AU.

The left panel of Fig. 8.1 shows a snapshot of the scaled divergence of the solar

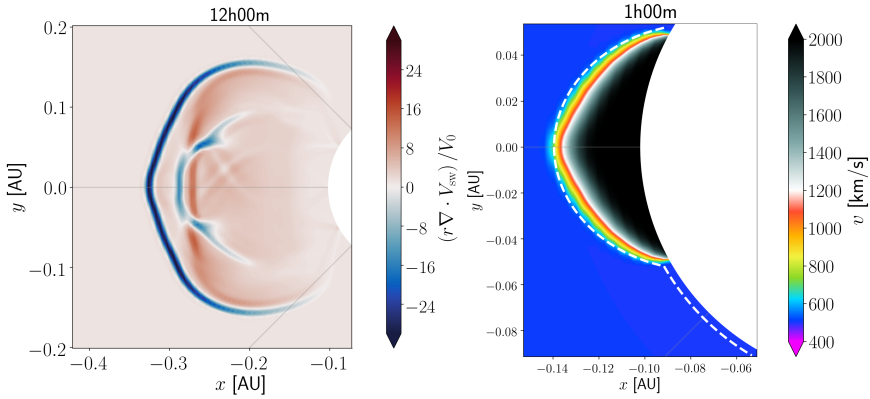

Figure 8.1: Left panel: a snapshot of the scaled divergence of the plasma velocity in the solar equatorial plane, 12 h after the CME injection. Right panel: a snapshot of the radial speed in the solar equatorial plane, 1 h after the CME injection. The dashed line indicates the particle injection region.

wind velocity $\mathbf{V}_{\rm sw}$, 12 h after the CME injection. The scaling factor is chosen to be $V_0 = 1000$ km/s, such that $r\nabla \cdot \mathbf{V}_{\rm sw}/V_0 = 1$ everywhere in a Parker solar wind with a speed of 500 km/s. The regions with a negative divergence correspond to compression regions, as they are characterised by converging flows. Due to the large difference between the CME speed and the background solar wind speed, a large amplitude compression wave with a strongly negative divergence forms in front of the CME. This compression wave corresponds to an MHD shock wave, as the CME speed is well above the fast magnetosonic speed of the ambient solar wind. Moreover, the interior of the CME shows a non-trivial structure, which is the result of the expansion of the CME into the solar wind. Contrary to the cone CME, a real CME contains an intrinsic magnetic field, e.g., with the topology of a flux-rope, which may considerably affect its evolution while propagating through interplanetary space (Verbeke et al., 2019; Scolini et al., 2019). We leave it for future work to extend the study presented in this chapter to magnetized CME models.

By using Eq. (8.1), the compression length scale of the simulated CME shock wave can be estimated. The maximal compression rate is expected to be found at the central region of the shock (i.e., the shock nose), where the shock normal is pointing in the radial direction (e.g., Rodríguez-Gasén et al., 2014). Moreover, the shock speed at the nose, V_s, can be estimated by tracking the point upstream of the shock where $\nabla \cdot \mathbf{V}_{\rm sw}$ switches sign. The plasma velocity in a frame co-moving with the shock nose becomes thus $\mathbf{U} = \mathbf{V}_{\rm sw} - V_s\mathbf{e}_r$. Upon using Eq. (8.1) at the centre of the shock wave (i.e., where $|\nabla \cdot \mathbf{U}|$ is maximal), we obtain that the compression length remains approximately constant during the simulation and equals $L_C \sim 1.5$ R$_\odot$. Moreover, it is calculated that

$L_C \sim \Delta r_s/3$, where Δr_s denotes the width of the region where $\nabla \cdot \mathbf{V}_{\mathrm{sw}} < 0$. These estimates are all obtained at the shock nose and, hence, they do not necessarily apply to the flanks. However, both $|\nabla \cdot \mathbf{U}|$ and U_n decrease towards the flanks of the shock, and as a result their ratio, L_C, will not vary significantly. This can also be deduced from the left panel of Fig. 8.1, since the width of the region where $\nabla \cdot \mathbf{V}_{\mathrm{sw}} < 0$ is of the same order of magnitude along the entire shock front.

8.2.2 100 keV proton injection

We use PARADISE to model the transport and acceleration of protons in the EUHFORIA solar wind described above. The white dashed line in the right panel of Fig. 8.1 indicates the source region from where we inject 100 keV protons into the solar wind as a delta function in both time and energy, that is,

$$j\,(r, \vartheta, \varphi, \mu, E, t = 0) = A(r, \vartheta, \varphi)\delta\,(t - 1\,\mathrm{h})\,\delta\,(E - 100\,\mathrm{keV})\,, \tag{8.4}$$

where j denotes the differential intensity, μ the cosine of the particle's pitch-angle, E the particle's energy, and (r, ϑ, φ) are spherical coordinates in a fixed frame. The function A describes a uniform particle injection from the source region shown in Fig. 8.1. This source region traces the shock front and extends to a region to the west of the CME. Particles propagating along IMF lines originating from this extended region will eventually encounter the flank of the shock, when the CME expands into the solar wind (see e.g., Fig. 8.2). The protons are injected at the half time, $t_{1/2} = 1$ h, of the cone CME model. This is the time it takes for the spherical CME to traverse halfway through the inner boundary (Scolini et al., 2018). By injecting the protons at $t_{1/2}$ and in front of the CME, we ensure that there is no artificial particle acceleration due to the sudden introduction of the cone CME at the inner boundary.

As discussed in detail in Section 3.3, PARADISE computes the directional particle intensity by solving the FTE, which contains different diffusion processes describing the effect of turbulence on the particle distributions. In this chapter, we only consider pitch-angle diffusion and no cross-field diffusion. However, the effect of the magnetic field gradient and curvature drifts are included in our simulations, such that cross-field transport is possible. For the pitch-angle diffusion, we use the SAS method of PARADISE, as described in Section 3.3.8. The magnitude of the scattering frequency is determined from Eq. (3.56), by assuming a Kolmogrov turbulence spectrum ($s = 5/3$) and by considering the following functional form for the parallel mean free path:

$$\lambda_{\parallel}(100\,\mathrm{keV}) = \begin{cases} \lambda_{\parallel}^{0} & \text{if } \nabla \cdot \mathbf{V}_{\mathrm{sw}} \geq 0 \\ \lambda_{\parallel}^{\mathrm{s}} & \text{if } \nabla \cdot \mathbf{V}_{\mathrm{sw}} < 0. \end{cases} \tag{8.5}$$

For the simulations presented in this chapter, it is always assumed that $\lambda_{\parallel}^{0} = 0.1$ AU. Moreover, we perform three simulations in which we consider different values for

the constant parameter $\lambda_{\parallel}^{s}$; i.e., $\lambda_{\parallel}^{s} = \lambda_{\parallel}^{0}$ for Case 1, $\lambda_{\parallel}^{s} = 0.01$ AU for Case 2, and $\lambda_{\parallel}^{s} = 0.001$ AU for Case 3.

The abrupt step-decrease of the mean free path for Cases 2 and 3 can introduce numerical artefacts in the calculated particle intensities[3]. This is because the integration time step (Eq. (3.48)) of a pseudo-particle residing just upstream or downstream of the $\nabla \cdot \mathbf{V}_{sw} < 0$ region is calculated from $\lambda_{\parallel}^{0}$ and not from the smaller $\lambda_{\parallel}^{s}$. If the resulting time step is too large, the pseudo-particle will be transported well inside the region where $\nabla \cdot \mathbf{V}_{sw} < 0$ within a single numerical time step. In other words, the pseudo-particle is "shot" deep into the region of small L_D, and has consequently an artificially lowered probability of escaping upstream. In our simulations, the maximal time step is therefore set to 5 s, such that a particle of 100 keV propagates a distance of at most $\Delta s_{\parallel} \sim 0.03$ R$_{\odot}$ in one time-step. The maximal displacement of a pseudo-particle into the shock wave (i.e., $\sim \Delta s_{\parallel} \cos\theta_{Bn}$) is therefore significantly smaller than L_D (see below), such that the artificial trapping of the pseudo-particles in the compression wave plays a limited role in our simulations.

A different approach to avoid numerical artefacts, without having to prescribe an overall small maximal time step, is by replacing the step-decrease in Eq. (8.5) by a smoother, more gradual decrease. This is done in the fourth case that we consider:

$$\lambda_{\parallel}(100\,\mathrm{keV}) = \begin{cases} \lambda_{\parallel}^{0} & \text{if } \nabla \cdot \mathbf{V}_{sw} \geq 0 \\ \max\left\{\lambda_{\parallel}^{s}, \lambda_{\parallel}^{0} \exp\left[\ln\left(\frac{\lambda_{\parallel}^{s}}{\lambda_{\parallel}^{0}}\right) \frac{|\nabla \cdot \mathbf{V}_{sw}|}{\alpha}\right]\right\} & \text{if } \nabla \cdot \mathbf{V}_{sw} < 0, \end{cases} \tag{8.6}$$

where we again choose $\lambda_{\parallel}^{0} = 0.1$ AU and $\lambda_{\parallel}^{s} = 0.001$ AU. The parameter α is a constant scaling factor, taken as

$$\alpha = \frac{1}{2} \max_{\forall t,\mathbf{x}} \{|\nabla \cdot \mathbf{V}_{sw}|\} = 3.5 \times 10^{-4}\,\mathrm{Hz}. \tag{8.7}$$

The maximum value of $|\nabla \cdot \mathbf{V}_{sw}|$ is obtained at the shock nose, at a distance of ~0.25 AU. Moreover, remark that Eq. (8.6) is a continuous function, both at the edges and inside the compression region. In addition, the dependence of $\lambda_{\parallel}$ on $\nabla \cdot \mathbf{V}_{sw}$ means that the parallel mean free path will be larger at the shock flanks than at the shock centre. The value of $|\nabla \cdot \mathbf{V}_{sw}|$ measured at the shock nose also decreases significantly from ~0.3 AU onward, and it has approximately halved by the time the shock reaches 1 AU, i.e., $\alpha \approx |\nabla \cdot \mathbf{V}_{sw}(1\,\mathrm{AU})|$ (at the shock nose). For case 4, the parallel mean free path inside the compression wave increases thus as the CME propagates further away from the Sun.

Since cross-field diffusion is not considered, we have that $\lambda_n = \lambda_{\parallel} \cos^2\theta_{B_n}$. Hence, to study how L_D compares to L_C for the different cases, it is useful to estimate

$$L_D/\lambda_{\parallel} = \frac{v \cos^2\theta_{B_n}}{3U_n}.$$

[3] I would like to thank R. Vainio for pointing this out.

$E_{\min} - E_{\max}$	$\langle E \rangle$
0.10 – 0.16	0.13
0.16 – 0.27	0.21
0.27 – 0.44	0.34
0.44 – 0.72	0.56
0.72 – 1.17	0.91
1.17 – 1.91	1.50
1.91 – 3.13	2.45
3.13 – 5.12	4.00
5.12 – 8.37	6.55
8.37 – 13.69	10.71

Table 8.1: Energy channels and their geometric mean $\langle E \rangle$ in MeV.

For a 100 keV proton located at the shock nose, we obtain that[4] $L_D/\lambda_\parallel \sim 1.4$, and this value is only weakly dependent on the radial coordinate in our simulations. This is because the decrease in the flow speed U_n (due to the slowdown of the shock) is partly compensated by the decrease in $\cos^2 \theta_{Bn}$ towards larger radial distances. Furthermore, we recall from Eq. (3.54) that the diffusion coefficient of the SAS method satisfies $D_{\mu\mu} \propto v^{2/3}$, such that $\lambda_\parallel \propto v^{1/3}$ and, hence, $L_D \propto v^{4/3}$. Particles of higher energy can traverse the compression wave thus more easily. For example, a 3 MeV proton will have a diffusive length scale that is one order of magnitude larger than that of a 100 keV proton.

For each simulation, 300 million pseudo-particles are injected and sampled in the phase-space volumes $2\pi r^2 \sin(\vartheta)\Delta\vartheta\Delta\varphi\Delta r\Delta E\Delta\mu$, with $\Delta r = 0.01$ AU, $\Delta\vartheta = 1°$, $\Delta\varphi = 0.5°$, $\Delta\mu = 0.1$, and $\log_{10}(\Delta E) = 0.213643$. The different energy channels considered in our simulations are listed in Table 8.1, and in the following we use the geometric mean $\langle E \rangle$ when referring to a specific channel. We remark that all energy channels are above the 100 keV injection energy of the protons, such that we only sample particles that have undergone acceleration. Moreover, the sampled pseudo-particle distribution is averaged over time-intervals of 10 minutes, to obtain better statistics.

The MHD snapshots are updated every 5 minutes, and a linear interpolation is performed to obtain the plasma variables at times between two snapshots (see Section 3.3.7 for more details). We have also performed the simulations of Case 3 with an MHD snapshot cadence of 10 minutes, and the same results were obtained.

Finally, we remark that in the remainder of this chapter, the used time coordinate is with respect to the particle injection instead of the CME injection.

[4] This value is obtained at the point where $|\nabla \cdot \mathbf{V}_{\rm sw}|$ is maximal. Just upstream of the compression wave, we obtain that $L_D/\lambda_\parallel \sim 0.8$, whereas in the trailing edge of the compression wave we obtain that $L_D/\lambda_\parallel \sim 5$.

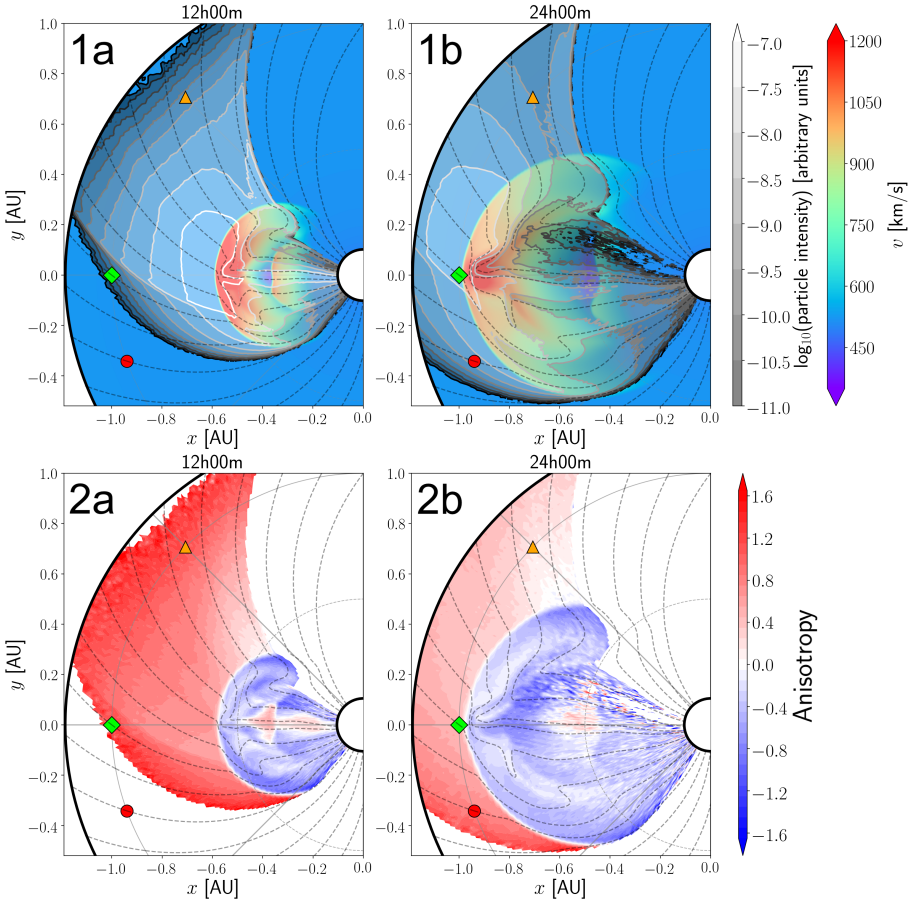

Figure 8.2: Panels 1a and 1b show in grey shades the energy-integrated omni-directional particle intensities of Case 1, plotted on top of the solar wind speed (rainbow colours) in the solar equatorial plane for the two indicated times. Panels 2a and 2b show the first-order parallel anisotropy of the energy-integrated directional intensities of Case 1. The dashed lines represent magnetic field lines projected on the equatorial plane, and the triangle, diamond, and circle denote the locations of the W45°, the CM, and the E20° observers (see text), respectively.

8.3 Results

8.3.1 Case 1 ($\lambda_{\parallel} = \lambda_{\parallel}^{s} = 0.1$ AU)

In this section, we discuss the results of the simulation performed for Case 1. By using the estimates for L_C (Section 8.2.1) and $L_D/\lambda_{\parallel}$ (Section 8.2.2), it is obtained that for

Case 1 the diffusion length scale is more than one order of magnitude larger than the compression length scale at the shock nose. As a result, particles can cross the shock wave multiple times, and thus sample each time its full compression ratio. However, since we have not included a foreshock or a turbulent sheath region behind the shock, particles cannot be efficiently trapped in the vicinity of the shock and, hence, their average number of shock crossings can expected to be limited.

Panel 1a and 1b of Fig. 8.2 show two snapshots of the omni-directional intensity integrated over energy (from 0.1 to 13.69 MeV) in the solar equatorial plane. The snapshots illustrate that both at 12 h and 24 h, the particle intensities peak at the CME shock. This is partly because the shock wave continuously accelerates the protons, such that it acts as a long-lasting source of energetic particles. When injecting the 100 keV protons with an isotropic PAD in front of the CME, about half of them propagate away from the CME towards larger radial distances. Since the unperturbed solar wind is an expanding plasma, these particles will lose energy due to adiabatic deceleration (e.g., Ruffolo, 1995). However, since the protons have a finite parallel mean free path, they will scatter and thus possibly reverse their propagation direction. Consequently, the CME will continuously encounter these particles while propagating through space, which are then accelerated to higher energies upon interacting with the shock.

Another way of illustrating that the shock acts as a source of energetic particles is by looking at the first-order parallel anisotropy, as defined in Eq. (4.8). The anisotropy is depicted in Panels 2a and 2b of Fig. 8.2, where the red and blue colours indicate anti-sunward and sunward streaming protons, respectively. These panels clearly illustrate how particles stream away from the CME driven shock. Moreover, the shock itself is characterised by an isotropic particle distribution.

In the absence of scattering, the particle's magnetic moment is conserved in the reference frame co-moving with the background plasma (e.g., le Roux et al., 2007). Consequently, the increased magnetic field strength in the compression region at the front of the CME will cause incoming particles to reverse their propagation direction. The CME shock wave acts thus as a magnetic mirror, which also contributes to the observed sign-switch in the anisotropy. Moreover, it means that particles can be efficiently trapped between the CME shock and the Sun for a prolonged amount of time. Particle scattering[5], GC drifts, and an evolving magnetic field prevent particles from being trapped permanently in the downstream region of the shock.

The three different symbols in the panels of Fig. 8.2 indicate stationary observers, all located at 1.0 AU in the solar equatorial plane. The green diamond is positioned in the centre of the CME trajectory and will be referred to as the central meridian (CM)

[5]Scattering can move the particle's velocity vector into the loss-cone of the magnetic mirror. However, under strong scattering conditions inside the compression wave (i.e., $L_D \ll L_C$), particles are advected with the plasma to the downstream region. In this case, efficient scattering leads thus also to particle trapping behind the CME shock, as is discussed in more detail Section 8.3.2

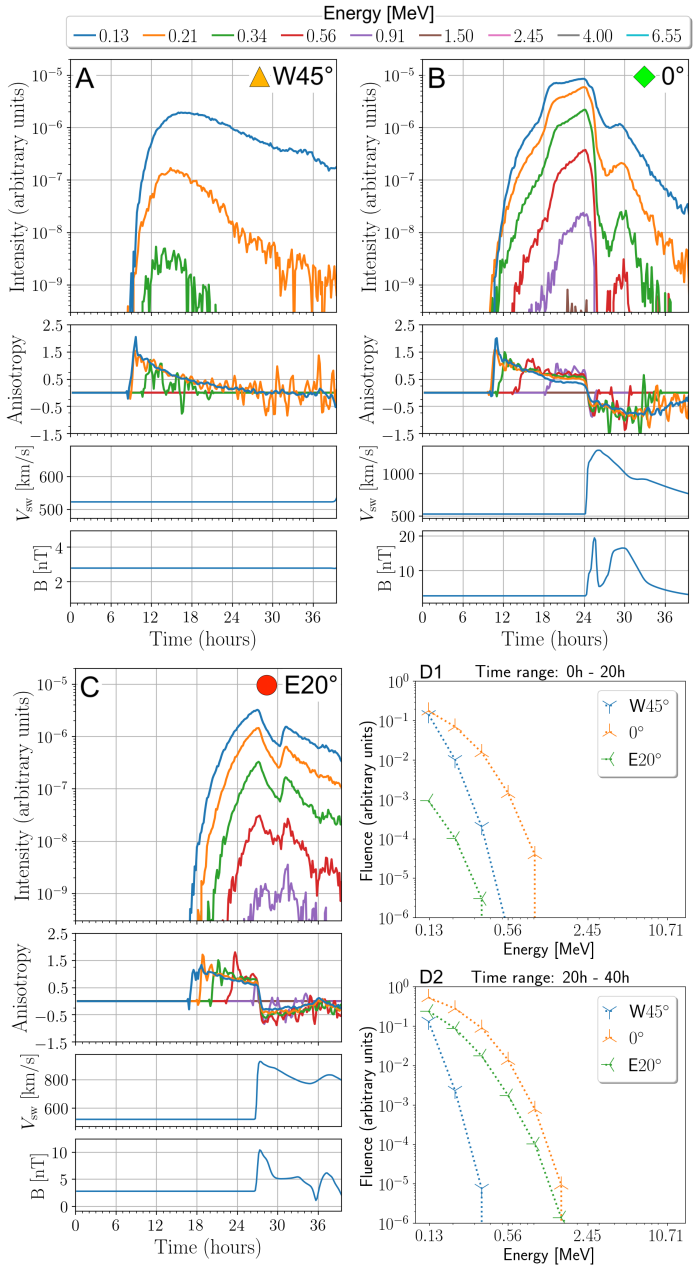

Figure 8.3: Panels A, B and C give, for Case 1, the omni-directional intensity, the anisotropy, the solar wind speed, and the magnetic field strength as measured by the W45°, the 0°, and the E20° observers, respectively. Panels D1 and D2 give the energy spectra derived from the particle fluences measured during the indicated time intervals.

observer. The red dot is located 20° east of the CM observer and will therefore be referred to as the E20° observer. The orange triangle is located 45° west of the CM observer, an will thus be referred to as the W45° observer. Panels A, B, and C of Fig. 8.3 show the omni-directional intensity and the first-order parallel anisotropy measured by these observers, as well as the solar wind speed and the magnetic field magnitude. We would like to point out that the fluctuations in the intensity and anisotropy profiles are due to limited statistics. Panels D1 and D2 of Fig. 8.3 give the energy spectra derived from the particle fluences, measured by the observers during the first and second half of the simulation, respectively.

The point at the shock front with which an observer connects magnetically is called the cobpoint (Connecting with the OBserver point; Heras et al., 1995). Due to the radial propagation of the CME in space, the cobpoint will typically move in clockwise direction along the shock front. At the start of the simulation, the cobpoint of the W45° is located at the centre of the CME shock. However, by the time that this observer starts measuring particles, the cobpoint has moved to the eastern flank of the shock. Panel A of Fig. 8.3 shows that the particle onset starts ~9 h after the proton injection. A magnetic field line originating from the eastern flank of the particle source region has a length of ~0.96 AU. Hence, a 130 keV particle would take ~8 h to arrive at the observer if it were to propagate scatter free, with $\mu = 1$, and at a constant speed. We recall that we only sample particles that have been accelerated above their 100 keV injection energy, that is, particles that have thus interacted with the CME shock. This, together with the effect of particle scattering and adiabatic deceleration explains why the particle onset in the 130 keV energy channel is only observed after ~9 h.

Within the simulated time, the CME shock does not cross the W45° observer, and as a result the observed anisotropies are mostly positive. Moreover, particles are only accelerated up to the 0.34 MeV channel, i.e., the acceleration efficiency along the eastern flank of the shock is limited. This can also be seen from the soft energy spectrum observed by the W45° observer, as illustrated in Panels D1 and D2 of Fig. 8.3.

For the CM observer, the particle onset occurs ~10 h after the particle injection. At that time, its cobpoint is located on the western flank of the shock, and moves subsequently towards the shock nose, where it arrives when the CME reaches the observer ~24 h after the particle injection. Comparing the intensity profiles of the W45° and the CM observers, it is seen that the latter detects particles of considerably higher energy. This is a result of the stronger negative divergence of the solar wind velocity near the centre of the shock, which leads to more particle acceleration. When the shock crosses the CM observer, the anisotropies switch sign, which is reminiscent to in-situ observations (Sanahuja & Domingo, 1987). Moreover, the intensities attain their peak value, which is to some extent similar to an energetic storm particle event (ESP event; see Section 1.3.1).

The CM observer measures a second intensity peak downstream of the CME shock, at

~30 h, which occurs during the passage of a compressed magnetic field region located behind the shock wave (see lower panel of Panel B). The compressed magnetic field lines bring particles closer together, increasing thus their number density.

The E20° observer also measures intensity profiles that peak with the CME shock passage. A notable difference with the other observers is that the E20° observer only connects magnetically to the shock ~17 h after the particle injection. As a result, the onset of the SEP event occurs ~8 h after the event onset measured by the other observers.

Panel D2 of Fig. 8.3 illustrates that in the second half of the simulation, the CM and the E20° observers measure a similar energy spectrum. Although this spectrum is derived from the particle fluence, it is mostly determined by the peak intensities of the different energy channels, which are obtained when the shock crosses the observers. In this regard, the CM observer measures a slightly harder spectrum than the E20° observer, because it crosses the shock at its central point, where $|\nabla \cdot \mathbf{V}_{sw}|$ is maximal.

As long as the observer is located upstream of the shock, the cobpoint moves smoothly along the shock front due to the nominal solar wind separating the observer and the CME (Heras et al., 1995). However, once downstream of the shock, the magnetic field is much more chaotic, and as a result the motion of the cobpoint along the shock front can vary abruptly. This explains the second intensity peak measured by the E20° observer after ~32 h. At that time, the corresponding cobpoint has moved rather abruptly to the centre of the CME shock, where the particle intensity is maximal (Fig. 8.2). However, it should be kept in mind that we are using a cone CME model, which does not provide a realistic description of the magnetic topology downstream of the shock wave. Hence, the calculated particle distributions inside the CME should be regarded as a test of the PARADISE model in handling complex solar wind and magnetic field configurations, rather than an attempt in reproducing the characteristics of a real gradual SEP event.

8.3.2 Case 2 ($\lambda_{\parallel}^{s} = 0.01$ AU) and Case 3 ($\lambda_{\parallel}^{s} = 0.001$ AU)

In this section, we look at the simulation results of Cases 2 and 3. By using that at the shock nose $L_C \sim 1.5\ R_\odot$ (Section 8.2.1) and $L_D/\lambda_{\parallel} \sim 1.4$ (Section 8.2.2), we obtain that L_D and L_C are of the same order of magnitude for Case 2, whereas L_D is about one order of magnitude smaller than L_C for Case 3. Particles will therefore have a limited probability of crossing the entire shock wave multiple times. This is especially true at the western flank of the shock (to which the E20° observer is connected), where λ_n decreases significantly due to the larger shock obliquity. In contrast, at the eastern flank the shock is close to parallel and λ_n is thus larger.

Figures 8.4 and 8.5 show the anisotropies, intensities, and energy spectra measured by

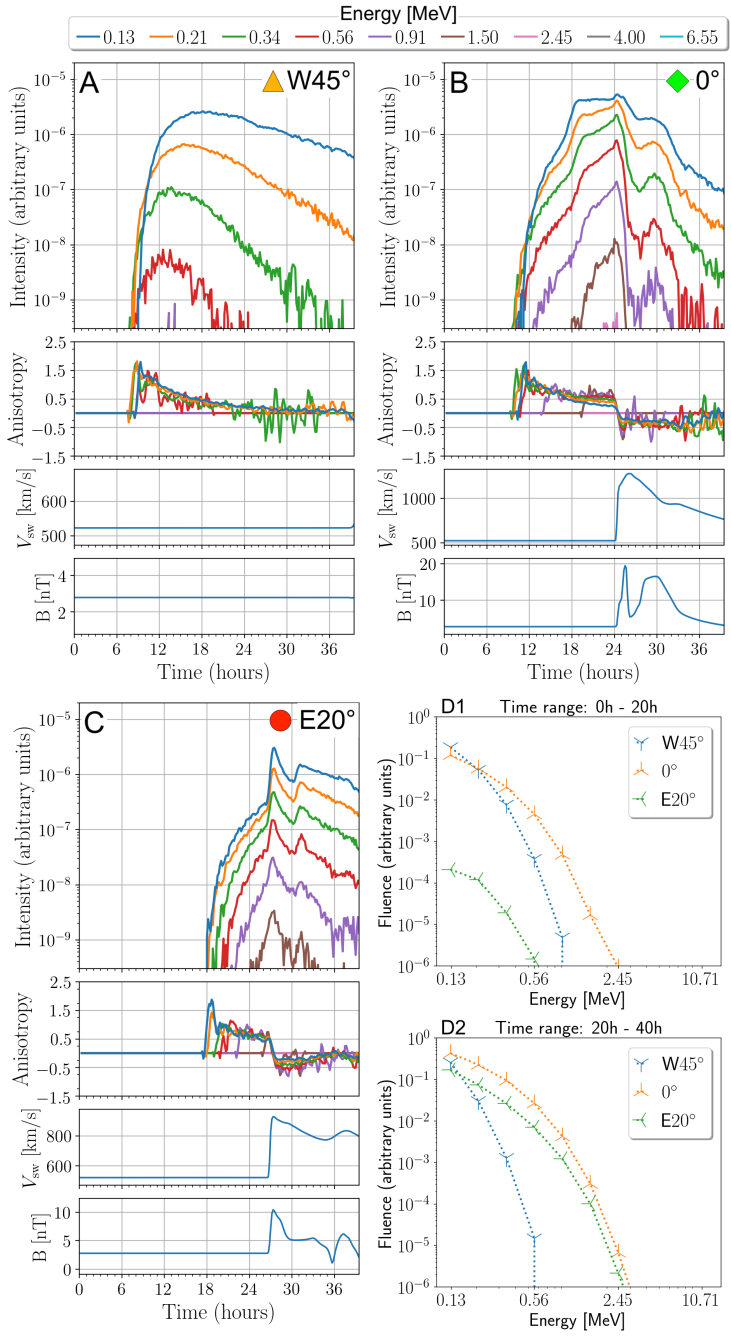

Figure 8.4: Same as Fig. 8.3, but for Case 2.

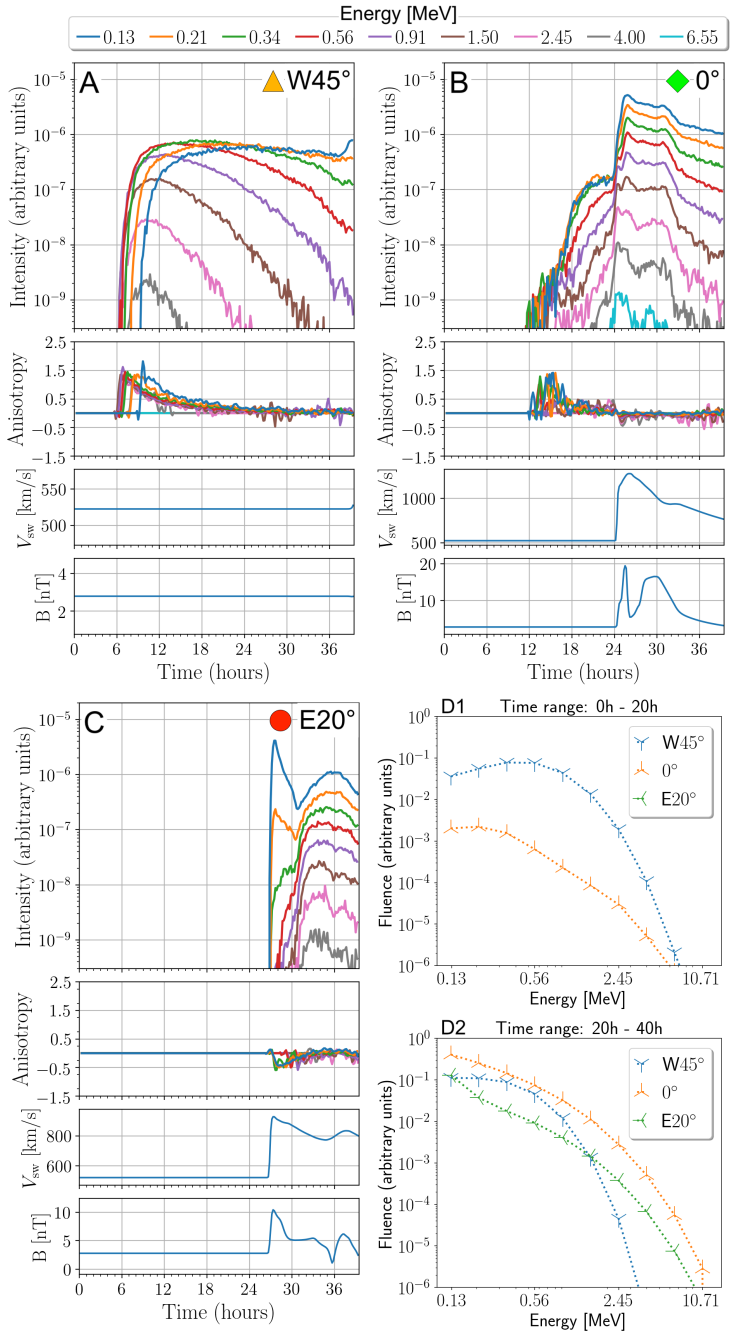

Figure 8.5: Same as Fig. 8.3, but for Case 3.

the three observers discussed previously, but now for Cases 2 and 3, respectively. For Case 2, it is seen that the W45° observer measures particles up to 0.56 MeV, whereas for Case 3 the same observer even measures particle intensities in the 4.00 MeV energy channel. These higher energies make that the particles also arrive earlier at the observer. Panel A of Fig. 8.5 shows that the onset of the SEP event for the W45° occurs after ~6 h, that is, about 3 h earlier than in Case 1[6]. Moreover, the particles that arrive first at the W45° observer are residing in the lowest 0.13 MeV energy channel for Case 1, whereas for Case 3 it are more energetic particles that reach the observer first. Consequently, the energy spectrum measured during the first half of the simulation has a positive slope for the W45° observer of Case 3, as can be seen from Panel D1 of Fig. 8.5. This indicates that the shock acceleration is sufficiently efficient, such that the more energetic particles, which have thus interacted longer with the shock, can still overtake the low energy particles that had only a limited interaction with the shock. The conclusion is thus that the particles can still efficiently escape the (quasi-parallel) eastern flank of the shock in both Cases 2 and 3, indicating that the diffusive length scale is large enough to avoid that the particles are efficiently advected to the downstream region.

For the CM observer of Case 2, the intensities obtained in the region downstream of the shock are higher than those of Case 1. This can be understood as a consequence of the smaller diffusive length scale L_D in Case 2, since particles will have a smaller probability to escape upstream of the shock wave, and hence more particles will be advected into the downstream region. Once downstream of the shock, particles are efficiently trapped both due to the small L_D across the shock and the enhanced magnetic field at the shock, which acts as a magnetic mirror (Section 8.3.1).

The effect of a small L_D on the energetic particle intensities becomes more obvious for the CM observer of Case 3 (Panel B of Fig. 8.5). Intensities increase by more than one order of magnitude in the trailing edge of the shock wave, indicating that particles are efficiently advected with the plasma flow through the $\nabla \cdot \mathbf{V} < 0$ region. This also explains why the intensities measured before the shock arrival are so low, since any particle interacting with the shock has only a small probability of escaping upstream of the shock wave.

The efficient particle advection through the compression wave is even much more pronounced at the western flank of the shock, as can be inferred from the proton intensity-time profiles measured by the E20° observer in Cases 2 and 3 (Panels C of Figs. 8.4 and 8.5, respectively). At this flank, the shock has a quasi-perpendicular geometry, and hence λ_n is very small (since cross-field diffusion is not included). For Case 3, particle intensities are even zero before the shock arrives, meaning that the probability of a particle to escape upstream is very small, and all particles are

[6] We want to point out that 6 hours is significantly larger than the time of flight of protons with energy above 0.5 MeV (propagating under scatter free conditions from the Sun to 1 AU). This delay in the onset of the particle intensities may be explained by the time the shock needs to accelerate particles to the measured energies, as well as the efficient trapping of particles near the shock due to the assumed scattering conditions.

thus advected downstream of the shock. A non-zero perpendicular mean free path would increase λ_n (Eq. (8.3)) and hence L_D near a quasi-perpendicular shock wave. Cross-field diffusion can thus facilitate that particles traverse the compression wave perpendicularly, such that they can more easily escape to the upstream region. We leave it for future work to investigate how perpendicular diffusion affects the results presented in this chapter.

Despite having $L_D/L_C < 1$ in Case 3, the acceleration occurring at the western flank and at the centre of the shock wave is not purely compressional acceleration. This is partly because the mean free path in the downstream region is equal to $\lambda_{\parallel}^0 = 0.1$ AU, and hence particles are no longer advected with the solar wind flow once leaving the shock wave. In addition, the diffusive length scale at the trailing edge of the compression wave is larger than at the centre or the upstream edge of the compression wave (footnote 4), suggesting that particles can still repeatedly diffuse into the $\nabla \cdot \mathbf{V}_{\rm sw} < 0$ region from the downstream region, where they subsequently accelerate. These particles will only propagate in the trailing edge of the $\nabla \cdot \mathbf{V}_{\rm sw} < 0$ region, before they are again advected downstream. In this case we cannot expect that particles get accelerated with the same efficiency as in a classical DSA process, since they will only sample small fractions of total compression ratio of the shock wave.

Panels D of Fig. 8.5 further illustrate how the three observers measure significantly different energy spectra because their cobpoints sample different regions of the shock at different times. The W45° observer does not measure the most energetic protons in the simulation, since its cobpoint has moved to the eastern shock flank by the time these protons are being energised around the centre of the shock. Finally, we remark that the energy spectra of the corresponding observers for Case 1 and 2 are similar, whereas the ones of Case 3 are significantly different, especially for the W45° observer. This illustrates the strong sensitivity of the shock acceleration mechanism to the assumed scattering conditions, and thus the need of a realistic description of the turbulence near the CME shock.

8.3.3 Case 4

The parallel mean free path for Case 4 is given by Eq. (8.6), with $\lambda_{\parallel}^s = 0.001$ AU. The minimum value for the mean free path inside the compression wave is thus the same as in Case 3. However, the assumed functional form of $\lambda_{\parallel}$ implies that $\lambda_{\parallel}^s$ is only attained in a fraction of the compression wave. As explained in Section 8.2.2, the parallel mean free path in the compression wave will also increase towards larger radial distances, and its value will be larger at the shock flanks than at the shock nose. Moreover, the diffusion length scale L_D will vary exponentially in the $\nabla \cdot \mathbf{V}_{\rm sw} < 0$ region, which makes the comparison between L_D and L_C not straightforward.

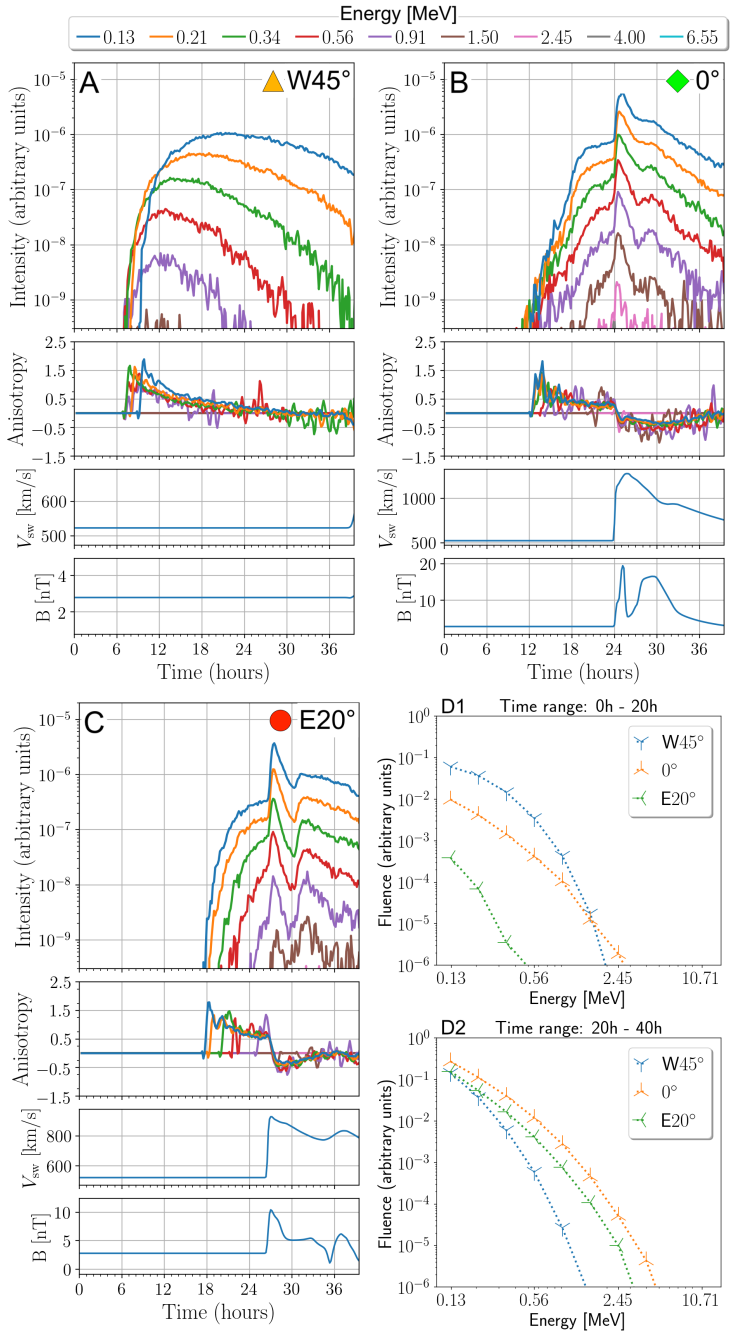

Figure 8.6: Same as Fig. 8.3, but for Case 4.

Panel A of Fig. 8.6 illustrates that the acceleration efficiency for Case 4 has decreased at the eastern flank of the CME, as compared to Case 3. This is to be expected, since the larger mean free path assumed for Case 4 implies that particles will escape the $\nabla \cdot \mathbf{V}_{\rm sw} < 0$ region more easily, and hence undergo less acceleration than in Case 3. The attained energies are however still higher than in Cases 1 and 2. Panel B of Fig. 8.6 shows that the CM observer measures a sudden enhancement of the particle intensities at the shock arrival, with the intensity peaks attained at the downstream edge of the $\nabla \cdot \mathbf{V}_{sw} < 0$ region. Although this intensity enhancement is smaller than in Case 3, it still implies that particles are efficiently advected through the compression wave, with only a low probability of escaping upstream of the shock. This is expected, since the region around the shock nose is characterised by larger values of $|\nabla \cdot \mathbf{V}_{\rm sw}|$, such that $\lambda_{\parallel} = \lambda_{\parallel}^{s}$ in a more substantial part of the $\nabla \cdot \mathbf{V}_{\rm sw} < 0$ region. Finally, Panel C of Fig. 8.6 illustrates that the E20° observer measures an intensity profile very similar to Case 2. The smaller values of $|\nabla \cdot \mathbf{V}_{\rm sw}|$ at the western flank of the shock produce a larger $\lambda_{\parallel}$ (and thus a larger L_D), and hence particles are less efficiently trapped as compared to Case 3.

8.4 Summary and discussion

In this chapter, we have discussed the results of different PARADISE simulations that modelled the (re-)acceleration and transport of low-energy protons in a nominal solar wind containing a CME. The solar wind was generated with EUHFORIA and a cone model was assumed for the CME. The protons were injected as a delta function in time from an extended uniform source region tracing the CME shock. Upon injection, all protons were given an initial energy of 100 keV.

In our simulations, the CME shock wave was shown to act as a source of energetic particles, due to continuous particle acceleration. This is expected, since the FTE contains the necessary physics to describe processes like first-order Fermi acceleration and shock-drift acceleration (e.g., le Roux & Webb, 2009). In addition, the strong magnetic field characterising the shock front reflects protons as a result of the (approximate) conservation of their first adiabatic invariant. Consequently, particles can be very efficiently trapped between the Sun and the shock wave.

We have discussed the anisotropy and omni-directional intensity profiles for three stationary observers located at 1 AU in the solar equatorial plane. Four different cases were studied, in which the parallel mean free path at the CME shock was varied. For Case 1, it was assumed that $\lambda_{\parallel}(100\,\text{keV}) = 0.1$ AU everywhere, and protons were observed to accelerate up to ~1.50 MeV at the centre of the shock wave. For Case 2 and 3, a smaller mean free paths at the shock wave lead to the acceleration of particles up to 2.45 MeV and 10.71 MeV, respectively. For Case 2, the diffusion length L_D at

the shock nose is of the same order of magnitude as the compression scale L_C of the simulated shock, whereas for Case 3 it is an order of magnitude smaller than L_C. This implies that particles will have a hard time to scatter across the compression wave multiple times, thus preventing a classical DSA process. However, since L_D is also not significantly smaller than L_C (especially at the downstream edge of the shock), and since a constant mean free path of 0.1 AU is assumed outside the compression wave, the limit of purely compressional acceleration is also not applicable. Most particles will not be capable of crossing the entire compression wave multiple times, but they can still repeatedly diffuse through parts of the $\nabla \cdot \mathbf{V}_{\rm sw} < 0$ region and hence gain energy. These particles will sample only fractions of the total compression ratio of the shock wave, and their acceleration is therefore expected to be less efficient than the DSA limit (but, as illustrated, the energy gains can still be significant).

For Case 3, the shock angle θ_{B_n} has a clear effect on the particle intensities along the shock front. At the eastern flank, where the shock is quasi-parallel, particles could gain energy efficiently and escape the upstream part of the shock. In contrast, at the western flank the shock has a quasi-perpendicular geometry, and hence λ_n is much smaller. As a consequence, for Case 3, we have at the western flank $L_D \ll L_C$, implying that particles are efficiently tied to the scattering centres advecting with the solar wind plasma. Particles have thus a small probability to escape upstream of the western shock flank, which was clearly reflected by the absence and by the small pre-shock particle intensities measured by the E20° and the CM observers, respectively. This effect was slightly mediated for Case 4, where the parallel mean free path was assumed to have an exponential dependence on $\nabla \cdot \mathbf{V}_{\rm sw}$. For this case, the smaller value of $|\nabla \cdot \mathbf{V}_{\rm sw}|$ at the western flank of the shock produces a larger λ_n as compared to Case 3, implying that particles have a larger chance of escaping upstream of the shock.

Given the strong dependence of both L_D and L_C on the properties of the shock wave, it is necessary to implement a method into PARADISE to determine the shock normal and the plasma parameters characterising the shock wave (Rodríguez-Gasén et al., 2011; Pomoell et al., 2015, and references therein), in order to prescribe more realistic scattering conditions. We plan to develop such a tool in the near future.

Due to their different angular (longitudinal) location with respect to the main direction of the propagation of the shock, the three observers, located at 1 AU have different cobpoints and hence they measure different omni-directional intensity profiles and energy spectra. Such variability of the shape of the intensity-time profiles of SEP events with the heliolongitude of the solar parent events was shown by in-situ observations of real SEP events (Cane et al., 1988). The variation of the intensity-time profiles due to the motion of the cobpoint along the shock front was firstly modelled by Heras et al. (1995) and Lario et al. (1998). These authors used a 1D particle transport model and a 2.5D MHD model (Wu et al., 1983) to obtain the intensity-time profiles of gradual SEP events in the upstream (pre-shock) region. The mobile particle source function was obtained by fitting observed SEP events (e.g., Aran et al., 2007), and hence particle

acceleration mechanisms were not modelled.

In order to make the simulation results fully comparable with real observed gradual SEP events, more realistic scattering conditions need to be assumed near the shock wave. In Cases 2, 3, and 4, the parallel mean free path was assumed to be small inside the compression wave, while in reality the mean free path is expected to be small in the foreshock region, located in front of a parallel or oblique shock wave (e.g., Beeck & Sanderson, 1989; Afanasiev et al., 2015), and in the turbulent sheath region, located downstream of the shock. To obtain DSA in our simulations, it is necessary to assume scattering conditions inside the $\nabla \cdot \mathbf{V}_{\mathrm{sw}} < 0$ region that satisfy $L_D \gg L_C$, such that the energetic particles propagate across the entire shock wave and thus sample the full compression ratio. Increasing the resolution of our MHD simulation, by using for example adaptive mesh refinement near the shock wave, is a straightforward manner to attain the $L_D \gg L_C$ scaling, without having to increase the mean free path significantly inside the shock wave.

The simulations presented in this chapter can be further extended in many different ways. For example, a particle transport effect that we did not include is cross-field diffusion, which could play an important role near highly oblique shocks (Zank et al., 2006). A large perpendicular mean free path at the western flank of the CME could significantly increase the diffusive length scale and hence prevent the efficient particle trapping observed in Case 3. Furthermore, an important extension of this study will be to consider more realistic particle injection profiles. For example, to model the shock acceleration of particles originating from the suprathermal tail of the solar wind population, a continuous injection of these low-energy particles into the shock wave has to be considered. In contrast, the high-energy particles are believed to be accelerated already in the lower corona (e.g., Roussev et al., 2004; Reames, 2009a,b). This implies that there already exists an energetic particle population covering a wide range of energies by the time that the CME reaches 0.1 AU, i.e., the inner boundary of EUHFORIA. This can, to some extent, be modelled by injecting a proton distribution with a power-law distribution in energy. However, to accurately model the onset of the gradual SEP event, the propagation of the CME and the energetic particles needs to be modelled from the low corona onward.

Finally, in a future study, we will use CME models with an intrinsic magnetic field and investigate how this modifies the results obtained in this chapter. A more realistic CME model will allow us to model e.g., the SEP reservoir effect (McKibben, 1972; Reames et al., 1996), and hence extend the study presented in Chapter 7 (see also Wijsen et al., 2020). In conclusion, the applicability of PARADISE to model energetic particle transport in dynamic solar wind configurations opens the possibility for numerous different studies that can help increase our understanding about gradual SEP events.

Chapter 9

Conclusion

"Still round the corner there may wait
A new road or a secret gate"
– J.R. R. Tolkien (The Lord of the Rings)

9.1 Summary

In this thesis, we have presented a study of the transport and acceleration of energetic particles in the inner heliosphere. This was done using the FTE, which describes the evolution of energetic particle distributions in space. As discussed in chapters 1 and 2, the FTE is valid under the assumption that the energetic particle distribution is gyrotropic, and that the particles propagate as test particles through a denser background plasma. The latter assumption can be relaxed by coupling the FTE to the equation describing the background plasma and its embedded turbulence.

In Chapter 2, a formal derivation of the FTE was presented, starting from the Vlasov equation under the assumption of a flat spacetime. It was discussed that for a non-relativistic background plasma, such as the solar wind, one can safely neglect the terms in the FTE that are of first or higher order in U/c, where U is the background plasma speed and c is the speed of light. This assumption does not put any restrictions on the speed of the energetic particles, i.e., the obtained FTE is also valid for near-relativistic particles. Therefore, when calculating the particle speed or kinetic energy, formulae of special relativity need to be used, since the Lorentz factor γ associated with the particles' speed can be significantly larger than one.

Our derivation of the FTE also illustrated that expressing the equation in GC coordinates is necessary in order to retain the effects of the GC drifts. This coordinate transformation needs to be performed before averaging the transport equation over the gyrophase. In that case, the spatial part of the FTE will contain a term that contains the polarization drift, the drifts due to a time-varying magnetic field, and the drifts due to the curvature and gradient of the background magnetic field. In addition, by including turbulent fluctuation in the background plasma, we showed that these GC drift terms lead to a pitch-angle dependent diffusion process perpendicular to the background magnetic field. We illustrated that under the assumptions of QLT, we recover the FLRW limit, which was derived by Jokipii (1966) in a different manner. These results suggest that non-vanishing GC drifts in a turbulent plasma may play an important role in the generation of cross-field diffusion in space.

In Chapter 3, we introduced a new numerical tool named PARADISE, which solves the FTE using a stochastic approach. The novelty of the model lies in its ability to solve the fully time-dependent and 5D FTE in a background solar wind that is generated by a time-dependent 3D MHD model. In this work, we used the EUHFORIA model to generate MHD solar wind configurations. PARADISE solves the FTE by integrating an equivalent set of Itô stochastic differential equations forward in time. Moreover, various pitch-angle and cross-field diffusion theories are available for use in PARADISE, which is made possible by a modular implementation structure.

In Chapter 4 we used PARADISE to solve the FTE in Parker solar winds of different speed and in a EUHFORIA solar wind containing a CIR. An impulsive injection of 4 MeV protons from the inner boundary of the model was hereby assumed, and simulations both without and with cross-field diffusion were considered. From the simulations with the Parker solar wind configurations, we found that the adiabatic deceleration of the energetic protons is significant, especially in fast solar wind. The PARADISE simulations with the EUHFORIA solar wind demonstrated that a CIR has several significant effects on the properties of the energetic particle distribution in interplanetary space. The compression and shock waves bounding the CIR were observed to accelerate protons above their initial injection energy. Moreover, the CIR structure acted as an efficient barrier, trapping protons for a prolonged time in the inner heliosphere. Finally, in our simulations we observed that a weak cross-field transport process happening inside the CIR can lead to a significant spreading of the protons at smaller radial distances outside the CIR. All of these results indicate that the background solar wind has a considerable influence on the properties of SEPs, illustrating thus the importance of having a realistic model for the solar wind.

In Chapter 5, the effect of a CIR on SEPs was further investigated by injecting 4 MeV protons from four different regions located at 0.1 AU. These regions were centred at different longitudes, and therefore magnetically connected to different regions of the solar wind. Consequently, the SEP intensities and anisotropies measured along IMF lines originating from these four injection regions were significantly different. It was

also illustrated that in our simulations, the reverse shock of the CIR is a much more efficient particle accelerator than its forward shock wave. In addition, the azimuthal intensity profile near the CIR were shown to be highly asymmetric, with a sharp intensity drop occurring at the SI inside the CIR. As discussed in the summary of Chapter 5, these findings agree with in-situ observations of energetic particles near CIRs. Furthermore, we found that depending on the underlying IMF topology, the azimuthal width of the particle distribution function can increase, decrease, or remain constant with heliocentric radial distance. We showed that these results remain true when the protons are subjected to a cross-field diffusion process. Finally, we illustrated that the non-nominal IMF topology perturbs the SEP distribution significantly (both in longitude and latitude), such that the shape of the original injection region is no longer discernible from the in-situ observations, unless the IMF structure between the observer and the Sun is known accurately. The results obtained in Chapter 5 illustrate that a model such as PARADISE can help understand the complexity of SEP events that are observed by multiple spacecraft simultaneously.

In Chapter 6, we extended the studies presented in Chapter 4 and 5 by considering different values for the perpendicular mean free paths of the energetic protons. We showed that in the rarefaction region trailing the CIR, cross-field diffusion is capable of dispersing the energetic protons efficiently, which leads to overall low values for the SEP intensities. This means that SEPs propagating in a rarefaction region may easily go undetected if their intensity drops below the pre-event intensity levels. Furthermore, we studied how the particles that are accelerated at the reverse and forward shock waves are strongly affected by the different levels of cross-field diffusion. It was shown that for a sufficiently strong cross-field diffusion process, the accelerated particle populations centred on the forward and reverse shock merge together into one single enveloping particle population.

Chapter 7 focused on the effect of the magnetic field gradient and curvature GC drifts on the decay phase of SEP events. We hereby investigated to what extent these particle drifts may affect the SEP reservoir or flood phenomenon. Using PARADISE, a proton population with a power law energy distribution ranging from 3 to 36 MeV was injected at 0.1 AU into a Parker solar wind configuration. We showed that a sudden drop is observed in the intensity profiles measured by observers that are magnetically connected to a point that is inside, yet in the proximity of the edges of the particle injection site. These intensity drops are the result of the GC drifts, and the energy dependence of the drifts makes that the drops occur at different times for different energy channels. Consequently, particle drifts prevent the SEP flood phenomenon from establishing. Furthermore, during the decaying phase of the SEP events, drifts are shown to strongly influence the energy spectra derived from the proton fluence. This is especially true for observers that are magnetically connected to the edges of the SEP injection region. Moreover, we have illustrated that the effect of the drifts is strongly enhanced in the MHD solar wind containing a CIR. This is due to the presence of strong magnetic field

gradients at the compression and shock waves bounding the CIR. Hence, for the SEP flood phenomenon to occur, the GC drifts need to be mitigated. We have illustrated that a sufficiently strong cross-field diffusion process might accomplish this.

In Chapter 8, we have demonstrated the capabilities of PARADISE in modelling energetic particles propagating through a dynamic solar wind containing a CME. This was done by injecting 100 keV protons in front of a cone CME, which propagated through a nominal solar wind generated by EUHFORIA. Our simulations illustrated that the CME driven shock continuously accelerates particles while propagating through interplanetary space. The shock wave also acts as an efficient magnetic mirror, such that particles can be trapped between the Sun and the CME shock for a prolonged amount of time. Moreover, we have illustrated that the efficiency of the shock wave in accelerating protons in our simulations strongly depends on the assumed scattering conditions near the shock. Finally, it was shown that different observers will measure vastly different intensity profiles, due to their different magnetic connection to the shock wave. This is similar to what is observed during real gradual SEP events. In conclusion, the results of this chapter have illustrated that PARADISE is a promising tool to study some of the complex physics involved during gradual SEP events.

9.2 Outlook

We conclude this work by highlighting some possible future applications of PARADISE, which can help to shed light on some of the prevailing open questions regarding energetic particles in our solar system. Possible studies include:

- A study of the acceleration of a suprathermal seed particle population at a compression or shock wave driven by either a high speed solar wind stream or a CME.
- A statistical study of a large number of multi-spacecraft SEP events, to disentangle the effects of cross-field diffusion, a non-nominal IMF topology, and an extended source region on the spreading of particles through the inner heliosphere.
- The previous study can be aided by also modelling Jovian electrons, since the magnetosphere of Jupiter can be regarded as a steady point source.
- The application of PARADISE in combination with different CME models, to study how the intrinsic magnetic field of a CME affects the properties of SEP events.

- A statistical study of a large number of gradual SEP events, to investigate which scattering conditions need to be assumed near a CME shock to obtain a reasonable match between the observed and the modelled particle intensities.
- The application of PARADISE and EUHFORIA to study the particle transport and acceleration in a solar wind containing multiple CMEs, or the combination of an impulsive and a gradual event. Such a study may shed light on the particle seed population that is accelerated during a gradual SEP event.
- The application of PARADISE together with a global MHD model of the solar corona, to study the early stages of an SEP event.

Furthermore, there remains a lot room for improving the PARADISE model. For example:

- Further optimization of the model, including particle splitting algorithms and artificial convective terms to more efficiently sample the phase-space regions of interest.
- Develop and include an efficient backward integration module into PARADISE, which can be coupled to a mobile semi-empirical injection source at a CME shock. Such a module can be useful for SEP forecasting applications.
- Combine PARADISE with a numerical tool that calculates how the modelled SEP radiation interacts with the shielding material of spacecraft, with living tissue, and with Earth's atmosphere, hereby including the production of secondary energetic particles produced out of collision with the primary SEPs.
- Include the feedback of the energetic particles on the Alfvén wave turbulence near shock waves.
- Include the feedback of the energetic particles on the large scale structure of the background plasma, for example by solving the MHD equations and the FTE together as a multi-fluid system.

In the years to come, our knowledge regarding SEP propagation and acceleration in the inner heliosphere is expected to increase significantly, due to the availability of the revolutionary data provided by the near-Sun spacecraft Parker Solar Probe and Solar Orbiter. Together with data obtained by near-Earth spacecraft, we will have high-quality SEP measurements from various vantage points in the inner heliosphere. Such multi-spacecraft observations will provide important constraints on the currently free parameters of particle transport models, such as the magnitude and the spatial dependence of the parallel and perpendicular mean free paths. In this work, it was illustrated that the large-scale solar wind structure strongly affects the transport of SEPs.

Therefore, to correctly interpret the data obtained from spacecraft and hence constrain turbulence related parameters such as the particle mean free paths, it is necessary to have a particle transport model that takes into account both the small-scale and the large-scale structures present in the solar wind. We believe that PARADISE is a first good step in the development of such a scale-bridging model. Moreover, the modular implementation of PARADISE makes it easy to further develop and improve the model's capabilities.

Appendix A

Gyro-averaging the particle's transport equation

"Just keep swimming."
– Dory (Finding Nemo)

In this appendix, the FTE as formulated in Eq. (2.82) is derived by averaging Eq. (2.81) over the gyrophase. To do so, the following instantaneous averaging operator[1] is defined for an arbitrary function g as:

$$\langle g(\mathbf{X}, p, \mu, \phi)\rangle_\phi = \frac{\int_0^{2\pi} g(\mathbf{X}, p, \mu, \phi)\mathcal{F}(\mathbf{X}, p, \mu, \phi)d\phi}{\int_0^{2\pi} \mathcal{F}(\mathbf{X}, p, \mu, \phi)d\phi} = \frac{1}{2\pi}\int_0^{2\pi} g(\mathbf{X}, p, \mu, \phi)d\phi, \quad \text{(A.1)}$$

where the last equality follows from the assumption that the particle distribution $\mathcal{F}$ is gyrotropic, i.e., $\mathcal{F}(\mathbf{X}, p, \mu, \phi) = (2\pi)^{-1}\mathcal{F}(\mathbf{X}, p, \mu)$. In other words, operator (A.1) is an average taken over a population of particles that have the same coordinates $(\mathbf{X}, p, \mu)$ and are uniformly distributed in ϕ, i.e., $\phi \sim \mathcal{U}[0, 2\pi)$, with $\mathcal{U}$ a uniform distribution. Note that Eq. (A.1) is an instantaneous average, and it can therefore not be regarded as an average over a single gyration trajectory of one particle. Instead, the population of particles over which we average are all located on a closed curve, which is approximately[2] a circle with the GC as origin and the Larmor radius as radius. The

[1] This averaging operator should not be confused with the ensemble average $\langle\cdot\rangle$ introduced in Section 2.6.

[2] If the magnetic field is not uniform, the Larmor radius is not constant. Hence, although the particles all have the same GC, they may be located at a different distance from the GC, which still equals the Larmor radius at their position.

particles are thus located at *different positions* in space, but they all have the *same GC* and their gyrophase is thus defined according to the same reference triad which has its polar-axis aligned with the magnetic field at the GC location. In contrast, when instead using the particles' exact locations $\mathbf{x}$ as the spatial coordinate in the FTE (i.e., by not considering a transformation to GC coordinates), operator (A.1) should be regarded as the instantaneous average over a distribution of particles particles which have the same μ and p, a uniform distribution in ϕ, and all located at the *same position* $\mathbf{x}$. This means that the particles all have *different GCs*, which are located on a circle with $\mathbf{x}$ as origin and the Larmor radius as radius. Moreover, in this case the ϕ coordinate is defined in a reference triad which has its polar-axis aligned with the magnetic field at the particles' location $\mathbf{x}$, and not at the GC. In summary, the meaning of the averaging operator A.1 is thus different depending on which spatial coordinate system is used (see also footnote 8 of Chapter 2). A related discussion can be found in Burger et al. (1985).

In the calculations presented below, we will repeatedly need the terms $\left\langle \mathbf{e}_p \right\rangle_\phi$ and $\left\langle \mathbf{e}_p \mathbf{e}_p \right\rangle_\phi$, where $\mathbf{e}_p = \mathbf{p}/p$ and $\mathbf{e}_p \mathbf{e}_p$ denotes a dyadic product. For clarity and convenience of reference, we start by calculating these two quantities. By expressing $\mathbf{e}_p$ in the Cartesian frame co-moving with the solar wind, it is found that

$$\begin{aligned} \left\langle \mathbf{e}_p \right\rangle_\phi &= \frac{1}{2\pi} \int_0^{2\pi} \left(\sin\theta\cos\phi \mathbf{e}_x + \sin\theta\sin\phi \mathbf{e}_y + \cos\theta \mathbf{b}_g \right) d\phi \\ &= \cos\theta \mathbf{b}_g \\ &= \mu \mathbf{b}_g, \end{aligned} \tag{A.2}$$

where it is used that $\langle \sin\phi \rangle_\phi = \langle \cos\phi \rangle_\phi = 0$. For $\left\langle \mathbf{e}_p \mathbf{e}_p \right\rangle_\phi$ we find that

$$\begin{aligned} \left\langle \mathbf{e}_p \mathbf{e}_p \right\rangle_\phi &= \frac{1}{2\pi} \int_0^{2\pi} \left(\sin\theta\cos\phi \mathbf{e}_x + \sin\theta\sin\phi \mathbf{e}_y + \cos\theta \mathbf{b}_g \right) \\ &\quad \times \left(\sin\theta\cos\phi \mathbf{e}_x + \sin\theta\sin\phi \mathbf{e}_y + \cos\theta \mathbf{b}_g \right) d\phi \\ &= \frac{1}{2\pi} \int_0^{2\pi} \left(\sin^2\theta\cos^2\phi \mathbf{e}_x \mathbf{e}_x + \sin^2\theta\sin^2\phi \mathbf{e}_y \mathbf{e}_\mathbf{y} + \cos^2\theta \mathbf{b}_g \mathbf{b}_g \right) d\phi \\ &= \frac{\sin^2\theta}{2} \mathbf{e}_x \mathbf{e}_x + \frac{\sin^2\theta}{2} \mathbf{e}_y \mathbf{e}_\mathbf{y} + \cos^2\theta \mathbf{b}_g \mathbf{b}_g, \end{aligned} \tag{A.3}$$

where the second and the last equality are obtained by using $\langle \sin\phi \rangle_\phi = \langle \cos\phi \rangle_\phi = 0$ and $\left\langle \sin^2\phi \right\rangle_\phi = \left\langle \cos^2\phi \right\rangle_\phi = 1/2$, respectively. Since $\{\mathbf{e}_x, \mathbf{e}_y, \mathbf{b}_g\}$ is an orthogonal basis, it holds that $\mathbf{e}_x \mathbf{e}_x + \mathbf{e}_y \mathbf{e}_y + \mathbf{b}_g \mathbf{b}_g = \mathbb{I}$, with $\mathbb{I}$ the identity tensor. Equation (A.3) can thus

be written as

$$\left\langle \mathbf{e}_p \mathbf{e}_p \right\rangle_\phi = \frac{1-\mu^2}{2}\left(\mathbb{I} - \mathbf{b}_g \mathbf{b}_g\right) + \mu^2 \mathbf{b}_g \mathbf{b}_g, \tag{A.4}$$

Before averaging the transport equation over the gyro-angle, we note that the mixed distribution function $\mathcal{F}$ was defined in Section 2.2.2 as

$$\mathcal{F}(\mathbf{X}, p, \mu, \phi, t) = \left(1 + \mathbf{U}_g \cdot \boldsymbol{v}/c^2\right) f(\mathbf{X}, p', \mu', \phi', t),$$

where we denoted the momentum coordinates in the inertial frame with a prime. For a gyro-tropic configuration, this becomes

$$\mathcal{F}(\mathbf{X}, p, \mu, t) = \left(1 + \mu v \mathbf{U}_g \cdot \mathbf{b}_g/c^2\right) f(\mathbf{X}, p', \mu', t), \tag{A.5}$$

where we used Eq. (A.2). To first order in U/c, we have thus that (see Section 2.2.2)

$$\mathscr{F}(\mathbf{X}, p, \mu, t) = \frac{\mathcal{F}(\mathbf{X}, p, \mu, t)}{1 + \mu v \mathbf{U}_g \cdot \mathbf{b}_g/c^2} \approx \left(1 - \mu v \mathbf{U}_g \cdot \mathbf{b}_g/c^2\right) \mathcal{F}(\mathbf{X}, p, \mu, t), \tag{A.6}$$

where the last equality holds to first order in U/c.

Applying the averaging operator (A.1) to Eq. (2.81) gives

$$\begin{aligned}
&\gamma\left(1 + v\frac{\mathbf{U}_g \cdot \left\langle \mathbf{e}_p \right\rangle_\phi}{c^2}\right)\frac{\partial \mathscr{F}}{\partial t} + \left[\left\langle (\boldsymbol{v}\cdot\mathbf{b})\,\mathbf{b}\right\rangle_\phi + \mathbf{U}_g + \left\langle \mathbf{V}_d \right\rangle_\phi\right] \cdot \frac{\partial \mathscr{F}}{\partial \mathbf{X}} \\
&+ \gamma\left[\left(\left\langle \mathbf{e}_p \right\rangle_\phi + v\frac{\mathbf{U}_g \cdot \left\langle \mathbf{e}_p \mathbf{e}_p \right\rangle_\phi}{c^2}\right) \cdot \frac{\partial \mathbf{b}_g}{\partial t} + \left(\left\langle \mathbf{e}_p \right\rangle_\phi \mathbf{U}_g + v\left\langle \mathbf{e}_p \mathbf{e}_p \right\rangle_\phi\right) : \nabla \mathbf{b}_g \right. \\
&\left. - \frac{1}{v}\left(\mathbf{b}_g - \mu\left\langle \mathbf{e}_p \right\rangle_\phi\right) \cdot \frac{d\mathbf{U}_g}{dt} - \left(\mathbf{b}_g \left\langle \mathbf{e}_p \right\rangle_\phi - \mu\left\langle \mathbf{e}_p \mathbf{e}_p \right\rangle_\phi\right) : \nabla \mathbf{U}_g \right] \frac{\partial \mathscr{F}}{\partial \mu} \\
&- \gamma^2 m\left(\left\langle \mathbf{e}_p \right\rangle_\phi \cdot \frac{d\mathbf{U}_g}{dt} + v\left\langle \mathbf{e}_p \mathbf{e}_p \right\rangle_\phi : \nabla \mathbf{U}_g\right)\frac{\partial \mathscr{F}}{\partial p} \\
&= \left(\frac{\delta \mathscr{F}}{\delta t}\right)_{\text{turb}},
\end{aligned} \tag{A.7}$$

where it is used that $\boldsymbol{v} = v\mathbf{e}_p$ and where $\left\langle \mathbf{e}_p \right\rangle_\phi \mathbf{U}_g$ and $\mathbf{b}_g \left\langle \mathbf{e}_p \right\rangle_\phi$ are dyadic products. The double dot symbol ":" denotes a tensor contraction, defined as $\mathbf{ab} : \mathbf{cd} = a_i b_j c_j d_i$, where the Einstein summation convention is utilised.

For clarity, we calculate the terms in Eq. (A.7) that contain dyadic products separately, starting with

$$\mathbf{U}_g \cdot \left\langle \mathbf{e}_p \mathbf{e}_p \right\rangle_\phi \cdot \frac{\partial \mathbf{b}_g}{\partial t} = \mathbf{U}_g \cdot \left(\frac{1-\mu^2}{2} \left(\mathbb{I} - \mathbf{b}_g \mathbf{b}_g \right) + \mu^2 \mathbf{b}_g \mathbf{b}_g \right) \cdot \frac{\partial \mathbf{b}_g}{\partial t}$$

$$= \frac{1-\mu^2}{2} \left(\mathbf{U}_g \cdot \frac{\partial \mathbf{b}_g}{\partial t} \right). \tag{A.8}$$

Here, Eq. (A.4) was used to obtain the first equality and $\mathbf{b}_g \cdot \partial \mathbf{b}_g / \partial t = (1/2)\partial(\mathbf{b}_g \cdot \mathbf{b}_g)/\partial t = 0$ to obtain the second equality. Next, we calculate

$$\left\langle \mathbf{e}_p \right\rangle_\phi \mathbf{U}_g : \nabla \mathbf{b}_g = \mu \mathbf{b}_g \mathbf{U}_g : \nabla \mathbf{b}_g = 0, \tag{A.9}$$

where (A.2) was used to obtain the first equality and $\mathbf{b}_g \mathbf{U}_g : \nabla \mathbf{b}_g = b_{gi} U_{gj} \partial b_{gi} / \partial x^j = (1/2) U_{gj} \partial (b_{gi}^2)/\partial x^j = 0$ for the second equality. Similarly, we have

$$\left\langle \mathbf{e}_p \mathbf{e}_p \right\rangle_\phi : \nabla \mathbf{b}_g = \left(\frac{1-\mu^2}{2} \left(\mathbb{I} - \mathbf{b}_g \mathbf{b}_g \right) + \mu^2 \mathbf{b}_g \mathbf{b}_g \right) : \nabla \mathbf{b}_g = \frac{1-\mu^2}{2} \nabla \cdot \mathbf{b}_g, \tag{A.10}$$

since we again have that $\mathbf{b}_g \mathbf{b}_g : \nabla \mathbf{b}_g = 0$. Finally, a straightforward calculation gives

$$\left(\mathbf{b} \left\langle \mathbf{e}_p \right\rangle_\phi - \mu \left\langle \mathbf{e}_p \mathbf{e}_p \right\rangle_\phi \right) : \nabla \mathbf{U}_g = \left[\mu \mathbf{b}_g \mathbf{b}_g - \mu \left(\frac{1-\mu^2}{2} \left(\mathbb{I} - \mathbf{b}_g \mathbf{b}_g \right) + \mu^2 \mathbf{b}_g \mathbf{b}_g \right) \right] : \nabla \mathbf{U}_g$$

$$= \frac{1-\mu^2}{2} \left(\mu \nabla \cdot \mathbf{U}_g - 3\mu \mathbf{b}_g \mathbf{b}_g : \nabla \mathbf{U}_g \right) \tag{A.11}$$

and

$$\left\langle \mathbf{e}_p \mathbf{e}_p \right\rangle_\phi : \nabla \mathbf{U}_g = \left(\frac{1-\mu^2}{2} \left(\mathbb{I} - \mathbf{b}_g \mathbf{b}_g \right) + \mu^2 \mathbf{b}_g \mathbf{b}_g \right) : \nabla \mathbf{U}_g$$

$$= \frac{1-\mu^2}{2} \nabla \cdot \mathbf{U}_g + \frac{3\mu^2 - 1}{2} \mathbf{b}_g \mathbf{b}_g : \nabla \mathbf{U}_g. \tag{A.12}$$

Upon substituting Eq. (A.2) and Eqs. (A.8) – (A.12) into Eq. (A.7), the following equation is obtained:

$$\begin{aligned}
&\gamma\left(1+\mu v\frac{\mathbf{U}_g\cdot\mathbf{b}_g}{c^2}\right)\frac{\partial\mathscr{F}}{\partial t}+\gamma\left[\langle(\boldsymbol{v}\cdot\mathbf{b})\,\mathbf{b}\rangle_\phi+\mathbf{U}_g+\langle\mathbf{V}_d\rangle_\phi\right]\cdot\frac{\partial\mathscr{F}}{\partial\mathbf{X}}\\
&+\frac{1-\mu^2}{2}\gamma\left[\frac{v}{c^2}\mathbf{U}_g\cdot\frac{\partial\mathbf{b}_g}{\partial t}+\nabla\cdot\mathbf{b}_g-\frac{2}{v}\mathbf{b}_g\cdot\frac{d\mathbf{U}_g}{dt}+\mu\nabla\cdot\mathbf{U}_g-3\mu\mathbf{b}_g\mathbf{b}_g:\nabla\mathbf{U}_g\right]\frac{\partial\mathscr{F}}{\partial\mu}\\
&-\gamma^2 mv\left(\frac{\mu}{v}\mathbf{b}_g\cdot\frac{d\mathbf{U}_g}{dt}+\frac{1-\mu^2}{2}\nabla\cdot\mathbf{U}_g+\frac{3\mu^2-1}{2}\mathbf{b}_g\mathbf{b}_g:\nabla\mathbf{U}_g\right)\frac{\partial\mathscr{F}}{\partial p}\\
&=\left(\frac{\delta\mathscr{F}}{\delta t}\right)_{\text{turb}}.
\end{aligned}\tag{A.13}$$

To compute $\langle(\boldsymbol{v}\cdot\mathbf{b})\,\mathbf{b}\rangle_\phi$, we consider a Taylor expansion of the magnetic unit vector around the GC location, i.e.,

$$\mathbf{b}=\mathbf{b}_g+r_L\left[\mathbf{e}_L\cdot\left(\nabla+\frac{\mathbf{U}_g}{c^2}\frac{\partial}{\partial t}\right)\right]\mathbf{b}_g+\cdots,\tag{A.14}$$

where $r_L:=\sqrt{1-\mu^2}p/qB_g$ and $\mathbf{e}_L:=\mathbf{b}_g\times\mathbf{p}/(\sqrt{1-\mu^2})p=-\sin\phi\mathbf{e}_x+\cos\phi\mathbf{e}_y$. The velocity vector of the particles can be decomposed as

$$\boldsymbol{v}=\mu v\mathbf{b}_g+\sqrt{1-\mu^2}v\mathbf{e}_\phi,\tag{A.15}$$

with $\mathbf{e}_\phi:=\mathbf{e}_L\times\mathbf{b}_g=\cos\phi\mathbf{e}_x+\sin\phi\mathbf{e}_y$. The instantaneous average of the parallel velocity $\boldsymbol{v}\cdot\mathbf{b}$ is then calculated as

$$\begin{aligned}
\langle(\boldsymbol{v}\cdot\mathbf{b})\,\mathbf{b}\rangle_\phi&=\mu v\mathbf{b}_g+r_L\sqrt{1-\mu^2}v\left[\left\langle\mathbf{e}_\phi\mathbf{e}_L\right\rangle_\phi:\left(\nabla\mathbf{b}_g+\frac{\mathbf{U}_g}{c^2}\frac{\partial\mathbf{b}_g}{\partial t}\right)\right]\mathbf{b}_g.\\
&=\mu v\mathbf{b}_g+\frac{r_L}{2}\sqrt{1-\mu^2}v\left[\left(\mathbf{e}_y\mathbf{e}_x-\mathbf{e}_x\mathbf{e}_y\right):\left(\nabla\mathbf{b}_g+\frac{\mathbf{U}_g}{c^2}\frac{\partial\mathbf{b}_g}{\partial t}\right)\right]\mathbf{b}_g\\
&=\mu v\mathbf{b}_g-\frac{r_L}{2}\sqrt{1-\mu^2}v\left[\left(\nabla\times\mathbf{b}_g\right)\cdot\mathbf{b}_g+\left(\frac{\mathbf{U}_g}{c^2}\times\frac{\partial\mathbf{b}_g}{\partial t}+\right)\cdot\mathbf{b}_g\right]\mathbf{b}_g,
\end{aligned}\tag{A.16}$$

where $\langle\mathbf{e}_L\rangle=0$ is used in to obtain the first equality, and the second equality is obtained by performing a calculation similar to (A.3). In addition, remark that we have neglected the higher order terms in Eq. (A.14), that is., Eq. (A.16) is valid to first order in r_L/L, where L denotes the characteristic length scale of the average background plasma (see Eq. (B.1)).

Upon using the definition of r_L at the GC location, we can write Eq. (A.16) as

$$\langle (\boldsymbol{v}\cdot\mathbf{b})\,\mathbf{b}\rangle_\phi = \mu v \mathbf{b}_g - \frac{1-\mu^2}{2}\frac{vp}{qB_g}\left[\left(\nabla\times\mathbf{b}_g\right)_\parallel + \left(\frac{\mathbf{U}_g}{c^2}\times\frac{\partial \mathbf{b}_g}{\partial t}\right)_\parallel\right], \tag{A.17}$$

where the subscripts $\parallel$ and $\perp$ are with respect to $\mathbf{b}_g$. By combining this result with Eq. (B.14), we obtain

$$\langle (\boldsymbol{v}\cdot\mathbf{b})\,\mathbf{b} + \mathbf{V}_d\rangle_\phi = \mu v \mathbf{b}_g + \mathbf{V}_{gd}, \tag{A.18}$$

with $\mathbf{V}_{gd}$ the particle drift velocity defined in Eq. (B.15). Substituting this result in Eq. (A.13) gives the following FTE:

$$\begin{aligned}
&\gamma\left(1+\mu v\frac{\mathbf{U}_g\cdot\mathbf{b}_g}{c^2}\right)\frac{\partial \mathscr{F}}{\partial t} + \gamma\left(\mu v\mathbf{b}_g + \mathbf{U}_g + \mathbf{V}_{gd}\right)\cdot\frac{\partial \mathscr{F}}{\partial \mathbf{X}} \\
&+ \frac{1-\mu^2}{2}\gamma\left(\frac{v}{c^2}\mathbf{U}_g\cdot\frac{\partial \mathbf{b}_g}{\partial t} + \nabla\cdot\mathbf{b}_g - \frac{2}{v}\mathbf{b}_g\cdot\frac{d\mathbf{U}_g}{dt} + \mu\nabla\cdot\mathbf{U}_g - 3\mu\mathbf{b}_g\mathbf{b}_g:\nabla\mathbf{U}_g\right)\frac{\partial \mathscr{F}}{\partial \mu} \\
&- \gamma^2 m v\left(\frac{\mu}{v}\mathbf{b}_g\cdot\frac{d\mathbf{U}_g}{dt} + \frac{1-\mu^2}{2}\nabla\cdot\mathbf{U}_g + \frac{3\mu^2-1}{2}\mathbf{b}_g\mathbf{b}_g:\nabla\mathbf{U}_g\right)\frac{\partial \mathscr{F}}{\partial p} \\
&= \left(\frac{\delta \mathscr{F}}{\delta t}\right)_{\text{turb}}.
\end{aligned} \tag{A.19}$$

Equation (A.19) is of the form

$$\frac{dt}{d\tau}\frac{\partial \mathscr{F}}{\partial t} + \frac{d\mathbf{X}}{d\tau}\frac{\partial \mathscr{F}}{\partial \tau} + \frac{d\mu}{d\tau}\frac{\partial \mathscr{F}}{\partial \mu} + \frac{dp}{d\tau}\frac{\partial \mathscr{F}}{\partial p} = \left(\frac{\delta \mathscr{F}}{\delta t}\right)_{\text{turb}}, \tag{A.20}$$

which can be recast to the more familiar formulation

$$\frac{\partial \mathscr{F}}{\partial t} + \frac{d\mathbf{X}}{dt}\frac{\partial \mathscr{F}}{\partial \tau} + \frac{d\mu}{dt}\frac{\partial \mathscr{F}}{\partial \mu} + \frac{dp}{dt}\frac{\partial \mathscr{F}}{\partial p} = \left(\frac{\delta \mathscr{F}}{\delta t}\right)_{\text{turb}}, \tag{A.21}$$

by dividing by $dt/d\tau$ and using the chain rule together with Eq. (2.40). In doing so, Eqs. (2.82) – (2.86) are obtained.

Appendix B

The Guiding Centre Drifts

"Arithmetic is being able to count up to twenty without taking off your shoes."
– Mickey Mouse

In this appendix, we derive Eq. (2.87) by calculating the gyro-average of the GC drift term $\langle \mathbf{V}_d \rangle_\phi$ (Eq. (2.66)) to first order in U/c and δ. The latter parameter is defined as $\delta \sim r_L/L \sim (\Omega T)^{-1}$, where L and T are the characteristic length and time scales of the background plasma, respectively. These scales can be defined as (e.g., Burger et al., 1985):

$$L \sim \min_{i,j} \left\{ \left| B \left(\frac{\partial B_j}{\partial x^i} \right)^{-1} \right|, \left| U \left(\frac{\partial U_j}{\partial x^i} \right)^{-1} \right| \right\} \tag{B.1}$$

$$T \sim \min_{i} \left\{ \left| B \left(\frac{\partial B_i}{\partial t} \right)^{-1} \right|, \left| U \left(\frac{\partial U_i}{\partial t} \right)^{-1} \right| \right\}. \tag{B.2}$$

By performing a Taylor expansion of the magnetic (unit) vector around the GC (like in Eq. (A.14)), we can write Eq. (2.66) as

$$\begin{aligned} \mathbf{V_d} = \frac{\mathbf{p}}{q} \times \left[\left(1 + \frac{\mathbf{U}_g \cdot \boldsymbol{v}}{c^2} \right) \frac{\partial}{\partial t} \left(\frac{\mathbf{b}_g}{B_g} \right) + \left(\boldsymbol{v} + \mathbf{U}_g \right) \cdot \nabla \left(\frac{\mathbf{b}_g}{B_g} \right) \right] \\ - \frac{\gamma}{\Omega} \left(\frac{\partial \mathbf{U}_g}{\partial t} + \left[(\boldsymbol{v} + \mathbf{U}_g) \cdot \nabla \right] \mathbf{U}_g \right) \times \mathbf{b}_g + O(\delta^2). \end{aligned} \tag{B.3}$$

Upon neglecting the $O(\delta^2)$ terms and averaging the remaining terms of Eq. (B.3) over the gyrophase, we obtain

$$\begin{aligned}\langle \mathbf{V}_d \rangle_\phi = &\frac{\mu p}{qB_g}\mathbf{b}_g \times \frac{d\mathbf{b}_g}{dt} + \frac{vp}{qc^2}\left\langle \mathbf{e}_p \times \left[\left(\mathbf{e}_p \cdot \mathbf{U}_g\right)\frac{\partial}{\partial t}\left(\frac{\mathbf{B}_g}{B_g^2}\right)\right]\right\rangle_\phi \\ &+ \frac{vp}{q}\left\langle \mathbf{e}_p \times \left[\left(\mathbf{e_p} \cdot \nabla\right)\left(\frac{\mathbf{B}_g}{B_g^2}\right)\right]\right\rangle_\phi \\ &+ \mathbf{b}_g \times \frac{\gamma m}{qB_g}\left[\frac{d\mathbf{U}_g}{dt} + \mu v\left(\mathbf{b}_g \cdot \nabla\right)\mathbf{U}_g\right],\end{aligned} \tag{B.4}$$

where Eq. (A.2) was used. To calculate the gyro-average of the second and third terms, we note that[1]

$$\mathbf{e}_p \times \left[\left(\mathbf{e}_p \cdot \mathbf{W}\right)\mathbf{V}\right] = \begin{pmatrix} \sin^2\theta\cos^2\phi W_x + \sin^2\theta\cos\phi\sin\phi W_y + \cos\theta\sin\theta\cos\phi W_z \\ \sin^2\theta\sin\phi\cos\phi W_x + \sin^2\theta\sin^2\phi W_y + \cos\theta\sin\theta\sin\phi W_z \\ \sin\theta\cos\theta\cos\phi W_x + \sin\theta\cos\theta\sin\phi W_y + \cos^2\theta W_Z \end{pmatrix} \times \mathbf{V},$$

with $\mathbf{V} := \mathbf{b}_g/B_g$ and $\mathbf{W}$ either equal to the operator[2] $\mathbf{U}_g\partial/\partial t$ or to the ∇-operator. Averaging over the gyro-phase gives then

$$\left\langle \mathbf{e}_p \times \left[\left(\mathbf{e}_p \cdot \mathbf{W}\right)\mathbf{V}\right]\right\rangle_\phi = \begin{pmatrix} \frac{1}{2}\sin^2\theta W_x \\ \frac{1}{2}\sin^2\theta W_y \\ \cos^2\theta W_z \end{pmatrix} \times \mathbf{V} = \begin{pmatrix} \frac{1}{2}\sin^2\theta W_y V_z - \cos^2\theta W_z V_y \\ \cos^2\theta W_z V_x - \frac{1}{2}\sin^2\theta W_x V_z \\ \frac{1}{2}\sin^2\theta\left(W_x V_y - W_y V_x\right) \end{pmatrix},$$

where we used that $\langle\sin\phi\rangle_\phi = \langle\cos\phi\rangle_\phi = 0$ and $\left\langle\sin^2\phi\right\rangle_\phi = \left\langle\cos^2\phi\right\rangle_\phi = 1/2$ to obtain the first equality. Since $\mathbf{b}_g \equiv \mathbf{e}_z$, we can rewrite this further as

$$\begin{aligned}\left\langle \mathbf{e}_p \times \left[\left(\mathbf{e}_p \cdot \mathbf{W}\right)\mathbf{V}\right]\right\rangle_\phi = &-\frac{1-\mu^2}{2}\mathbf{b}_g \times \left[\mathbf{W}\left(\mathbf{b}_g \cdot \mathbf{V}\right)\right] + \frac{1-\mu^2}{2}\mathbf{b}_g\left[\mathbf{b}_g \cdot (\mathbf{W}\times\mathbf{V})\right] \\ &+ \mu^2\mathbf{b}_g \times \left[\left(\mathbf{b}_g \cdot \mathbf{W}\right)\mathbf{V}\right].\end{aligned} \tag{B.5}$$

[1] We use here that $\mathbf{e}_p = \sin\theta\cos\phi\mathbf{e}_x + \sin\theta\sin\phi\mathbf{e}_y + \cos\theta\mathbf{b}_g$

[2] The operator $\mathbf{U}_g\partial/\partial t$ is defined here as $\mathbf{e}_x U_x\partial/\partial t + \mathbf{e}_y U_y\partial/\partial t + \mathbf{e}_z U_z\partial/\partial t$, which is similar to the operator $\nabla = \mathbf{e}_x\partial/\partial x + \mathbf{e}_y\partial/\partial y + \mathbf{e}_z\partial/\partial z$. It would be more natural to introduce the operator $(\mathbf{U}_g/c^2)\partial/\partial t$, since it has the same dimensions as the ∇-operator and it makes the second and third term of Eq. (B.4) symmetric. However, for notational convenience, we do not include the $1/c^2$ term here.

By using this expression together with $\mathbf{V} = \mathbf{b}_g/B_g$ and $\mathbf{W} = \mathbf{U}_g \frac{\partial}{\partial t}$, it is straightforward to show that

$$\left\langle \mathbf{e}_p \times \left[\left(\mathbf{e}_p \cdot \mathbf{U}_g \right) \frac{\partial}{\partial t} \left(\frac{\mathbf{B}_g}{B_g^2} \right) \right] \right\rangle_\phi = \frac{1-\mu^2}{2} \left\{ \frac{1}{B_g^2} \frac{\partial B_g}{\partial t} \left(\mathbf{b}_g \times \mathbf{U}_g \right) + \frac{1}{B} \left[\mathbf{b}_g \cdot \left(\mathbf{U}_g \times \frac{\partial \mathbf{b}_g}{\partial t} \right) \right] \mathbf{b}_g \right\}$$
$$+ \mu^2 \left[\mathbf{b}_g \times \left(\frac{\mathbf{b}_g \cdot \mathbf{U}_g}{B_g} \right) \frac{\partial \mathbf{b}_g}{\partial t} \right]. \tag{B.6}$$

Analogously, but with $\mathbf{W} = \nabla$, one finds

$$\left\langle \mathbf{e}_p \times \left[\left(\mathbf{e}_p \cdot \nabla \right) \left(\frac{\mathbf{B}_g}{B_g^2} \right) \right] \right\rangle_\phi = \frac{1-\mu^2}{2} \left\{ \frac{1}{B_g^2} \mathbf{b}_g \times \left(\nabla B_g \right) + \frac{1}{B_g} \left[\mathbf{b}_g \cdot \left(\nabla \times \mathbf{b}_g \right) \right] \mathbf{b}_g \right\}$$
$$+ \mu^2 \left\{ \frac{1}{B_g} \mathbf{b}_g \times \left[\left(\mathbf{b}_g \cdot \nabla \right) \mathbf{b}_g \right] \right\}. \tag{B.7}$$

Equations (B.8) and (B.7) can be further rewritten as[3]

$$\left\langle \mathbf{e}_p \times \left[\left(\mathbf{e}_p \cdot \mathbf{U}_g \right) \frac{\partial}{\partial t} \left(\frac{\mathbf{B}_g}{B_g^2} \right) \right] \right\rangle_\phi = \frac{1-\mu^2}{2} \left[\frac{1}{B_g^2} \frac{\partial B_g}{\partial t} \left(\mathbf{b}_g \times \mathbf{U}_g \right) + \frac{1}{B} \left(\mathbf{U}_g \times \frac{\partial \mathbf{b}_g}{\partial t} \right)_\parallel \right]$$
$$+ \mu^2 \left[\frac{1}{B_g} \left(\mathbf{U}_g \times \frac{\partial \mathbf{b}_g}{\partial t} \right)_\perp \right] \tag{B.8}$$

and

$$\left\langle \mathbf{e}_p \times \left[\left(\mathbf{e}_p \cdot \nabla \right) \left(\frac{\mathbf{B}_g}{B_g^2} \right) \right] \right\rangle_\phi = \frac{1-\mu^2}{2} \left[\frac{1}{B_g^2} \mathbf{b}_g \times \left(\nabla B_g \right) + \frac{1}{B_g} \left(\nabla \times \mathbf{b}_g \right)_\parallel \right]$$
$$+ \mu^2 \left[\frac{1}{B_g} \left(\nabla \times \mathbf{b}_g \right)_\perp \right], \tag{B.9}$$

where

$$\left(\mathbf{U}_g \times \frac{\partial \mathbf{b}_g}{\partial t} \right)_\parallel := \left(\mathbf{b}_g \cdot \mathbf{U}_g \times \frac{\partial \mathbf{b}_g}{\partial t} \right) \mathbf{b}_g, \tag{B.10}$$

$$\left(\mathbf{U}_g \times \frac{\partial \mathbf{b}_g}{\partial t} \right)_\perp := \mathbf{U}_g \times \frac{\partial \mathbf{b}_g}{\partial t} - \left(\mathbf{U}_g \times \frac{\partial \mathbf{b}_g}{\partial t} \right)_\parallel, \tag{B.11}$$

$$(\nabla \times \mathbf{b}_g)_\parallel := (\mathbf{b}_g \cdot \nabla \times \mathbf{b}_g) \mathbf{b}_g, \tag{B.12}$$

$$(\nabla \times \mathbf{b}_g)_\perp := \nabla \times \mathbf{b}_g - (\nabla \times \mathbf{b}_g)_\parallel. \tag{B.13}$$

[3] To obtain this result, one needs to use that $\left(\mathbf{b}_g \cdot \mathbf{W} \right) \mathbf{b}_g = -\mathbf{b}_g \times (\mathbf{W} \times \mathbf{b}_g)$, and subsequently utilise a triple vector product identity.

Substituting Eqs. (B.8) and (B.9) into Eq. (B.4) gives:

$$\langle \mathbf{V}_d \rangle_\phi = \frac{\left(1-\mu^2\right) vp}{2qB_g} \left[\left(\frac{\mathbf{U}_g}{c^2} \times \frac{\partial \mathbf{b}_g}{\partial t} \right)_{\|} + (\nabla \times \mathbf{b}_g)_{\|} \right] + \mathbf{V}_{gd}, \tag{B.14}$$

with

$$\begin{aligned} \mathbf{V}_{gd} := & \frac{\mu p}{qB_g} \left(\mathbf{b}_g \times \frac{d\mathbf{b}_g}{dt} \right) \\ & + \frac{vp}{c^2 qB_g} \left[\frac{1-\mu^2}{2B_g} \frac{\partial B_g}{\partial t} \left(\mathbf{b}_g \times \mathbf{U}_g \right) + \mu^2 \left(\mathbf{U}_g \times \frac{\partial \mathbf{b}_g}{\partial t} \right)_{\perp} \right] \\ & + \frac{vp}{qB_g} \left[\frac{1-\mu^2}{2B_g} \mathbf{b}_g \times \nabla B_g + \mu^2 (\nabla \times \mathbf{b}_g)_{\perp} \right] \\ & + \mathbf{b}_g \times \frac{\gamma m}{qB_g} \left[\frac{d\mathbf{U}_g}{dt} + \mu v \left(\mathbf{b}_g \cdot \nabla \right) \mathbf{U}_g \right]. \end{aligned} \tag{B.15}$$

Remark that the second term of Eq. (B.15) can be obtained from the third term by simply replacing the operator $(\mathbf{U}/c^2)\partial/\partial t$ by the ∇-operator and vice versa. Moreover, the parallel "drift" terms in Eq. (B.14) appear with an opposite sign in the gyro-average of the particle velocity (see (A.17)), and cancel thus each other out (see Eq. (A.18)).

Under the assumption that the magnetic field is varying only slowly in time, i.e., $(T\Omega)^{-1} \ll 1$, and that $U_g \ll v$, the magnetic field gradient and curvature drifts will be the dominant GC drifts, and we can approximate (B.15) as

$$\mathbf{V}_{gd} \approx \frac{pv}{qB_g} \left[\frac{1-\mu^2}{2B_g} \left(\mathbf{b}_g \times \nabla B_g \right) + \mu^2 (\nabla \times \mathbf{b}_g)_{\perp} \right]. \tag{B.16}$$

Appendix C

Stochastic Differential Equations

Po: "How did I do?"
Master Shifu: "There is now a Level Zero."
– Kung Fu Panda

In this appendix, we illustrate that a stochastic variable that satisfies a forward Itô SDE, has a conditional probability distribution that satisfies a KFE. This is done by first deriving Itô's Lemma, and subsequently calculating its expectation value. The derivation given below is informal, and a more mathematically rigorous approach can be found in Kallenberg (2002). Moreover, for notational simplicity, we limit ourselves to a one-dimensional stochastic variable, although it is straightforward to generalize the discussion provided below to a multi-dimensional setting.

Suppose f is an arbitrary scalar function that is sufficiently smooth so that it can be expanded in a Taylor series, that is,

$$\Delta f(\zeta) = \frac{df}{d\zeta}\Delta\zeta + \frac{1}{2}\frac{\partial^2 f}{\partial\zeta^2}\Delta\zeta^2 + \dots, \tag{C.1}$$

where the dots include the higher order terms in $\Delta\zeta$. We now assume that ζ is a stochastic variable, satisfying the Itô SDE given in Eq. (3.1). Substituting Eq. (3.1) into the Taylor expansion of f gives

$$\Delta f = \frac{\partial f}{\partial\zeta}(\mathsf{A}\Delta t + \mathsf{B}\Delta W) + \frac{1}{2}\frac{d^2 f}{d\zeta^2}(\mathsf{A}^2\Delta t^2 + \mathsf{B}^2\Delta W^2 + 2\mathsf{AB}\Delta t\Delta W) + \dots \tag{C.2}$$

It follows from the properties of a Wiener process that $\Delta W \sim \mathcal{N}(0, \Delta t)$, and therefore it can be assumed that $\Delta t \Delta W$ goes faster to zero than Δt. The last term in Eq. (C.1) can thus be neglected to first order in Δt. Evidently, the term $\mathsf{A}^2 \Delta t^2$ can also be neglected to first order in Δt. Moreover, it follows from the properties of a normal distribution that the expectation value of ΔW^2 is Δt, such that we can write $\Delta W^2 = \Delta t + \chi$, where χ is a random variable with zero mean. It is straightforward to show that the variance of ΔW^2, and hence χ, equals $2\Delta t^2$. As a result, χ can be neglected to first order in Δt, such that we can use $\Delta W^2 = \Delta t$ in Eq. (C.2). Hence, the following formula is obtained for $\Delta t \to 0$

$$\begin{aligned} df &= \frac{df}{d\zeta}(\mathsf{A}dt + \mathsf{B}dW) + \frac{1}{2}\frac{d^2 f}{d\zeta^2}\mathsf{B}^2 dt \\ &= \left[\mathsf{A}(\zeta(t))\frac{df(\zeta(t))}{d\zeta} + \frac{\mathsf{B}(\zeta(t))^2}{2}\frac{d^2 f(\zeta(t))}{d\zeta^2}\right]dt + \mathsf{B}(\zeta(t))\frac{df(\zeta(t))}{d\zeta}dW. \end{aligned} \tag{C.3}$$

This formula is called Itô's Lemma and can be regarded as a generalisation of the chain-rule to stochastic calculus.

We can now proceed by taking the expectation value, denoted by $\langle\cdot\rangle$, of Itô's lemma, which gives

$$\langle df \rangle = \left\langle \mathsf{A}(\zeta(t))\frac{df(\zeta(t))}{d\zeta} + \frac{\mathsf{B}(\zeta(t))^2}{2}\frac{d^2 f(\zeta(t))}{d\zeta^2}\right\rangle dt. \tag{C.4}$$

since $\langle df \rangle = d\langle f \rangle$, we find thus that[1]

$$\frac{d\langle f \rangle}{dt} = \left\langle \mathsf{A}(\zeta(t))\frac{df(\zeta(t))}{d\zeta} + \frac{\mathsf{B}(\zeta(t))^2}{2}\frac{d^2 f(\zeta(t))}{d\zeta^2}\right\rangle. \tag{C.5}$$

Recall now from Eq. (3.1) that the initial state of ζ is denoted by ζ^0. Hence, the stochastic variable ζ has a conditional probability function $p(\zeta, t \,|\, \zeta^0, t_0)$, such that

$$\frac{d\langle f \rangle}{dt} = \frac{d}{dt}\int f(\zeta) p(\zeta, t \,|\, \zeta^0, t_0) d\zeta \tag{C.6}$$

$$= \int f(\zeta)\frac{\partial}{\partial t}\left[p(\zeta, t \,|\, \zeta^0, t_0)\right] d\zeta. \tag{C.7}$$

[1] Note that one cannot write

$$\left\langle \frac{df(\zeta(t))}{dt} \right\rangle,$$

since the Wiener process $\zeta(t)$ is nowhere differentiable and hence f will also not be differentiable to the coordinate t.

Combining Eqs. (C.5) and (C.6) gives then

$$\int f(\zeta)\frac{\partial p}{\partial t}d\zeta = \int \left[\mathsf{A}(\zeta)\frac{df(\zeta)}{d\zeta} + \frac{\mathsf{B}(\zeta)^2}{2}\frac{d^2 f(\zeta)}{d\zeta^2}\right] p d\zeta$$

$$= \int f(\zeta)\left[-\frac{\partial}{\partial\zeta}\left(\mathsf{A}(\zeta)p\right) + \frac{1}{2}\frac{\partial^2}{\partial\zeta^2}\left(\mathsf{B}(\zeta)^2 p\right)\right] d\zeta, \tag{C.8}$$

where the last equality follows from an integration by parts where the surface terms are discarded. Since f is an arbitrary function, it follows that the conditional probability p satisfies

$$\frac{\partial p(\zeta,t)}{\partial t} = -\frac{\partial}{\partial\zeta}\left[\mathsf{A}(\zeta,t)p(\zeta,t)\right] + \frac{1}{2}\frac{\partial^2}{\partial\zeta^2}\left[\mathsf{B}(\zeta,t)^2 p(\zeta,t)\right], \tag{C.9}$$

which is a KFE.

Bibliography

Ackermann, M., Ajello, M., Allafort, A., et al. 2013, Science, 339

Afanasiev, A., Battarbee, M., & Vainio, R. 2015, A&A, 584, A81

Afanasiev, A. & Vainio, R. 2013, ApJS, 207, 29

Agueda, N. & Vainio, R. 2013, J. Space Weather Space Clim., 3, A10

Agueda, N., Vainio, R., Lario, D., & Sanahuja, B. 2008, ApJ, 675, 1601

Agueda, N., Vainio, R., & Sanahuja, B. 2012, ApJS, 202, 18

Alsabti, A. W. & Murdin, P. 2017, Handbook of Supernovae (Springer International Publishing)

Anderson, B. R., Skoug, R. M., Steinberg, J. T., & McComas, D. J. 2012, J. Geophys. Res. Space Phys., 117

Aran, A. 2007, PhD thesis, Univ. Barcelona

Aran, A., Lario, D., Sanahuja, B., et al. 2007, A&A, 469, 1123

Axford, W. I., Leer, E., & McKenzie, J. F. 1982, A&A, 111, 317

Axford, W. I., Leer, E., & Skadron, G. 1977, Conf. Proc. ICRC, 11, 132

Baade, W. & Zwicky, F. 1934, Physical Review, 46, 76

Barnes, C. W. & Simpson, J. A. 1976, ApJ, 210, L91

Batchelor, G. K. 1953, The Theory of Homogeneous Turbulence (Cambridge University Press)

Battarbee, M., Laitinen, T., & Vainio, R. 2011, A&A, 535, A34

Battarbee, M., Vainio, R., Laitinen, T., & Hietala, H. 2013, A&A, 558, A110

Beeck, J. & Sanderson, T. R. 1989, J. Geophys. Res., 94, 8769

Beeck, J. & Wibberenz, G. 1986, ApJ, 311, 437

Bell, A. R. 1978, Mon. Not. R. Astron. Soc., 182, 147

Bieber, J. W., Chen, J., Matthaeus, W. H., Smith, C. W., & Pomerantz, M. A. 1993, J. Geophys. Res., 98, 3585

Bieber, J. W., Matthaeus, W. H., Smith, C. W., et al. 1994, ApJ, 420, 294

Bieber, J. W., Wanner, W., & Matthaeus, W. H. 1996, J. Geophys. Res., 101, 2511

Bird, D. J., Corbató, S. C., Dai, H. Y., et al. 1995, ApJ, 441, 144

Blandford, R. D. 1980, ApJ, 238, 410

Blandford, R. D. & Ostriker, J. P. 1978, ApJ, 221, L29

Blasi, P. 2004, Astroparticle Physics, 21, 45

Blasi, P. 2013, A&AReview, 21, 70

Bolton, S. J., Janssen, M., Thorne, R., et al. 2002, Nature, 415, 987

Borovikov, D., Sokolov, I. V., Roussev, I. I., Taktakishvili, A., & Gombosi, T. I. 2018, ApJ, 864, 88

Bruno, R. & Carbone, V. 2005, Living Rev. Sol. Phys., 2, 4

Bruno, R., Carbone, V., Vörös, Z., et al. 2009, Earth, Moon, and Planets, 104, 101

Bruno, R., Trenchi, L., & Telloni, D. 2014, ApJ, 793, L15

Burger, R. A., Moraal, H., & Webb, G. M. 1985, Ap&SS, 116, 107

Burlaga, L. F. 1974, J. Geophys. Res. (1896-1977), 79, 3717

Bučík, R., Innes, D. E., Mason, G. M., et al. 2018, ApJ, 852, 76

Candia, J. & Roulet, E. 2004, J. Cosmol. Astropart. Phys., 2004, 007

Cane, H. V., Mewaldt, R. A., Cohen, C. M. S., & von Rosenvinge, T. T. 2006, J. Geophys. Res. Space Phys., 111, A06S90

Cane, H. V., Reames, D. V., & von Rosenvinge, T. T. 1988, J. Geophys. Res., 93, 9555

Chancellor, J. C., Scott, G. B. I., & Sutton, J. P. 2014, Life (Basel, Switzerland), 4, 491

Chandrasekhar, S. 1950, Philos. Trans. R. Soc. A, 242, 557

Chenette, D. L., Conlon, T. F., Pyle, K. R., & Simpson, J. A. 1977, ApJ, 215

Chotoo, K., Schwadron, N. A., Mason, G. M., et al. 2000, J. Geophys. Res., 105, 23107

Chuychai, P., Ruffolo, D., Matthaeus, W. H., & Meechai, J. 2007, ApJ, 659, 1761

Classen, H.-T., Mann, G., & Keppler, E. 1998, A&A, 335, 1101

Corrsin, S. 1951, J. Appl. Phys, 22, 469

Cranmer, S. R., Gibson, S. E., & Riley, P. 2017, Space Sci. Rev., 212, 1345

Crooker, N. U., Gosling, J. T., Bothmer, V., et al. 1999, Space Sci. Rev., 89, 179

Dalla, S., Balogh, A., Krucker, S., et al. 2003, Geophysical Research Letters, 30, 8035

Dalla, S., Marsh, M. S., & Battarbee, M. 2017, ApJ, 834, 167

Dalla, S., Marsh, M. S., Kelly, J., & Laitinen, T. 2013, J. Geophys. Res. Space Phys., 118, 5979

Dalla, S., Marsh, M. S., & Laitinen, T. 2015, ApJ, 808, 62

de Pater, I. & Goertz, C. K. 1990, J. Geophys. Res. Space Phys., 95, 39

Debbasch, F., Rivet, J. P., & van Leeuwen, W. A. 2001, Physica A Stat. Mech. Appl., 301, 181

Decker, R. B. 1988, Space Sci. Rev., 48, 195

Decker, R. B., Pesses, M. E., & Krimigis, S. M. 1981, J. Geophys. Res., 86, 8819

Desai, M. & Giacalone, J. 2016, Living Rev. Sol. Phys., 13, 3

Desai, M. I., Marsden, R. G., Sanderson, T. R., et al. 1998, J. Geophys. Res., 103, 2003

Domingo, V., Fleck, B., & Poland, A. I. 1995, Sol. Phys., 162, 1

Drake, J. F., Cassak, P. A., Shay, M. A., Swisdak, M., & Quataert, E. 2009, ApJ, 700, L16

Drake, J. F., Swisdak, M., & Fermo, R. 2013, ApJ, 763, L5

Dresing, N., Gómez-Herrero, R., Heber, B., et al. 2014, A&A, 567, A27

Dresing, N., Gómez-Herrero, R., Klassen, A., et al. 2012, Sol. Phys., 281, 281

Dröge, W. 2000, ApJ, 537, 1073

Dröge, W. 2003, ApJ, 589, 1027

Dröge, W., Kartavykh, Y. Y., Dresing, N., Heber, B., & Klassen, A. 2014, J. Geophys. Res. Space Phys., 119, 6074

Dröge, W., Kartavykh, Y. Y., Dresing, N., & Klassen, A. 2016, ApJ, 826, 134

Dröge, W., Kartavykh, Y. Y., Klecker, B., & Kovaltsov, G. A. 2010, ApJ, 709, 912

Drury, L. O. & Voelk, J. H. 1981, ApJ, 248, 344

Dwyer, J. R., Mason, G. M., Mazur, J. E., et al. 1997, ApJ, 490, L115

Earl, J. A. 1973, ApJ, 180, 227

Effenberger, F. 2014, ASP Conf. Ser., 488, 201

Engelbrecht, N. E. 2019, ApJ, 880, 60

Engelbrecht, N. E., Strauss, R. D., le Roux, J. A., & Burger, R. A. 2017, ApJ, 841, 107

Erdos, G., Balogh, A., & Jota, J. 1999, Proc. ICRC, 6, 316

Feldman, W. C., Asbridge, J. R., Bame, S. J., & Gosling, J. T. 1976, J. Geophys. Res., 81, 5054

Fermi, E. 1949, Physical Review, 75, 1169

Fisk, L. A., Kozlovsky, B., & Ramaty, R. 1974, ApJ, 190, L35

Fisk, L. A. & Lee, M. A. 1980, ApJ, 237, 620

Florinski, V., Decker, R. B., Roux, J. A. l., & Zank, G. P. 2009, Geophys. Res. Lett., 36

Fox, N. J., Velli, M. C., Bale, S. D., et al. 2016, Space Sci. Rev., 204, 7

Fraschetti, F. 2016, ASTRA Proc., 2, 63

Gardiner, C. W. 2004, Handbook of Stochastic Methods for Physics, Chemistry and the Natural Sciences, 3rd edn., Vol. 13 (Berlin: Springer-Verlag)

Geiss, J., Gloeckler, G., & Von Steiger, R. 1995, Space Sci. Rev., 72, 49

Giacalone, J., Drake, J. F., & Jokipii, J. R. 2012, Space Sci. Rev., 173, 283

Giacalone, J. & Jokipii, J. R. 1999, ApJ, 520, 204

Giacalone, J. & Jokipii, J. R. 2012, ApJ, 751, L33

Giacalone, J., Jokipii, J. R., & Kóta, J. 2002, ApJ, 573, 845

Giacalone, J., Jokipii, J. R., & Kóta, J. 2005, Geophys. Monogr. Ser, 156, 41

Goedbloed, H., Keppens, R., & Poedts, S. 2019, Magnetohydrodynamics of Laboratory and Astrophysical Plasmas (Cambridge University Press)

Goldstein, M. L., Roberts, D. A., & Matthaeus, W. H. 1995, ARA&A, 33, 283

Goldstein, M. L., Wicks, R. T., Perri, S., & Sahraoui, F. 2015, Philos. Trans. R. Soc. A, 373, 20140147

Gómez-Herrero, R., Dresing, N., Klassen, A., et al. 2015, ApJ, 799, 55

Gopalswamy, N., Akiyama, S., Yashiro, S., et al. 2014, Geophys. Res. Lett., 41, 2673

Gordon, B. E., Lee, M. A., Möbius, E., & Trattner, K. J. 1999, J. Geophys. Res., 104, 28263

Gosling, J. T. 1996, ARA&A, 34, 35

Gosling, J. T., Asbridge, J. R., Bame, S. J., & Feldman, W. C. 1978, J. Geophys. Res. Space Phys., 83, 1401

Green, M. S. 1951, J. Chem. Phys., 19, 1036

Hadamard, J. 1902, Princeton University Bulletin, 49

Hapgood, M. 2011, Adv. Space Res., 47, 2059

Hasselmann, K. & Wibberenz, G. 1968, Z. Geophys., 34, 353

Hasselmann, K. & Wibberenz, G. 1970, ApJ, 162, 1049

He, H.-Q. & Wan, W. 2016, Mon. Not. R. Astron. Soc., 464, 85

He, H. Q., Zhou, G., & Wan, W. 2017, ApJ, 842, 71

Hedgecock, P. C. 1975, Sol. Phys., 42, 497

Heita, P. K. N. 2019, Master thesis, North-West University (South Africa)

Heras, A. M., Sanahuja, B., Lario, D., et al. 1995, ApJ, 445, 497

Heras, A. M., Sanahuja, B., Sanderson, T. R., Marsden, R. G., & Wenzel, K. P. 1994, J. Geophys. Res., 99, 43

Heras, A. M., Sanahuja, B., Smith, Z. K., Detman, T., & Dryer, M. 1992, ApJ, 391, 359

Honda, M. & Honda, Y. S. 2004, ApJ, 617, L37

Horbury, T. & Schmidt, J. 1999, Space Sci. Rev., 89, 61

Horne, R. B., Thorne, R. M., Glauert, S. A., et al. 2008, Nat. Phys., 4, 301

Howes, G. G. & Quataert, E. 2010, ApJ, 709, L49

Hu, J., Li, G., Ao, X., Zank, G. P., & Verkhoglyadova, O. 2017, J. Geophys. Res. Space Phys., 122, 10,938

Intriligator, D. S., Jokipii, J. R., Horbury, T. S., et al. 2001, J. Geophys. Res. Space Phys., 106, 10625

Isenberg, P. A. 1997, J. Geophys. Res., 102, 4719

Jian, L., Russell, C. T., Luhmann, J. G., & Skoug, R. M. 2006, Sol. Phys., 239, 337

Jokipii, J. R. 1966, ApJ, 146, 480

Jokipii, J. R. 1987, ApJ, 313, 842

Jokipii, J. R. & Giacalone, J. 2007, ApJ, 660, 336

Jokipii, J. R., Giacalone, J., & Kota, J. 2003, ICRC28, 6, 3685

Jokipii, J. R., Levy, E. H., & Hubbard, W. B. 1977, ApJ, 213, 861

Kahler, S. W., Kazachenko, M., Lynch, B. J., & Welsch, B. T. 2017, J. Phys.: Conf. Ser., 900, 012011

Kaiser, M. L., Kucera, T. A., Davila, J. M., et al. 2008, Space Sci. Rev., 136, 5

Kaiser, T. B., Jones, F. C., & Birmingham, T. J. 1973, ApJ, 180, 239

Kallenberg, O. 2002, Foundations of Modern Probability, Probability and Its Applications (Springer New York)

Kallenrode, M. 2004, Space Physics: An Introduction to Plasmas and Particles in the Heliosphere and Magnetospheres, Advanced Texts in Physics (Springer)

Kennel, C. F., Coroniti, F. V., Scarf, F. L., et al. 1986, J. Geophys. Res., 91, 11917

Kirk, J. G., Schneider, P., & Schlickeiser, R. 1988, ApJ, 328, 269

Klassen, A., Dresing, N., Gómez-Herrero, R., & Heber, B. 2015, A&A, 580, A115

Klassen, A., Dresing, N., Gómez-Herrero, R., Heber, B., & Müller-Mellin, R. 2016, A&A, 593, A31

Klassen, A., Dresing, N., Gómez-Herrero, R., Heber, B., & Veronig, A. 2018, A&A, 614, A61

Klecker, B., McNab, M. C., Blake, J. B., et al. 1995, ApJ, 442, L69

Klein, K.-L., Krucker, S., Lointier, G., & Kerdraon, A. 2008, A&A, 486, 589

Klimas, A. J. & Sandri, G. 1971, ApJ, 169, 41

Klimas, A. J. & Sandri, G. 1973, ApJ, 180, 937

Kloeden, P. & Platen, E. 1992, Numerical Solution of Stochastic Differential Equations, Applications of Mathematics (Springer-Verlag)

Kocharov, L., Kovaltsov, G. A., Torsti, J., Anttila, A., & Sahla, T. 2003, J. Geophys. Res. Space Phys., 108, 1404

Kocharov, L., Laivola, J., Mason, G. M., Didkovsky, L., & Judge, D. L. 2008a, ApJS, 176, 497

Kocharov, L., Pizzo, V. J., Zwickl, R. D., & Valtonen, E. 2008b, ApJ, 680, L69

Kocharov, L., Vainio, R., Kovaltsov, G. A., & Torsti, J. 1998, Sol. Phys., 182, 195

Kocharov, L. G., Torsti, J., Laitinen, T., & Vainio, R. 1997, Sol. Phys., 175, 785

Kolmogorov, A. 1941, Akademiia Nauk SSSR Doklady, 30, 301

Kopp, A., Büsching, I., Strauss, R. D., & Potgieter, M. S. 2012, Comput. Phys. Commun., 183, 530

Kota, J. & Jokipii, J. R. 1991, Geophys. Res. Lett., 18, 1797

Kóta, J., Manchester, W. B., Jokipii, J. R., de Zeeuw, D. L., & Gombosi, T. I. 2005, AIP Conf. Ser., 781, 201

Kozarev, K., Schwadron, N. A., Dayeh, M. A., et al. 2010, Space Weather, 8, S00E08

Kozarev, K. A., Evans, R. M., Schwadron, N. A., et al. 2013, ApJ, 778, 43

Krupp, N., Woch, J., Lagg, A., et al. 2002, Geophysical Research Letters, 29, 26

Krymsky, G. F. 1977, Dokl. Akad. Nauk SSSR, 234, 1306

Kubo, R. 1957, J. Phys. Soc. Jpn, 12, 570

Kunow, H., Wibberenz, G., Green, G., Müller-Mellin, R., & Kallenrode, M.-B. 1991, Energetic Particles in the Inner Solar System (Springer-Verlag), 152

Laitinen, T., Dalla, S., & Marsh, M. S. 2013, ApJ, 773, L29

Lampa, F. 2011, PhD thesis, Osnabrück University

Lario, D. 1997, PhD thesis, Univ. Barcelona

Lario, D., Aran, A., Agueda, N., & Sanahuja, B. 2007, Adv. Space Res., 40, 289

Lario, D., Aran, A., Gómez-Herrero, R., et al. 2013, ApJ, 767, 41

Lario, D., Berger, L., Decker, R. B., et al. 2019, AJ, 158, 12

Lario, D., Decker, R. B., Roelof, E. C., & Viñas, A. F. 2015a, ApJ, 813, 85

Lario, D., Decker, R. B., Roelof, E. C., & Viñas, A. F. 2015b, J. Phys.: Conf. Ser., 642, 012014

Lario, D., Kwon, R.-Y., Riley, P., & Raouafi, N. E. 2017, ApJ, 847, 103

Lario, D., Kwon, R.-Y., Vourlidas, A., et al. 2016, ApJ, 819, 72

Lario, D., Raouafi, N. E., Kwon, R.-Y., et al. 2014, ApJ, 797, 8

Lario, D., Sanahuja, B., & Heras, A. M. 1998, ApJ, 509, 415

le Roux, J. A. & Webb, G. M. 2009, ApJ, 693, 534

le Roux, J. A. & Webb, G. M. 2012, ApJ, 746, 104

le Roux, J. A., Webb, G. M., Florinski, V., & Zank, G. P. 2007, ApJ, 662, 350

le Roux, J. A., Zank, G. P., Milano, L. J., & Matthaeus, W. H. 2004, ApJ, 602, 396

Lee, M. A. 1983, J. Geophys. Res., 88, 6109

Li, G., Zank, G. P., & Rice, W. K. M. 2003, J. Geophys. Res. Space Phys., 108, 1082

Linker, J. A., Caplan, R. M., Schwadron, N., et al. 2019, 1225, 012007

Littlejohn, R. G. 1983, J. Plasma Phys., 29, 111

Littlejohn, R. G. 1988, Phys. Rev. A, 38, 6034

Luhmann, J. G., Ledvina, S. A., Odstrcil, D., et al. 2010, Adv. Space Res., 46, 1

Mahajan, S., Machabeli, G., Osmanov, Z., & Chkheidze, N. 2013, Scientific Reports, 3

Malkov, M. A. & Drury, L. O. 2001, Reports on Progress in Physics, 64, 429

Markovskii, S. A., Vasquez, B. J., Smith, C. W., & Hollweg, J. V. 2006, ApJ, 639, 1177

Marsh, M. S., Dalla, S., Kelly, J., & Laitinen, T. 2013, ApJ, 774, 4

Marshall, F. E. & Stone, E. C. 1978, J. Geophys. Res., 83, 3289

Mason, G. M., Desai, M. I., & Li, G. 2012, ApJ, 748, L31

Mason, G. M., Li, G., Cohen, C. M. S., et al. 2012a, ApJ, 761, 104

Mason, G. M., Li, G., Cohen, C. M. S., et al. 2012b, ApJ, 761, 104

Mason, G. M., Mazur, J. E., Dwyer, J. R., Reames, D. V., & von Rosenvinge, T. T. 1997, ApJ, 486, L149

Mason, G. M. & Sanderson, T. R. 1999, Space Sci. Rev., 89, 77

Mason, G. M., von Steiger, R., Decker, R. B., et al. 1999, Space Sci. Rev., 89, 327

Matsumoto, M. & Nishimura, T. 1998, ACM Trans. Model. Comput. Simul., 8, 3–30

Matthaeus, W. H., Bieber, J. W., Ruffolo, D., Chuychai, P., & Minnie, J. 2007, ApJ, 667, 956

Matthaeus, W. H. & Goldstein, M. L. 1982, J. Geophys. Res. Space Phys., 87, 10347

Matthaeus, W. H., Goldstein, M. L., & Roberts, D. A. 1990, J. Geophys. Res., 95, 20673

Matthaeus, W. H., Gray, P. C., Pontius, Jr., D. H., & Bieber, J. W. 1995, Phys. Rev. Lett., 75, 2136

Matthaeus, W. H., Qin, G., Bieber, J. W., & Zank, G. P. 2003, ApJ, 590, L53

Matthaeus, W. H. & Smith, C. 1981, Phys. Rev. A, 24, 2135

Matthaeus, W. H., Smith, C. W., & Bieber, J. W. 1999, AIP Conf. Ser., 471, 511

Mazur, J. E., Mason, G. M., Dwyer, J. R., et al. 2000, ApJ, 532, L79

McDonald, F. B., Cline, T. L., & Simnett, G. M. 1972, J. Geophys. Res. (1896-1977), 77, 2213

McKibben, R. B. 1972, J. Geophys. Res., 77, 3957

Meyer, P., Parker, E. N., & Simpson, J. A. 1956, Phys. Rev., 104, 768

Minnie, J., Bieber, J. W., Matthaeus, W. H., & Burger, R. A. 2007, ApJ, 670, 1149

Misner, C. W., Thorne, K. S., & Wheeler, J. A. 2017, Gravitation

Müller, D., Marsden, R. G., St. Cyr, O. C., & Gilbert, H. R. 2013, Sol. Phys., 285, 25

Müller, D., Zouganelis, I., St. Cyr, O. C., Gilbert, H. R., & Nieves-Chinchilla, T. 2020, Nat. Astron., 4, 205

Ng, C. K. & Reames, D. V. 1994, ApJ, 424, 1032

Ng, C. K. & Reames, D. V. 2008, ApJLetters, 686, L123

Odstrcil, D. 2003, Adv. Space Res., 32, 497

Odstrcil, D., Riley, P., & Zhao, X. P. 2004, J. Geophys. Res. Space Phys., 109, A02116

Odstrčil, D. & Pizzo, V. J. 1999, J. Geophys. Res., 104, 483

Øksendal, B. 2003, Stochastic Differential Equations: An Introduction with Applications, Hochschultext / Universitext (Springer)

Osmanov, Z., Mahajan, S., Machabeli, G., & Chkheidze, N. 2014, Mon. Not. R. Astron. Soc., 445, 4155

Pacheco, D., Agueda, N., Aran, A., Heber, B., & Lario, D. 2019, A&A, 624, A3

Pacheco, D., Agueda, N., Gómez-Herrero, R., & Aran, A. 2017, J. Space Weather Space Clim., 7

Parker, E. N. 1958, ApJ, 128, 664

Parker, E. N. 1965, Planet. Space Sci., 13, 9

Pesses, M. E., Eichler, D., & Jokipii, J. R. 1981, ApJ, 246, L85

Pierrard, V. & Lazar, M. 2010, Solar Physics, 267, 153

Pierre Auger Collaboration, Aab, A., Abreu, P., et al. 2017, Science, 357, 1266

Pilipp, W. G., Miggenrieder, H., Montgomery, M. D., et al. 1987, J. Geophys. Res. Space Phys., 92, 1075

Pizzo, V. J. 1991, J. Geophys. Res., 96, 5405

Pomoell, J., Aran, A., Jacobs, C., et al. 2015, J. Space Weather Space Clim., 5, A12

Pomoell, J. & Poedts, S. 2018, J. Space Weather Space Clim., 8, A35

Pomoell, J. & Vainio, R. 2012, ApJ, 745, 151

Potgieter, M. 2013, Living Rev. Sol. Phys., 10

Potgieter, M. S., Haasbroek, L. J., Ferrando, P., & Heber, B. 1997, Adv. Space Res., 19, 917

Potgieter, M. S., Le Roux, J. A., & Burger, R. A. 1989, J. Geophys. Res., 94, 2323

Potgieter, M. S. & Moraal, H. 1985, ApJ, 294, 425

Powell, K. G., Roe, P. L., Linde, T. J., Gombosi, T. I., & De Zeeuw, D. L. 1999, J. Comput. Phys., 154, 284

Prinsloo, P. L., Strauss, R. D., & Le Roux, J. A. 2019, ApJ, 878, 144

Ptuskin, V. S., Rogovaya, S. I., Zirakashvili, V. N., et al. 1993, A&A, 268, 726

Pyle, K. R. & Simpson, J. A. 1977, ApJ, 215, L89

Qin, G., Matthaeus, W. H., & Bieber, J. W. 2002a, ApJ, 578, L117

Qin, G., Matthaeus, W. H., & Bieber, J. W. 2002b, Geophys. Res. Lett., 29, 1048

Qin, G. & Shalchi, A. 2014, Applied Physics Research, 6, 1

Qin, G. & Shalchi, A. 2016, ApJ, 823, 23

Qin, G. & Wang, Y. 2015, ApJ, 809, 177

Qin, G., Zhang, M., Dwyer, J. R., Rassoul, H. K., & Mason, G. M. 2005, ApJ, 627, 562

Reames, D. V. 1999, Space Sci. Rev., 90, 413

Reames, D. V. 2009a, ApJ, 706, 844

Reames, D. V. 2009b, ApJ, 693, 812

Reames, D. V. 2013, Space Sci. Rev., 175, 53

Reames, D. V. 2017, Solar energetic particles: a modern primer on understanding sources, acceleration and propagation (Springer-Verlag)

Reames, D. V., Barbier, L. M., & Ng, C. K. 1996, ApJ, 466, 473

Reames, D. V., Barbier, L. M., Von Rosenvinge, et al. 1997a, ApJ, 483, 515

Reames, D. V., Kahler, S. W., & Ng, C. K. 1997b, ApJ, 491, 414

Reid, G. C. 1964, J. Geophys. Res., 69, 2659

Rice, W. K. M., Zank, G. P., & Li, G. 2003, J. Geophys. Res. Space Phys., 108, 1369

Richardson, I. G. 2004, Space Sci. Rev., 111, 267

Richardson, I. G. 2018, Living Rev. Sol. Phys., 15, 1

Richardson, I. G., von Rosenvinge, T. T., Cane, H. V., et al. 2014, Sol. Phys., 289, 3059

Riffert, H. 1986, ApJ, 310, 729

Riley, P., Linker, J. A., Lionello, R., & Mikic, Z. 2012, J. Atmos. Sol.-Terr. Phys, 83, 1

Rodríguez-Gasén, R., Aran, A., Sanahuja, B., Jacobs, C., & Poedts, S. 2011, Adv. Space Res., 47, 2140

Rodríguez-Gasén, R., Aran, A., Sanahuja, B., Jacobs, C., & Poedts, S. 2014, Sol. Phys., 289, 1745

Roelof, E. C. 1969, in Lectures in High-Energy Astrophysics, ed. H. Ögelman & J. R. Wayland, 111

Roelof, E. C., Gold, R. E., Simnett, G. M., et al. 1992, Geophys. Res. Lett., 19, 1243

Roth, I. & Temerin, M. 1997, ApJ, 477, 940

Roussev, I. I., Sokolov, I. V., Forbes, T. G., et al. 2004, ApJ, 605, L73

Ruffolo, D. 1995, ApJ, 442, 861

Ruffolo, D. & Matthaeus, W. H. 2013, Phys. Plasmas, 20, 012308

Russell, C. T., Mewaldt, R. A., Luhmann, J. G., et al. 2013, ApJ, 770, 38

Sanahuja, B. & Domingo, V. 1987, J. Geophys. Res. Space Phys., 92, 7280

Schlickeiser, R. 1989, ApJ, 336, 243

Schlickeiser, R. 2002, Cosmic Ray Astrophysics

Schlickeiser, R. 2011, ApJ, 732, 96

Schlickeiser, R. & Jenko, F. 2010, J. Plasma Phys., 76, 317–327

Schrijver, C. J., Dobbins, R., Murtagh, W., & Petrinec, S. M. 2014, Space Weather, 12, 487

Schrijver, C. J., Kauristie, K., Aylward, A. D., et al. 2015, Adv. Space Res., 55, 2745

Schrijver, C. J., Title, A. M., Yeates, A. R., & DeRosa, M. L. 2013, ApJ, 773, 93

Schwadron, N. A., Bale, S., Bonnell, J., et al. 2020, ApJS, 246, 33

Schwadron, N. A., Fisk, L. A., & Gloeckler, G. 1996, Geophys. Res. Lett., 23, 2871

Schwadron, N. A., Gorby, M., Török, T., et al. 2014, Space Weather, 12, 323

Schwadron, N. A., Lee, M. A., Gorby, M., et al. 2015, ApJ, 810, 97

Schwadron, N. A., Townsend, L., Kozarev, K., et al. 2010, Space Weather, 8, S00E02

Scolini, C., Rodriguez, L., Mierla, M., Pomoell, J., & Poedts, S. 2019, A&A, 626, A122

Scolini, C., Verbeke, C., Poedts, S., et al. 2018, Space Weather, 16, 754

Shalchi, A. 2005, Physics of Plasmas, 12, 052905

Shalchi, A. 2006, A&A, 453, L43

Shalchi, A. 2008, Plasma Physics and Controlled Fusion, 50, 055001

Shalchi, A., ed. 2009, Astrophys. Space Sci. Lib., Vol. 362, Nonlinear Cosmic Ray Diffusion Theories

Shalchi, A. 2010, ApJ, 720, L127

Shalchi, A. 2011, Adv. Space Res., 47, 1147

Shalchi, A., Bieber, J. W., & Matthaeus, W. H. 2004, ApJ, 604, 675

Shalchi, A., Li, G., & Zank, G. P. 2010, Ap&SS, 325, 99

Shalchi, A. & Weinhorst, B. 2009, Adv. Space Res., 43, 1429

Shalchi, A., Škoda, T., Tautz, R. C., & Schlickeiser, R. 2009, A&A, 507, 589

Skilling, J. 1971, ApJ, 170, 265

Smith, C. W., Hamilton, K., Vasquez, B. J., & Leamon, R. J. 2006, ApJ, 645, L85

Smith, E. J. & Wolfe, J. H. 1976, Geophys. Res. Lett., 3, 137

Sokolov, I. V., Roussev, I. I., Gombosi, T. I., et al. 2004, ApJ, 616, L171

Speiser, T. W. 1965, J. Geophys. Res., 70, 4219

Stone, E. C., Burlaga, L. F., Cummings, A. C., et al. 1990, AIP Conf. Proc., 203, 48

Stone, E. C., Cummings, A. C., McDonald, F. B., et al. 2005, Science, 309, 2017

Stone, E. C., Cummings, A. C., McDonald, F. B., et al. 2008, Nature, 454, 71

Strauss, R. D. & Fichtner, H. 2015, ApJ, 801, 29

Strauss, R. D. & le Roux, J. A. 2019, ApJ, 872, 125

Strauss, R. D., le Roux, J. A., Engelbrecht, N. E., Ruffolo, D., & Dunzlaff, P. 2016, ApJ, 825, 43

Strauss, R. D., Potgieter, M. S., Ferreira, S. E. S., Fichtner, H., & Scherer, K. 2013, ApJ, 765, L18

Strauss, R. D. T., Dresing, N., & Engelbrecht, N. E. 2017, ApJ, 837, 43

Strauss, R. D. T. & Effenberger, F. 2017, Space Sci. Rev., 212, 151

Tautz, R. C. & Shalchi, A. 2012, ApJ, 744, 125

Tautz, R. C., Shalchi, A., & Schlickeiser, R. 2008, ApJ, 685, L165

Taylor, G. I. 1922, Proc. London Math. Soc., s2-20, 196

Taylor, G. I. 1938, Proc. R. Soc. A, 164, 476

Teegarden, B. J., McDonald, F. B., Trainor, J. H., Webber, W. R., & Roelof, E. C. 1974, J. Geophys. Res. (1896-1977), 79, 3615

Temerin, M. & Roth, I. 1992, ApJ, 391, L105

Torsti, J., Kocharov, L. G., Vainio, R., Anttila, A., & Kovaltsov, G. A. 1996, Sol. Phys., 166, 135

Tsurutani, B. T., Ho, C. M., Arballo, J. K., Goldstein, B. E., & Balogh, A. 1995, Geophys. Res. Lett., 22, 3397

Tsurutani, B. T. & Lakhina, G. S. 1997, Reviews of Geophysics, 35, 491

Tsurutani, B. T., Smith, E. J., Pyle, K. R., & Simpson, J. A. 1982, J. Geophys. Res., 87, 7389

Tylka, A. J., Cohen, C. M. S., Dietrich, W. F., et al. 2005, ApJ, 625, 474

Tylka, A. J. & Lee, M. A. 2006, ApJ, 646, 1319

Vainio, R. 1998, PhD thesis, Dep. of Physics, FIN-20014 Turku University, Finland

Vainio, R. 2003, A&A, 406, 735

Vainio, R. & Afanasiev, A. 2018, Astrophys. Space Sci. Libr., Vol. 444, Particle Acceleration Mechanisms, ed. O. E. Malandraki & N. B. Crosby, 45–61

Vainio, R. & Laitinen, T. 2007, ApJ, 658, 622

Vainio, R. & Laitinen, T. 2008, J. Atmos. Sol.-Terr. Phys, 70, 467

Vainio, R., Pönni, A., Battarbee, M., et al. 2014, J. Space Weather Space Clim., 4, A08

Van den Berg, J. P. 2019, Master thesis, North-West University (South Africa)

van der Holst, B., Sokolov, I. V., Meng, X., et al. 2014, ApJ, 782, 81

Verbeke, C., Pomoell, J., & Poedts, S. 2019, A&A, 627, A111

Verkhoglyadova, O. P., Zank, G. P., & Li, G. 2015, Physics Reports, 557, 1

Völk, H. J. 1973, Ap&SS, 25, 471

Wang, Y. & Qin, G. 2015, ApJ, 806, 252

Wang, Y., Qin, G., & Zhang, M. 2012, ApJ, 752, 37

Wang, Y., Qin, G., Zhang, M., & Dalla, S. 2014, ApJ, 789, 157

Wang, Y.-M., Pick, M., & Mason, G. M. 2006, ApJ, 639, 495

Wawrzynczak, A., Modzelewska, R., & Kluczek, M. 2015, J. Phys.: Conf. Ser., 633, 012058

Webb, G. M. 1983, A&A, 127, 97

Webb, G. M. 1985, ApJ, 296, 319

Webb, G. M. & Gleeson, L. J. 1977, Ap&SS, 50, 205

Webb, G. M. & Gleeson, L. J. 1979, Ap&SS, 60, 335

Webb, G. M., Kota, J., Zank, G. P., & Lu, J. Y. 2001, Proc. ICRC, 8, 3326

Wiedenbeck, M. E., Mason, G. M., Cohen, C. M. S., et al. 2013, ApJ, 762, 54

Wijsen, N., Aran, A., Pomoell, J., & Poedts, S. 2019a, A&A, 622, A28

Wijsen, N., Aran, A., Pomoell, J., & Poedts, S. 2019b, A&A, 624, A47

Wijsen, N., Aran, A., Pomoell, J., & Poedts, S. 2019c, J. Phys.: Conf. Ser., 1332, 012018

Wijsen, N., Aran, A., Sanahuja, B., Pomoell, J., & Poedts, S. 2020, A&A, 634, A82

Woitas, J., Ray, T. P., Bacciotti, F., Davis, C. J., & Eislöffel, J. 2002, ApJ, 580, 336

Wu, S. T., Dryer, M., & Han, S. M. 1983, Sol. Phys., 84, 395

Wu, Z., Chen, Y., Li, G., et al. 2014, ApJ, 781, 17

Zank, G. P. 2014, Transport Processes in Space Physics and Astrophysics, Lecture Notes in Physics (New York: Springer-Verlag)

Zank, G. P., Li, G., Florinski, V., et al. 2006, J. Geophys. Res. Space Phys., 111, A06108

Zank, G. P., Pauls, H. L., Cairns, I. H., & Webb, G. M. 1996, J. Geophys. Res., 101, 457

Zank, G. P., Rice, W. K. M., le Roux, J. A., Cairns, I. H., & Webb, G. M. 2001, Physics of Plasmas, 8, 4560

Zhang, M. 1999, ApJ, 513, 409

Zhang, M. 2006, J. Geophys. Res. Space Phys., 111, A04208

Zhang, M., Qin, G., & Rassoul, H. 2009, ApJ, 692, 109

Zhao, L., Li, G., Ebert, R. W., et al. 2016, J. Geophys. Res. Space Phys., 121, 77

Curriculum Vitae

Nicolas Wijsen

PERSONAL DETAILS

Citizenship	Belgian
Birthdate	11 March 1994
Address	Kerkstraat 76, 9473 Welle, Belgium
Mobile	+32 478 99 73 08
E-Mail	nicolas.wijsen@gmail.com

EDUCATION

Double PhD – KU Leuven & University of Barcelona Oct. 2016 – Apr. 2020
PhD fellow at the Research Foundation - Flanders (FWO).
Centre for mathematical Plasma-Astrophysics, KU Leuven, Belgium
Institute of Cosmos Sciences, University of Barcelona, Spain
Supervisors: Prof. Dr. S. Poedts and Dr. A. Aran

Master Astronomy and Astrophysics – KU Leuven Sept. 2014 – June 2016
Greatest distinction with congratulations of the Board of Examiners

Master Thesis – KU Leuven & University of Helsinki
"Extrapolation of the Solar Coronal Magnetic Field by Means of an Optimization Method"
Supervisors: Prof. Dr. S. Poedts , Prof. Dr. E. Kilpua, Dr. J. Pomoell

Bachelor in Mathematics – KU Leuven Sept. 2011– Jul. 2014
Greatest distinction

SCIENTIFIC EXPERIENCE

Member of an International Space Science Institute (ISSI) team 2020–2021
"Using energetic electron and ion observations to investigate solar wind structures and infer solar wind magnetic field configurations"
Team leaders: Prof. Dr. G. Li and Dr. L. Wang
Bern, Switzerland and Bejing, China

Summer school: Towards Future Research on Space Weather 2 – 7 Jul. 2019
San Juan, Argentina

Research stay at the University of Barcelona 11 Mar. – 16 Nov. 2019
Research stay in the context of my double PhD.
Barcelona, Spain

Invited research visit to the North-West University 15 – 30 Sept. 2018
Collaboration with Prof. Dr. D. T. Strauss and his research team.
Potchefstroom, South Africa

Research stay at the University of Barcelona, Sept. 2017 – Aug. 2018
Research stay in the context of my double PhD.
Funded by the KU Leuven Junior Research Mobility Program (JuMo).
Barcelona, Spain

Heliospheric Summer School 1 – 8 Aug. 2017
NASA's Living With a Star program and the Cooperative Programs for the Advancement of Earth System Science.
Boulder, Colorado, USA

ERASMUS European Exchange Program Aug. 2015 – Dec. 2015
Master thesis research at the Space Physics Research Group of the University of Helsinki.
Helsinki, Finland

AWARDS

Astronomy & Astrophysics Prize – 1st place 30 June 2016
KU Leuven
The Astronomy & Astrophysics Prize is awarded to a student for achieving an outstanding result in the Master of Astronomy & Astrophysics education program. To win the price, the student has to graduate with “Greatest Distinction with Congratulations of the Examination Committee", and with the highest score among the students.

Paul Smeyers Prize – 1st place 30 June 2016
KU Leuven
The Paul Smeyers prijs honours a highly creditable master thesis in astronomy on the basis of the results of the second term of exams.

Odissea Prize – 2nd place 7 Mar. 2017
Federal Minister of Science and Belgian senate
The Odissea Award honors young graduates that accomplished an outstanding thesis in space research.

PEER-REVIEWED JOURNAL ARTICLES

Wijsen N., Aran A., Sanahuja B., Pomoell J., and Poedts S. 2020
The effect of drifts on the decay phase of SEP event,
A&A, forthcoming

Wijsen N., Aran A., Pomoell J., and Poedts S. Nov. 2019
Spreading protons in the heliosphere: a note on cross-field diffusion effects,
J. Phys.: Conf. Ser., 1332 012018

Wijsen N., Aran A., Pomoell J., and Poedts S. Apr. 2019
Interplanetary spread of solar energetic protons near a high-speed solar wind stream,
A&A, 624, A47

Wijsen N., Aran A., Pomoell J., and Poedts S. Jan. 2019
Modelling three-dimensional transport of solar energetic protons in a corotating interaction region generated with EUHFORIA
A&A, 622, A28

INVITED TALKS

"Modelling the acceleration and transport of energetic particles near an interplanetary CME" Jan. 2021
***Wijsen N.**, Pomoell J., Lario D., Aran A., et al.*
43th COSPAR Scientific Assembly, Sidney, Australia

"Modelling of solar energetic particles in a corotating interaction region" 21 Feb. 2019
***Wijsen N.**, Aran A., Pomoell J., and Poedts S.*
18th Annual International Astrophysics Conference, Pasadena, USA

"Modelling solar energetic particles with EUHFORIA" 18 Sept. 2018
***Wijsen N.**, Aran A., Pomoell J. and Poedts S.*
Colloquium at North-West University, Potchefstroom, South Africa

"Three-dimensional modelling of solar energetic particle events with EUHFORIA" 17 Jul. 2018
***Wijsen N.**, Aran A., Pomoell J., and Poedts S.*
42nd COSPAR Scientific Assembly, Pasadena, USA

CONTRIBUTED TALKS

"Solar energetic particles experience EUHFORIA's CMEs in PARADISE" 10 Dec. 2019
***Wijsen N.**, Aran A., Pomoell J., and Poedts S.*
AGU 2019 fall meeting, San Francisco, USA

"Modelling of solar energetic particles in a corotating interaction region" 4 Jul. 2019
***Wijsen N.**, Aran A., Pomoell J., and Poedts S.*
Towards Future Research on Space Weather Drivers, San Juan, Argentina

"On the transport of solar energetic protons near and within a corotating interaction region" 8 Apr. 2019
***Wijsen N.**, Aran A., Pomoell J., and Poedts S.*
EGU General Assembly 2019, Vienna, Austria

"A new model for realistic 3D simulations of solar energetic particle events" 2 Feb. 2018
***Wijsen N.**, Aran A., Pomoell J., and Poedts S.*
ICCUB Winter Meeting, Barcelona, Spain

CONTRIBUTED POSTERS

"Modelling the angular response of EPD/EPT: Application to the electron event observed on 21 April 2019" 10 Dec. 2019
Aran A., D. Pacheco, ***Wijsen N.****, D. Lario, et al.,*
AGU 2019 fall meeting, San Francisco, USA

"Solar energetic particles experience EUHFORIA's non-nominal solar winds in PARADISE" 19 Nov. 2019
Wijsen N.*, Aran A., Pomoell J., and Poedts S.*
16th European Space Weather Week, Liège, Belgium

"Modelling Solar Energetic Particle Events Using EUHFORIA" 5 Nov. 2018
Wijsen N.*, Aran A., Pomoell J., and Poedts S.*
15th European Space Weather Week, Leuven, Belgium

"Using EUHFORIA to study solar energetic particle events" 19 June 2018
Wijsen N.*, Aran A., Pomoell J., and Poedts S.*
15th International Solar Wind Conference, Brussels, Belgium

"Modelling Solar Energetic Particle Propagation in Realistic Heliospheric Solar Wind Conditions Using a Combined MHD and Stochastic Differential Equation Approach" 13 Dec. 2017
Wijsen N.*, Aran A., Pomoell J., and Poedts S.*
AGU 2017 Fall Meeting, New Orleans, Louisiana, USA

"Modelling Solar Energetic Particle Propagation in 3D Heliospheric Solar Wind Conditions" 30 Nov. 2017
Wijsen N.*, Aran A., Pomoell J., and Poedts S.*
14th European Space Weather Week, Ostend, Belgium

SCIENCE OUTREACH TALKS

"Predicting space weather: why is it important and how to do it" 19 Feb. 2018
Jornada d'Investigadors Predoctorals Interdisciplinària (JIPI)
Barcelona, Spain

TEACHING EXPERIENCE

Mathematics for geography students Feb. – Apr. 2020
Teaching assistant of exercise sessions.

Differential Equations for bio-engineers Sept. – Dec. 2018
Teaching assistant of exercise sessions.

Linear algebra for bio-engineers Feb. – June 2017
Teaching assistant of exercise sessions

Differential equations for bio-engineers Sept. – Dec. 2016
Teaching assistant of exercise sessions.

SKILLS

Languages	Dutch (native)
	English (fluent)
	French (good command)
	Spanish (good command)
Programming	Python, C++, Matlab, Maple, Java



FACULTY OF SCIENCE
DEPARTMENT OF MATHEMATICS
CENTRE FOR MATHEMATICAL PLASMA-ASTROPHYSICS
Celestijnenlaan 200B
B-3001 Leuven
nicolas.wijsen@gmail.com